

UNIVERSITÉ PARIS DIDEROT (Paris 7)

École doctorale d'Astronomie et Astrophysique d'Ile de France

# THÈSE

présentée pour obtenir le grade de

**Docteur en Sciences de l'Université Paris 7**

par

**DIANE CORMIER**

---

## The physical properties in the interstellar medium of low-metallicity dwarf galaxies

Thèse dirigée par : Dr. Suzanne MADDEN

Réalisée au Laboratoire AIM du CEA à Saclay

Soutenue le 26 Novembre 2012

### Membres du Jury :

Prof. Françoise COMBES	Examineur
Prof. Deidre HUNTER	Rapporteur
Prof. Jacques LE BOURLOT	Président du jury
Dr. Suzanne MADDEN	Directrice de thèse
Dr. Albrecht POGLITSCH	Examineur
Prof. Alexander TIELENS	Rapporteur



# Abstract

The *Herschel Space Observatory* offers a new far-infrared (FIR) view on the interstellar medium (ISM) cooling in galaxies, especially in dwarf galaxies thanks to the program “The *Herschel* Dwarf Galaxy Survey” (DGS). My thesis has focused on the study of the gas properties of the dwarf galaxies from the DGS, investigating the role of the most important MIR and FIR tracers from the multi-phase ISM, and particularly of the ionised and neutral gas coolants with *Herschel*. Complementary observations of the CO molecule that I obtained from ground-based telescopes have helped elucidate the structure and conditions of the low metallicity ISM.

We study the full DGS sample as well as compare this sample to more metal-rich galaxies. We find that the FIR lines, and particularly the [O III]  $88\mu\text{m}$  and [C II]  $157\mu\text{m}$  lines, are exceptionally bright in dwarf galaxies. They comprise a larger fraction of the total infrared luminosity  $L_{\text{TIR}}$  than in the more metal-rich sample, and together contribute up to a few percent of  $L_{\text{TIR}}$ , indicating enhanced cooling of the gas. Bright [O I] lines trace the presence of photodissociation regions (PDRs), while the high [C II]/TIR and [O III]/TIR ratios indicate the presence of diffuse gas with large volume filling factor and UV photons escaping far from the H II regions. We have also obtained new CO data in a subsample of the DGS that confirms the faintness of CO compared to  $L_{\text{TIR}}$  and the FIR cooling lines at low metallicity. CO emission is likely to arise from small molecular clumps of very low filling factors, diluted in single-dish observations. This is evidence for large-scale photodissociation and translates in high [C II]/CO(1-0) ratios which, in the Local Group Magellanic type galaxy NGC 4214, for example, can be interpreted in terms of evolution of the different star-forming regions.

Observations are interpreted with radiative transfer models to determine the physical conditions of the gas. As a benchmark case, I have focused on one galaxy of the DGS, the starburst Haro 11, and modeled its multi-phase ISM, considering all of the good signal-to-noise (S/N) MIR and FIR spectral lines from *Spitzer* and *Herschel* ( $\sim 20$  lines). Haro 11 is modeled with 3 main gas components: a compact H II region, dense PDRs with very low volume filling factor, and an extended diffuse ionised/neutral medium. This modeling step not only confirms the leaky ISM picture, but enables us to derive conditions of the gas (density, radiation field, filling factors), and to establish a complete mass budget of the different phases modeled. In particular, we find a CO-to-H<sub>2</sub> conversion factor,  $X_{\text{CO}}$ , higher than that of the Galaxy and a large reservoir of unseen dark gas. Nevertheless, Haro 11 is an outlier on the Schmidt-Kennicutt law, pointing out the role of environment (merger in this case) in the star formation process.

**Keywords:** interstellar medium; ISM phases; H II regions; photodissociation regions; molecular clouds; fine-structure cooling lines; infrared; FIR spectroscopy; starbursts; dwarf galaxies; blue compact dwarfs; metallicity; dust; star formation.





# Résumé

Le télescope spatial *Herschel* offre une nouvelle vue sur le refroidissement du milieu interstellaire (MIS) des galaxies dans l’infra-rouge lointain (FIR), et en particulier des galaxies naines grâce au programme “The *Herschel* Dwarf Galaxy Survey” (DGS). Le MIS des galaxies naines présente des signatures très différentes des galaxies normales, plus riche en métaux. Il est notamment fortement affecté et sculpté par les vents stellaires et leur environnement, contrôlant l’évolution globale de ces galaxies. L’actuelle présence d’une intense activité de formation d’étoiles et faible métallicité ont pour conséquence de réarranger l’organisation des multiples phases constituant le MIS de ces galaxies. La modification de la structure du nuage résulte observationnellement dans des propriétés du gaz et de la poussière intéressantes, qui incluent une émission accrue de la poussière chaude, un excès d’émission dans le submillimétrique, des raies de structure fine intenses, et peu de gaz moléculaire observé par rapport à leur apparente activité de formation d’étoiles. Cela reflète aussi des processus de chauffage et de refroidissement dominants et une possible répartition des mécanismes physiques jouant sur la formation d’étoiles différents (voir Chapitre 1).

Mon travail de thèse repose sur l’étude des propriétés du gaz des galaxies naines du DGS, qui sont des galaxies de l’Univers Local riches en gaz, à faible métallicité, et formant activement des étoiles. Elles ont peut-être joué un rôle important dans l’Univers jeune. J’ai examiné le rôle des traceurs les plus importants dans l’infra-rouge moyen et lointain du MIS multi-phases, et en particulier des refroidisseurs du gaz ionisé et du gaz neutre avec *Herschel*. Des observations complémentaires de la molécule CO, que j’ai obtenues grâce à des télescopes au sol, ont aidé à mieux comprendre la structure et les conditions physiques du MIS à faible métallicité.

Si les premières observations des raies de structure fine FIR dans les galaxies naines grâce aux télescopes *KAO* et *ISO* révèlent des raies intenses, *Herschel* confirme cela de manière statistique, accédant à de plus faibles métallicités et plus faibles brillances de surface. Le DGS a été conçu pour étudier les propriétés du gaz et de la poussière dans 48 galaxies naines proches à faible métallicité.

Une partie de mon travail a été dédiée à la réduction de l’ensemble des données spectroscopiques du DGS de l’instrument *Herschel*/PACS qui comprennent les raies FIR : [C II]  $157\mu\text{m}$ , [O I]  $63$  et  $145\mu\text{m}$ , [O III]  $88\mu\text{m}$ , [N III]  $57\mu\text{m}$ , [N II]  $122$  et  $205\mu\text{m}$  (Chapitre 2). J’ai, pour cela, contribué à certains scripts de réduction du pipeline spectroscopique *Herschel*/PACS et au logiciel de créations de cartes PACSman (Lebouteiller et al. 2012), spécifiquement développé pour PACS. Les données spectroscopiques PACS représentent 160 h du programme DGS. Toutes les galaxies naines ont été observées en [C II]  $157\mu\text{m}$ , la plupart en [O I]  $63\mu\text{m}$  et [O III]  $88\mu\text{m}$ , et quelques unes en [O I]  $145\mu\text{m}$ , [N III]  $57\mu\text{m}$ , [N II]  $122$  et  $205\mu\text{m}$ . Les cartes de flux et profils de raies sont présentés en Appendix B.

Dans l’interprétation de ces données, j’ai comparé cet échantillon de galaxies naines avec des galaxies plus riches en métaux, en étudiant les possibles corrélations des raies FIR avec des paramètres globaux (métallicité,  $L_{\text{TIR}}$ , photométrie à 60 and 100  $\mu\text{m}$ , voir Chapitre 3). Nous trouvons que les raies FIR, et tout particulièrement les raies de [O III] 88  $\mu\text{m}$  et de [C II] 157  $\mu\text{m}$ , sont très brillantes dans les galaxies naines. Ces raies représentent une fraction plus importante de la luminosité infrarouge totale  $L_{\text{TIR}}$  dans les galaxies naines que dans les galaxies plus riches en métaux, remplissant un espace de paramètres parfois très différent. Ensemble, les raies FIR contribuent à hauteur de quelques pourcents de  $L_{\text{TIR}}$ , indiquant un conséquent refroidissement du gaz à l’échelle de la galaxie. Lorsque l’on zoome sur les régions actives des Nuages de Magellan, les rapports de luminosité de raies sur  $L_{\text{TIR}}$  apparaissent globalement plus élevés que les valeurs intégrées sur les galaxies entières, ce qui confirme que les galaxies naines sont dominées par l’émission de leur régions de formation d’étoiles même à très grande échelle. Les raies de [O I] sont brillantes et montrent la présence de régions de photodissociation (PDRs), alors que les rapports élevés de [C II]/TIR et [O III]/TIR indiquent la présence de gaz diffus remplissant une grande fraction du volume, et des photons ultra-violet (UV) qui parcourent de grandes distances au-delà des régions H II. Cependant, des structures et facteurs de remplissage différents peuvent être responsables de l’écart observé dans les valeurs de [C II]/TIR. Les rapports de raies peuvent être interprétés en termes d’excitation des différentes raies FIR.

Nous avons aussi acquis de nouvelles données CO pour un sous-échantillon du DGS (Chapitre 5), et observé les transitions de CO J $\rightarrow$ 1-0, CO J $\rightarrow$ 2-1, et CO J $\rightarrow$ 3-2, grâce aux télescopes au sol *Mopra*, *APEX*, et *IRAM*. Sur 6 galaxies observées, 5 sont détectées dans au moins une de ces transitions de CO, dont 2 galaxies qui n’avaient jamais été détectées en CO auparavant. Ces observations confirment la faible intensité de CO à faible métallicité par rapport à  $L_{\text{TIR}}$  et à l’intensité des raies de refroidissement FIR. Toutes ces galaxies, excepté Haro 11, semblent être dominées par leur réservoir de gaz H I plutôt que par leur réservoir gaz moléculaire. L’émission de CO provient certainement de nuages moléculaires fragmentés remplissant un volume négligeable, dilués dans les observations à antenne unique. Cela témoigne du processus de photodissociation à grande échelle, et se traduit en rapport [C II]/CO(1-0) élevé qui, dans le cas de la galaxie irrégulière du Groupe Local NGC 4214, par exemple, s’interprète en terme d’évolution des différentes régions de formation d’étoiles (Cormier et al. 2010).

Les observations sont interprétées par l’utilisation de modèles de transfert radiatifs afin de déterminer les conditions physiques du gaz. Comme étude de référence, je me suis concentrée sur une galaxie du DGS, la galaxie bleue compacte Haro 11, et j’ai modélisé son MIS multi-phases en considérant toutes les raies de l’infrarouge moyen et lointain avec un bon signal-sur-bruit provenant des télescopes *Spitzer* et *Herschel* ( $\sim 20$  raies spectrales). Le modèle de Haro 11 est constitué de 3 composantes de gaz principales : une région H II compacte, des PDRs denses à faible facteur de remplissage, et un milieu diffus ionisé/neutre étendu (Cormier et al. 2012a). Cette étape de modélisation permet non seulement de confirmer l’image d’un MIS poreux établie précédemment, mais aussi de déterminer les conditions caractérisant le gaz (densité, champs de radiation, facteurs de remplissage), et d’établir un bilan complet en masse des différentes phases du MIS modélisées. En particulier, nous trouvons un facteur de conversion CO-H<sub>2</sub>,  $X_{\text{CO}}$ , plus grand que la valeur de la Galaxie, et un important réservoir de gaz sombre. Cependant, Haro 11 reste en désaccord avec la relation de Schmidt-Kennicutt,

mettant un avant le rôle de l'environnement (fusion de galaxies dans ce cas) dans le processus de formation d'étoiles.

Ce travail sur les galaxies naines présente cependant des limitations observationnelles et de modélisation, notamment pour la phase moléculaire, dans la mesure où la distribution des sources d'émission et principaux processus contrôlant cette émission à faible métallicité ne sont pas connus. Si l'effet de champs magnétiques ou de la turbulence a été brièvement abordé ici, le rôle de l'énergie mécanique, des rayons cosmiques, ou de chocs n'a pas été traité. Une meilleure description du MIS à faible métallicité sera possible grâce des observations à haute résolution spatiale et spectrale, avec, par exemple, l'interféromètre *ALMA*. Ce type d'étude sera très important pour comprendre et interpréter les observations des galaxies à haut redshift. Si *ALMA* dévoile les phases froides du MIS dans le submm pour les galaxies proches, les raies FIR sont à présent accessibles à haut redshift.

**Mots-clés :** milieu interstellaire ; phases du MIS ; régions H II ; régions de photodissociation ; nuages moléculaires ; raies de structure fine de refroidissement ; infra-rouge ; spectroscopie FIR ; flambée de formation d'étoiles ; galaxies naines ; galaxies bleues compactes ; métallicité ; poussière ; formation d'étoiles.



# Contents

<b>Introduction</b>	<b>2</b>
<b>1 The Interstellar Medium of Dwarf Galaxies</b>	<b>3</b>
1.1 Properties of Dwarf Galaxies	4
1.1.1 Definition and classification	4
1.1.2 Galaxy evolution and star formation histories	6
1.1.3 Metallicity and ISM enrichment	10
1.1.4 Dynamics and Morphology	13
1.1.5 Motivations	15
1.2 Phases of the Interstellar Medium	15
1.2.1 Ionised phase	15
1.2.2 Neutral atomic phase	16
1.2.3 Molecular phase	17
1.2.4 Observable tracers	18
1.2.5 Spectral energy distribution	26
1.3 Metallicity effect on the ISM of dwarf galaxies	27
1.3.1 Dust properties	27
1.3.2 Gas properties	29
1.3.3 Open questions	38
<b>2 The <i>Herschel</i> telescope</b>	<b>41</b>
2.1 The <i>Herschel</i> Mission	42
2.1.1 General description	42
2.1.2 Comparison to pre- <i>Herschel</i> facilities	42
2.1.3 Low metallicity galaxies observed with <i>Herschel</i>	42
2.1.4 The Dwarf Galaxy Survey	44
2.2 The PACS Spectrometer	49
2.2.1 Technical specifications	49
2.2.2 Data processing	51
2.2.3 Global flux extraction	54
<b>3 <i>Herschel</i> results of the Dwarf Galaxies</b>	<b>57</b>
3.1 <i>Herschel</i> data of the DGS sample	58
3.1.1 Statistics on the observations	58
3.1.2 Line fluxes of the DGS galaxies	59
3.2 Correlation diagrams and ISM properties	62
3.2.1 Method	62
3.2.2 Lack of trend with metallicity: Figure 3.2	63

3.2.3	PACS line ratios . . . . .	65
3.2.4	Relation of FIR fine-structure lines with $L_{TIR}$ , star formation indicator . . . . .	70
3.2.5	Conclusions . . . . .	77
3.3	A look into the ISM of the nearby Magellanic-type dwarf galaxy NGC 4214 . . . . .	78
3.3.1	Properties of the Local Group galaxy, NGC 4214 . . . . .	78
3.3.2	<i>Herschel</i> /PACS spectral maps . . . . .	78
3.3.3	Conditions in the 3 star-forming regions . . . . .	78
3.3.4	Need for higher spatial/spectral resolution . . . . .	81
3.3.5	Paper published in A&A, 2010, 518, 57 . . . . .	82
<b>4</b>	<b>Modeling the Interstellar Medium of Dwarf Galaxies</b>	<b>87</b>
4.1	Modeling State of the Art . . . . .	88
4.1.1	From LTE to radiative transfer . . . . .	88
4.1.2	Existing PDR models and specific use . . . . .	91
4.2	A multi-phase picture of the Interstellar Medium of Haro 11 . . . . .	93
4.2.1	Description of the method . . . . .	93
4.2.2	Paper accepted in A&A, August 28 2012 . . . . .	96
<b>5</b>	<b>Probing the cold Interstellar Medium of Dwarf Galaxies</b>	<b>121</b>
5.1	Ground-based CO observations . . . . .	122
5.1.1	A few tools for Radio Astronomy . . . . .	122
5.1.2	Sample selection . . . . .	124
5.1.3	Mopra observations . . . . .	128
5.1.4	APEX observations . . . . .	129
5.1.5	IRAM observations . . . . .	130
5.2	Empirical diagnostics . . . . .	130
5.2.1	Line ratios . . . . .	130
5.2.2	Molecular gas mass . . . . .	133
5.2.3	RADEX model . . . . .	134
5.3	Detailed modeling of Haro 11 . . . . .	135
5.3.1	Rotational diagrams of the $H_2$ molecule . . . . .	135
5.3.2	Full radiative transfer modeling . . . . .	136
5.4	Star formation and total gas reservoir . . . . .	140
5.4.1	Star formation tracers . . . . .	140
5.4.2	Which gas phase is fuelling the star formation? . . . . .	141
5.4.3	Gas depletion times . . . . .	143
5.5	Conclusions on the molecular gas reservoir . . . . .	144
<b>6</b>	<b>Discussion</b>	<b>145</b>
6.1	Limitations of this work . . . . .	146
6.1.1	Observational limits . . . . .	146
6.1.2	Modeling limits . . . . .	147
6.2	Perspectives . . . . .	150
6.2.1	<i>SOFIA</i> . . . . .	150
6.2.2	<i>ALMA</i> . . . . .	151
6.2.3	<i>CCAT</i> . . . . .	154
6.2.4	Calibrating tracers of star formation . . . . .	154
6.2.5	Multi-phase analysis . . . . .	154

Conclusions .....	157
Acknowledgements .....	159
Glossary .....	161
Appendices .....	163
A The Dwarf Galaxy Sample – Observing information	163
B The Dwarf Galaxy Sample – Spectral maps and line profiles	167
Bibliography .....	175





# List of Figures

1.1	Schematic of the ISM phases. . . . .	16
1.2	Photoelectric effect on grains and PAHs. . . . .	17
1.3	Diagrams of the FIR fine-structure levels. . . . .	20
1.4	Theoretical ratios of [C II] and [N II] with density. . . . .	21
1.5	Excitation potentials and critical densities for <i>Spitzer</i> and <i>Herschel</i> lines. . . . .	25
1.6	Extinction curves of the Milky Way and Magellanic Clouds. . . . .	26
1.7	Synthetic spectral energy distribution of a galaxy. . . . .	27
1.8	SED comparison of 5 different spectral type galaxies. . . . .	28
1.9	Illustration of the cloud onion structure. . . . .	32
1.10	Variation of $\alpha_{CO}$ with metallicity. . . . .	34
1.11	[C II] and CO(1-0) intensities as a function of metallicity. . . . .	36
1.12	$L_{[CII]}/L_{FIR}$ versus $L_{CO}/L_{FIR}$ . . . . .	37
2.1	Metallicity and stellar mass histograms for the DGS. . . . .	45
2.2	Path of light in the PACS spectrometer optical train. . . . .	49
2.3	PACS line sensitivities. . . . .	50
2.4	Telescope movement in the different PACS observing modes. . . . .	51
2.5	PACS data reduction steps with HIPE. . . . .	52
2.6	PACSMAN line fitting and map projection for II Zw 40. . . . .	54
2.7	PACSMAN flux extraction for II Zw 40. . . . .	55
2.8	PACS point source correction. . . . .	56
3.1	Histogram of observed and detected lines in the DGS. . . . .	59
3.2	PACS lines – metallicity diagnostics. . . . .	64
3.3	[O III]/[C II] versus 60/100 $\mu$ m and $L_{TIR}$ . . . . .	66
3.4	[O I]63/[C II] versus 60/100 $\mu$ m and $L_{TIR}$ . . . . .	67
3.5	[O III]/[O I]63 versus 60/100 $\mu$ m and $L_{TIR}$ . . . . .	68
3.6	[O I]145/[O I]63 versus 60/100 $\mu$ m and $L_{TIR}$ . . . . .	69
3.7	[N II]122/[C II] versus 60/100 $\mu$ m and $L_{TIR}$ . . . . .	69
3.8	[O III]/[N II]122 versus 60/100 $\mu$ m and $L_{TIR}$ . . . . .	71
3.9	[N III]/[N II]122 versus 60/100 $\mu$ m and $L_{TIR}$ . . . . .	71
3.10	[C II]157 / TIR versus 60/100 $\mu$ m and $L_{TIR}$ . . . . .	73
3.11	[O I]63 / TIR versus 60/100 $\mu$ m and $L_{TIR}$ . . . . .	73
3.12	[O I]145 / TIR versus 60/100 $\mu$ m and $L_{TIR}$ . . . . .	74
3.13	([C II]157+[O I]63) / TIR versus 60/100 $\mu$ m and $L_{TIR}$ . . . . .	75
3.14	[O III]88 / TIR versus 60/100 $\mu$ m and $L_{TIR}$ . . . . .	76
3.15	([C II]157+[O I]63+[O III]88) / TIR versus 60/100 $\mu$ m and $L_{TIR}$ . . . . .	76
3.16	NGC 4214 <i>HST</i> , PACS, and <i>OVRO</i> maps. . . . .	79

3.17	NGC 4214 individual SEDs. . . . .	80
3.18	NGC 4214 KOSMA- $\tau$ PDR diagnostic. . . . .	81
4.1	Cloud geometries in PDR models. . . . .	92
4.2	Input and output parameters of the CLOUDY models. . . . .	94
4.3	Stellar spectra from STARBURST99. . . . .	95
4.4	Hydrogen, density, and temperature profiles with CLOUDY. . . . .	97
5.1	Atmospheric transmission in the submm. . . . .	123
5.2	<i>HST</i> images with CO beams for 6 dwarf galaxies of the DGS. . . . .	126
5.3	<i>Mopra</i> CO(1-0) spectra. . . . .	129
5.4	<i>APEX</i> CO(2-1) and CO(3-2) spectra. . . . .	131
5.5	<i>IRAM</i> CO(1-0) and CO(2-1) spectra. . . . .	132
5.6	RADEX modeling of the CO data. . . . .	136
5.7	H <sub>2</sub> excitation diagrams for Haro 11. . . . .	137
5.8	Schematic of the CLOUDY model layers. . . . .	138
5.9	CO luminosities predicted with CLOUDY. . . . .	139
5.10	Temperature profile and CO ratios in the molecular phase with CLOUDY. . . . .	140
5.11	[C II], CO(1-0), and L <sub>TIR</sub> . . . . .	141
5.12	Observed $\Sigma_{\text{SFR}}$ versus $\Sigma_{\text{gas}}$ . . . . .	142
5.13	Modeled $\Sigma_{\text{SFR}}$ versus $\Sigma_{\text{gas}}$ for Haro 11. . . . .	143
6.1	Simulated <i>SOFIA</i> /GREAT spectra of NGC 4214. . . . .	152
6.2	Simulated <i>ALMA</i> observations of Haro 11. . . . .	153
6.3	<i>Herschel</i> /FTS spectrum and SLED of 30Doradus. . . . .	155
6.4	Strategy of a multi-phase modeling of galaxies. . . . .	156

# List of Tables

1.1	Global parameters of dwarf galaxies. . . . .	6
1.2	General properties of selected fine-structure cooling lines. . . . .	24
2.1	Telescope capabilities comparison. . . . .	42
2.2	General properties of the DGS sample . . . . .	47
3.1	Line fluxes of the DGS galaxies. . . . .	60
3.2	PACS line and line-to-TIR median ratios of the DGS galaxies. . . . .	65
5.1	Radio antennas general specifications. . . . .	124
5.2	General properties of the dwarf subsample. . . . .	127
5.3	New CO fluxes. . . . .	133
5.4	CO line ratios. . . . .	134
5.5	Observed H <sub>2</sub> masses using $X_{\text{CO}}$ . . . . .	135
5.6	Star formation rates. . . . .	140
A.1	Technical details on the DGS observations. . . . .	163



# Introduction

The interstellar medium of dwarf galaxies shows different signatures than normal metal-rich galaxies. With low mass, low metallicity, their ISM can be strongly affected by stellar winds and the environment, controlling the global evolution of those galaxies. In this work, we are particularly interested in low metallicity star-forming dwarf galaxies of the Local Universe, which are gas-rich and show evident ongoing star formation. These may be examples of galaxies which have played important roles in the early Universe. The intrinsic characteristics of these low metallicity dwarf galaxies result in interesting dust and gas properties, with enhanced warm dust emission, submillimeter excess emission, strong fine-structure lines, and little observed molecular gas compared to the observed star formation activity.

One of the most important consequences of the low metallicity ISM and presence of young ongoing star formation is a rearrangement of the multiple phases that constitute the ISM. The modification of the cloud structure, with smaller molecular cores, and hence of the global ISM structure, results observationally in the prevalence/deficit of specific ISM tracers, namely the FIR fine-structure/molecular lines. This also reflects dominant cooling and heating processes and the possible different distribution of the physical mechanisms acting on the star formation process (Chapter 1).

First evidence of bright FIR cooling lines in dwarf galaxies was brought by the *Kuiper Airborn Observatory* (KAO) and the *Infrared Space Observatory* (ISO), and *Herschel* confirms this with statistical grounds going to lower metallicities, fainter objects, and accessing important fainter FIR lines than previous studies. The “*Herschel* Dwarf Galaxy Survey” (DGS) is designed to investigate the dust and gas properties in 48 nearby low metallicity dwarf galaxies.

Part of my work was dedicated to the reduction of *Herschel*/PACS spectroscopy data (Chapter 2), and their interpretation, studying correlations with global tracers (metallicity,  $L_{\text{TIR}}$ , 60 and 100  $\mu\text{m}$  colors, see Chapter 3). To go beyond this empirical analysis, we investigate the physical conditions of the different ISM phases using PDR models (Chapter 4). We adopt a multi-phase approach to self-consistently model the observed dust and gas emission from the UV to the submillimeter wavelength range. To elucidate the obvious contrast between observed active star formation and lack of molecular gas in dwarf galaxies, we have obtained new molecular data of low-J CO lines. This enables us to establish mass budgets and discuss the star formation law in these galaxies (Chapter 5). Knowing the mass repartition is essential to understand what gas phase plays a (in)direct role in star formation. We stress observational and theoretical limitations of the method employed to get to the ISM physical conditions, and draw precautions in the interpretation of models, especially for the molecular gas of dwarf galaxies (Chapter 6). A better description of the low metallicity ISM should arise from high resolution (spatial or spectral) data, with, e.g., the *Stratospheric Observatory For Infrared Astronomy* (SOFIA) and the *Atacama Large Millimeter Array* (ALMA). In the

---

long term, this line of work in dwarf galaxies will be important to understand and interpret observations of high-redshift galaxies.

# Chapter 1

## The Interstellar Medium of Dwarf Galaxies

### Contents

---

<b>1.1</b>	<b>Properties of Dwarf Galaxies</b>	<b>4</b>
1.1.1	Definition and classification	4
1.1.2	Galaxy evolution and star formation histories	6
1.1.3	Metallicity and ISM enrichment	10
1.1.4	Dynamics and Morphology	13
1.1.5	Motivations	15
<b>1.2</b>	<b>Phases of the Interstellar Medium</b>	<b>15</b>
1.2.1	Ionised phase	15
1.2.2	Neutral atomic phase	16
1.2.3	Molecular phase	17
1.2.4	Observable tracers	18
1.2.5	Spectral energy distribution	26
<b>1.3</b>	<b>Metallicity effect on the ISM of dwarf galaxies</b>	<b>27</b>
1.3.1	Dust properties	27
1.3.2	Gas properties	29
1.3.3	Open questions	38

---

This Chapter aims to give an overview of our current understanding of the ISM of dwarf galaxies. General properties of dwarf galaxies and their interest as astronomical subjects are outlined in Section 1.1, with an emphasis on star-forming dwarf galaxies, the focus of my thesis work. A more detailed description of the ISM composition, and dust and gas properties at low metallicity are presented in Section 1.2 and 1.3.

## 1.1 Properties of Dwarf Galaxies

### 1.1.1 Definition and classification

#### General characteristics

The exact criteria to define a dwarf galaxy are not strictly defined, although it is accepted that they are generally small in size (e.g.  $R_{25}$  radius; typically  $R_{25} < 5$  kpc), with low luminosity (e.g. absolute  $V$ -band magnitude  $M_V$ ;  $-6 < M_V < -18$  mag), low surface brightness ( $\mu$ ), and low mass ( $M_{total}$ , dynamical mass;  $10^6 < M_{total} < 10^{10} M_\odot$ ). In that perspective both luminosity or mass criteria could be used. The threshold of  $M_V = -18$  mag is often adopted to distinguish dwarfs from normal, more massive galaxies (e.g. [Thuan & Martin 1981](#)). In terms of mass, galaxies with mass  $M_{total} < 10^{10} M_\odot$  can be considered as dwarfs. Dwarf galaxies are usually relatively simple systems with stars bathing in an ISM material gravitationally bound. Their stellar content can be as high as  $10^9$  stars, on the order of several hundred times less than that of the Milky Way. Their star formation can be bursty to quasi-continuous with sporadic bursts (see Section 1.1.2).

Dwarf galaxies are the most common type of galaxy in the universe, but their low surface brightness restricts their study to the nearby universe, in which they contribute to  $\sim 10\%$  of the total luminosity density. The Local Group contains  $\sim 100$  galaxies out to a distance of about 3 Mpc, 70 of them being dwarf galaxies ([McConnachie 2012](#)). As an extreme example, Ursa Minor (DDO 199) is a dwarf spheroidal close to the Milky Way with  $M_V = -8.9$  mag,  $L_V = 3 \times 10^5 L_\odot$ ,  $M_{total} = 2 \times 10^7 M_\odot$ , and  $M_{HI}/L_B \leq 0.25 M_\odot/L_\odot$ .

#### Morphological classification

A morphological classification emerges from [van den Bergh \(1959\)](#) to sort out dwarf galaxies, which is completed by [Grebel \(2001\)](#). We summarize the general properties of each category in Table 1.1, for a rough comparison, knowing that properties are not unique even within a morphological type.

1. **Dwarf Spirals (dS):** are the small-size equivalents of large spiral galaxies, with clear arm patterns. They are symmetric with both a disk and a bulge component, and are usually more massive than the other types of dwarfs. They are characterised by central surface brightness  $\mu_V \geq 23$  mag arcsec $^{-2}$ ,  $M_{HI} \leq 10^9 M_\odot$ , and  $M_{total} \leq 10^{10} M_\odot$ . They are found in clusters and in the field. They show rotation and are gas-rich.
2. **Dwarf Irregulars (dIrr):** exhibit irregular shapes, especially from the optical, with scattered bright H II regions. They are well described by exponential surface brightness profiles. They are characterised by  $\mu_V \leq 23$  mag arcsec $^{-2}$ ,  $M_{HI} \leq 10^9 M_\odot$ , and  $M_{total} \leq 10^{10} M_\odot$ . They are found in clusters, groups, and in the field. The most massive have well defined rotation curves, with rotation velocities on the order of  $\sim 60$  km s $^{-1}$ . They have large gaseous contents. The H I is clumpy near the sites of star formation (e.g. [Hodge et al. 1991](#)), with diffuse warmer emission all around ([Young & Lo 1996, 1997](#)). They



all host H II regions of sizes a few hundreds parsecs with very different morphologies determined from H $\alpha$  (Hunter et al. 1993). The center of H I emission coincides with the optical center in most cases, but it can be off-centered or presenting a ring-like structure.

3. **Blue Compact Dwarfs (BCD):** have no specific shape but usually consist of several concentrated star clusters as they are compact star-forming galaxies, also referred to as H II galaxies. Their name arises from blue colors (measured in the  $B$ -band with  $M_B$ ) of young hot massive stars due to recent burst of star formation. They are characterised by  $\mu_V \leq 19$  mag arcsec $^{-2}$ ,  $M_{HI} \leq 10^9 M_\odot$ , and  $M_{total} \leq 10^{10} M_\odot$ . They are usually found isolated. They show rotation and a large reservoir of gas.
4. **Dwarf Ellipticals (dE):** exhibit spherical or elliptical shapes, with compact central stellar densities. They are characterised by  $\mu_V \leq 21$  mag arcsec $^{-2}$ ,  $M_V > -17$  mag,  $M_{HI} \leq 10^8 M_\odot$ , and  $M_{total} \leq 10^9 M_\odot$ . They are found close to more massive galaxies. They show no rotation and little gaseous content with often asymmetric distribution and distinct kinematics. There is a subcategory of nucleated dwarfs, which have luminous H II knots forming a nuclei but no global structure.
5. **Dwarf Spheroidals (dSph):** exhibit a spheroidal shape and are the faintest and least massive of the dwarf galaxies. They are characterised by  $\mu_V \geq 22$  mag arcsec $^{-2}$ ,  $M_V > -14$  mag,  $M_{HI} \leq 10^5 M_\odot$ , and  $M_{total} \sim 10^7 M_\odot$ . They show no rotation, no central concentration, and have very little gaseous content. The H I is diffuse, usually spatially offset from the optical and they usually do not have H II emission.
6. **Tidal Dwarfs:** are a specific category of dwarf galaxies that form out of debris from a merger event or interactions with more massive galaxies. Hence their characteristics (mass, size, gas content, etc.) depend essentially on the progenitor. In particular, they do not contain dark matter (or very little), they may exhibit higher metallicities and can be more massive ( $M_{HI} \sim 2 \times 10^9 M_\odot$ ) than classical dwarf galaxies (Duc & Mirabel 1999). Their relation to the other types of dwarfs is unclear. Numerical simulations show that a fraction of a few percent or more of dwarf satellites may have a tidal origin (Bournaud 2010).

The smaller dwarfs are early-type, rather symmetric and spheroidal, and the largest ( $>500$ pc) are late-type irregulars. Between the dIrr and dSph are the transition types. How a proto-dwarf galaxy becomes one of these galaxy types is not known. There is no unified evolutionary scenario to explain the different types of dwarf galaxies and links between those types. Evolution can be internal, relying on initial conditions (angular momentum, strength of the first burst – Skillman & Bender (1995)), or external, relying on the environment, with end products elliptical and spheroidal early-type galaxies (Kunth & Östlin 2000).

Beyond these specifications, most dwarf galaxies are unique individuals. In particular, they span a large range of luminosities, metallicities (down to  $1/50 Z_\odot$  for I Zw 18), and star formation histories. *The sample of dwarf galaxies analysed in this work consist of BCDs and star-forming irregular galaxies. Both categories are gas-rich, forming stars, and, in general, slow solid-body rotators.*

**Table 1.1.** Global parameters of dwarf galaxies.

Parameters	Galaxy type					
	dS	dIrr	BCD	dE	dSph	Milky Way
$M_V$ [mag]	$>-18$	$>-16$	$>-18$	$>-17$	$>-14$	-21
$\mu_V$ [mag arcsec $^{-2}$ ]	$\geq 23$	$\leq 23$	$\leq 19$	$\leq 21$	$\geq 22$	-
$M_{total}$ [ $M_\odot$ ]	$\leq 10^9$	$\leq 10^9$	$\leq 10^9$	$\leq 10^9$	$\sim 10^7$	$\sim 10^{12}$
$M_{HI}$ [ $M_\odot$ ]	$\leq 10^{10}$	$\leq 10^{10}$	$\leq 10^{10}$	$\leq 10^8$	$\leq 10^5$	$3 \times 10^9$
$M_{HI}/L_B$ [ $M_\odot/L_\odot$ ]	$0.1 < < 1$	$\geq 1$	$0.1 < < 1$	$< 0.01$	$< 0.01$	0.2
Properties						
Shape and size	spiral, extended, late-type	irregular, extended, late-type	central compact clusters late-type	elliptical, small early-type	spheroidal, small early-type	barred spiral, extended late-type
Gas content	rich	rich	rich	poor	poor	rich
Rotation	yes	yes, solid-body	yes, solid-body	no (/yes)	no	yes
Star formation	slow, cont. <sup>(a)</sup>	episodic/cont.	episodic, bursty	low, cont.	low, cont.	cont.
Clustering	yes/no	yes/no	no	yes	yes	-

(a) continuous.

## Surveys of low metallicity galaxies

Most dwarf galaxies beyond the Local Group, including those of the sample studied in this work, have names belonging to early surveys of metal-poor galaxies. [Kunth & Östlin \(2000\)](#) review these surveys among which the [Haro \(1956\)](#) and [Zwicky & Zwicky \(1971\)](#) galaxies, the Second Byurakan Survey (SBS; [Markarian 1967](#)), the University of Michigan survey (UM; [MacAlpine et al. 1977](#)), and the Hamburg/SAO Survey ([Ugryumov et al. 2003](#)), played a major role in finding low metallicity galaxies. Selection criteria, based on the fact that they are star-forming, making their detection easier, were used, such as morphology (compactness; e.g. Zwicky), colors (blue or UV excess; e.g. SBS, UM), or emission lines ( $H\alpha$ ,  $H\beta$ , optical metallic lines; e.g. Haro).

[Izotov et al. \(2006a\)](#) and more recently [Izotov et al. \(2012\)](#) carried out a systematic search for metal-deficient galaxies based on emission line criteria in the Sloan Digital Sky Survey (SDSS; [York et al. 2000](#)), which scanned about 1/4 of the sky, providing deep spectroscopy in the optical. Also making use of the SDSS, AVOCADO will provide a statistical analysis of the UV to NIR properties of thousands of nearby dwarf galaxies ([Sánchez-Janssen & Sánchez-Janssen 2011](#)).

### 1.1.2 Galaxy evolution and star formation histories

#### Evolution more than formation

The popularity in studying dwarf galaxies grew from the thought that they are at the base of galaxy formation. The main epoch of galaxy formation is found to be around redshift  $z \sim 1 - 2$  ([Madau et al. 1996](#)). In the hierarchical scenario of structure formation ([Dekel & Silk 1986](#)), massive galaxies form out of successive merging of building blocks which should be found at redshifts  $\geq 2$ . As a consequence, massive galaxies are not young systems but should be metal-rich, and their building blocks are low mass metal-poor objects, typically dwarf galaxies. Such dwarfs are below detection at high-redshift, making local dwarf galaxies their closest analogues. However, this scenario is challenged by signatures of downsizing ([Cowie](#)

et al. 1996), in which active star formation appears first in massive galaxies and proceeds to lower mass systems at current epoch. Hence the role of dwarf galaxies in galaxy formation is more debatable.

The interest of dwarf galaxies in galaxy evolution remains valid, as they seem to have experienced relatively little metal enrichment and few star formation episodes. If we consider them to be young objects caught at early stages of their evolution, dwarf galaxies may resemble chemically unevolved systems from the early universe. From that perspective, they may pose as interesting nearby frameworks for high-redshift studies.

However the comparison is not straightforward. No dwarf galaxy is, strictly speaking, a pristine environment as they all show evidence for intermediate-age or old stellar population, hinting towards complex and unique star formation histories. The study of star formation histories and differences between types of dwarf galaxies (e.g. Gallagher 1996; Dolphin et al. 2005) is central to understand galaxy formation and evolution.

### Stellar population and Wolf-Rayet signatures

UV and optical studies bring detailed information on the stellar content and on the ionised gas properties of galaxies, with some limitations due to severe extinction by dust, which is more important in spiral galaxies than in dwarf galaxies. Photometric data are key to recover the star formation histories in dwarf galaxies. The need for deep observations is now matched with, e.g., the *Hubble Space Telescope* (*HST*). Once correcting for reddening, comparing the photometry of stellar populations via color-magnitude diagrams to stellar evolutionary models adapted to the low age and low metallicity (Schaller et al. 1992; Bertelli et al. 1994) gives insight on the different population ages. Recent star formation ( $\leq 500$  Myr) is accessed by main-sequence stars, blue loop stars, red supergiants, Wolf-Rayet stars. Older populations ( $\geq 1$  Gyr) are traced by asymptotic giant branch, and red giant branch stars. Horizontal branch stars (e.g. RR Lyrae stars) trace ancient populations  $\geq 10$  Gyr. Cluster population analysis in dwarf galaxies, as done in, e.g., Adamo et al. (2010, 2011), are challenging due to the mixing of several populations, the difficulty to resolve clusters in distant objects, and their rapid evolution during the first 10 Myr.

It is established from stellar population studies that many dwarf galaxies host an old stellar population (e.g. NGC 6822; Pox186, Doublier et al. 2000; I Zw 18, Tosi et al. 2007), but none contains only old stars. Their oldest population often consists of red horizontal branch stars and hence is younger than galactic globular clusters. Most irregulars and BCDs are dominated by a star-forming complex, dense super star cluster (SSC) and/or massive O-B association (Terlevich et al. 1991), sitting in a more extended older stellar population (Hodge et al. 1991). For instance, Mrk 996 is a BCD with a starburst of age 3.5-4.5 Myr (James et al. 2009), and an older stellar population of age  $\geq 1$  Gyr (Thuan et al. 2008).

The ongoing activity of BCDs is the progenitor of massive stars such as Wolf-Rayet (WR) stars. These are extreme Population I stars characterised by broad emission lines from high-velocity winds. WR stars are signatures of vigorous star formation during the past 10 Myr. Their presence depend on mass-loss rate, metallicity, star formation rate (SFR) for high-mass stars and the high-mass end of the initial mass function (IMF) (Massey & Johnson 1998). WR signatures, namely a broad He II 4686 Å feature or bumps (blending of He II and metal lines) around 4650 Å (blue) and 5808 Å (red), are observed in, e.g., He 2-10 (Allen et al.

1976), I Zw 18 (Legrand et al. 1997). Galaxies with strong WR signatures are referred to as WR galaxies (Conti 1991). WR stars are thought to contribute to metal enrichment through stellar winds (see Section 1.1.3). Their occurrence decreases with decreasing metallicity as only the most massive stars with strong stellar winds can become WR stars, and the winds are driven by metals (especially iron, e.g. Vink & de Koter 2005). Pustilnik et al. (2004) relate the presence of Wolf-Rayet stars in a sample of 8 BCDs to merger events which trigger short intense bursts.

The combined presence of young massive stellar populations (and higher fraction relative to older populations) and low metallicities observed (hence lower dust content) result in general hard(er) radiation fields throughout most of the galaxy (e.g. Campbell et al. 1986). The hardness of the radiation field is defined by the proportion of hard photons and hence by the shape of the stellar spectrum at short wavelength (in the UV). Hard photons are essentially produced in starbursts by massive stars. Optical emission line diagnostics are often used as indicators of the hardness of the UV radiation field (e.g. Kewley et al. 2001). The hardness of the radiation field is known to decrease with increasing age, due to the evolution of the stellar population off the main sequence after a few Myr (e.g. Levesque et al. 2010; see also Fig. 4.3), and with increasing metallicity. In metal-rich environments, metals in the atmosphere of massive stars absorb a large fraction of the hard photons produced by the star (continuum metal blanketing Kewley et al. 2001), resulting in softer radiation fields in the H II region compared to more metal-poor environments. This harder radiation at low metallicity is seen in the presence of high ionisation lines in the H II region (Thuan & Izotov 2005; Madden et al. 2006). While massive stars are often invoked as the origin of the production of hard photons, Thuan & Izotov (2005) suggest that the emission of [Ne V] observed in 4 BCDs is probably due to fast radiative shocks associated with supernova explosions of the most massive stars in the compact SSCs.

### Modes of star formation

The majority of dwarf galaxies formed the bulk of their mass prior to  $z \sim 1$  (Weisz et al. 2011). Star formation may occur continuously and/or episodically depending on the gas reservoir. High mass gas-rich dwarf galaxies, such as spirals, have enough gas to sustain continuous star formation at a relatively constant rate, which in turn contributes to metal enrichment. Low mass gas-poor dwarf galaxies, mainly ellipticals and spheroidals, show continuous star formation at a decreasing rate, or episodic star formation (Hunter 1997). If the gas consumed is internal, then there is no gas accumulated between the star formation episodes, and the star formation activity may stop anytime. Gas-poor dIrrs may evolve at some point to dSphs, although dSphs are not simply gas-free dIrrs, but have structural differences with no common origin or single evolutionary endpoint (James 1991). Hunter et al. (1994) show that present day surface brightness of dIrr would be lower than dSph after evolutionary fading. Weisz et al. (2011) find a strong morphology-density relation among dwarf galaxies, indicating that gas-rich dwarfs require external mechanisms (e.g., ram pressure and tidal stripping and tidal forces) to transit to gas-poor dwarfs.

Dwarf galaxies are often thought to be inefficient in forming stars, as their gas densities are lower than the critical threshold found in normal galaxies (Kennicutt 1989). This may be a particular case for low surface brightness and early-type dwarf galaxies, but BCDs and many irregular galaxies are definitely active, usually not everywhere in the galaxy but with star

formation concentrated in one or several knots. They can host very compact and luminous SSCs, with ongoing star formation and surface SFRs comparable to those of spiral galaxies (Hunter 1997; NGC 1705, Melnick et al. 1985; NGC 1569, Arp & Sandage 1985; NGC 1140, Hunter et al. 1994; He 2-10, Johnson et al. 2000; Billett et al. 2002). This is especially the case in BCDs due to their compactness.

BCDs exhibit episodic (every  $10^8$  yr, Hodge et al. 1989) violent (up to  $10 M_{\odot} \text{ yr}^{-1}$  Thuan & Martin 1981) star formation bursts which last a few  $10^6$  yr. Their gas is consumed so intensely that they could not maintain such activity through most of their history (Searle & Sargent 1972). Their star formation is concentrated towards the center, probably because they have low angular momentum (van Zee et al. 2001). These bursts dominate the evolution of the galaxy, and in between the bursts, low level continuous star formation may still occur.

### Triggers of star formation

Stellar clusters are generally formed from the collapse and fragmentation of giant molecular clouds (Lada & Lada 2003). Lacking spiral density waves, dwarf galaxies require other triggering mechanisms. What mechanisms are responsible for the triggering, maintaining, and propagation of their star formation activity is not clear. Star formation patterns are not unique and may hint towards different mechanisms at play.

Star formation is rather a local process, regulated by gravitational instabilities, pressure in the disk of irregulars, and modification of the ISM by massive stars (random gas motions, feedback from supernovae, mechanical energy from stellar winds) (Hunter 1997). Without shear, dwarf galaxies may grow larger concentrated gas clouds that are less stable and may collapse quickly to form giant H II regions, which, in turn, may affect more profoundly the ISM than if formed in smaller regions. The complex star formation histories and discrepancies with high-redshift histories may show evidence of delayed star formation compared to more massive galaxies (Weisz et al. 2011). Billett et al. (2002) state that massive star clusters in dwarf galaxies are formed from large-scale perturbations (flows and gravitational instabilities). Flows in the ionised gas are seen in several BCDs (e.g. Marlowe et al. 1995). Once formed, the clusters are less likely disrupted as cluster destruction mechanisms are weaker in low mass galaxies. For example, Gil de Paz et al. (2000) suggest that the evolution of a massive nuclear starburst in Mrk 86 blew away large amount of gas, which, in turn, formed new generations of stars in the shell.

Star formation histories are sensitive to the environment. In some cases, the disagreement between gas content and star formation histories may suggest the presence of accreted gas through gravitational interactions to trigger new star formation episodes. Compared to more massive galaxies, the effect of such interaction in dwarfs can be dramatic. This may explain observed peculiarities such as asymmetric distributions, complex velocity fields, offsets in the stellar and neutral gas kinematic components, or complex chemical-enrichment histories. Past or current interactions with other galaxies or merger events are obvious possibilities to explain the star formation activity in these systems, which may be enhanced by gas flows and accretion, favoring large-scale mixing of the ISM, or inhibited by stripping. Several BCDs show signs of mergers (Östlin et al. 1999) and host SSCs comparable to that of giant mergers. However, interactions are not apparent for all dwarf galaxies, from the lack of tidal debris in the outer regions of most dwarf galaxies and because many seem isolated (e.g. Portas et al. 2011).



If gravitational interactions can explain part of the observed activity, it usually cannot account for all of it, although fainter unseen companions may be present (Pustilnik et al. 2001). In particular, Hunter & Elmegreen (2004) demonstrate that the role and distance of the companion to the host galaxy is not obviously correlated to the activity. In BCDs, both their central concentration, which affects the critical threshold for star formation (van Zee et al. 2001), and the presence of companions, could be responsible for the triggering of their star formation. Both scenarios, as well as possible accretion from a smaller object, are investigated in a detailed analysis of the H I structure of the BCD VII Zw 403 by Simpson et al. (2011), without conclusive answers.

### 1.1.3 Metallicity and ISM enrichment

Dwarf galaxies, and particularly irregulars and BCDs, are often metal-deficient (Binggeli 1994; Walsh et al. 1997), with metallicities below solar ( $Z_{\odot} = 12 + \log(O/H)_{\odot} = 8.69$  Asplund et al. 2009). Izotov et al. (2012) list the 17 most metal-poor galaxies to date, with  $12 + \log(O/H) \leq 7.34$ , including SBS 0335-052 (Izotov et al. 2009), DDO 68 (Izotov & Thuan 2007), and I Zw 18 (Thuan et al. 2005). Those objects are key to access primordial abundances of metals and, most importantly, of helium, which is mainly produced during the Big Bang nucleosynthesis, with primordial abundance relative to hydrogen  $Y_p \sim 0.256$  (e.g. Izotov & Thuan 2010).

Metals as heavy as iron are created during stellar evolution and released in the ISM when stars die, and metals beyond iron are synthesized during a supernova event. Since massive stars are short-lived compared to lower mass stars, metal enrichment is not a linear function of time.

### Abundance determination

Abundances define the fraction of heavy elements in the ISM and can be measured several ways (reviewed in Kunth & Östlin 2000), including: photometry of resolved stellar populations (red giant branch population gives  $[Fe/H]$ ); spectroscopy of individual stars (Fe, Ca, Da Costa et al. (1991)); spectroscopy of ionised gas from planetary nebulae or H II regions (O, N, S, C, Ne, etc., Garnett (1990)). Stellar methods are usually used in gas-poor galaxies, and H II region methods in gas-rich galaxies. *IUE*, *HST*, *FUSE* were key missions in accessing metallicities.

A frequent way of determining abundances from H II regions is first to correct observed optical nebular emission lines for extinction, and then derive gas properties (density and temperature). This can be done assuming a two-zone (low and high-ionisation) or a complete photoionisation model. The density is measured from  $[S\ II]\ \lambda 6717/\lambda 6731$  or  $[O\ II]\ \lambda 3726/\lambda 3729$  doublets. Their ratio is most sensitive to the density around their critical densities. The temperature is measured from  $[O\ III]$ ,  $[S\ III]$ ,  $[N\ II]$  triplets (typically  $[O\ III]\ \lambda 4363/(\lambda 4959 + \lambda 5007)$ ), which are directly observed or inferred. Relative abundances of, e.g.,  $N^+/O^+$  are less sensitive to the electron temperature. The gas conditions are used to derive line emissivities and, in turn, ionic abundances. Then ionic abundances are converted to total elemental abundances using ionisation correction factors (e.g. Izotov et al. 2006b).

Nebular abundances are sensitive to temperature fluctuations to first order, and to the presence of dust to second order (Skillman 1998), giving intrinsic uncertainties of  $\sim 0.1$  dex. Looking at the effect of dust on metallicity determination, Shields & Kennicutt (1995) show

that the mixing of dust in the H II region plays a role in the heating of the gas and affects extinction corrections. Metals (essentially Si and Fe) can also deplete onto grains (Henry 1993). H II region abundances are generally more reliable for low metallicity regions with high temperature exciting stars than for high metallicity regions. The presence of composite stellar populations and the faintness of dwarf galaxies limit stellar metallicity diagnostics. The different methods and assumptions can lead to discrepancies of up to a factor 5 in the metallicity determination (e.g. Kewley & Ellison 2008). Little sensitive to extinction and electron temperature, spectroscopy in the IR can also give access to reliable abundances, using, for example, [O III] transitions at 88 and  $52\mu\text{m}$  from *Herschel*, or the [S III] 18.7 and  $33.5\mu\text{m}$  lines from *Spitzer*, which provide a measure of the density.

Alternatively, neutral clouds illuminated by a background source are observed through atomic absorption lines which can also provide abundances in the neutral gas (Kunth et al. 1994).

### Chemical abundance variations

Are the metallicity values valid on global scales? Metallicities clearly depend on the probed medium (i.e. method used), as well as on the efficiency and timescale of ISM mixing. Radial abundance variations in spiral galaxies indicate rather inefficient mixing. If star formation is not particularly concentrated and occurs in different places, global abundances are likely to be uniform. Stellar winds and supernovae ejecta may also help uniform mixing over large spatial scales and short timescales. Observationally, nebular abundances are usually found well mixed on spatial scales, but discrepancies (as much as an order of magnitude) between nebular and neutral gas abundances are observed (Lebouteiller et al. 2004). The concentrated star formation and solid-body rotation of BCDs would suggest inefficient mixing. Kpc-scale inhomogeneities are expected in dwarf galaxies (Roy & Kunth 1995).

Abundances do not scale for all elements, and deficiencies of specific elements can be observed. O is produced in massive stars and injected in the ISM early on via supernovae explosions. The O/H abundance is found homogeneous on large spatial scales (e.g. Pagel et al. 1978; Kobulnicky & Skillman 1996; Kehrig et al. 2008), indicating rather well mixing of newly produced elements with the ISM. While Kunth & Sargent (1986) argue that H II regions can pollute themselves on short timescales, it is also believed that new elements are return in a hot ISM phase which stays invisible for a long time. C and N can be produced in high and intermediate mass stars and hence be injected later on in the ISM. Therefore low  $C/O$  and  $N/O$  ratios are expected at low metallicity, after a recent burst, and higher values at higher metallicity or after a long quiescent period of star formation. These ratios can, in principle, be used as clocks to determine the age the last burst. Izotov & Thuan (1999) find relatively constant ratios at low metallicities ( $12 + \log(O/H) < 7.6$ ) in BCDs, implying a primary origin of heavy elements in high mass stars.

In several BCDs, the  $N/O$  and He II ratios are found to be high (e.g. Pagel et al. 1986; Pérez-Montero et al. 2011), both locally and on galaxy-wide scales. N and He enrichments can be explained by: (1) WR stellar winds (e.g. Brinchmann et al. 2008), (2) inflows of un-enriched gas (e.g. Köppen & Hensler 2005), (3) differences in the star formation rate (e.g. Henry et al. 2000), (4) shock excitation; but the importance of each scenario is not fully known. WR stars are most commonly invoked to account for ISM enrichment in BCDs (Section 1.1.2). However, in NGC 5352, both WR stars and N enrichment are present. Kobulnicky et al. (1997) find that both are not clearly spatially associated, and that part of the N enrichment

may be a result from pollution from its young stellar cluster rather than a WR origin.

Progress is being made to explore the origin of N enrichment and spatial behaviors of abundance variations using integral-field spectroscopy. The detection rate and spatial distribution of WR signatures are now reachable due to improvements in instrumental sensitivity and spatial resolution (Kehrig et al. 2008; James et al. 2009; Cairós et al. 2010; Pérez-Montero et al. 2011), while the spectral resolution can decompose line profiles into several components characterised by different electron densities and temperatures, resulting in more accurate metallicity determinations. James et al. (2009) performed such analysis on Mrk 996 with *VLT/VIMOS* to re-examine its metallicity. They derived a metallicity of  $12 + \log(O/H) = 8.37$ , higher than that of Thuan et al. (1996). They also find that the N enrichment from evolved massive stars is present in the broad line region of the inner galaxy (associated with strong kinematics), but not in the narrow line region.

### Metal enrichment and star formation history

An empirical linear relation between metallicity and luminosity ( $L - Z$ , the luminosity being taken as the  $B$ -band magnitude) or mass has been established (e.g. Skillman et al. 1989), with dwarf galaxies sitting at the low end of this relation. The zero-point of the  $L - Z$  relation varies on the type of objects, particularly between ellipticals and irregular galaxies or BCDs which are more luminous than their metallicities suggest, although the scatter is large for BCDs (Kunth & Östlin 2000). The relation holds statistically for extremely metal-poor galaxies (Izotov et al. 2012), apart from a few exceptions (IZw 18, SBS 0335-052) which are too bright for their metallicity. This implies that dwarf galaxies evolve more slowly due to smaller mass densities or that metals are ejected more efficiently due to low gravitational potential, which plays a key role in the subsequent evolution of a system.

More generally, this relation hampers detections of metal-poor galaxies and their subsequent study (including metallicity calculation). For that matter, the metallicity of high-redshift galaxies has often been inferred from the  $L - Z$  relation. The zero-point of this relation appears to vary with redshift, by decreasing metallicity with increasing redshift for a given luminosity (Shapley et al. 2004).

Outliers of the  $L - Z$  relation are found to be more metal poor than their histories and stellar populations would tell. The discrepancy between metal enrichment and star formation histories observed in several dwarf galaxies is intriguing. A debate around the age of IZw 18 arose from its low metallicity ( $12 + \log(O/H) = 7.18$ , Izotov et al. 1999), indicating that the galaxy must be young. However, high ages are hinted by high  $C/O$  and  $N/O$  ratios, and evolutionary models (Kunth et al. 1995), although baring uncertainties. NIR *HST*/NICMOS photometry finally revealed the presence of a 1-5 Gyr stellar population (Östlin et al. 1999), while overall IZw 18 is dominated by a 10-20 Myr population of red supergiants. From *HST*/ACS images, the age was later revised to an upper limit of 500 Myr by Izotov & Thuan (2004), while Tosi et al. (2007) find the presence of a red giant branch population of age at least 2 Gyr and up to 13 Gyr (Contreras Ramos et al. 2011). Similarly, the metallicity of SBS 0335-052W is known to be around  $12 + \log(O/H) = 7.12$ , with the presence of an old stellar population of age  $\leq 500$  Myr (Izotov et al. 2005).

How to reconcile the metallicity and star formation histories is not clear. Possible explanations are the accretion of primordial gas (e.g. IC 10, Wilcots & Miller 1998), or the formation, more efficient in low potential systems, of galactic winds from supernovae (thought to be the



source of X-ray gas, [Martin 1999](#)), and starburst-driven outflows, which can expel metals. The later point supports the hypothesis that dwarf galaxies can be the dominant source of metal enrichment of the intergalactic medium.

With SDSS data and complementary 6.5-m MMT and 3.5-m APO spectroscopy, [Izotov et al. \(2012\)](#) determined the metallicity of 42 low metallicity galaxies, as low as  $12 + \log(O/H) = 7.12$ . One of their main findings is a metallicity floor at  $12 + \log(O/H) = 6.9$ , or  $Z = 1/60 Z_{\odot}$ , (observed in a region of SBS 0335-052W by [Izotov et al. \(2009\)](#), while the average metallicity for this galaxy is 7.12), below which no galaxies are found. They suggest that matter from which dwarf galaxies are formed is enriched to that common metallicity level by Population III stars. These would be first generation stars and source of pre-enrichment as they formed before the main epoch of galaxy formation.

#### 1.1.4 Dynamics and Morphology

##### H I content

H I observations at  $\lambda = 21$  cm bring information on the global structure of the ISM of galaxies, on the mass distribution, as well as on the kinematics of the interstellar neutral atomic gas. H I fills a large volume of galaxies, between H II regions and molecular clouds, as ionising photons have a limited reach, and can extend far beyond its optical counterpart.

The H I distribution in galaxies normally reveals a significant fraction of the gas reservoir and, thus, the galaxy morphology. The H I mass ( $M_{HI}$ ) is correlated with the galaxy blue luminosity ( $L_B$ ). Gas-rich dwarf galaxies have  $M_{HI}/L_B$  increasing with decreasing luminosity ([Staveley-Smith et al. 1992](#)), implying that low luminosity galaxies have a large reservoir of H I, not yet converted into stars. BCDs and active irregulars have similar  $M_{HI}/L_B$ , with  $0.1 < M_{HI}/L_B < 1.0$ , and lower surface brightness galaxies have higher  $M_{HI}/L_B > 1$ .

The absolute mass of H I is small in dwarf galaxies compared to more massive galaxies, but their gas fraction, given by  $M_{HI}/L_B$ , are high ([Roberts & Haynes 1994](#)). The spirals and irregulars usually have a large reservoir of H I, with a H I-to-total mass ratio  $\geq 5\%$ , while spheroidals have little H I, with a ratio  $\leq 0.1\%$ . Spheroidals and ellipticals tend to be companions of more massive galaxies (e.g. [Jerjen et al. 2000](#)), while irregulars are more widely distributed, and seem to be more gas deficient as they are closer to the host galaxy. Tidal and ram pressure stripping may have removed the gas, although it is still not clear how exactly. The dwarf spheroidal NGC 205 is a typical example of this lack of gas, or “missing ISM mass”, which [De Looze et al. \(2012\)](#) explain by supernovae feedback that expel the gas from the inner to the outer regions of the galaxy, and/or by tidal interaction with the spiral galaxy M 31. On the other hand, the extended H I content seen in many irregulars shows a complex structure that may be remnant of the galaxy formation process, or provoked by external perturbations. It does not appear to act directly in the star formation process but may be a slow reservoir that fuels the center ([Hunter 1997](#)).

##### Kinematics and dark matter

H I can also trace dark matter in dwarf galaxies, which dominates the kinematics and is present at a larger fraction in dwarf galaxies than in spiral galaxies ([Brinks & Taylor 1994](#)). Dark matter is more concentrated in the halo compared to spirals.

H I data give information on the column density of atomic gas, radial distribution, on the position angle, inclination, and rotation velocities using specific rotation curve models to fit the velocity field (e.g. tilted-ring model, [Carignan & Beaulieu 1989](#)). Using a mass

model, one can reproduce the H I and stellar radial distributions, and infer the mass of the halo from the rotation curve. Typically, rotational velocity and scale length are used for rotationally-supported systems, and velocity dispersion and exponential scale length are used for pressure-supported systems (e.g. VII Zw 403, [Simpson et al. 2011](#)). The latter study is based on data from the LITTLE THINGS program (LITTLE: Local Irregulars That Trace Luminosity Extremes, THINGS: The HI Nearby Galaxy Survey; [Hunter et al. 2012](#)), dedicated to H I observations with the *VLA* in a large sample of nearby dwarf irregulars. Dwarf galaxies have no bulge component, simplifying the interpretation of rotation curves. dIrr rotation curves have masses constrained at large radii interpreted by the presence of an extended dark matter halo.

In many dwarf galaxies, H I data have revealed the presence of dark companions, invisible in optical bands, out to large distances from the host dwarf galaxy. Indeed, most galaxies are not isolated but are found in pairs or groups ([Makarov & Karachentsev 2011](#)). Interactions between the host galaxy and its companions may be a triggering factor to the observed star formation activity of dwarf galaxies ([Brinks & Taylor 1994](#), and see Section 1.1.2). The mass of these companions is an order of magnitude lower than the host galaxy.

### Dwarf galaxies in numerical simulation

Numerical simulations are useful tools to understand the global morphologies observed and the role of environment on the evolution of dwarf galaxies. For example, the irregular shapes of dwarf galaxies are often attributed to interactions with companions or merger events that can be reproduced numerically. This enables us to understand the shape, ages, and gas transfers. For instance, [Besla et al. \(2012\)](#) investigate the interaction history of the dwarf galaxies, the Magellanic Clouds, with the Milky Way, and show that the kinematics and structure of the Large Magellanic Cloud (LMC) is coherent with a direct collision with the Small Magellanic Cloud (SMC). They are able to precisely numerically reproduce the large-scale gas distribution of the Magellanic Clouds as well as the internal structure and morphology of the LMC.

Cosmological hydrodynamic simulations also bring insight on global star formation histories. By modeling the dynamics, collapse of gas, and star formation upon specific criteria (overdensities, converging flows, rapid cooling), one can access global SFR and large-scale properties through cosmic times. However, the episodic nature of the bursts is difficult to reproduce. The main limitation of these simulations is the computing resources. Small-scale (subparsec) structures and physics (requiring low temperatures), which seem to drive star formation in dwarfs, are barely accessible for full-size galaxies, although approximations and local subgridding can be done ([Nagamine 2010](#)). Finer treatments of the physics and chemistry of the cool gas in dwarfs are being included (e.g. [Valcke et al. 2008](#); [Christensen et al. 2012](#)). For example, the addition of turbulence effects from radiation pressure or supernovae feedback, can both help cloud collapse through shock waves compressing the gas, and prevent collapse through dissipation of energy ([Bournaud et al. 2010](#); [Krumholz & Thompson 2012](#)).

The study of dwarf galaxies also has cosmological implications, such as the missing satellite problem. Current simulations of dark matter distribution do predict an increasing number of small size halos at present epoch, residing in dwarf galaxies, while the number of observed dwarfs is far lower ([Moore et al. 1999](#)). Possible explanations are that these halos are isolated

without a visible counterpart and therefore invisible, which is supported by the fact that some dwarf galaxies are dominated by dark matter (Simon & Geha 2007), or that these halos are tidally-stripped dwarf galaxies, hence of low surface brightness and thus difficult to detect.

### 1.1.5 Motivations

Dwarf galaxies are interesting astronomical objects to study in terms of cosmology (dark matter, primordial abundances), and on the large-scale (galaxy formation), intermediate-scale (global star formation, evolution, enrichment), and small-scale (ISM processes) aspects.

The previous sections demonstrate the utility of dwarf galaxies in cosmological and intermediate-scale studies, and outline the following important topics:

- the influence of environment on galaxy morphology, galaxy evolution and star formation, what triggers and regulates quiescent star formation or episodic bursts;
- the origin of the morphology – density relation, the link between morphological types;
- how stellar evolution proceeds in chemically young systems, gas loss mechanisms, enrichment as a function of time;
- the presence and nature of dark matter and satellite orbits.

Answers to the long-standing problems in these fields may reside at lower size scales, rather than global properties. The analysis of the ISM conditions and physical processes in the different gas phases may shed light on the observed global aspects. We focus on the ISM properties of dwarfs in Sections 1.2 and 1.3.

## 1.2 Phases of the Interstellar Medium

The ISM of galaxies is composed of dust and gas, the emission of which is associated with a variety of ISM phases dictated by the local conditions (mainly ionisation parameter, temperature, density). In starburst systems, the path of a photon describes well the ISM structure as the physical and chemical processes are governed by (non-)ionising photons. This section aims to briefly outline the characteristics of a simple three-phase model – namely ionised/atomic/molecular phases – to which we recurrently refer in this work. Figure 1.1 is an illustration of this layered three-phase structure. For a more detailed and complete picture of the physics and chemistry of the ISM, I refer to Hollenbach & Tielens (1999); Tielens (2005) and Osterbrock & Ferland (2006).

### 1.2.1 Ionised phase

UV photons ( $>13.6$  eV) are produced by hot young stars, typically O and B stars, that ionise the dense material around, forming H II regions. H II regions are characterised by electron temperatures  $>10\,000$  K and a range of densities, from  $1\text{ cm}^{-3}$  in the diffuse regions to  $10^5\text{ cm}^{-3}$  in the most compact regions. Escaping photons from the H II region can create a diffuse ionised phase of large volume filling factor.

In the ionised phase, the gas is primarily heated by photoionisation. Fine-structure lines are excited by collisions with  $e^-$  and cool by radiative decay in the UV to IR wavelength range. This is seen by UV and optical ionic absorption lines, and in emission with hydrogen recombination lines. Balmer transitions of H $\alpha$  at  $6563\text{ \AA}$  and H $\beta$  at  $4861\text{ \AA}$  are the most commonly observed, in particular for extinction determination along the line of sight. In

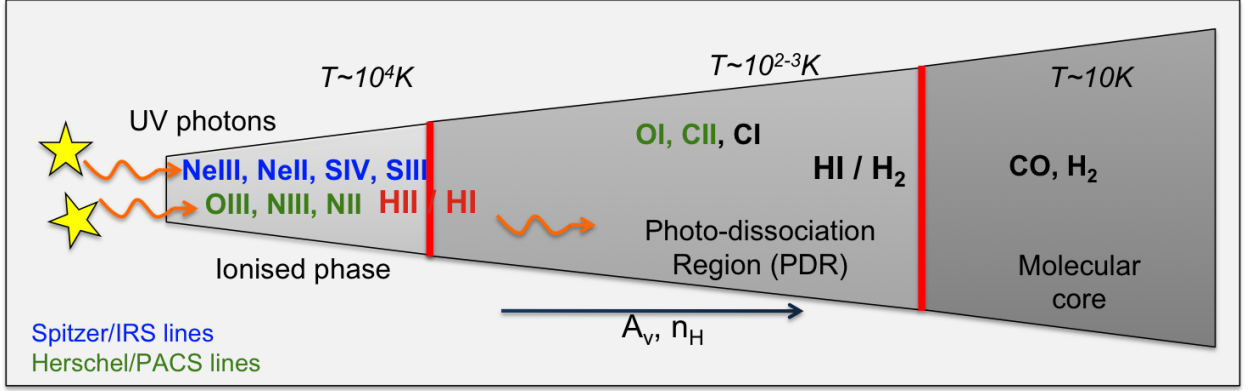


**Figure 1.1.** Phases of the ISM of starburst galaxies. This is a simplified view of the layered structure of a cloud comprising an ionised, atomic, and molecular phase. The UV photons produced by stars ionise their surrounding, forming the H II region traced by ionic lines. As the energy of the photons goes below 13.6 eV, hydrogen becomes neutral and most elements are atomic, forming the photodissociation regions. Further inside the cloud, the visual extinction and density increase, and the temperature drops, molecules start to form. This is the molecular core, typically traced by CO, site of star formation.

general terms, low ionisation species (e.g.  $N^+$ ,  $O^+$ ) probe the more diffuse gas phases, and high ionisation species (e.g.  $Ne^{++}$ ,  $O^{++}$ ) probe the denser H II regions, as the most energetic photons are likely absorbed close to the ionising stars. Uncaptured electrons are at the origin of free-free emission which dominates the spectrum in the radio.

### 1.2.2 Neutral atomic phase

The neutral phase is widely defined as the medium where hydrogen is no longer ionised, and molecules have not formed yet. The radiation field is set by FUV photons with energies  $h\nu < 13.6$  eV. Hence the neutral medium is composed of neutral atomic species (e.g. [O I], [C I]) as well as ionic species with ionisation potential lower than that of hydrogen (e.g. [C II], [S II], [Si II]). This neutral phase can be characterised with a range of temperatures and densities, from a warm diffuse medium ( $n_H \leq 1 \text{ cm}^{-3}$ ,  $T \sim 5000$  K) to a cold dense medium ( $n_H \sim 50 \text{ cm}^{-3}$ ,  $T \sim 100$  K). It also usually normally fills a large volume in galaxies.

In this picture, photodissociation regions (PDRs) are defined as the regions that separate the H II regions and the molecular phases, such as the Orion Bar (Tielens & Hollenbach 1985). Penetrating FUV photons, with  $6 < h\nu < 13.6$  eV, dominate the physical and chemical processes of these regions by dissociating and ionising molecular species. PDRs globally include all phases dominated by FUV photons, hence the neutral atomic and part of the molecular phase. They are also referred to as Photon-Dominated Regions (Sternberg & Dalgarno 1995). In this work, we often refer to PDRs as the dense neutral phase around molecular cores, to distinguish it from diffuse neutral gas (not directly associated with star-forming clouds). The visual extinction,  $A_V$ , varies typically from 0.1 mag (ionisation front) to 10 mag (inner edge of the cloud) in the PDR, which leads to different observed cooling lines (Hollenbach & Tielens 1999). In particular,  $C^+$  recombines to form  $C^0$  and molecular hydrogen starts to form in the PDR for  $A_V \geq 1$  mag. PDRs are bright in the IR dust continuum, atomic fine-structure cooling lines, and molecular lines.

Chemistry in the PDR is initiated by reactions with photons and  $H^0$ . The formation and

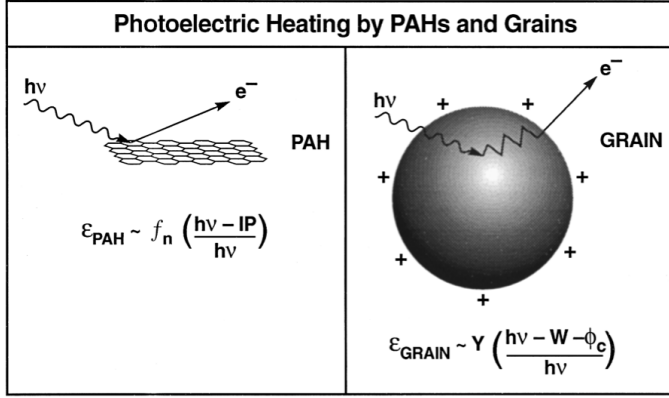


**Figure 1.2.** Schematic of the photoelectric effect on interstellar grains and PAHs from [Hollenbach & Tielens \(1999\)](#). The efficiency,  $\epsilon$ , of the process is a function of the yield,  $Y$ , in the case of grains, which measures the probability that the electron escapes, or, for PAHs, of the fraction,  $f_n$ , of PAHs that can still be ionised by FUV photons. Electrons must overcome the work function,  $W$ , and coulomb potential,  $\phi_c$ , for charged grains, or the ionisation potential,  $IP$ , for PAHs to be injected in the gas phase.

photodissociation of  $H_2$  is also central, acting as a triggering condition for most of the gas phase chemistry.

Dust grains are primarily heated by absorption of starlight. In dense regions, collisions are a secondary heating source. They cool by re-radiation at longer wavelengths. While large dust grains can reach thermal equilibrium, hence cooling in a continuum emission in the FIR/submm, smaller grains are stochastically heated because of their limited heat capacity, and cool via discrete emission bands in the MIR.

The gas is predominantly heated through the photoelectric effect acting on dust particles. As FUV photons are absorbed by the dust, energetic electrons diffuse in the dust grain with enough energy to be injected in the gas phase. This is illustrated by Figure 1.2. The work function of grains is typically  $\sim 5$  eV. The efficiency of this process is dependant on the grain size and charge. Hence the major actors in the photoelectric heating are the most numerous and smallest dust particles, the polycyclic aromatic hydrocarbons (PAHs), and the small grains, all emitting in the MIR wavelength range. The charge of the grain depends on the balance between photoionisation and recombination with an electron, which is controlled by  $\gamma = G_0 T^{1/2} / n_e$  (where  $G_0$  is the radiation field in Habing units, [Tielens & Hollenbach 1985](#)). In turn, the gas is heated and gets collisionally excited ([Bakes & Tielens 1994](#)). The electron fraction, relative to hydrogen, is  $\sim 10^{-4}$  in the PDR.

FUV pumping of  $H_2$  is another source of heating in the PDR. It operates via Lyman-Werner electronic transitions ( $\Delta E > 11.2$  and  $12.3$  eV). From electronically excited states, the  $H_2$  molecule can cool by pure fluorescence for densities below  $n_{crit}$ , or can be followed by collisional de-excitation, cascading through vibrationally excited levels of the ground state, which then heat the gas. In 10-15% of the cases it leads to  $H_2$  dissociation. The ionisation of  $C^0$  releasing an  $e^-$  in the gas phase, the formation of  $H_2$ , and the photodissociation of  $H_2$ , can also contribute to the gas heating ([Tielens & Hollenbach 1985](#)). Cosmic rays (and X-rays) are a secondary source of heating which becomes increasingly important in warm diffuse regions, while gas-grain collisions may be important in dense regions.

The cooling of the gas is done through fine-structure line transitions, by radiative decay or collisional de-excitation in high density regimes ( $n_H > n_{crit}$ ).

### 1.2.3 Molecular phase

The molecular phase starts with the formation of molecules, the most important and abundant being  $H_2$ . Other molecules such as CO, CS, HCN,  $O_2$ , etc., are also produced in the molecular cloud. This phase is characterised by high densities ( $> 10^3 \text{ cm}^{-3}$ ), low gas temperatures ( $\sim 10$  K), and low volume filling factor, as it is generally found in discrete clumps



of sizes on the order of a few tens of parsecs. Molecular clouds are usually self-gravitating rather than in pressure equilibrium with the other ISM phases.

The formation of many molecules in the ISM, including  $\text{H}_2$ , occurs on the surface of interstellar dust grains and are released in the gas phase by evaporation. Other molecules are formed in the gas phase by collisions, provided enough shielding is present. Generally, molecular dissociation occurs through a transition to the continuum of an excited state, or through radiative decay to the continuum of the ground state (for  $\text{H}_2$ ).  $\text{H}_2$  is protected from photodissociation by either self-shielding or shielding from dust grains. For column densities  $> 10^{14} \text{ cm}^{-2}$ , the Lyman-Werner bands become optically thick and  $\text{H}_2$  can self-shield.

The FUV flux and low energy cosmic rays ( $\simeq 100 \text{ MeV}$ ) are a primary heating source in the molecular clouds. Molecules are mainly excited by collisions and shocks, or directly from their formation. The cooling of molecules is done through vibrational and rotational transitions in the IR and submm wavelength range. The energies involved in these transitions are smaller than for atomic transitions, thus the cooling is more efficient.

The presence of observed linewidths, greater than that expected from thermal motion of the gas, can indicate important turbulence effects. Turbulence is a consequence of the mechanical energy released to the ISM by winds of early-type stars or supernovae explosions. Magnetic fields are also an important source of energy and pressure, especially inside dense clouds, as their strengths increase with density. Magnetic pressure, pressure due to cosmic rays, and turbulence provide support against gravitational collapse of the gas.

#### 1.2.4 Observable tracers

Tracers of the ISM are numerous in the large spectral range of galaxies. Optical and UV cooling lines are powerful probes of the ionised gas state and extinction by dust. At longer wavelengths, cooling lines from the ionised, atomic, and molecular phases are observed in the MIR, FIR, and mm with the advantage of being little affected by extinction. Properties of the FIR lines observed by *Herschel*, as well as selected *Spitzer* MIR and molecular tracers discussed in this work, are presented here and summarized in Table 1.2. Critical densities and excitation potential of the *Spitzer* and *Herschel* lines are shown in Figure 1.5, taken from (from Kennicutt et al. 2011). Important optical and UV lines are briefly mentioned and used in this study.

#### FIR fine-structure lines

First results on the FIR fine-structure lines, and particularly the  $[\text{C II}] 157\mu\text{m}$  and  $[\text{N II}] 122$  and  $205\mu\text{m}$  lines, were obtained in the Galaxy with the *COsmic Background Explorer* (*COBE*; Wright et al. 1991). The FIR fine-structure lines were observed in the nearby universe by the *ISO* and more recently by *Herschel*, as well as by the airborne telescopes *KAO* and *SOFIA*. The plethora of *ISO* findings on the FIR and MIR emission of galaxies are reviewed in Genzel & Cesarsky (2000). These cooling lines are important diagnostics of the FUV flux, gas density, temperature, and filling factor of the PDR and ionised regions (e.g. Tielens & Hollenbach 1985; Wolfire et al. 1990; Kaufman et al. 2006). In the PDR, the FUV radiation field is generally noted  $G_0$  and is measured in units of the equivalent Habing (1968) flux of  $1.6 \times 10^{-3} \text{ erg cm}^{-2} \text{ s}^{-1}$ , approximately the average interstellar radiation field of the Galaxy.

★ [C II] 157 $\mu$ m

The [C II] line is one of the most important coolants of the ISM, as carbon is the fourth most abundant element. It has been observed and studied in a variety of objects, such as Galactic PDRs (Bennett et al. 1994), spiral galaxies (Stacey et al. 1991), low metallicity galaxies (Poglitsch et al. 1995; Madden et al. 1997), ultra-luminous IR galaxies (ULIRGs, Luhman et al. 1998), and high-redshift galaxies (Maiolino et al. 2009; Stacey et al. 2010; Hailey-Dunsheath et al. 2010; De Breuck et al. 2011). The ionisation potential of C<sup>0</sup> is 11.26 eV, below that of hydrogen, thus it can be found outside of H II regions, in the neutral phase. Its critical density, the density above which collisions dominate the de-excitation process, is 50 cm<sup>-3</sup> with e<sup>-</sup> and 3 × 10<sup>3</sup> cm<sup>-3</sup> with H atoms. Hence C<sup>+</sup> can originate from diffuse ionised gas as well as diffuse neutral gas or the surface layers of PDRs (up to A<sub>V</sub>~5), which can render the interpretation of its emission difficult.

The [C II] 157 $\mu$ m line corresponds to the <sup>2</sup>P<sub>3/2</sub> – <sup>2</sup>P<sub>1/2</sub> magnetic dipole transition of C<sup>+</sup>. A schematic of the fine-structure transition is shown in Figure 1.3. [C II] is excited by collisions with e<sup>-</sup>, hydrogen atoms, or molecules. It requires only 91.3 K to be excited hence it can cool any warm neutral phase. Considering ionised and neutral collision partners, the intensity of [C II] is given by (Madden et al. 1997):

$$I_{[CII]}(H+e) = 2.35 \times 10^{-21} N(C^+) \times \left[ \frac{2e^{-91.3/T}}{1 + 2e^{-91.3/T} + n_{crit}(H)/n_H} + \frac{2e^{-91.3/T}}{1 + 2e^{-91.3/T} + n_{crit}(e)/n_e} \right]$$

The relative contribution of each medium to its observed intensity is a function of density and ionisation degree. At low-density, the [C II] intensity is sensitive to the density and column density while at high-density it is sensitive to the column density.

★ [O I] 63 $\mu$ m and [O I] 145 $\mu$ m

O<sup>0</sup> has an ionisation potential of 13.62 eV, just above that of hydrogen. The first two fine-structure transitions require excitation energies of 228 and 325 K above the ground state, corresponding to the [O I] 63 $\mu$ m and 145 $\mu$ m lines. Their critical densities are 5 × 10<sup>5</sup> cm<sup>-3</sup> and 10<sup>5</sup> cm<sup>-3</sup> respectively. Hence [O I] is only found in neutral gas and usually arises from warm dense regions. It can also exist at much higher A<sub>V</sub> in the PDR than [C II] since the formation of CO and O<sub>2</sub> occurs at larger A<sub>V</sub> (~10) than the transition of C<sup>+</sup> into C<sup>0</sup> (~3). The ratio of the two [O I] lines is an indicator of the gas temperature for T ≈ 300 K. It is a density tracer for high temperatures and high densities.

Since [O I] can exist deep into the cloud at high A<sub>V</sub>, its emission can be affected by optical depth effects, particularly for the lower level transition at 63 $\mu$ m. In the optically thin limit, the [O I] 63 $\mu$ m, just above the ground state, is brighter than the 145 $\mu$ m line. [O I] 63 $\mu$ m is actually one of the brightest PDR cooling lines with [C II] (e.g. Bernard-Salas et al. 2012).

★ [O III] 88 $\mu$ m

O<sup>+</sup> has ionisation potential of 35.12 eV, and critical density 500 cm<sup>-3</sup>. The [O III] 88 $\mu$ m line (<sup>3</sup>P<sub>1</sub> – <sup>3</sup>P<sub>0</sub>) is found in the ionised gas only, and because it requires energetic photons, it is generally accepted that it comes from the H II regions rather than interclump diffuse media.

In principle, with the [O III] transition at 52 $\mu$ m (<sup>3</sup>P<sub>2</sub> – <sup>3</sup>P<sub>1</sub>), the ratio of the two lines provide good constraint on the density of the H II region (Lebouteiller et al. 2012). However, the [O III] 52 $\mu$ m line is not accessible by *Herschel* for our sample of dwarf galaxies.

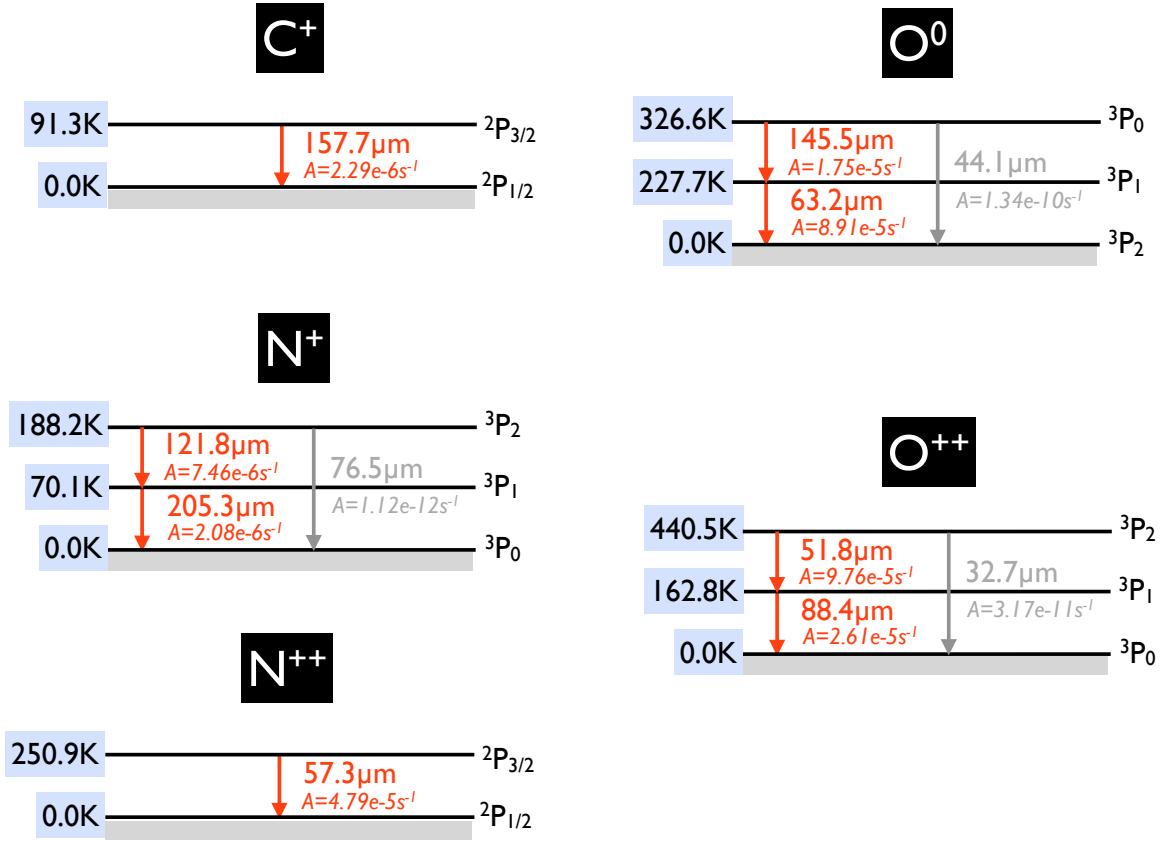


**Figure 1.3.** FIR fine-structure levels within the electronic ground state of  $\text{C}^+$ ,  $\text{O}^0$ ,  $\text{O}^{++}$ ,  $\text{N}^+$ , and  $\text{N}^{++}$ . Transitions observed with PACS appear in red. Excitations temperatures and Einstein coefficients for spontaneous emission  $A$  are indicated. Critical densities are listed in Table 1.2.



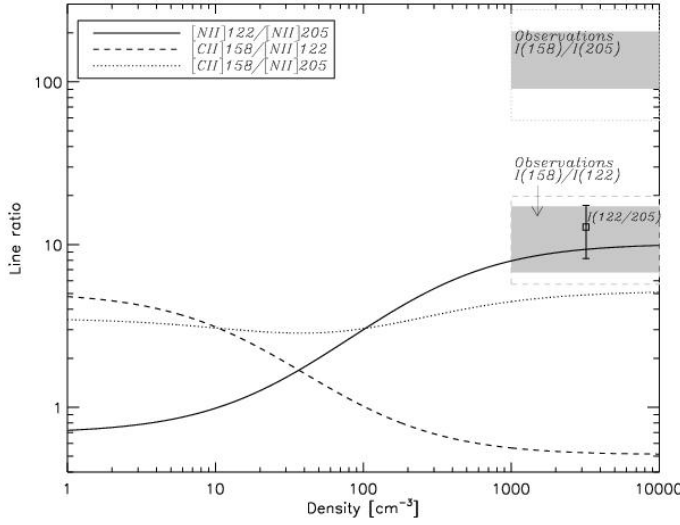


**Figure 1.4.** Theoretical ratios of  $[\text{N II}] 205/122\mu\text{m}$ ,  $[\text{C II}]/[\text{N II}]205\mu\text{m}$ , and  $[\text{C II}]/[\text{N II}]122\mu\text{m}$  at temperature 9000 K as a function of electron density (from [Bernard-Salas et al. 2012](#)). This can be used to estimate the contribution of the diffuse ionised gas to the  $[\text{C II}]$  line.

★  $[\text{N III}] 57\mu\text{m}$

$\text{N}^{++}$  has an excitation potential of 29.60 eV and critical density with  $e^-$  of  $3 \times 10^3 \text{ cm}^{-3}$  hence it arises in ionised gas only and is usually associated with H II regions. Being at two different ionisation stages, the ratio of  $[\text{N III}]57/[\text{N II}]122\mu\text{m}$  is a measure of the effective temperature,  $T_{\text{eff}}$ , of the ionising stars ([Rubin et al. 1994](#)).

★  $[\text{N II}] 122\mu\text{m}$  and  $[\text{N II}] 205\mu\text{m}$

$\text{N}^0$  has ionisation potential of 14.53 eV hence it is found only in the ionised gas. The critical densities with  $e^-$  are  $300 \text{ cm}^{-3}$  and  $45 \text{ cm}^{-3}$  for  $[\text{N II}] 122\mu\text{m}$  and  $[\text{N II}] 205\mu\text{m}$  respectively. Being in the same ionisation stage, their ratio is a good electron density tracer of the diffuse ionised gas as shown by Figure 1.4. This ratio is insensitive to elemental abundance and electron temperature.

Because  $[\text{C II}]$  can be found in the diffuse ionised gas, part of its emission can correlate with the  $[\text{N II}]$  emission. Hence the  $[\text{N II}]$  lines can, in principle, be used to disentangle the fraction of  $[\text{C II}]$  from the ionised gas to that from the PDR only. This is shown in Figure 1.4. The critical densities with  $e^-$  and excitation temperatures of  $[\text{C II}]$  and  $[\text{N II}] 205\mu\text{m}$  are very similar, thus their ratio is mostly dependant on the relative abundance of  $\text{C}^+$  and  $\text{N}^+$  ([Oberst et al. 2006](#)).

### MIR fine-structure lines

The MIR fine-structure lines are exhaustive in the range scanned by the *ISO*/SWS, *Spitzer*/IRS, and *SOFIA*/EXES. They are mainly nebular ionic lines, excited by collisions, of sulphur, neon, iron, argon, silicate, oxygen, and provide diagnostics on the ionised gas.

★  $[\text{Ne III}] 15.56\mu\text{m}$

$\text{Ne}^{++}$  has an excitation potential of 40.96 eV and critical density with  $e^-$  of  $3 \times 10^5 \text{ cm}^{-3}$  hence it arises in ionised gas only and is usually associated with the dense H II regions. Being at two different ionisation stages, the ratio of  $[\text{Ne III}]/[\text{Ne II}]$  is a measure of the hardness of the radiation field and is less sensitive to density than the optical  $[\text{O II}]$  or  $[\text{S II}]$  doublets as

they have similar critical densities. Similarly, [Ne III] and [Ne II] are insensitive to temperature fluctuations in the H II region where  $T \sim 10\,000$  K.

★ [Ne II]  $12.81\mu\text{m}$

Ne<sup>+</sup> has an excitation potential of 21.56 eV and critical density with  $e^-$  of  $7 \times 10^5 \text{ cm}^{-3}$  hence is arises in the ionised gas only.

★ [S IV]  $10.51\mu\text{m}$

S<sup>++</sup> has ionisation potential of 34.79 eV, and critical density  $5 \times 10^4 \text{ cm}^{-3}$ . It is found in the ionised gas only, and traces rather dense H II regions. The ratio of [S IV]/[S III]18 $\mu\text{m}$  is an indicator of the hardness of the radiation field, also less dependant on density than the optical lines (and compared to [S IV]/[S III]33 $\mu\text{m}$  as well).

★ [S III]  $18.71\mu\text{m}$  and [S III]  $33.48\mu\text{m}$

S<sup>+</sup> has an ionisation potential of 23.34 eV and arises from the ionised gas. The transitions at 18.71 and 33.48 $\mu\text{m}$  have critical densities of  $2 \times 10^4 \text{ cm}^{-3}$  and  $7 \times 10^3 \text{ cm}^{-3}$  respectively. The ratio of the two [S III] lines measures reliably the density in the H II regions, as it is not very sensitive to the electronic temperature and to extinction as opposed to optical doublets of [O II] or [S II] often used (Houck et al. 1984).

These MIR lines have globally high excitation potential and high critical densities, hence they trace (compact) H II regions. The [Fe II] 25.99 $\mu\text{m}$  (7.90 eV) and [Si II] 34.82 $\mu\text{m}$  (8.15 eV) have ionisation potentials below that of hydrogen so they can be found in both the ionised and warm neutral gas. *Spitzer* MIR fine-structure line studies in dwarf galaxies include Houck et al. (2004); Wu et al. (2006); Madden et al. (2006); Hunt et al. (2006); Hunter & Kaufman (2007); Thuan et al. (2008).

## Molecular lines

★  $\text{H}_2$  rotational lines

In principle,  $\text{H}_2$  is the most abundant molecule. Since it has no permanent dipole moment, dipole transitions are forbidden, and  $\text{H}_2$  does not emit at long wavelengths (mm). However, rotational quadrupole transitions ( $\Delta J = \pm 2$ ) can occur and are visible in the MIR from *Spitzer*. They are divided into ortho- (antiparallel nuclear spin, even  $J$  number) and para- (parallel spin, odd  $J$  number) transitions.  $\text{H}_2$  lines seen in emission in the IR are rotational-vibrational transitions in the electronic ground state. The MIR  $\text{H}_2$  lines (3.4 to 28 $\mu\text{m}$ ) are pure rotational transitions ( $\Delta \nu = 0$ ), while the NIR (1 to 4 $\mu\text{m}$ ) are vibrational transitions ( $\Delta \nu = \pm 1$ ). Since they require excitation temperatures  $T > 500$  K, they are generally tracing warm neutral phases.

$\text{H}_2$  can also be seen in absorption in the UV in the Lyman-Werner band electronic transitions, from warm and cold diffuse gas in front of strong UV sources.

$\text{H}_2$  emission is seen in a variety of objects: in outflows (Neufeld et al. 2009); PDRs (Tielens et al. 1993; Sheffer et al. 2011); nebulae (Lebouteiller et al. 2006); etc. It is detected in dwarf galaxies in emission with *Spitzer* (Hunt et al. 2010) and in absorption with *FUSE* (Tumlinson et al. 2002; Cannon et al. 2006).

### ★ CO rotational lines

$^{12,13}\text{CO}$  rotational lines are the most common tracers of molecular clouds (e.g. Dame et al. 2001; Wilson et al. 2009). CO is the second most abundant molecule and has rotational transitions in the FIR and submm. Since its rotational energy ( $5 \times 10^{-4}$  eV) is lower than its vibrational energy (0.27 eV), cooling by rotational transitions is more efficient.

The rotational energy levels are given, to first order, by (here following the notation of Tielens 2005):

$$\frac{E_r}{hc} = B_e J(J+1),$$

where  $B_e$  is the rotational constant, and  $J$  the rotational quantum number. Transitions are allowed for  $\Delta J = \pm 1$ , hence they are evenly spaced in frequency. The CO transitions are often referred to as 'low-J' and 'high-J' transitions in the literature. The low-J lines generally correspond to the 2.60, 1.30, and 0.87 mm transitions, i.e.  $J = 1, 2, 3$ , which are the most commonly observed, while high-J transitions may correspond to  $J > 3$ .

Low-J CO lines are tracers of the cold molecular gas phases. The excitation temperature and critical density increase with level transition, hence the higher transitions trace warmer and/or denser gas phases. At low density ( $\leq 10^4 \text{ cm}^{-3}$ ), low-J CO line ratios are indicative of the density of the medium, while at high density they are good diagnostics of the gas temperature (LTE conditions, see Section 5.2.3). Since CO starts to form relatively deeply into the cloud, optical depth can affect its observed intensity. The low-J CO lines, and particularly CO ( $J \rightarrow 1-0$ ) and CO ( $J \rightarrow 2-1$ ), are often optically thick. At high optical depth, the CO lines are also likely thermalised.

Receivers exist at ground-based telescopes for local universe low-J CO lines (CO  $J=3 \rightarrow 2$ ,  $2 \rightarrow 1$ ,  $1 \rightarrow 0$ ), with single-dish antennas (e.g. APEX/SHeFI, IRAM/30m, JCMT/HARP, ATNF/Mopra), and interferometers (e.g. SMA, ALMA, IRAM/PdB), as well as for high-J CO lines (e.g. CO  $J=7 \rightarrow 6$  with APEX/CHAMP<sup>+</sup>) or the Caltech Submillimeter Observatory (CSO), although the high-J lines are mostly visible from space due to the poor atmospheric transmission, with, for example, the instrument SPIRE onboard *Herschel*.

### UV and optical lines

A wealth of UV and optical studies grew from the *HST* and *Galaxy Evolution Explorer* (*GALEX*) missions. Temperatures required to excite UV and optical lines are such that they are generally encountered in H II regions of starburst galaxies. The most important tracers of the nebulae are the H I recombination lines, as well as metallic lines such as [N II], [S II], [O II], [O III] excited by collisions with  $e^-$ .

The recombination lines of H $\alpha$  ( $\lambda 6563 \text{ \AA}$ ) and H $\beta$  ( $\lambda 4861 \text{ \AA}$ ) of the hydrogen Balmer series are among the brightest lines observed, and therefore common tracers of the ionised gas. In particular, their ratio is used to estimate dust extinction along the line of sight (e.g. Calzetti et al. 1994).

As mentioned in Section 1.1.3, the [S II] and [O II] lines measure the electron density since they have similar excitation temperatures and different critical densities, while the [O III] and [N II] lines give electron temperatures.

**Table 1.2.** General properties of selected fine-structure cooling lines.

Line	Wavelength ( $\mu\text{m}$ )	Transition	E. P. (eV)	I. P. (eV)	$\Delta E/k$ (K)	Critical density ( $\text{cm}^{-3}$ )
<i>Spitzer/IRS</i>			(a)	(b)	(c)	(d)
[S IV]	10.51	$^2P_{3/2} - ^2P_{1/2}$	34.79	47.22	1 369	$5 \times 10^4$ [e]
[Ne II]	12.81	$^2P_{1/2} - ^2P_{3/2}$	21.56	40.96	1 123	$7 \times 10^5$ [e]
[Ne III]	15.56	$^3P_1 - ^3P_2$	40.96	63.45	925	$3 \times 10^5$ [e]
[S III]	18.71	$^3P_2 - ^3P_1$	23.34	34.79	769	$2 \times 10^4$ [e]
[S III]	33.48	$^3P_1 - ^3P_0$	23.34	34.79	430	$7 \times 10^3$ [e]
[Si II]	34.82	$^2P_{3/2} - ^2P_{1/2}$	8.15	16.35	413	$3 \times 10^5$ [H], $1 \times 10^3$ [e]
Hu $\alpha$	12.37	$^7S_1 - ^6S_1$	-	13.60	1 163	-
H2	28.22	(0,0) S(0)	4.48	15.43	510	$7 \times 10^2$ [H]
H2	17.03	(0,0) S(1)	4.48	15.43	1 015	$2 \times 10^4$ [H]
H2	12.28	(0,0) S(2)	4.48	15.43	1 682	$2 \times 10^5$ [H]
H2	9.66	(0,0) S(3)	4.48	15.43	2 504	$9 \times 10^5$ [H]
[Fe III]	22.93	$^5D_3 - ^5D_4$	16.19	30.65	627	$1 \times 10^5$ [e]
[O IV]	25.89	$^2P_{3/2} - ^2P_{1/2}$	54.94	77.41	555	$1 \times 10^4$ [e]
[Fe II]	25.99	$a^6D_{7/2} - a^6D_{9/2}$	7.90	16.19	554	$2 \times 10^6$ [H], $1 \times 10^4$ [e]
[Ar III]	8.99	$^3P_1 - ^3P_2$	27.63	40.74	2 060	$3 \times 10^5$ [e]
[Ar II]	6.99	$^2P_{1/2} - ^2P_{3/2}$	15.76	27.63	1 600	$4 \times 10^5$ [e]
[Ne V]	14.32	$^3P_2 - ^3P_1$	97.12	126.21	592	$3 \times 10^4$ [e]
<i>Herschel/PACS</i>						
[C II]	157.74	$^2P_{3/2} - ^2P_{1/2}$	11.26	24.38	91	$3 \times 10^3$ [H], 50 [e]
[O III]	88.36	$^3P_1 - ^3P_0$	35.12	54.94	163	$5 \times 10^2$ [e]
[O I]	63.18	$^3P_1 - ^3P_2$	-	13.62	228	$5 \times 10^5$ [H]
[O I]	145.52	$^3P_0 - ^3P_1$	-	13.62	99	$1 \times 10^5$ [H]
[N III]	57.32	$^2P_{3/2} - ^2P_{1/2}$	29.60	47.45	251	$3 \times 10^3$ [e]
[N II]	121.9	$^3P_2 - ^3P_1$	14.53	29.60	118	$3 \times 10^2$ [e]
[N II]	205.18	$^3P_1 - ^3P_0$	14.53	29.60	70	45 [e]
Optical	( $\text{\AA}$ )					
[O III]	5007	$^1D_2 - ^3P_2$	35.12	54.94	29 000	$7 \times 10^5$ [e]
[O III]	4959	$^1D_2 - ^3P_1$	35.12	54.94	29 000	$7 \times 10^5$ [e]
[O III]	4363	$^1S_0 - ^1D_2$	35.12	54.94	33 000	$2 \times 10^7$ [e]
[O II]	3729	$^2D_{5/2} - ^4S_{3/2}$	13.62	35.12	39 000	$3 \times 10^3$ [e]
[O II]	3726	$^2D_{3/2} - ^4S_{3/2}$	13.62	35.12	39 000	$2 \times 10^4$ [e]
[S II]	6716	$^2D_{5/2} - ^4S_{3/2}$	10.36	23.34	21 000	$1 \times 10^3$ [e]
[S II]	6731	$^2D_{3/2} - ^4S_{3/2}$	10.36	23.34	21 000	$4 \times 10^3$ [e]
[N II]	6583	$^1D_2 - ^3P_2$	14.53	29.60	22 000	$7 \times 10^4$ [e]
[N II]	6548	$^1D_2 - ^3P_1$	14.53	29.60	22 000	$7 \times 10^4$ [e]
[N II]	5755	$^1S_0 - ^1D_2$	14.53	29.60	25 000	$1 \times 10^7$ [e]
Frequency (GHz)						
Ground-based						
$^{12}\text{CO}$	115.27 <sup>(e)</sup>	$J \rightarrow 1 - 0$	11.09	14.01	5.5	$1.1 \times 10^3$
$^{12}\text{CO}$	230.54	$J \rightarrow 2 - 1$	11.09	14.01	16.6	$6.7 \times 10^3$
$^{12}\text{CO}$	345.80	$J \rightarrow 3 - 2$	11.09	14.01	33.3	$2.1 \times 10^4$

(a) Excitation potential. Energy required to create the specie.

(b) Ionisation potential. Energy required to ionise the specie. For H<sub>2</sub> and CO, it is the binding energy.

(c) Excitation temperature  $T = \Delta E/k$  required to populate the transition level.

(d) Critical densities  $n_{\text{crit}}$  are noted [e] for collisions with electrons ( $T = 10\,000\text{ K}$ ), [H] with hydrogen atoms ( $T = 100\text{ K}$ ), and [H<sub>2</sub>] with molecular hydrogen ( $T = 10\text{ K}$ , in the optically thin limit).

(e) Frequency of the transition in GHz.

References: Malhotra et al. (2001), Giveon et al. (2002), Kaufman et al. (2006), Tielens (2005), and Osterbrock & Ferland (2006).

## Dust tracers

Dust plays an important role in the global energy balance of galaxies, acting in the cooling and heating of the ISM through the photoelectric effect, described in Section 1.2.2. It absorbs

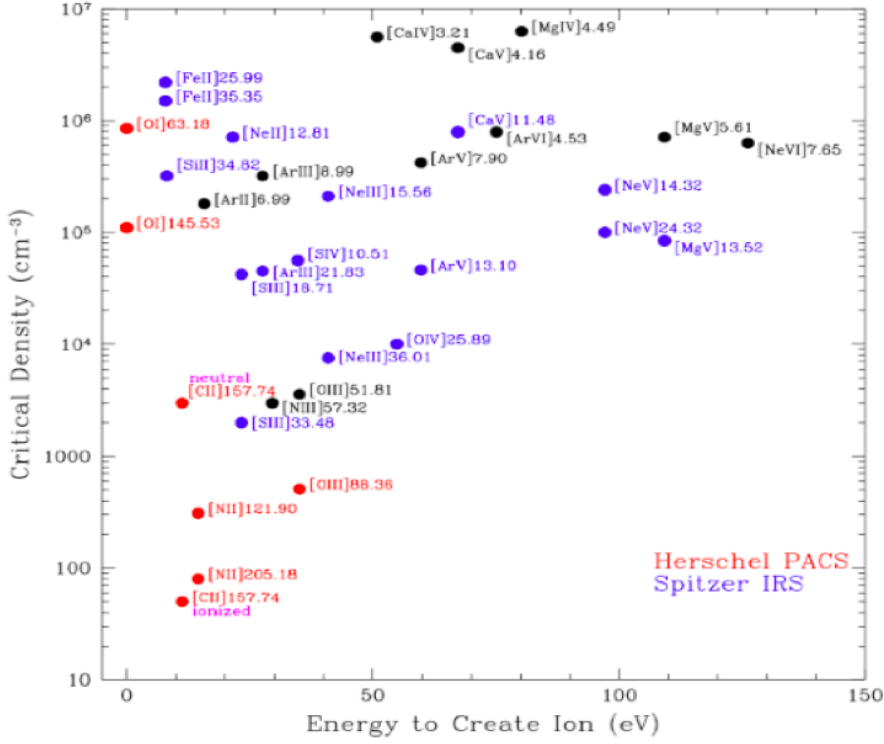


**Figure 1.5.** Excitation potential (E.P.) versus critical density ( $n_{crit}$ ) for the fine-structure lines within the *Spitzer* and *Herschel* ranges; from Kennicutt et al. (2011). The broad parameter space sampled indicate the broad range and mixture of physical conditions probed.

starlight, causing extinction longwards 912 Å, and reemits it in the IR to submm range. Dust is formed in the envelope of evolved stars and is present in all ISM phases where it can survive. Dust grains are injected in the ISM via stellar winds and can be destroyed by shock waves of e.g. supernovae. The composition of dust is not perfectly known but it is considered to be principally made of silicate and carbon components, and to enclose most of the heavy elements of the ISM. Dust grains exist in galaxies with a distribution of sizes. The standard model of the size distribution of grains is the MRN model from Mathis et al. (1977), which considers a power law size distribution:

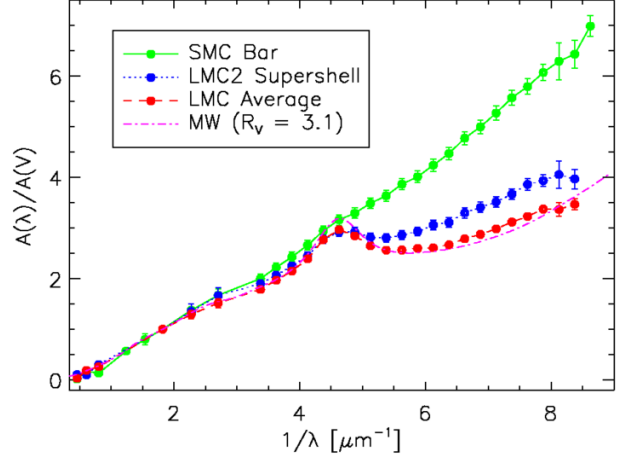
$$n(a) \propto a^{-3.5},$$

where  $a$  is the grain size in the range 50-2500 Å. PAHs are at the small size end of the distribution. Spectral energy distributions (SEDs) of galaxies are reproduced by standard models using a combination of silicate and carbon grains, with the carbon grains taking the form of graphite (Draine & Li 2007) or amorphous carbon grains. The dust masses, involved in modeling the observed SEDs of dwarf galaxies using graphite, are often too high to reconcile with chemical evolution for low metallicity environments (Galliano et al. 2011). Instead, the use of more emissive dust grains, such as amorphous carbons (Zubko et al. 2004), which are enriched in H atoms ( $\sim 33\%$ ), may be more appropriate.

The different composition and size distribution of dust grains results in a different extinction law at low metallicity compared to Galactic. Extinction is non-uniform as the dust distribution is generally clumpy. Figure 1.6 shows the extinction curves of the Milky Way, LMC, and SMC, characteristic of quiescent and more active regions respectively. The total-to-selective extinction ratio  $R_V$  is defined as:

$$R_V = A_V / E(B - V),$$

**Figure 1.6.** Extinction curves of the Milky Way (pink,  $R_V=3.1$ ), LMC (red,  $R_V=3.4$ ), LMC-2 (blue,  $R_V=2.8$ ), and SMC (green,  $R_V=2.7$ ); from [Gordon et al. \(2003\)](#). The bump at 2175 Å is due to the presence of graphite or carbon-rich particles, while the different extinction in the UV-optical is due to the presence of intermediate-size ( $\sim 100$  Å) to big grains (2000 Å).



where  $A_V$  is the visual extinction and  $E(B - V)$  the B-V color.  $R_V$  is sensitive to the grain size, composition, and shape, with  $R_V=3.1$  in the diffuse ISM, and  $R_V=5.5$  in denser environments such as the Orion Nebula. The different curves can be reproduced with different mixture of grains ([Weingartner & Draine 2001](#)).

Dust grains emit in the MIR to submm continuum and hence their emission is easily observable in photometry. The dust continuum has been sampled by space telescopes in the following bands:

- 12, 25, 60, and 100  $\mu\text{m}$  with *IRAS*;
- between 2.5 and 16  $\mu\text{m}$ , essentially at 7 and 15  $\mu\text{m}$ , with *ISO/ISOCAM*;
- 3.6, 4.5, 5.8, 8.0  $\mu\text{m}$  with *Spitzer/IRAC*, and 24, 70, 100  $\mu\text{m}$  with *Spitzer/MIPS*;
- 70, 100, 160  $\mu\text{m}$  with *Herschel/PACS*, and 250, 350, 500  $\mu\text{m}$  with *Herschel/SPIRE*.

Longer wavelengths are also accessible from the ground with, e.g., the 870  $\mu\text{m}$  band at *APEX/LABOCA* or the 450  $\mu\text{m}$  and 850  $\mu\text{m}$  bands at *JCMT/SCUBA*.

Emission in the MIR, typically the 24  $\mu\text{m}$ , is due to smaller size grains ( $< 200$  Å), and is often dominated by dust residing in the H II regions or warm phases. Larger grains ( $\sim 1000$  Å) emit in the FIR, typically at 60 to 160  $\mu\text{m}$ , from more diffuse ionised gas and neutral gas. The coldest phases associated with the molecular clouds emit in the submm at 250-500  $\mu\text{m}$ .

PAHs are large molecules of  $\sim 50$  C atoms that cool via vibrational (bond bending and stretching modes) transitions in distinct emission bands in the MIR. They are observed in spectroscopy with the instrument IRS onboard *Spitzer* with prominent features at 6.2, 7.7, 8.6, 11.3, and 12.7  $\mu\text{m}$ , and they also contribute, in part, to the 7  $\mu\text{m}$  *ISOCAM* band, the 12  $\mu\text{m}$  *IRAS* band, and the 5.8 and 8.0  $\mu\text{m}$  IRAC bands. They are generally destroyed in H II regions and normally peak in PDRs.

### 1.2.5 Spectral energy distribution

SEDs of galaxies are a good mean to understand the global energy balance in galaxies, throughout the UV-radio wavelength range, as illustrated by Figure 1.7.

Such global picture gives information on the bolometric luminosity of galaxies. Restricting ourselves to the IR wavelength range, FIR (40 to 120  $\mu\text{m}$ ) or total IR (TIR, 3 to 1100  $\mu\text{m}$ ) luminosities can be derived. When lacking observational constraints to properly integrate the SEDs, empirical formulae are used, calibrated on SEDs of normal star-forming galaxies, such as the [Helou et al. \(1988\)](#) and [Sanders & Mirabel \(1996\)](#) formulae based on *IRAS* fluxes,



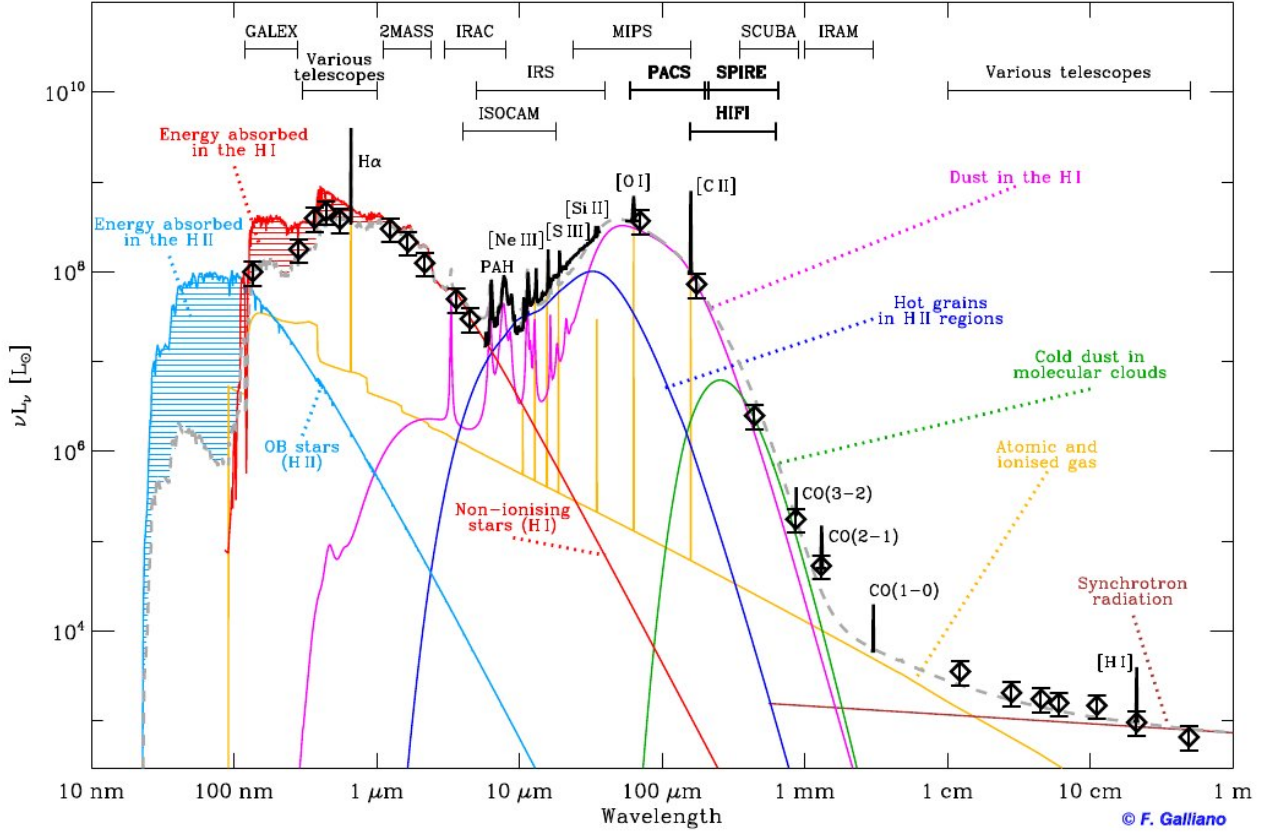


**Figure 1.7.** Example of a synthetic spectral energy distribution (SED) of a galaxy. Stellar spectra of ionising stars and older stars are shown in blue and red colors respectively. Part of the stellar energy is absorbed by dust, causing extinction in the UV-optical, and reemitted in the IR (small grains in blue, big grains and PAHs in purple, very cold dust in green), indicating the energetic balance throughout the UV-radio wavelength range. Cooling from the gas and free-free emission appears in yellow. Observations are overlotted with dark symbols.

the Dale & Helou (2002) and Draine & Li (2007) formula based on *Spitzer* fluxes, and now formulae based on *Herschel* fluxes (e.g. Boquien et al. 2011; Galametz et al. 2012).

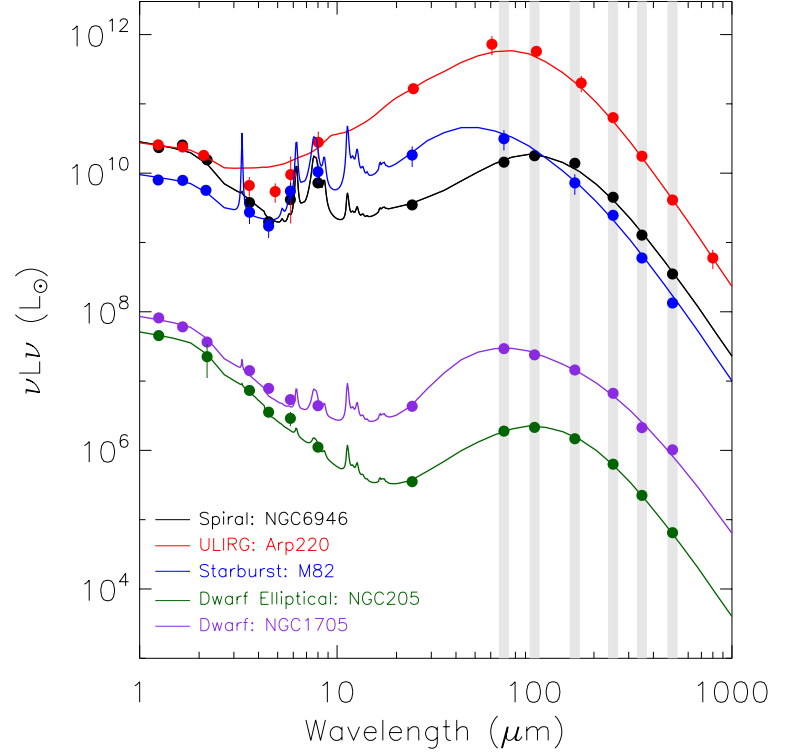
### 1.3 Metallicity effect on the ISM of dwarf galaxies

#### 1.3.1 Dust properties

Despite the low metallicity, dust is not negligible in dwarf galaxies and demonstrates particularly different properties compared to more metal-rich galaxies. The most noticeable to the observer, and which are linked to environment or intrinsic dust properties, are:

- a shift of the peak of the dust emission to shorter wavelength. This results in generally higher 60 or 70/100 $\mu$ m ratios, observed in photometry originally by *IRAS* (Melisse & Israel 1994), and now seen with *Herschel* (Madden et al. 2012a; Rémy et al. 2012). As the peak of the SED is due to thermal radiation from dust grains, the shift translates in global warmer dust temperatures. Figure 1.8 is an illustration of the SED of galaxies of several spectral types, in which the SEDs of the classic starburst M82 and of the dwarf starburst galaxy NGC 1705 peak at  $\sim 50\text{--}70\mu\text{m}$ , and the SEDs of the other spectral types peak at  $\sim 100\mu\text{m}$ .

**Figure 1.8.** SED comparison of 5 different spectral type galaxies: the star-forming dwarf galaxy NGC 1705 (purple, O’Halloran et al. 2010), the spiral galaxy NGC 6946 (black, Aniano et al. 2012), the ULIRG Arp 220 (red), the metal-rich starburst M 82 (blue, Roussel et al. 2010), and the dwarf elliptical NGC 205 (green, De Looze et al. 2012). Taken from Madden et al. (2012b). The SED of NGC 1705 is noticeably fainter, and illustrates the typical properties observed in dwarf galaxies.



- *a steep rise of the continuum emission in the MIR and a dearth of PAHs.* This results in higher 24/12μm ratios observed by *IRAS* and *Spitzer*. In the MIR, the SED is shaped by the low level of PAHs and the presence of more abundant small and very small grains ( $\sim 30$  Å; e.g. Sauvage et al. 1990; Galliano et al. 2003, 2005; Engelbracht et al. 2005; Madden et al. 2006; Wu et al. 2008). The hard radiation fields present in star-forming regions, combined with the paucity of the low metallicity ISM, destroy the larger molecules such as PAHs and grains into smaller particles. Such reshaping of the dust size distribution has an impact on the physical processes of the ISM and, in turn, on the observed gas properties (Section 1.2).
- *a flatter SED peak.* Combined with the steep MIR rise and a peak at short wavelength, the SED of dwarf galaxies is often dominated by the contribution of stochastically heated warm dust grains in the H II regions.
- *excess submm emission at wavelengths longward of 500μm* (Galliano et al. 2003, 2005; Galametz et al. 2011; O’Halloran et al. 2010; Madden et al. 2011). First known to exist in dwarf galaxies via 850μm and 870μm from *JCMT/SCUBA* and *APEX/LABOCA*, this excess corresponds to emission that remains after fitting the dust SEDs. It is not accounted for by molecular lines, free-free or synchrotron emission either. The origin of this excess remains unknown, but has been suggested to be due to: (1) very cold dust ( $T < 10$ K, Galliano et al. 2005; Galametz et al. 2011); (2) temperature dependent grain opacity (e.g. Lisenfeld et al. 2002; Meny et al. 2007; Galliano et al. 2011; Paradis et al. 2011); (3) rapidly spinning dust grains (e.g. Draine & Lazarian 1998; Bot et al. 2010; Ysard et al. 2011); or (4) magnetic nanoparticles (Draine & Hensley 2012). The implications of any of the possible scenarios are various. Dust masses are signif-



icantly biased by the coldest phases. Thus the very cold dust interpretation of the submm excess leads to very different (higher) dust mass and hence observed dust-to-gas mass ratios often in conflict with the expected elemental abundances. A massive, currently overlooked, gas reservoir may make this solution possible, and for which the cold dust should therefore exist in self-shielded conditions. However, recent mapping at  $500\mu\text{m}$  *Herschel* with 10 pc resolution in the Large Magellanic Cloud ( $Z \sim 1/3 Z_\odot$ ) reveals a submm excess that ranges from 15% to 40% compared to that expected from dust SED models. They find that the excess may be diluted over large spatial scales for unresolved objects, and that it does not seem spatially correlated with the densest molecular gas phases (Galliano et al. 2011).

The spinning dust scenario, on the other hand, should better correlate spatially with the PAHs or the ionised gas. Since the different interpretations of the submm excess depend on the environment, localising the spatial distribution of the excess with respect to the star formation sites and the molecular gas will help constrain its origin.

Great advances on that matter are now possible with the unprecedented capabilities of *Herschel* and *ALMA*. More details on what *ALMA* can bring in the studies of dwarf galaxies are laid out in Chapter 6. A systematic study of the submm excess and D/G ratios in the dwarf galaxies of the *Herschel* “Dwarf Galaxy Survey” program is presented in Rémy et al. (2012). This will extend previous studies to fainter and lower metallicity galaxies.

Modeling observations constrained from the IR to the mm with accurate dust composition and properties is essential for the determination of dust and gas mass, extinction, star formation properties, etc.

### 1.3.2 Gas properties

#### Star formation law

Galactic studies have demonstrated that stars form by gravitational collapse of high density molecular clouds, containing essentially molecular  $\text{H}_2$ . The study of star formation on large scales in external galaxies is not straightforward. It is generally understood that stars are formed through gravitational instabilities above a specific gas density threshold  $\Sigma_{\text{crit}}$  (e.g. Toomre 1964; Kennicutt 1989). Then the star formation activity is related to the reservoir of gas via the Schmidt-Kennicutt law (e.g. Schmidt 1959; Kennicutt 1998):

$$\Sigma_{\text{SFR}} \propto (\Sigma_{\text{gas}})^n, \text{ with } n \simeq 1.4. \quad (1.1)$$

$\Sigma_{\text{SFR}}$  is the surface star formation rate, and  $\Sigma_{\text{gas}}$  the surface gas density. This relation was first calibrated on galaxies as a whole, with global quantities. This gas reservoir is the driver of galaxy formation and evolution.

#### Star formation rate determination

The star formation activity in galaxies can be evaluated from several tracers, which depend on the evolutionary stage probed. The usual tracers include the FUV magnitude,  $\text{H}\alpha$  emission, FIR luminosity, or radio luminosity. All these tracers are connected to the presence of massive stars.

UV and optical tracers are direct probes of the stellar activity. The recent star formation in H II regions is derived from  $\text{H}\alpha$  observations (e.g. Kennicutt et al. 2008) or from FUV

tracing OB stars in low density low surface-brightness galaxies (e.g. Lee et al. 2011). Both are affected by dust attenuation and require a correction to accurately recover the SFR.  $H\alpha$  emission may also have a contribution from the  $[N\text{ II}]$  6583 Å. This contamination can be partly to fully excluded using narrow-band filters when imaging or high spectral resolution in spectroscopy.

Dust absorbs starlight and re-emits in the FIR, translating the global energy balance between UV/optical and FIR. This also makes the FIR emission a good tracer of the current star formation, and shows the complementarity between UV/optical and IR tracers to uncover SFRs. Dust emission at  $24\mu\text{m}$  is typically due to heating by young massive stars, and has proven to accurately trace the ongoing dust-obscured star formation (Calzetti et al. 2007). It is particularly useful to have a well-calibrated monochromatic emission when data is missing from the full SED and total IR luminosities are uncertain. Combinations of  $H\alpha$  and  $24\mu\text{m}$  data are calibrated in Kennicutt et al. (2007), and combinations of FUV and  $24\mu\text{m}$  data are used in Bigiel et al. (2008), as prescriptions to describe the obscured and unobscured star formation activity. Radio continuum emission is also a good tracer of highly obscured regions. For example, at 1.4 GHz with the VLA, this emission is due to non-thermal synchrotron radiation from accelerated particles in, e.g., supernova remnants. Hence it traces star formation through the supernova rate (e.g. Condon 1992).

On the other hand, H I and molecular lines trace future star formation, before clouds collapse and form H II regions.

#### *Slope of the Schmidt-Kennicutt law*

Variations in the slope of the power law in Equation 1.1 have been observed according to the type of object studied, the gas phase and scale length considered. The value of 1.4 from Kennicutt (1998) was found for a total gas reservoir of H I+H<sub>2</sub> in nearby IR-bright and spiral galaxies. Boissier et al. (2003) derive a slope of  $\sim 2$  in nearby disc galaxies. Daddi et al. (2010) obtain a similar slope in distant ( $z > 0.5$ ) star-forming galaxies.

Different relations are found when looking closely at particular galaxy types, smaller size scales, or gas reservoirs (H I and/or H<sub>2</sub>). For example, in a spatial analysis of the SMC, Bolatto et al. (2011) find a slope of 2.2 between star formation rate and total gas surface density, comparable to that found in the outer disks of spiral galaxies (Bigiel et al. 2010). However, studies of dwarf galaxies are limited to a small sample of nearby targets, as both CO (hence H<sub>2</sub>) and H I can be challenging to observe. Studies are also made to link separately  $\Sigma_{\text{HI}}$  only, and  $\Sigma_{\text{H}_2}$  only to  $\Sigma_{\text{SFR}}$ . Leroy et al. (2005) find a slope of 1.4 in spiral galaxies and 1.3 in dwarf galaxies considering the molecular gas only. A detailed resolved (750 pc scale) study by Bigiel et al. (2008) was performed over the optical disks of nearby spirals and starburst galaxies from the THINGS (Walter et al. 2008) and HERACLES (HERA CO Line Extragalactic Survey; Leroy et al. 2009b) surveys. They demonstrate a linear correlation (slope  $\sim 1$ ) between  $\Sigma_{\text{SFR}}$  and  $\Sigma_{\text{H}_2}$ , while the slope between  $\Sigma_{\text{SFR}}$  and  $\Sigma_{\text{HI}+\text{H}_2}$  is 1.85. In particular, they find that the atomic gas alone correlates poorly with SFR, contrary to the molecular gas. The surface density of H I presents a threshold for high column densities, at  $\Sigma_{\text{H}_2} \sim 9 \text{ M}_\odot \text{ pc}^{-2}$ , above which only molecular gas is found. Finally, relations with other gas species related to the SFR can also exist. For example, Gao & Solomon (2004) find that the dense gas tracer, HCN, correlates with a slope of  $\sim 1$  with SFR in (U)LIRGs.

From a theoretical point of view, the different slopes may be explained according to the star formation mechanism preferred (gravitational instabilities, collisions, etc.; see Bigiel et al. 2008 for details). While the cold gas is directly linked to the sites of star formation, the total gas as a whole does correlate with star formation rate in galaxies. Recent studies

have shown that molecules may not actually be needed for triggering star formation, but cold atomic/molecular high density clumps are (Glover & Clark 2012). For metallicities below a few percent of solar, Krumholz (2012) explain that the chemical timescale to convert H I to H<sub>2</sub> can become much larger than the thermal and free-fall timescales of the cloud, in which the cooling is essentially done through fine-structure lines (e.g. carbon), leading to star formation before molecules form. What is the role of the different ISM phases, especially of the H I reservoir? How do they act and over what timescales related to the star formation process?

#### *Gas depletion times*

The slope of the Schmidt-Kennicutt law is directly related to the gas depletion time  $\tau_{dep} = \Sigma_{gas}/\Sigma_{SFR}$ . There is evidence that the star formation law in galaxies is mostly regulated by the molecular gas rather than the total (molecular and atomic) gas content of galaxies, and that the timescale to convert molecular gas into stars is universal and around  $\tau_{dep} \sim 2$  Gyr (Kennicutt et al. 2007; Bigiel et al. 2008; Leroy et al. 2008; Genzel et al. 2012). This universality can be understood if star formation is a local process independent of environment and set by constant molecular cloud properties (e.g. Bolatto et al. 2008). Bolatto et al. (2011) show that, in the SMC, molecular gas depletion times are dependant on the spatial scale considered, with lower  $\tau_{dep}$  at larger scales, and  $\tau_{dep} \sim 1.6$  Gyr at 1 kpc scale typical of the previous studies. Bigiel et al. (2011) show that the gas depletion time increases with galactocentric radius outside the optical radius of galaxies, with an average value of 100 Gyr. Saintonge et al. (2011) find that the gas depletion time is not constant but an increasing function of stellar mass with an average lower value of  $\tau_{dep} \sim 1$  Gyr in the COLD GASS survey. The COLD GASS survey observes a large sample of volume-limited massive galaxies ( $10^{10} M_{\odot} < M_{\star}$ ) hence it contains more low mass and extreme galaxies compared to Leroy et al. (2008), which tend to deviate from a constant  $\tau_{dep}$ . Similarly, from the GASS survey, Schiminovich et al. (2010) and Saintonge et al. (2011) find a depletion time of atomic H I of 3 Gyr, but with a larger scatter than for H<sub>2</sub>.

Is it the gas itself under localised physical processes (turbulence) that triggers star formation or are other global parameters such as the local potential well, pressure, rotation, or chemical enrichment of massive galaxies at play? The fraction of H<sub>2</sub> to H I, and thus the formation of giant molecular clouds (GMC), depends on local conditions. Leroy et al. (2008) emphasize that point stating that the star formation efficiency in H<sub>2</sub>-dominated regions is independent of global parameters (radius, stellar mass, pressure, etc.) but is rather set by smaller scale physics (shocks, turbulence, H<sub>2</sub> formation, balance of ISM phases).

Depletion times are found to be different in high and low mass galaxies. In high mass galaxies, feedback processes preventing the gas from forming stars are important, resulting in long depletion times. The shorter depletion times found in low mass galaxies may reveal an enhanced star formation efficiency due to starbursts triggered locally, or uncertainties on the determination of the gas mass, as in dwarf galaxies. Hunter et al. (1998) show that irregular dwarf galaxies start forming stars from more stable gas than spirals.

#### **Cloud structure at low metallicity**

Although many dwarf galaxies are actively forming stars and host a large reservoir of atomic H I, detecting molecular gas in these objects turns out to be challenging. Cold H<sub>2</sub> is not directly traceable because it has no dipole moment. The second most abundant molecule CO is therefore the most common molecular gas tracer, but is difficult to detect in low-

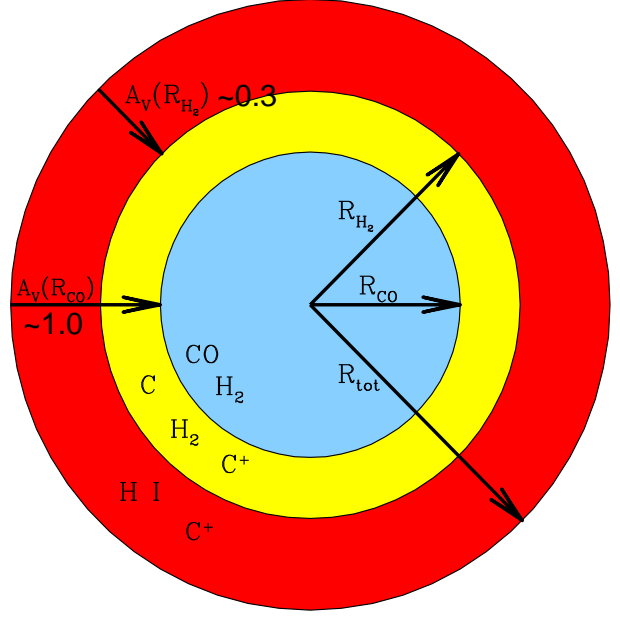


**Figure 1.9.** Illustration of a molecular cloud with PDR layers; from [Wolfire et al. \(2010\)](#). The layers are successively composed of atomic  $\text{H I}$  (red),  $\text{H}_2$  without CO (yellow; the “dark gas”), and  $\text{H}_2$  coexisting with CO (blue).

metallicity dwarf galaxies ([Taylor et al. 1998](#); [Leroy et al. 2011](#); [Schruba et al. 2012](#)). These dwarf galaxies often host active bursty star formation. This makes us wonder where the fuel for this star formation is. Is star formation occurring differently in these environments? Is the faintness of CO a result of little molecular gas content, or does it imply that CO becomes a poor tracer of  $\text{H}_2$  in the low-metallicity ISM of dwarf galaxies?

The dearth of CO can be a direct result of the chemical evolution or due to the structure and conditions of the ISM. PDR modeling at low metallicity demonstrates the profound effects on the gas temperatures, which result in an enhanced CO emission from higher-J transitions, and on the structure of the PDR envelope. The low dust content and the strong FUV field from the nearby young star clusters characteristic of star-forming dwarf galaxies ([Madden et al. 2006](#)) photodissociates molecules that are not efficient in self-shielding, such as CO which is not sufficiently abundant (e.g. [Wolfire et al. 2010](#); [Shetty et al. 2011](#)). This shifts the transition from atomic to molecular gas further into the cloud, reduces the relative size of the CO clump, and increases the volume of the PDR (see Figure 1.9). CO is thus confined to small clouds of diameter on the order of tens of parsecs, which are difficult to observe from single-dish telescopes (see Chapter 5) because of beam dilution.

On the other hand,  $\text{H}_2$  can be more effective at self-shielding and survive in the C-emitting envelope of PDRs ([Poglitsch et al. 1995](#); [Madden et al. 1997](#); [Glover et al. 2010](#); [Wolfire et al. 2010](#)). This molecular gas not traced by CO has been referred to as the “dark gas” and may be a potential large reservoir for star formation ([Grenier et al. 2005](#); [Wolfire et al. 2010](#); [Krumholz et al. 2011](#)). This dark component, invisible from the commonly used gas tracers, CO or  $\text{H I}$ , was also shown to be present in solar neighbourhood clouds by  $\gamma$ -ray observations ([Grenier et al. 2005](#)). Recently, FIR continuum observations of the Large Magellanic Cloud ( $1/2 Z_\odot$ ) with *Herschel* and of our Galaxy with *Planck* likewise suggest that there is more molecular gas than that traced by the CO(1-0) line ([Roman-Duval et al. 2010](#); [Galliano et al. 2011](#); [Planck Collaboration et al. 2011](#)).

### The $X_{\text{CO}}$ conversion factor

Determining the molecular gas mass in dwarf galaxies is challenging. The molecular gas mass is usually derived from CO observations as a tracer of the cold  $\text{H}_2$  using the CO-to- $\text{H}_2$  conversion factor,  $X_{\text{CO}}$ , which relates the observed CO intensity to the column density of  $\text{H}_2$ :

$$\begin{aligned} X_{\text{CO}} &= N(\text{H}_2)/I_{\text{CO}}, \\ X_{\text{CO,gal}} &= 2.3 \times 10^{20} [\text{cm}^{-2} (\text{K km s}^{-1})^{-1}]. \end{aligned} \quad (1.2)$$

Alternatively, this conversion factor can be directly written as:

$$\begin{aligned} \alpha_{\text{CO}} &= M_{\text{H}_2}/L_{\text{CO}}, \\ \alpha_{\text{CO}} &= X_{\text{CO}} \times m_{\text{H}_2} \times \frac{\Omega}{4\pi d_L^2}, \\ \alpha_{\text{CO,gal}} &= 4.4 [\text{M}_\odot (\text{K km s}^{-1} \text{ pc}^2)^{-1}]. \end{aligned} \quad (1.3)$$

$\Omega$  is the source solid angle and  $d_L$  the luminosity distance. The  $X_{\text{CO}}$  factor was first calibrated on observations of CO(J=1-0) in resolved Galactic molecular clouds assumed to be virialised, with average value  $X_{\text{CO,gal}}$  (e.g. [Strong et al. 1988](#)). The principle is based on the dynamical equilibrium of the cloud, for which in the virial theorem, the observed line width of the CO line describes the size of the CO-emitting cloud. The virial mass is inferred from molecular cloud sizes and velocity dispersions, and linked to the CO luminosity via the mass-luminosity relation ([Solomon et al. 1987](#)). Such method was applied to Local Group irregular galaxies such as IC 10, NGC 6822, or NGC 4214 by [Wilson & Reid \(1991\)](#), [Wilson \(1992\)](#), and [Ohta et al. \(1993\)](#), who already found that the conversion factor may be higher at low metallicities than that of the Galaxy.

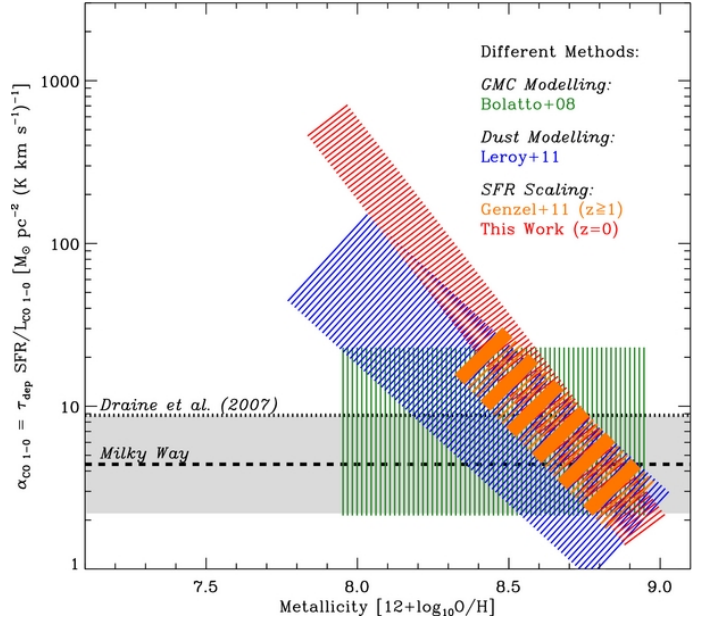
As stated previously, at low metallicity, the relation between total amount of  $\text{H}_2$  and observed CO is more ambiguous. The dependence of  $X_{\text{CO}}$  on metallicity, resulting from the geometry of the low metallicity clouds, is poorly constrained. In the CO-emitting cores, [Bolatto et al. \(2008\)](#) find  $X_{\text{CO}}$  values close to Galactic values from the analysis of spatially resolved clouds in a sample of local dwarf galaxies. However, the  $\text{H}_2$  accounted for by the CO cores is only a fraction of the total amount of  $\text{H}_2$  ([Madden et al. 1997](#); [Leroy et al. 2007](#)). This is also supported by numerical simulations of GMCs from [Glover & Mac Low \(2011\)](#) who find a constant conversion factor at large  $A_V$  ( $>3$ ), i.e. in the dense CO cores, and a steep increase in the  $X_{\text{CO}}$  with decreasing  $A_V$ .

For galaxies with unresolved clouds, as is the case for most dwarf galaxies beyond the Local Group, there is no clear recipe to convert the CO emission to  $\text{H}_2$  column densities. Several studies, based on different observational methods, have tried to calibrate the relation of  $X_{\text{CO}}$  with metallicity (Figure 1.10). [Schruba et al. \(2012\)](#) analyse the CO(2-1) emission of a sample of 16 dwarf galaxies from the HERACLES survey ([Leroy et al. 2009b](#)), and derive  $\alpha_{\text{CO}}$  values based on a constant depletion timescale. Despite the lack of firm detections at low metallicity, and sometimes stacking the data, they find a slope of  $\sim -2$  relating  $\log \alpha_{\text{CO}}$  to  $\log Z$ . [Genzel et al. \(2012\)](#) perform a similar analysis of CO(3-2) and CO(2-1) observations in a sample of massive star-forming galaxies at  $z \geq 1$ , and find a slope between  $-1.3$  and  $-1.8$ . From hydrodynamic simulations and radiative transfer modeling, [Narayanan et al. \(2012\)](#) find a dependence with metallicity of  $-1.65$ .

Dust also provides an indirect measure of the gas reservoir via the dust-to-gas (D/G) mass



**Figure 1.10.** Variation of the CO-to-H<sub>2</sub> conversion factor,  $\alpha_{CO}$ , with metallicity; taken from [Schruba et al. \(2012\)](#). The horizontal dashed line indicate the value of  $\alpha_{CO}$  in the Milky Way,  $\alpha_{CO,gal}$ , and the dotted line the value from [Draine et al. \(2007\)](#) from dust modeling of the SINGS sample. The stripped bands show the range and scatter of the  $\alpha_{CO}$  values found in several studies using different methods. Steep slopes of  $\alpha_{CO}$  with metallicity may hint towards high fractions of dark gas at low metallicity.



ratio. Since the gas is difficult to directly quantify at low metallicity, by modeling the dust emission and assuming a D/G mass ratio, one can get to the gas mass, and, when knowing the atomic gas mass, derive the molecular gas mass as in [Israel \(1997\)](#); [Leroy et al. \(2009a, 2011\)](#); [Galliano et al. \(2011\)](#):

$$\Sigma_{H_2} = (\Sigma_{dust} \times DGR^{-1}) - \Sigma_{HI}$$

[Leroy et al. \(2011\)](#) constrain the dust properties and solve for single D/G values to derive indirect gas masses, based on spatially resolved observations of Local group galaxies. They find close to Galactic values of  $\alpha_{CO}$  for M 33 ( $\sim 1/3 Z_{\odot}$ ) and  $\alpha_{CO} > 50$  for the SMC ( $1/5 Z_{\odot}$ ). Based on the same method, [Bolatto et al. \(2011\)](#) conduct a spatial analysis of the molecular gas distribution in the SMC using local D/G ratios, and find average value  $\alpha_{CO} = 220$ . Similarly, in a large sample of late-type galaxies, [Boselli et al. \(2002b\)](#) find a linear decrease of  $\log X_{CO}$  with increasing  $\log Z$  based on dust modeling and a metallicity dependent D/G. However, as mentioned earlier, dust mass determination and the behavior of D/G with respect to metallicity also hold uncertainties. The relatively large scatter in  $X_{CO}$  found for a given metallicity reflect that other parameters are at play ([Israel 1997](#)).

### Dark-gas tracers

#### • The warm H<sub>2</sub> gas

While the cold H<sub>2</sub> is not observable, rotational transitions of warm H<sub>2</sub> in the MIR are. Low level transitions of H<sub>2</sub>, from S(0) to S(7), from *Spitzer*/IRS observations have been detected in dwarf galaxies, but are faint (e.g. [Hunt et al. 2010](#)). The excitation of these transitions require  $T > 500$  K, hence, in principle, they give good constraints on the warm PDR conditions, but may be subject to extinction. [Roussel et al. \(2007\)](#) performed an analysis and quantification of the molecular gas, of both warm H<sub>2</sub> from IRS spectra and cold H<sub>2</sub> from ground-based CO observations, in the SINGS galaxy sample ([Kennicutt et al. 2003](#)), which comprises a wide variety of 75 local galaxies. They found that the fraction of cold to warm H<sub>2</sub> in normal galaxies is roughly between 5 and 20%. Hence the MIR H<sub>2</sub> lines do not trace the bulk of the molecular gas in these galaxies. In dwarf galaxies, the clumpy nature of the

ISM combined with the strong UV fields, which enhance the PDR envelope, may result in globally higher gas temperature in the PDR as well, enhancing the excitation of warm  $\text{H}_2$  (and high-J CO lines). However these transitions do not trace the cold PDR and associated  $\text{H}_2$ , which would carry more of the molecular gas mass. Without clear quantification of both the cold and warm  $\text{H}_2$  in dwarf galaxies, firm conclusions on the total molecular gas mass cannot be drawn. More data, in a large sample of low metallicity environments, would be needed. If the fraction of warm to cold  $\text{H}_2$  in dwarf galaxies were truly higher than in normal galaxies, the connection of this warm gas to star formation would still remain unclear. As star formation is known to occur in cold dense clumps, this gas would need to cool on very short timescales.

- *The [C II] 157 $\mu\text{m}$  line*

[C II] is one of the most important coolant of the ISM, and more specifically of the PDR around molecular clouds illuminated by massive stars, [C II] is found bright in dwarf galaxies as observed from the *KAO* (Poglitsch et al. 1995; Israel et al. 1996; Madden et al. 1997), *ISO* (Hunter et al. 2001), and *Herschel*, as will be shown in this work. It is understood from both observations (e.g. Crawford et al. 1985; Stacey et al. 1991) and models (e.g. Kaufman et al. 1999; Wolfire et al. 2010) that  $\text{C}^+$  is spatially associated with the PDR envelopes surrounding CO, thus tracing molecular clouds, and it is also correlated to the FIR emission, thus tracing the UV field strength. Moreover, the effect of metallicity is not as dramatic for  $\text{C}^+$  as for CO, which suffers from diminished filling factors when dust attenuation drops.  $\text{C}^+$  is expected to be much brighter than CO at lower metallicities, as illustrated in Figure 1.11. Hence  $\text{C}^+$  is potentially a good star formation tracer (e.g. Stacey et al. 1991, 2010), and maybe better than the typical [O I] PDR lines which can be affected by optical depth effects or excited by shocks (Hollenbach & McKee 1989). Boselli et al. (2002a) and de Looze et al. (2011) have assessed the reliability of [C II] as a star formation tracer from *ISO* observations of late-type and normal star-forming galaxies, calibrating [C II] respectively with  $\text{H}\alpha + [\text{N II}]$  and FUV+24 $\mu\text{m}$  to trace both the dust-enshrouded and unobscured activity. de Looze et al. (2011) find:

$$SFR [M_{\odot} \text{yr}^{-1}] = \frac{(L_{[\text{C II}]} [\text{ergs}^{-1}])^{0.983}}{1.028 \times 10^{40}}, \quad (1.4)$$

warning that this relation may not hold for quiescent galaxies and ULIRGs where a deficit is observed. This is also discussed in Section 3.2.4. Several factors may also hamper the reliability of this correlation, including the possible different origins of the [C II] line (in terms of media and excitation sources).

Evidence for the presence of a significant reservoir of CO-dark molecular gas, on the order of 10 to 100 times more  $\text{H}_2$  compared to that inferred by CO, is suggested by the exceptionally high [C II]-to-CO ratio found dwarf galaxies (Madden 2000; Hunter et al. 2001). It has been demonstrated that [C II]/CO(1-0) can effectively be used as a star formation tracer in nearby normal galaxies (Stacey et al. 1991) and high-redshift galaxies ( $z \sim 1-2$ , Stacey et al. 2010), with average values between 2 000 and 4 000 (for star forming galaxies). [C II]/CO(1-0) ratios in dwarf galaxies range from 4 000 to as high as 80 000 in the star-forming region 30-Doradus in the LMC (Poglitsch et al. 1995). Such high ratios, shown in Figure 1.12, are a result of the cloud structure with smaller CO cores and a larger PDR envelope which can in principle be traced by [C II]. A detailed study of the [C II] emission in IC 10 by Madden et al. (1997) has proven that it cannot be explained by heating from  $\text{H}^0$  collisions only but require an extra excitation source, such as  $\text{H}_2$ .

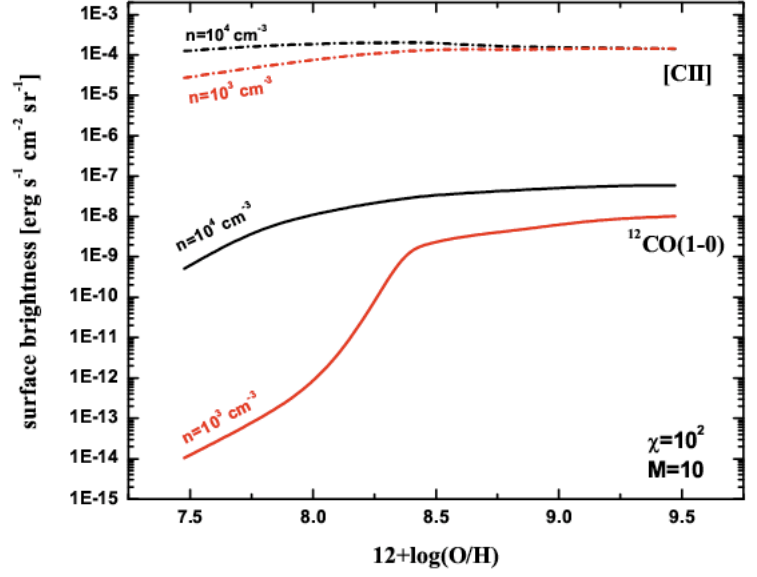


**Figure 1.11.** from Röllig et al. (2006a). [C II]158 $\mu$ m (dashed-dotted) and  $^{12}\text{CO}(1-0)$  (solid) surface brightness as a function of metallicity for two different densities (red and dark) using KOSMA- $\tau$ .

#### • Other line tracers

A result from the cloud structure is that, in addition to [C II], [C I] is also coexisting with  $\text{H}_2$  before CO starts to form. [C I] probes the inner layers of PDRs (Bayet et al. 2004; Kramer et al. 2005; Israel et al. 2006). Hence in principle [C I] could be a useful star formation and dark-gas tracer. [C I] is present in the submm wavelength regime with two fine-structure transitions,  $^3P_1 - ^3P_0$  at 609 $\mu$ m, and  $^3P_2 - ^3P_1$  at 370 $\mu$ m. Observations of [C I] in our closest neighbours, the Magellanic Clouds (Pineda et al. 2008, 2012), show that the ratio of [C II]/[C I] is on the order of 10. The [C II]/[C I] ratio is a measure of the FUV field (Gerin & Phillips 2000). [C I] observations in dwarf galaxies are sparse due to the faintness of these lines and the relatively poor atmospheric transmission at these wavelengths from ground-based facilities such as, for example, NANTEN2, JCMT, APEX, or ALMA. [C I] lines are also available with SPIRE onboard *Herschel*.

From numerical simulations of low metallicity molecular clouds, Glover & Clark (2012) compute the fractional abundances of  $\text{H}_2$  and  $\text{C}^+/\text{C}/\text{CO}$  at various metallicities. At the time corresponding to the onset of star formation (2 to 5 Myr), they find a global decrease in abundance of  $\text{H}_2$  relative to H, of [C I], CO relative to C, and a relative increase in abundance of  $\text{C}^+$  relative to C with decreasing metallicity. At a metallicity of  $1/3 Z_\odot$ , the fraction of  $\text{H}_2$  decreases by 15%, by 70% for [C I], by 80% for CO, and increases by 50% for  $\text{C}^+$ . Hence relative to CO, both  $\text{C}^+$  and, more marginally, [C I] become more abundant as metallicities decrease. For metallicities below  $1/10 Z_\odot$ , carbon is in the form of  $\text{C}^+$  at 99%.

Other molecular tracers would be challenging to detect at low metallicity since the same conditions apply as for CO. However, the emission from a few species might be relatively enhanced due to the extreme physical conditions of dwarf galaxies. For instance, low-J CO lines are the most commonly observed in galaxies as they are more accessible from the ground. The global warmer temperatures in dwarfs and hard radiation field, may also favor emission from higher-J CO lines ( $\geq J \rightarrow 4-3$ ). High CO line ratios, of CO  $J \rightarrow 2-1/\text{CO } J \rightarrow 1-0$ , are observed in, e.g., the SMC (Bolatto et al. 2003). High-J CO lines trace warmer and denser



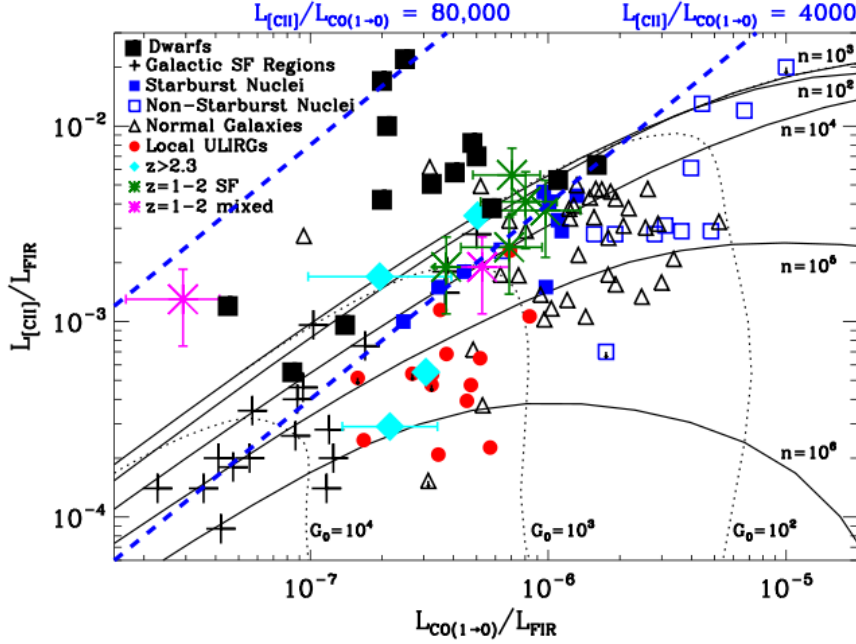


**Figure 1.12.**  $L_{[C II]}/L_{FIR}$  vs  $L_{CO}/L_{FIR}$  from Madden et al. (2012b). With high ratios, dwarf galaxies occupy a different parameter-space than normal galaxies. This plot is completed with new CO(1-0) and [C II] observations of dwarfs in Chapter 5.

gas phases and, hence, can be more accurate star formation tracers (Bayet et al. 2009b). High CO transitions, up to  $J \rightarrow 7 - 6$ , are observed with the *CSO* in the dwarf galaxies, IC 10 (Bayet et al. 2006), and He 2-10 (up Bayet et al. 2004). These lines are still relatively faint. Similarly, the dense PDR tracer  $HCO^+$ , with a transition at 3.36 mm of  $J \rightarrow 1 - 0$ , might be enhanced in dwarf galaxies. Seale et al. (2012) detect  $HCO^+ J \rightarrow 1 - 0$  and  $HCN J \rightarrow 1 - 0$  in the LMC.

Other dense gas tracers such as HCN or CS would also be ideal to probe the coldest phases of molecular clouds. Since their emission is clumpy and they are less abundant ( $< 10^{-6}$  relative to H) than CO, they would also suffer from beam dilution and be difficult to detect (e.g. Bayet et al. 2009a). HCN observations were attempted with *APEX* in NGC 5253 and He 2-10, but remain undetected (Vanzi et al. 2009).

PDR modeling from Bayet et al. (2009c) demonstrates that the relative abundances of HCN and  $HCO^+$  do not decrease as dramatically as CO or  $H_2O$  with metallicity ( $1/10 < Z [Z_\odot] < 1$ ), CN and OH are even enhanced. These could stand as molecular alternative tracers to CO in the low metallicity PDR. However their abundance relative to H is still very low. OH and  $H_2O$  transitions, in principle, can be accessed with *Herschel*, but the required sensitivity is beyond that capable to attempt detections in dwarf galaxies. The spatial resolution and sensitivity of *ALMA* would give these molecules a chance to be detected in dwarf galaxies.

#### • Dust-to-Gas mass ratio

Differences between the total molecular gas mass derived from the D/G mass ratio and the molecular gas mass determined classically from CO observations with the  $X_{CO}$  conversion factor would pinpoint the fraction of dark gas present.

If the proportion of heavy elements in the gas and dust were to scale with metallicity, as determined by chemical evolution models based, for example, on observations of the Galaxy (Dwek 1998), deriving the gas mass from the dust mass would be straightforward. However, observations of both the dust and gas in low metallicity galaxies seem to find a steeper trend

between D/G and metallicity rather than a linear correlation (Lisenfeld & Ferrara 1998; James et al. 2002; Bot et al. 2004; Walter et al. 2007; Madden et al. 2012a). From a chemical point of view, this might be interpreted by metals being less effectively incorporated into dust and remaining in the gas phase, or elements being removed from dust grains through processing by the radiation field or shocks, for example. Discrepancies between observed dust abundances and expected abundances from supernova-condensed dust for low metallicity are noted in Galliano et al. (2008).

Great uncertainties still remain in characterising the dust properties in dwarf galaxies, particularly at long wavelengths where the question of the origin of the submm excess and consequences on the dust properties has a major influence on dust mass. For instance, by modeling the excess with very cold dust, the dust mass can increase by a factor of a few (Galametz et al. 2009, 2011).

The D/G mass ratio is, in principle, a strong means to access the molecular reservoir of galaxies, especially at low metallicity where it is difficult to observe CO and the  $X_{\text{CO}}$  conversion factor is poorly constrained. Nevertheless, metallicity effects also act on the dust properties, and the weak reliability of both dust mass determination and adopted D/G ratio make the use of the D/G mass ratio in getting to the dark gas doubtful.

### 1.3.3 Open questions

Advances in studying dwarf galaxies, in particular with the development of more sensitive instruments and state-of-the-art numerical simulations, have lead to detailed analysis of their ISM and to a better understanding of their global properties, and yet many unanswered questions remain.

Here is a list of important problems concerning dwarf galaxies today that should nurture studies in the future:

- What is the link between dwarf galaxy and early universe beyond chemical enrichment?
- What is the role of the different ISM phases in the star formation process at low metallicities?
- What is the role of metallicity (direct or indirect through e.g.  $A_V$ ) on the physical processes and ISM evolution?
- What is the structure of the different phases in low metallicity galaxies, and how does it compare to the more metal-rich counterparts?
- What are the best observational means to constrain the ISM structure and quantify the total molecular gas in low metallicity galaxies?

Some of the striking questions around dwarf galaxies can be tackled at long wavelength, in the FIR/submm range, by probing the PDR and molecular clouds which are directly linked to star formation. In particular, the effect of metallicity on the cloud structure highlights the importance of the PDRs relative to the molecular cores.

The advent of the *Herschel* telescope has provided a unique opportunity to study the dust and gas in chemically unevolved systems. My thesis work has focused on the gas properties of dwarf galaxies, in the FIR essentially, but also in the MIR and submm. The analyses of these cooling lines, which probe simultaneously the main phases of the ISM, the H II regions, PDRs, and molecular clouds, enable us to assess the dominating physical conditions in a range of physically different sources. In this context, the multi-wavelength approach brings

new insight on the ISM properties of dwarf galaxies, with an encompassing picture of the ISM structure, and of the relative importance of the different ISM phases in the overall assembly of galaxy's components.



## Chapter 2

# The *Herschel* telescope

### Contents

---

<b>2.1</b>	<b>The <i>Herschel</i> Mission . . . . .</b>	<b>42</b>
2.1.1	General description . . . . .	42
2.1.2	Comparison to pre- <i>Herschel</i> facilities . . . . .	42
2.1.3	Low metallicity galaxies observed with <i>Herschel</i> . . . . .	42
2.1.4	The Dwarf Galaxy Survey . . . . .	44
<b>2.2</b>	<b>The PACS Spectrometer . . . . .</b>	<b>49</b>
2.2.1	Technical specifications . . . . .	49
2.2.2	Data processing . . . . .	51
2.2.3	Global flux extraction . . . . .	54

---

## 2.1 The *Herschel* Mission

### 2.1.1 General description

The *Herschel* Space Observatory is the fourth ‘cornerstone’ mission in the ESA science programme (Pilbratt et al. 2010). The observatory was launched in space on the 14th of May 2009, and is orbiting at the Lagrangian point L2. It is designed to observe the cold universe in the FIR-submm domain, from 55 to 670  $\mu\text{m}$ . The instruments are cooled by a helium tank to reach unprecedented sensitivities, but limiting the lifetime of the mission to 3 years. Unlike ground-based facilities, space observations are not affected by atmospheric perturbations and water absorption, which affect these wavelengths. *Herschel* is equipped with a 3.5-m primary mirror and carries 3 instruments onboard: PACS, SPIRE, and HIFI, for both imaging and spectral acquisition. The main science objectives of the mission are to understand galaxy formation and evolution, unveil the physics and chemistry of the ISM, and study the early stages of star and planet formation, by probing different epochs of the universe, from Solar System objects to galaxies at redshifts up to  $\sim 3$ .

### 2.1.2 Comparison to pre-*Herschel* facilities

Several space missions dedicated to IR-mm studies have preceded *Herschel*, including the first IR space mission *IRAS*, *ISO*, and *Spitzer*, as well as the airborne facility *KAO*. A comparison of the global specifications of these telescopes with *Herschel*, and with the new generation of instruments onboard *SOFIA* is given in Table 2.1. *Herschel* offers complementary observations of wavelength ranges not accessible before, as well as better spatial and spectral resolutions. In particular, it opens studies of dust emission of galaxies in the redshift window up to  $z \sim 3$ , which was limited to  $z \sim 2$  with *Spitzer*.

**Table 2.1.** Telescope capabilities comparison.

Telescope	Launch	Lifetime (year)	Wavelength ( $\mu\text{m}$ )	Spatial res. <sup>(a)</sup> ( $''$ )	Spectral res. $\Delta R/R$	Sensitivity <sup>(a,b)</sup> (mJy)
<i>KAO</i>	1974	21	1-500	30	$\sim 10^4$	200
<i>IRAS</i>	1983	1	12-100	150	-	200
<i>ISO</i>	1995	3	2-240	60	$10^2 - 10^4$	10
<i>Spitzer</i>	2003	9+	3-35	40	$10^2 - 10^3$	1
<i>Herschel</i>	2009	3+	55-670	10	$10^2 - 10^7$	1
<i>SOFIA</i>	2011	1+	0.3-1 600	10	$10^3 - 10^8$	10

Information taken from the *SOFIA* website: <http://www.sofia.usra.edu/Science/telescope/>.

(a) The spatial resolution and sensitivity numbers are given at 100  $\mu\text{m}$ .

(b) The sensitivity is the broadband sensitivity given as 1- $\sigma$ , 1h execution time.

### 2.1.3 Low metallicity galaxies observed with *Herschel*

The better sensitivity of *Herschel* has opened a window on the ISM of low surface brightness objects, and low metallicity dwarf galaxies in particular. Several programs have targeted

low metallicity dwarf galaxies with *Herschel*. We outline the most relevant programs related to the ISM study and this work here (priority 2 programs are not listed):

- The “*Dwarf Galaxy Survey*” or “*The ISM in Low Metallicity Environments: Bridging the Gap Between Local Universe and Primordial Galaxies*” (P.I. S. C. Madden), a 125.2 h GTKP project presented in Sect. 2.1.4;
- Madden et al. (2012b); Galametz et al. (2010); O’Halloran et al. (2010); Cormier et al. (2012a); Rémy et al. (2012); Cormier et al. (2012b);
- “*Star formation and activity in infrared bright galaxies at  $0 < z < 1$  (SHINING)*” (P.I. E. Sturm, co-I. S. C. Madden), a 333.5 h GTKP project of the PACS consortium, which observed primarily ULIRGs and active galactic nuclei (AGNs) up to redshift 1. It includes 85.5 h for dwarf galaxies which are also presented in Sect. 2.1.4 as part of the DGS;
- Papers on the dwarf galaxies: Cormier et al. (2010); Lebouteiller et al. (2012);
- “*Star Formation and ISM properties in the lowest metal-poor galaxies observed by Herschel*” (P.I. S. C. Madden), a 10.2 h OT2 project which observed 2 dwarf galaxies (IZw 18 and SBS 0335-052) in PACS spectroscopy to complement the DGS dataset;
- “*Unveiling the Warm Molecular Gas in Blue Compact Dwarf Galaxies*” (P.I. V. Lebouteiller), a 8.3 h GT2 project which observed 2 galaxies (He 2-10 and IC 10) in SPIRE spectroscopy to investigate the CO excitations, temperatures of the molecular clouds, and gas reservoir. It complements the DGS dataset as well.

This is a total of 230 h for the DGS.

### Star-forming dwarf galaxies

- “*Key Insights on Nearby Galaxies: A Far-Infrared Survey with Herschel (KINGFISH)*” (PI: R. Kennicutt), a 540.7 h KPOT project which observed a sample of 61 nearby galaxies in photometry and PACS spectroscopy to spatially characterize the ISM structure and physical processes at play. It includes a couple of irregular low metallicity galaxies such as DDO 53 or DDO 154;
- Kennicutt et al. (2011); Croxall et al. (2012);
- “*Dust-Based Molecular Gas Maps of Nearby Low-Metallicity Galaxies*” (P.I. A. Leroy), a 20.1 h OT1 project which observed 3 galaxies (Holmberg II, IC 2574, and NGC 4236) in PACS photometry to model dust SEDs and access gas mass with the D/G ratio, calibrate  $X_{\text{CO}}$  and assess star formation efficiencies at low metallicity;
- “*Characterizing Molecular Clouds at Low Metallicity*” (P.I. D. Hunter), a 53.8 h OT1 project which observed 5 galaxies (DDO 155, DDO 69, DDO 70, DDO 75, and WLM) in PACS spectroscopy to study the properties of the atomic/molecular gas and investigate the star formation process at low metallicity;
- “*Dust and Star Formation at Low Metallicities*” (P.I. D. Hunter), a 12.3 h OT2 project which observed 4 galaxies (DDO 69, DDO 70, DDO 75, and DDO 210) in PACS and SPIRE photometry to analyse the dust properties and relate them to the gas content traced by H I and the star formation at very low metallicity;
- “*Extreme star formation in low-metallicity dusty blue compact dwarf starbursts*” (P.I. L. Hunt), a 16.3 h OT2 project which observed 23 BCDs in PACS and SPIRE photometry to model SEDs, derive dust mass, compare with their gaseous content and global parameters (SFR, metallicity). This dataset is very complementary to the DGS sample;
- “*Exploring the Dust Content of Galactic Winds with Herschel: The Dwarf Galaxy Population*” (P.I. S. Veilleux), a 38.1 h OT2 project which observed 4 dwarf galax-

ies with known outflows (NGC 1569, NGC 1800, NGC 3077, and NGC 5253) in PACS (and SPIRE) photometry to model the dust emission and wind properties.

### Magellanic Clouds

- “*HERschel Inventory of The Agents of Galaxy Evolution (HERITAGE) in the Magellanic Clouds*” (P.I. M. Meixner), a 271.4 h KPOT project which mapped the SMC and LMC with PACS and SPIRE photometers to study the cycle of matter on the ISM and particularly of YSOs and the dust properties and mass;
- Meixner et al. (2010); Hony et al. (2010); Roman-Duval et al. (2010); Gordon et al. (2010); Boyer et al. (2010); Otsuka et al. (2010); Kim et al. (2010); Sewilo et al. (2010); Galliano et al. (2011);
- “*Characterizing the life cycle of interstellar matter in the Magellanic Clouds with CII and CI*” (P.I. J. Pineda), a 61.8 h OT1 project which observed 54 regions of the SMC and LMC with HIFI for velocity-resolved [C II] and C I to compare with CO, establish a complete carbon inventory and access the dark gas reservoir;
- “*The Mass and Structure of Molecular Gas in the Small Magellanic Cloud and the Herschel Legacy at Low Metallicity*” (P.I. A. Bolatto), a 46.4 h OT2 project which observed 5 regions of the SMC in PACS and SPIRE spectroscopy to provide a quantification and calibration of the dark molecular gas;
- “*The Submillimeter Continuum in the Magellanic Clouds*” (P.I. C. Engelbracht), a 16.5 h OT2 project which observed several regions of the SMC and LMC in SPIRE spectroscopy to access the FIR/submm continuum level and focus on the nature of the submm excess.

### Quiescent dwarf galaxies

- “*Herschel Virgo Cluster Survey (HeViCS)*” (P.I. J. Davies), a 301.8 h KPOT project that mapped 4 fields of the Virgo Cluster with PACS and SPIRE photometry to analyse the cold dust in the intra-cluster medium and build multi-wavelength SEDs, as well as 14 galaxies in PACS spectroscopy;
- Papers related to dwarf galaxies: de Looze et al. (2010); Grossi et al. (2010);
- “*Herschel study of the ISM in Local Group dwarf ellipticals*” (P.I. I. de Looze), a 4.5 h OT2 project which observed 3 dwarf ellipticals (NGC 205, NGC 185, and NGC 147) in PACS and SPIRE photometry to analyse the dust emission, particularly of the diffuse regions, and tackle the missing ISM problem of these gas-poor environments;

#### 2.1.4 The Dwarf Galaxy Survey

The “Dwarf Galaxy Survey” (DGS) is a *Herschel* Guaranteed Time Key Program led by Suzanne Madden. It is one of the three programs of the SPIRE Local Galaxies consortium (SAG2); the two other programs being the “Herschel Reference Survey” (HRS), led by Steve Eales, and the “Very Nearby Galaxy Survey” (VNGS), led by Christine Wilson. The DGS is a 230 h project which aims to study the dust and gas properties with the PACS and SPIRE instruments in a sample of 48 dwarf galaxies.

The PACS (70, 100, and 160  $\mu\text{m}$ ) and SPIRE (250, 350, and 500  $\mu\text{m}$ ) photometry observations are necessary to probe the peak and Rayleigh-Jean’s tail of the dust SED and to constrain SED models. In turn, we can investigate the dust properties – and in particular



the submm excess – radiation field, dust mass, D/G ratios, etc.

The PACS (55-210 $\mu$ m) and SPIRE (195-670 $\mu$ m) spectrometers give access to the FIR fine-structure cooling lines and the CO ladder, from J=4-3 to J=13-12. By probing different ISM phases, they provide information on the filling factors and physical conditions of these phases, as well as on the ISM morphology.

Both the dust and gas observations reveal a coherent multiphase picture of the ISM.

The details on the program and the galaxy sample are presented in the [Madden et al. \(2012b\)](#) overview paper. The list of galaxies and their general properties can be found in Table 2.2. The metallicity of these dwarfs range from 1/50  $Z_{\odot}$  (IZw 18) to near solar metallicity (He 2-10). They have different shapes, most being irregular (VII Zw 403), others spiral (NGC 4214). And their star-formation activity also varies, from quiescent with  $\text{SFR} \sim 5 \times 10^{-4} M_{\odot} \text{ yr}^{-1}$  (UGC 4483), to extremely active with  $\text{SFR} \sim 25 M_{\odot} \text{ yr}^{-1}$  (Haro 11). All of them are nearby galaxies, no further than 200 Mpc, enabling us to relate the observed variations to the physics occurring within their ISM.

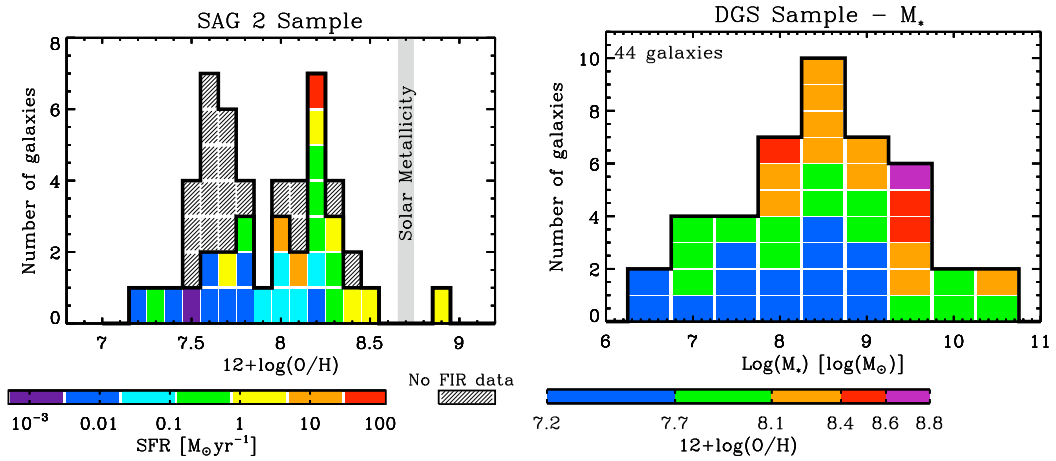


**Figure 2.1.** Histogram of metallicities color-coded by SFR (*left*) and stellar mass color-coded by metallicity (*right*) for the DGS sample.

Figure 2.1 (*left* panel) is a histogram sorting the galaxies by metallicity, and color-coded by SFR. The metallicity distribution shows two peaks, at  $12 + \log(O/H) = 7.6$  and  $8.2$ , with median value of  $8.0$ . The metallicity spans 2 orders of magnitude and the SFR 4 orders of magnitude. Extended galaxies have a combination of active and more diffuse regions. The most metal-poor galaxies are on the low end of the SFR range as they are usually the lower surface brightness objects. But, on average, for a given metallicity, several galaxies with differing SFRs are sampled, which enables us to study the role of both parameters on the ISM physical conditions and evolution. The *right* panel of Fig. 2.1 shows that the range of stellar mass  $M_*$  also spans 4 orders of magnitude, with  $M_*$  as low as  $10^6 M_{\odot}$  (Pox 186).  $M_*$  is well sampled, with the peak of the distribution at  $3 \times 10^8 M_{\odot}$ . The lowest metallicity galaxies have lower stellar mass globally, but the intermediate-metallicity galaxies are well spread throughout the stellar mass range.

In PACS spectroscopy, a total of 35 compact galaxies and 13 extended galaxies, including 8 regions in the LMC, were observed as part of the DGS. The total time dedicated to the PACS spectroscopy alone is 152.7 h. My work focuses on the data reduction and analysis of the PACS spectroscopy, which is described in Sect. 2.2. We obtained pointed observations for the compact objects, and mappings of entire galaxies (NGC 1569) or specific star-forming regions of extended objects such as 30-Doradus and N11 in the LMC.



**Table 2.2.** General properties of the DGS sample from Madden et al. (2012b).

Source Name	Coordinates (J2000)	Distance (Mpc)	Metallicity $12 + \log(O/H)$	$M_B$ (mag)	$D_{25}$ ( $''$ )	$M_*$ ( $10^8 M_\odot$ )	$M_{HI}$ ( $10^8 M_\odot$ )	$\log L_{TIR}$ ( $L_\odot$ )	SFR ( $M_\odot \text{ yr}^{-1}$ )
Haro 11	0h36m52.30s -33d33m20s	92.1	8.2	-20.55	$0.5' \times 0.4'$	339.0	$\leq 1.0$	11.22	28.6
Haro 2	10h32m32.0s +54d24m02s	21.7	8.45	-18.28	$1.2' \times 0.8'$	20.8	4.9	9.72	0.9058
Haro 3	10h45m22.4s +55d57m37s	19.3	8.46	-18.29	$1.2' \times 0.8'$	18.8	11.3	9.67	0.8097
He 2-10	08h36m15.1s -26d42m34s	8.7	8.93	-17.25	$1.9' \times 1.4'$	18.2	3.1	9.66	0.7902
HS 0017+1055	00h20m21.4s 11d 12m 21s	79.1	7.63	-16.23	-	1.9	$\leq 1.74$	-	-
HS 0052+2536	00h54m56.4s +25d53m08s	191.0	8.07	-19.56	-	43.6	$\leq 482$	-	-
HS 0822+3542	08h25m55.5s +35d32m32s	11	7.4	-12.4 <sup>(1)</sup>	$0.27' \times 0.12'$	0.003	0.77	$\leq 7.04$	$\leq 0.0019$
HS 1222+3741	12h24m 36.7s +37d24m37s	181.7	7.64	-17.9	$0.12' \times 0.11'$	14.6	-	-	-
HS 1236+3937	12h39m20.2s +39d21m05s	86.3	7.47	-16.0	$0.34' \times 0.09'$	12.8	-	-	-
HS 1304+3529	13h06m24.2s +35d13m43s	78.7	7.66	-17.73	$0.28' \times 0.21'$	4.2	-	-	-
HS 1319+3224	13h21m19.7s +32d08m25s	86.3	7.59	-15.68	$0.14' \times 0.11'$	0.9	-	-	-
HS 1330+3651	13h33m08.3s +36d36m33s	79.7	7.66	-17.81	$0.29' \times 0.19'$	6.3	-	-	-
HS 1442+4250	14h44m12.8s +42d37m44s	14.4	7.63	-15.15	$1.13' \times 0.26'$	-	3.0	$\leq 7.59$	$\leq 0.0068$
HS 2352+2733	23h54m56.7s +27d49m59s	116.7	8.4	-17.05	-	1.8	$\leq 230.0$	-	-
I Zw 18	09h34m02.0s +55d14m28s	18.2	7.2	-15.22	$0.3' \times 0.3'$	0.2	0.86	$\leq 7.74$	$\leq 0.0095$
II Zw 40	05h55m42.6s +03d23m32s	12.1	8.1	-14.93	$0.56' \times 0.22'$	4.7	5.7	9.4	0.4334
IC 10	00h20m17.3s +59d18m14s	0.7	8.3	-12.43	$6.8' \times 5.9'$	-	1.17	7.7	0.009
LMC	05h23m34.5s -69d45m22s	0.05	8.5	-17.58	$645' \times 550'$	20	5.0	9.15	0.24
Mrk 1089	05h01m37.7s -04d15m28s	56.6	8.0	-20.46	$0.61' \times 0.23'$	119.0	150.0	7.1	0.002
Mrk 1450	11h38m35.7s +57d52m27s	19.8	8.0	-13.86 <sup>(1)</sup>	$0.40' \times 0.31'$	0.86	0.43	8.44	0.0471
Mrk 153	10h49m05.0s +52d20m08s	40.3	7.8	-18.03	$0.54' \times 0.30'$	6.9	6.41	8.97	0.1598
Mrk 209	12h26m15.9s +48d29m37s	5.8	7.8	-13.67	$0.8' \times 0.6'$	0.18	0.74	7.49	0.0054
Mrk 930	23h31m58.3s +28h56m50s	77.8	8.1	-	$0.43' \times 0.43'$	44.3	30.4	10.26	3.119
NGC 1140	02h54m33.6s -10d01m40s	20.0	8.29	-18.55	$1.7' \times 0.9'$	23.4	35.0	9.52	0.574
NGC 1569	04h30m49.0s +64d50m53s	3.1	8.2	-15.75	$3.6' \times 1.8'$	5.4	1.8	9.04	0.1895
NGC 1705	04h54m13.5s -53d21m40s	5.1	8.21	-15.73	$1.9' \times 1.4'$	1.2	1.0	7.82	0.0114
NGC 2366	07h28m54.6s +69d12m57s	3.2	7.9	-16.18	$8.1' \times 3.3'$	1.2	7.4	8.13	0.0233
NGC 4214	12h15m39.2s +36d19m37s	2.9	8.3	-17.11	$8.5' \times 6.6'$	5.0	4.08	8.73	0.0929
NGC 4449	12h28m11.1s +44d05m37s	4.2	8.3	-17.94	$6.2' \times 4.4'$	15.0	11.0	9.33	0.3646
NGC 4861	12h59m02.3s +34d51m34s	7.5	8.0	-16.84	$4.0' \times 1.5'$	1.8	4.79	8.49	0.0535
NGC 5253	13h39m55.9s -31d38m24s	4.0	8.2	-16.87	$5.0' \times 1.9'$	6.7	1.59	9.14	0.2401
NGC 625	01h35m04.6s -41d26m10s	3.9	8.1	-16.20	$5.8' \times 1.9'$	2.9	1.25	8.41	0.0444
NGC 6822	19h44m57.7s -14d48m12s	0.5	8.2	-13.19	$415.5' \times 13.5'$	0.79	0.55	7.6	0.0068
Pox 186	13h25m48.6s -11d36m38s	18.3	7.75	-12.17 <sup>(1)</sup>	-	0.01	$\leq 0.02$	-	-
SBS 0335-052	03h37m44.0s -05d02m40s	56.0	7.3	-16.02	$0.23' \times 0.20'$	4.3	4.6	$\leq 9.23$	$\leq 0.2943$
SBS 1159+545	12h02m02.4s +54d15m50s	57.0	7.5	-15.08	$0.20' \times 0.10'$	0.5	$\leq 0.63$	-	-
SBS 1211+540	12h14m02.4s +53d45m17s	19.3	7.65	-13.43	$0.26' \times 0.17'$	0.1	0.56	-	-
SBS 1249+493	12h51m52.5s +49d03m28s	110.8	7.74	-	$0.10' \times 0.10'$	4.4	10.0	-	-
SBS 1415+437	14h17m01.4s +43d30m05s	13.6	7.6	-14.99 <sup>(1)</sup>	$0.75' \times 0.15'$	-	4.37	$\leq 7.78$	$\leq 0.0104$
SBS 1533+574	15h34m13.8s +57d17m06s	54.2	8.07	-16.69 <sup>(1)</sup>	$0.67' \times 0.67'$	11.0	30.0	-	-
SMC	00h52m44.8s -72d49m43s	0.06	8.0	-16.19	$320' \times 185'$	18	4.2	8.02	0.018
Tol 0618-402	06h20m02.5s -40d18m09s	150.8	7.7	-	$0.4' \times 0.3'$	109.0	-	$\leq 9.91$	$\leq 1.4046$
Tol 1214-277	12h17m17.1s -28d02m33s	120.5	7.5	-17.00	$0.08' \times 0.05'$	1.9	3.22	-	-

*Continued on next page*

**Table 2.2.** General properties of the DGS sample from [Madden et al. \(2012b\)](#).

Source Name	Coordinates (J2000)	Distance (Mpc)	Metallicity $12 + \log(O/H)$	$M_B$ (mag)	$D_{25}$ ( $'$ ) <sup>2</sup>	$M_*$ ( $10^8 M_\odot$ )	$M_{HI}$ ( $10^8 M_\odot$ )	$\log L_{TIR}$ ( $L_\odot$ )	SFR ( $M_\odot \text{ yr}^{-1}$ )
UGC 4483	08h37m03.0s +69d46m31s	3.2	7.5	-12.53	$1.4' \times 0.7'$	0.03	0.32	6.61	0.0007
UGCA 20	01h43m14.7s +19d58m32s	11	7.58	-14.43	$3.1' \times 0.8'$	0.18	2.78	-	-
UM 133	01h44m41.3s +04d53m26s	22.7	7.63	-15.72 <sup>(1)</sup>	$1.0' \times 1.0'$	0.80	4.0	-	-
UM 311	01h15m34.40s -00d51m46s	23.5	8.3	-19.22	$0.11' \times 0.10'$	-	24.7	9.73	0.9361
UM 448	11h42m12.4s +00d20m03s	87.8	8.0	-20.02	$0.4' \times 0.4'$	241.0	60.0	10.86	12.361
UM 461	11h51m33.3s -02d22m22s	13.2	7.8	-13.73	$0.30' \times 0.22'$	0.26	1.2	7.8	0.0108
VII Zw 403	11h27m59.9s +78d59m39s	4.5	7.7	-13.77	$1.4' \times 0.8'$	0.10	0.69	7.23	0.0029

References for all the dwarfs (except the Magellanic Clouds) are given in [Madden et al. \(2012b\)](#).

$L_{TIR}$  is derived from *Spitzer* fluxes using the [Dale & Helou \(2002\)](#) formula, and SFR from  $L_{TIR}$  using the [Kennicutt \(1998\)](#) formula.

For the LMC and SMC, *Spitzer* fluxes used to derive  $L_{TIR}$  and SFR are from [Lawton et al. \(2010\)](#).

Stellar and  $H I$  mass are from [Kim et al. \(1998\)](#) for the LMC, and from [Stanimirović et al. \(2004\)](#) for the SMC.

(1): corrected for Galactic extinction

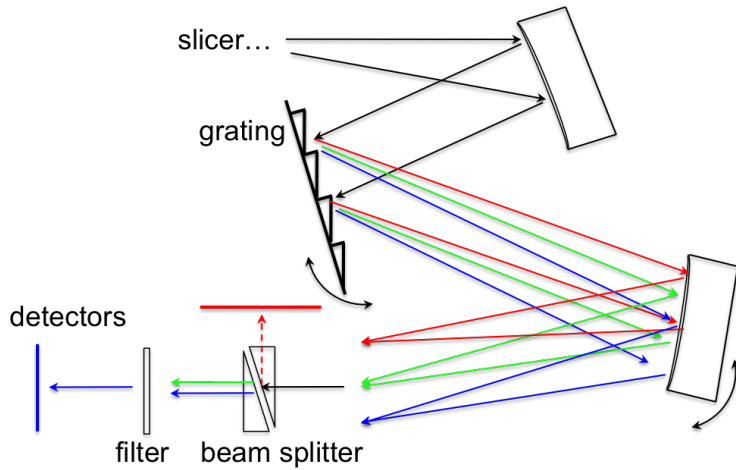


**Figure 2.2.** Artist view of the path of light into the PACS spectrometer optical train, from the beam splitter onto the detectors. This is a schematic not to scale, where true optics has been rearranged for a better view (e.g. the spectrometer is Littrow-mounted so rays enter and exit the spectrometer at the same place).

## 2.2 The PACS Spectrometer

### 2.2.1 Technical specifications

#### Instrument design

The Photodetector Array Camera & Spectrometer (PACS) has been designed under the leadership of Albrecht Poglitsch (Poglitsch et al. 2010). It consists of two sub-instruments, a photometer observing in 3 bands ( $60\text{--}85\mu\text{m}$ ,  $85\text{--}125\mu\text{m}$ , and  $125\text{--}210\mu\text{m}$ ), and an integral-field spectrometer working in the wavelength range  $55\text{--}210\mu\text{m}$ , separated in 2 bands (blue and red).

The spectrometer is composed of a  $5\times 5$  spatial pixel (spaxel) array, offering a 2D field of view (FOV) of  $47''\times 47''$ . Light passes through the entrance optics, with calibration sources and the chopper, common to both the photometer and the spectrometer, and then enters into the spectrometer train. The 2D field is transformed into a 1D array of  $1\times 25$  pixels by an image slicer, before entering the grating. Light is then diffracted along 3 orders: order 1 ( $102\text{--}210\mu\text{m}$ ), which will fall on the detectors of the red band, and order 2 ( $71\text{--}105\mu\text{m}$ ) and order 3 ( $55\text{--}73\mu\text{m}$ ), one of which is selected by a beam splitter before impacting the detectors of the blue band. Simultaneous observing in the red and blue bands are therefore possible. The grating can move from  $25^\circ$  to  $70^\circ$  with defined steps to cover the desired full wavelength range of each order. Figure 2.2 illustrates the path of the light onto the detectors. The detectors are two Ge:Ga photoconductors arrays with  $16\times 25$  pixels on which the 16 spectral elements of the 25 spaxels are imaged.

#### Capabilities

Sensitivities are on the order of  $8\text{--}10\times 10^{-18}\text{ W m}^{-2}$  in the blue band, and  $4\times 10^{-18}\text{ W m}^{-2}$  in the red band. Theoretical point-source line sensitivities as a function of wavelength are shown in Figure 2.3.

The spectral resolution also depends on the observed order and wavelength. It is in the range  $c\delta\lambda/\lambda \sim 55\text{--}320\text{ km s}^{-1}$ , and typically  $240\text{ km s}^{-1}$  at  $157\mu\text{m}$  (order 1),  $125\text{ km s}^{-1}$  at  $88\mu\text{m}$  (order 2), and  $90\text{ km s}^{-1}$  at  $63\mu\text{m}$  (order 3). The instantaneous coverage of the 16 spectral pixels varies from  $600$  to  $2900\text{ km s}^{-1}$ , corresponding to  $0.15\text{--}1.0\mu\text{m}$ .

Pointing accuracies are less than  $2''$ .

On the border of the grating orders, there is some overlap from grating order  $n+1$  into

grating order  $n$  that causes spectral leakage. In particular, the edge of the first order, at  $\sim 200\mu\text{m}$  is contaminated by signal from the edge of the second order at  $\sim 100\mu\text{m}$ . The [N II]  $205\mu\text{m}$  line is therefore difficult to observe and to calibrate due to this leakage.

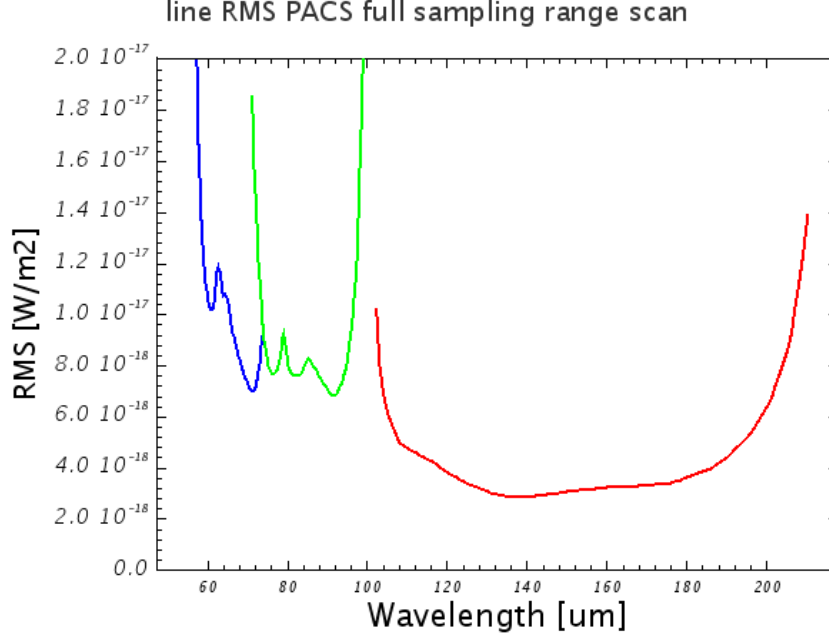


**Figure 2.3.** PACS line sensitivities; taken from the PACS Observer’s Manual ([http://herschel.esac.esa.int/Docs/PACS/html/pacs\\_om.html](http://herschel.esac.esa.int/Docs/PACS/html/pacs_om.html)).

### Observing modes

Several observing modes are available, depending on the targeted object. We distinguish two types of observation requests (AORs): the line spectroscopy, scanning a fixed and relatively short wavelength range ( $\sim 1\mu\text{m}$ ) around a selected line, and the range spectroscopy, in which the user defines the wavelength range to scan. We used line spectroscopy AORs for our sample. Range spectroscopy may be necessary in specific cases when e.g. the line width is greater than the fixed range, as can be the case in outflowing winds of supernovae remnants, or when the precise line center is not well known, as can be the case for distant galaxies with uncertainties on the redshift. A complementary SED mode scans the entire wavelength range within a grating order with low spectral sampling, providing information on the continuum level, as well as on the spectral lines within the range for bright objects.

The two observing techniques are the chop-nod and unchopped grating scan modes. Their concept is illustrated in Figure 2.4. 46 dwarf galaxies from the DGS were done in chop-nod mode, and 6 were done in unchopped mode.

- **Chop-nod:** This mode is designed to observe faint lines in compact objects. The sequence of this mode is to point first on the source (nod A), while the optics chops to an off-position, and then point off the source (nod B) and chop on nod A. Chopper throws can be  $1.5'$ ,  $3'$ , or  $6'$ . The goal of chopping and nodding is to remove the telescope background, which varies with the chopper angle, and recover the flux of the source. *The sampling density per resolution element is higher than 3 samples per FWHM of an*

unresolved line at all wavelengths with 43, 46 and 48 grating steps in the first, second and third order respectively.

- **Unchopped grating scan:** This mode is designed to observe extended objects or crowded fields where no area free of emission lies within 6'. Instead of chopping off the source, the array and optics stay all the time on the source. An additional off-source pointed observation must be obtained to remove the telescope background. *There are 75 grating steps in faint line, 50 in bright line. The up/down grating scans are faster and repeated twice.*

Line sensitivities are comparable in the two modes, although the continuum is better recovered in chop-nod mode. All observations start with a calibration block, followed by nod A and nod B blocks in chop-nod mode, or ON-source and OFF-source blocks in unchopped mode. Individual patterns can be repeated several times to reach the desired sensitivity and/or for mapping purposes. Both pointed observations and mappings larger than the FOV can be done.

More details on the instrument specificities and observing techniques can be found in the PACS Observer's Manual and in Poglitsch et al. (2010), or at <http://herschel.esac.esa.int/twiki/bin/view/Public/PacsCalibrationWeb>.

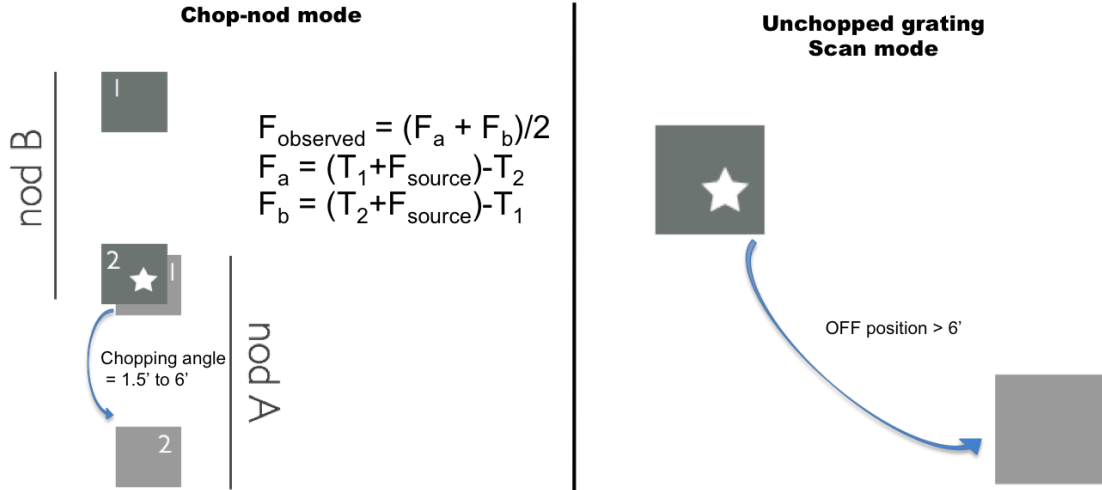


**Figure 2.4.** Illustration of the movement of the telescope for both observing spectroscopic modes: chop-nod (*left*) and unchopped grating scan (*right*).

### 2.2.2 Data processing

The dwarf galaxies were observed between November 2009 and August 2011. I was responsible for inspecting the data and processing the spectral cubes.

#### Data reduction

The data are downloaded from the Herschel Science Archive (HSA) and reduced with the Herschel Interactive Processing Environment (HIPE, Ott 2010). We reprocessed the observations from the raw data (level 0) to spectral data cube (level 2) using standard pipeline scripts available within HIPE (Fig. 2.5).

Data cubes are initially of size  $16 \times 25 \times n_{\text{timeline}}$ , containing the signal of the 16 spectral pixels, 25 spaxels as a function of time. In the first part of the pipeline (level 0 to level 0.5), the astrometry and information from the instrument are read. Masks for bad and noisy pixels, and for a moving the chopper and grating are also applied. From level 0.5 to level 1, glitches are flagged, and the calibration is applied. In the chop-nod case, signal from the chopper position is subtracted. At the end, the data is reorganised as spectra, i.e. signal as a function of wavelength in cubes of size  $n_{\lambda} \times 5 \times 5$  (PACS array). From level 1 to level 2, a spectral flat-field correction is applied, and outlier data points are masked by a sigma-clipping. In the unchopped case, a background subtraction and transient correction are also applied, which are explained below. The spectral cubes are then saved as FITS files with extensions for the signal, coordinates, masks, etc. Individual cubes are created for each raster position (mapping observation) and for each nod (A and B, in the chop-nod case). In the pipeline, there are additional steps to create a wavelength grid and rebin the data on it, and combine the nods. However we choose to save the unbinned data cubes to keep all the spectral information.

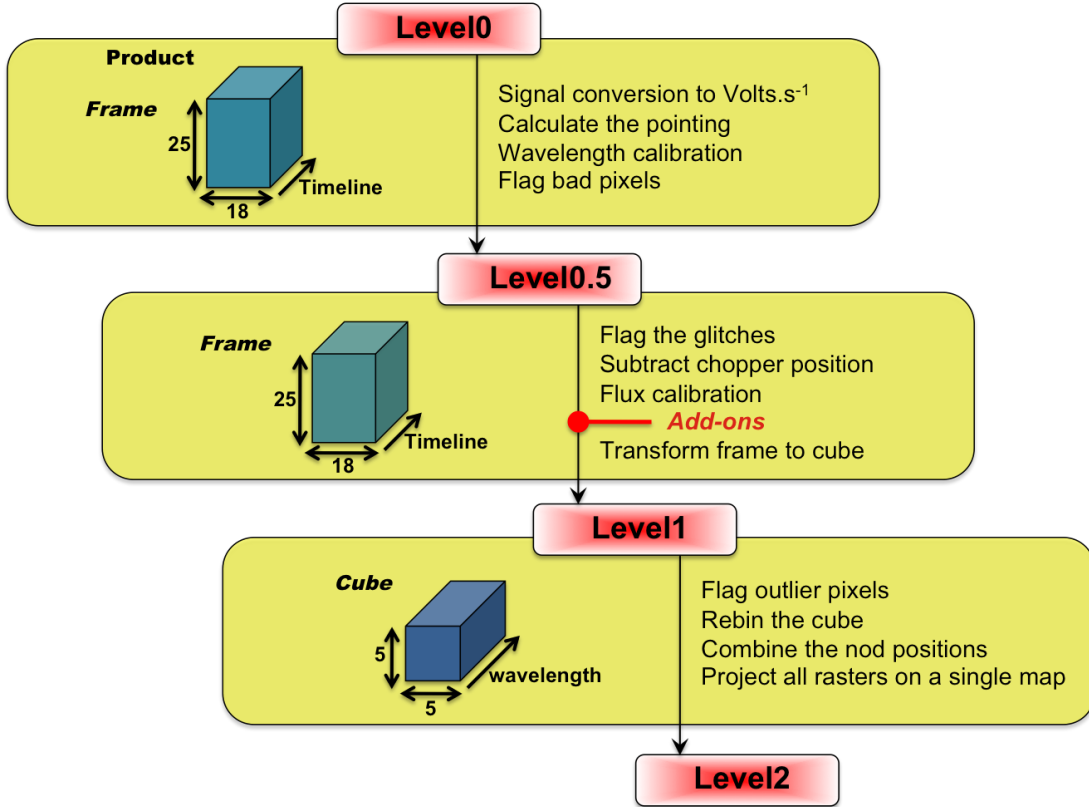


**Figure 2.5.** Steps of the data reduction in HIPE, from the raw data (level 0) to science quality spectral cubes (level 2). Additions to the standard pipeline script are applied at level 1 (indicated in red).

### Add-ons to the unchopped script

For the unchopped scan observations, we used additional scripts developed by the ICC when the observing mode was released to improve the quality of the data at the level 1, including:

- 1) a linear drift correction of the signal with time,



2) a median shift correction, assuming that the signal in each scan explores the same wavelength range and should stay the same, and

3) a linear spectral flat-field.

These modules were later included in the pipeline scripts.

We also implemented two modules of our own:

1) a transient correction procedure, which either fits an exponential or uses a multi-resolution technique to identify the transient as the largest scale. It is described in [Lebouteiller et al. \(2012\)](#). Transients are cosmic ray hits that provoke a variation in the response of the detector, which takes time to go back to its “normal” level. In chop-nod mode, they are removed by the effect of the chopper, but they appear frequently in unchopped observations, always after the calibration block is taken, and randomly during the observation. Some transients may be of large amplitude and therefore must be corrected to recover the line.

A transient removal procedure was also included afterwards in the pipeline script, modeling the transients with a series of functions. This procedure is very long and less reliable so we do not use it.

2) an off-subtraction procedure which smoothes the off-signal to have an accurate shape of the continuum and interpolates it to the wavelength grid of the on-signal before subtracting it. Depending on the number of off-spectra taken, we have tried several combinations before subtracting it, by taking the off-spectrum closest in time to the on-spectrum, averaging the off-spectra before and after the on-spectrum, or taking the average of all off-spectra. We have found that the 3 tested options give similar results in terms of rms, as long as the observations are relatively short. By default, we have removed the average of the off-spectra before and after the on-spectrum in our observations. *A procedure that averages all the off-spectra and subtracts it from the rebinned data exists in the pipeline but is not suited to our purposes.*

### Spectral flux maps analysis

Once the spectral cubes are exported from HIPE, we use the software PACSMAN version 3.4 for the analysis. It was written in IDL by Vianney Lebouteiller and described in [Lebouteiller et al. \(2012\)](#). I have marginally contributed to its development during my thesis for the purpose of exploiting the *Herschel* data of dwarf galaxies.

The first step is to do a line fitting to measure the line flux in all the spatial positions (PACSMAN\_ *fit.pro*). A polynomial curve of order 2 is first fitted to the continuum, and a fit to the continuum and line is then performed. An example of line profile and fit is shown in Fig. 2.6 (*left*). The instrument profile is assumed to be Gaussian, although skewed profiles can be seen if the observed object is a point-source not centered on the array. Corrections must be applied in that case, but we never encountered this in our observations. Errors are not propagated in HIPE and are calculated as the dispersion in a given wavelength bin. Additional keywords may be selected in case of line/range spectroscopy, if the spectral line is shifted or broadened and initial parameters fail to do a proper fit.

Once flux values are calculated for each spatial position, the data is projected on a new grid of subpixel resolution of 3'' (PACSMAN\_ *map.pro*). This step is necessary for mapping observations to combine the raster positions together in a final map and to recover the best spatial resolution possible (see PACS ICC calibration document PICC-KL-TN-038). Fig. 2.6 (*right*) is an illustration of the raster projection. When more than one spaxel fall on the same subpixel, a fraction of the flux from each raster spaxel is considered. In the end, I obtained flux maps for each galaxy and each spectral line (that we show in Appendix B).

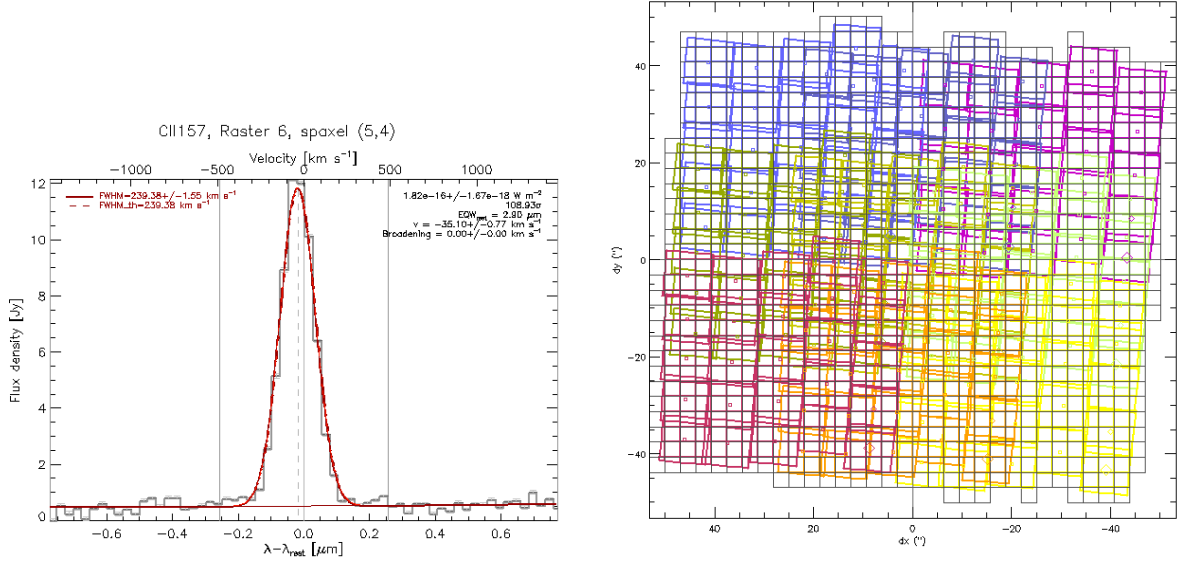


**Figure 2.6.** *Left:* Example of a [C II] line profile (dark) and fit (red) in a spaxel of the II Zw 40 observation, which consist of a  $3 \times 3$  raster map. *Right:* Raster projection of the [C II] observation of II Zw 40 onto a subgrid of  $3''$  pixels. Each raster of  $5 \times 5$  spaxels has a different color, the small squares are the spaxel centers of a raster.

I iterated this reduction and analysis process for all galaxies I have reduced, including the 48 dwarf galaxies from the DGS and SHINING programs, the 14 star-forming low metallicity dwarf galaxies in the Virgo Cluster from the HeVICS program (P.I. J. Davies), and the 24 ULIRGs from the HERUS program (reduction only). HERUS is a 250 h OT1 project by D. Farrah which samples the starburst and AGN properties in  $z < 0.2$  ULIRGs.

The DGS and SHINING targets were executed in line spectroscopy chop-nod mode for 42 galaxies, and unchopped mode for 6 galaxies (see Appendix 6.2.5). We observed from 1 spectral line, the [C II]  $157\mu\text{m}$ , in the faintest cases, up to 7 lines, [C II] 157, [O III] 88, [O I] 63, [O I] 145, [N III] 57, [N II] 122, and [N II]  $205\mu\text{m}$ , in the brightest galaxies. The HeVICS targets were all executed in line spectroscopy chop-nod, in the [O I] 63, [O III] 88, and [C II]  $157\mu\text{m}$  lines. The HERUS targets were executed in range spectroscopy, using chop-nod, in the [O III] 52, [N III] 57, [O I] 63, [N II] 122, [O I] 145, [C II]  $157\mu\text{m}$  (and simultaneously in the blue band OH  $79\mu\text{m}$ ) lines.

### 2.2.3 Global flux extraction

For each galaxy, a global line flux is then extracted. If the source is point-like and well centered<sup>1</sup> on the PACS array, most of the signal will be detected in the central spaxel, but part of the source flux will fall on the adjacent spaxels and may be diluted in the noise level for faint objects. In order to recover the total flux, a correction factor must be applied, depending on the observed wavelength (Figure 2.8).

In the case of extended or elongated objects I performed an aperture extraction with sky subtraction (PACSMAN\_analysis.pro) to measure the total flux of star-forming regions or

1. To assess this condition, I looked at the projection of the PACS footprint on an optical image (typically r-band). In case of doubt on the size of the galaxy, I applied both methods and checked that the results were comparable.

entire galaxies. A 2D gaussian surface can also be fitted to the spectral map to determine the source spatial extent. Figure 2.7 is an illustration of the flux extraction and distribution in II Zw 40.

There are two caveats to this method, which can introduce large uncertainties on the measured flux. First, for point-like objects that do not fall in the center of the PACS array, the flux may be distributed in 2 to 4 spaxels, as for a slightly extended object, except that a correction factor still needs to be applied. In this case, we can combine the inner  $3 \times 3$  spaxels before fitting the line profile, and apply the corresponding correction factor to the flux obtained in the  $3 \times 3$  spaxels. Second, for faint extended objects, it may be difficult to determine the size of the galaxy over which to do the aperture extraction since the signal will drop at the edges. A small aperture may yield a lower limit on the flux, and a large aperture, which would mainly add noise, may yield an upper limit. We take the mean value as the total flux and half the difference as the uncertainty on the flux.

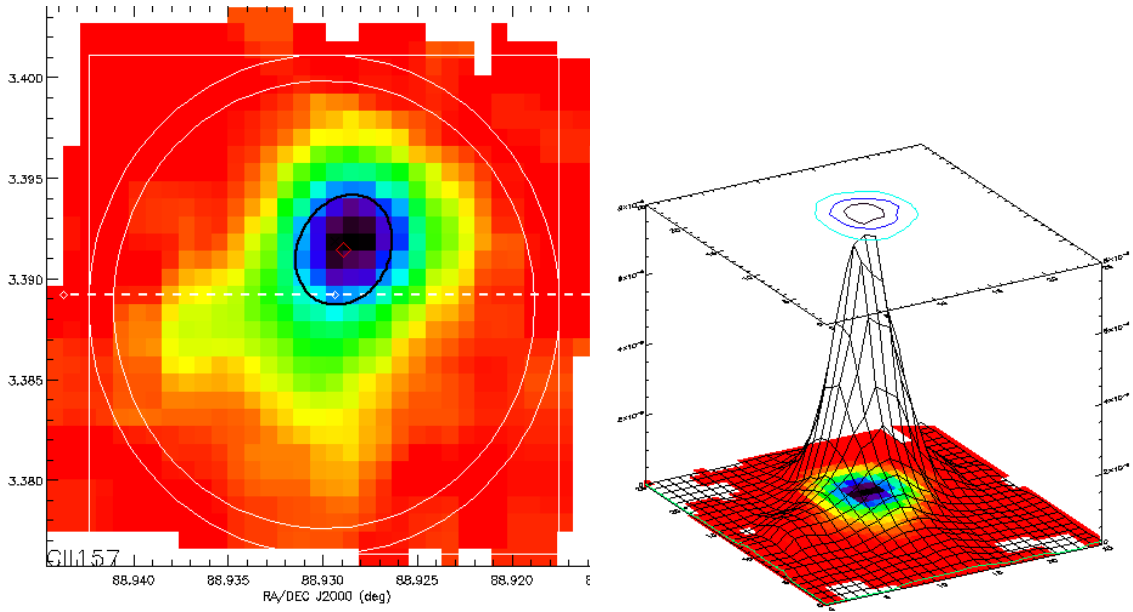


**Figure 2.7.** *Left:* [C II] flux map of II Zw 40 with an aperture of  $40''$  radius and annulus (white circles) to measure the total flux of the source. The black diamond and ellipse indicate the center and FWHM of the 2D Gaussian fit. *Right:* 3D flux distribution which has a shape close to that of a Gaussian.

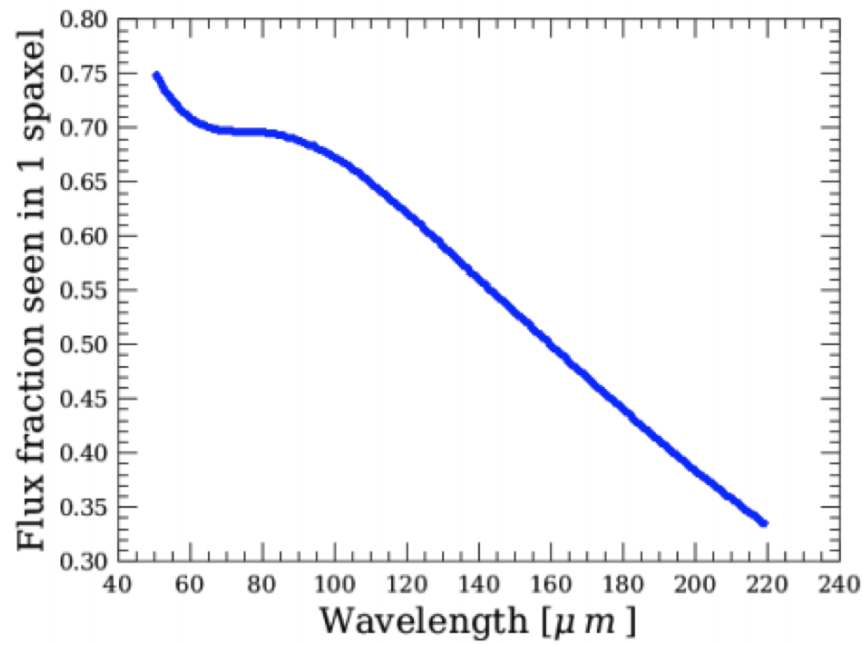


**Figure 2.8.** Point-source correction to apply to the flux of the central spaxel to recover the total flux of the object; taken from the PACS Observer’s Manual.

# Chapter 3

## *Herschel* results of the Dwarf Galaxies

### Contents

---

<b>3.1</b>	<b><i>Herschel</i> data of the DGS sample</b>	<b>58</b>
3.1.1	Statistics on the observations	58
3.1.2	Line fluxes of the DGS galaxies	59
<b>3.2</b>	<b>Correlation diagrams and ISM properties</b>	<b>62</b>
3.2.1	Method	62
3.2.2	Lack of trend with metallicity: Figure 3.2	63
3.2.3	PACS line ratios	65
3.2.4	Relation of FIR fine-structure lines with $L_{TIR}$ , star formation indicator	70
3.2.5	Conclusions	77
<b>3.3</b>	<b>A look into the ISM of the nearby Magellanic-type dwarf galaxy NGC 4214</b>	<b>78</b>
3.3.1	Properties of the Local Group galaxy, NGC 4214	78
3.3.2	<i>Herschel</i> /PACS spectral maps	78
3.3.3	Conditions in the 3 star-forming regions	78
3.3.4	Need for higher spatial/spectral resolution	81
3.3.5	Paper published in A&A, 2010, 518, 57	82

---

### 3.1 *Herschel* data of the DGS sample

#### 3.1.1 Statistics on the observations

The *Herschel* observations of the DGS sample are presented in Appendix B. Details on the observations, such as OBSID, map sizes, lines observed, etc., can be found in Table A.1 of Appendix 6.2.5. The data reduction within HIPE was done with build versions 4 to 8. For each galaxy and each spectral line observed, we show the spectral flux maps as well as line profiles over the peak of emission or the non-detections. Table 3.1 summarizes the measured fluxes in the DGS galaxies. For point-like galaxies, a point-like correction is used to derive total fluxes, and for objects that were fully mapped (i.e. where the signal-to-noise drops at the edge of the map), we extract the flux within an aperture of size indicated in Table 3.1. There are 10 galaxies for which the total fluxes are not rigorously measured: UM 311, NGC 1569, NGC 4214, NGC 4861, NGC 625, NGC 1705, NGC 2366, Mrk 1089, Mrk 153, and Mrk 209. They are noted with an asterisk (\*) in Table 3.1. For UM 311, this is because the field around this galaxy is crowded. It lies in a complex of 3 H II compact knots located in between 2 spiral galaxies. UM 311 itself actually falls at the edge of our PACS maps and its emission cannot be isolated, hence we give the flux within an aperture of 20'' comprising the 3 knots. For the other galaxies, we still detect signal at the edge of the maps, almost exclusively for the [C II] line, which we learn can be quite extended. Hence, we may be missing some of the emission, although the bulk is captured in our maps. We estimate the flux loss to be less than approximately 20% for these galaxies.

Finally, there are 5 local galaxies that were intentionally not completely mapped as their extent is larger than 6', and overheads in mapping with PACS are prohibitive. Only selected regions were observed in the nearby Local Group galaxies: IC 10, NGC 4449, NGC 6822, and the Magellanic Clouds. The S/N of the PACS lines in these regions is generally >10 even at the edge of the maps. Hence we do not measure the total galaxy emission from the PACS lines. As the size of the maps in these regions do not match for all observed lines, instead of a total flux, we indicate in Table 3.1 the surface brightness over the peak of emission, in one or several parts of the maps.

The [C II] line was targeted in all objects, along with the [O III] and [O I] 63 $\mu$ m lines for almost all objects ( $\sim 85\%$ ). For the brightest galaxies (30%), the [O I] 145 $\mu$ m and [N II] 122 $\mu$ m lines were also observed, and in a very few cases (7%) the [N II] 205 $\mu$ m and [N III] 57 $\mu$ m lines as well. Figure 3.1 shows a histogram of how many galaxies were observed in each spectral line and how many were detected. The [C II], [O III] and [O I] 63 $\mu$ m are the brightest lines, detected in more than 90% of the cases, and on average are at least 10 times brighter than the other lines. The [N II] 205 $\mu$ m was only attempted a few times and never detected as it located at the edge of the spectral band, suffering from leakage (see Section 2.2).

As an example, Haro 3 was observed in all spectral lines except the [N II] 205 $\mu$ m, and we find that the [O III] line is the brightest, followed by [C II], fainter than [O III] by factor of 1.5, [O I] 63 $\mu$ m fainter by a factor of 3, [N III] fainter by a factor of 15, and [O I] 145 $\mu$ m and [N II] 122 $\mu$ m fainter by a factor  $\sim 50$ .

We note that spectral profiles of the [O III], [O I] 63 $\mu$ m, and sometimes the [C II] lines are found broadened, by up to  $\sim 150$  km s $^{-1}$ , compared to the instrumental profile (of width  $\sim 125$ , 90, and 240 km s $^{-1}$  respectively) in the brightest sources. Although we do not carry a detailed analysis on the kinematics since the spectral resolution is poor, such broadening indicates the possible presence of outflows in some cases, or that multiple components contribute to

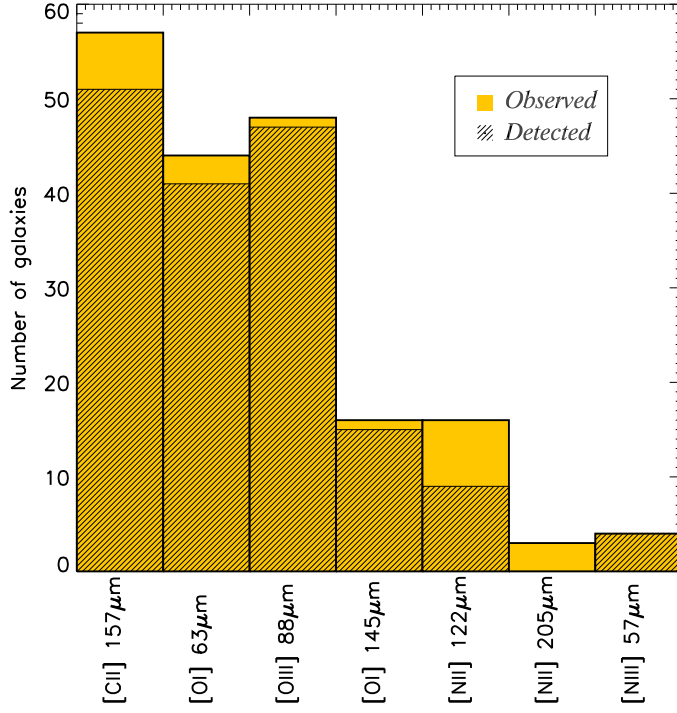


**Figure 3.1.** Histogram of the number of observed PACS lines and detections in the DGS program.

the emission of those lines. We also note that in the few sources where the [N II] 122μm line is well detected (e.g. LMC-30Dor or NGC 4214, see Appendix B p.174), a dip is seen on the blue wing of the line profile, which might not be just an instrumental effect, but rather a real absorption feature due to the presence of molecules, such as H<sub>2</sub>O (Fischer et al. 2010).

### 3.1.2 Line fluxes of the DGS galaxies



**Table 3.1.** Line fluxes of the DGS galaxies.

Source Name	Extraction <sup>(a)</sup>	[C II] 157 $\mu$ m	[O I] 63 $\mu$ m	[O III] 88 $\mu$ m	Observed Spectral Line	[N II] 122 $\mu$ m	[N II] 205 $\mu$ m	[N III] 57 $\mu$ m
<i>Compact or extended fully mapped sources</i>								
Haro 11	20	7.44 $\pm$ 0.07 ( $\times 10^2$ )	6.65 $\pm$ 0.17 ( $\times 10^2$ )	1.80 $\pm$ 0.02 ( $\times 10^3$ )	56.3 $\pm$ 4.0	30.8 $\pm$ 4.7	$\leq 7.7$	2.50 $\pm$ 0.21 ( $\times 10^2$ )
Haro 2	20/25	8.89 $\pm$ 0.02 ( $\times 10^2$ )	5.07 $\pm$ 0.09 ( $\times 10^2$ )	1.16 $\pm$ 0.01 ( $\times 10^3$ )	-	-	-	-
Haro 3	25/35	1.24 $\pm$ 0.01 ( $\times 10^3$ )	5.75 $\pm$ 0.05 ( $\times 10^2$ )	1.90 $\pm$ 0.01 ( $\times 10^3$ )	47.3 $\pm$ 1.8	35.5 $\pm$ 5.5	-	1.39 $\pm$ 0.17 ( $\times 10^2$ )
He 2-10	25/30	5.46 $\pm$ 0.04 ( $\times 10^3$ )	3.21 $\pm$ 0.07 ( $\times 10^3$ )	4.14 $\pm$ 0.06 ( $\times 10^3$ )	-	-	-	1.00 $\pm$ 0.10 ( $\times 10^3$ )
HS 0017+1055	pt	3.16 $\pm$ 0.68	-	10.1 $\pm$ 1.9	-	-	-	-
HS 0052+2536	pt	$\geq 24.9$ #	$\geq 10.7$ #	$\geq 32.2$ #	-	-	-	-
HS 0822+3542	pt	$\leq 2.58$	-	-	-	-	-	-
HS 1222+3741	pt	2.54 $\pm$ 0.72	-	11.1 $\pm$ 1.1	-	-	-	-
HS 1236+3937	pt	$\leq 4.20$	-	-	-	-	-	-
HS 1304+3529	pt	16.4 $\pm$ 1.4	-	23.4 $\pm$ 3.3	-	-	-	-
HS 1319+3224	pt	3.16 $\pm$ 1.08	-	3.08 $\pm$ 2.02	-	-	-	-
HS 1330+3651	pt	16.9 $\pm$ 1.3	5.54 $\pm$ 2.59	21.1 $\pm$ 0.1	-	-	-	-
HS 1442+4250	pt	$\geq 6.01$ #	-	-	-	-	-	-
HS 2352+2733	pt	2.60 $\pm$ 0.86	-	9.74 $\pm$ 1.43	-	-	-	-
II Zw 40	25/40	8.97 $\pm$ 0.03 ( $\times 10^2$ )	5.58 $\pm$ 0.05 ( $\times 10^2$ )	3.83 $\pm$ 0.01 ( $\times 10^3$ )	4.33 $\pm$ 0.32 ( $\times 10^2$ )	3.42 $\pm$ 2.19 ( $\times 10^2$ )	-	-
I Zw 18	15	6.95 $\pm$ 0.53	-	-	-	-	-	-
Mrk 1089 *	20	7.55 $\pm$ 0.01 ( $\times 10^2$ )	2.28 $\pm$ 0.02 ( $\times 10^2$ )	6.31 $\pm$ 0.57 ( $\times 10^2$ )	16.4 $\pm$ 3.2	12.1 $\pm$ 1.2	-	-
Mrk 1450	20	51.9 $\pm$ 1.3	33.2 $\pm$ 6.4	2.66 $\pm$ 0.07 ( $\times 10^2$ )	-	$\leq 1.73$	-	-
Mrk 153 *	20	56.9 $\pm$ 2.6	26.0 $\pm$ 4.1	84.7 $\pm$ 5.7	-	-	-	-
Mrk 209 *	20	84.1 $\pm$ 2.8	45.5 $\pm$ 11.1	4.48 $\pm$ 0.10 ( $\times 10^2$ )	-	-	-	-
Mrk 930	20	2.15 $\pm$ 0.02 ( $\times 10^2$ )	1.41 $\pm$ 0.07 ( $\times 10^2$ )	4.44 $\pm$ 0.03 ( $\times 10^2$ )	8.06 $\pm$ 0.37	$\leq 3.75$	-	-
NGC 1140	20/45	1.23 $\pm$ 0.02 ( $\times 10^3$ )	3.68 $\pm$ 0.20 ( $\times 10^2$ )	1.04 $\pm$ 0.01 ( $\times 10^3$ )	25.3 $\pm$ 1.7	16.7 $\pm$ 1.7	-	-
NGC 1569 *	50	1.05 $\pm$ 0.01 ( $\times 10^4$ )	5.39 $\pm$ 0.08 ( $\times 10^3$ )	2.13 $\pm$ 0.01 ( $\times 10^4$ )	-	-	-	-
NGC 1705 *	35	4.88 $\pm$ 0.04 ( $\times 10^2$ )	1.21 $\pm$ 0.25 ( $\times 10^2$ )	5.75 $\pm$ 0.20 ( $\times 10^2$ )	-	-	-	-
NGC 2366 *	30	3.15 $\pm$ 0.02 ( $\times 10^2$ )	2.67 $\pm$ 0.13 ( $\times 10^2$ )	2.4 $\pm$ 0.06 ( $\times 10^3$ )	-	-	-	-
NGC 4214 *	55	7.00 $\pm$ 0.12 ( $\times 10^3$ )	2.16 $\pm$ 0.04 ( $\times 10^3$ )	6.03 $\pm$ 0.05 ( $\times 10^3$ )	1.12 $\pm$ 0.05 ( $\times 10^2$ )	50.5 $\pm$ 8.3	$\leq 22.1$	-
NGC 4861 *	20	1.82 $\pm$ 0.20 ( $\times 10^2$ )	1.96 $\pm$ 0.06 ( $\times 10^2$ )	1.16 $\pm$ 0.01 ( $\times 10^3$ )	10.7 $\pm$ 1.1	-	-	-
NGC 5253	30/50	5.37 $\pm$ 0.48 ( $\times 10^3$ )	3.24 $\pm$ 0.01 ( $\times 10^3$ )	1.03 $\pm$ 0.01 ( $\times 10^4$ )	1.94 $\pm$ 0.05 ( $\times 10^2$ )	86.2 $\pm$ 9.1	-	-
NGC 625 *	30/50	1.79 $\pm$ 0.27 ( $\times 10^3$ )	5.57 $\pm$ 0.61 ( $\times 10^2$ )	2.34 $\pm$ 0.001 ( $\times 10^3$ )	-	-	-	-
Pox 186	pt	3.36 $\pm$ 0.60	-	30.5 $\pm$ 1.8	-	-	-	-
SBS 0335-052	pt	6.16 $\pm$ 1.48	-	22.2 $\pm$ 1.0	-	-	-	-
SBS 1159+545	pt	5.06 $\pm$ 0.79	5.29 $\pm$ 1.23	4.51 $\pm$ 1.39	-	-	-	-
SBS 1211+540	pt	3.78 $\pm$ 1.00	-	-	-	-	-	-
SBS 1249+493	pt	2.66 $\pm$ 0.60	-	-	-	-	-	-
SBS 1415+437	20	43.9 $\pm$ 1.8	48.7 $\pm$ 3.1	63.2 $\pm$ 3.1	-	-	-	-
SBS 1533+574	20	53.9 $\pm$ 1.5	35.2 $\pm$ 1.1	87.6 $\pm$ 7.3	-	-	-	-
Tol 1214-277	pt	$\leq 4.62$	3.81 $\pm$ 1.11	17.4 $\pm$ 1.4	-	-	-	-
UGC 4483	pt	10.9 $\pm$ 0.9	$\geq 1.67$ #	20.9 $\pm$ 1.5	-	-	-	-
UM 133	15	16.9 $\pm$ 1.8	15.4 $\pm$ 2.2	15.0 $\pm$ 2.4	-	-	-	-
UM 311 *	20	4.38 $\pm$ 1.14 ( $\times 10^2$ )	2.53 $\pm$ 0.51 ( $\times 10^2$ )	6.33 $\pm$ 0.44 ( $\times 10^2$ )	-	$\leq 10.5$	-	-
UM 448	20/25	8.53 $\pm$ 0.27 ( $\times 10^2$ )	6.03 $\pm$ 0.06 ( $\times 10^2$ )	1.20 $\pm$ 0.01 ( $\times 10^3$ )	3.78 $\pm$ 0.09 ( $\times 10^2$ )	1.79 $\pm$ 0.27 ( $\times 10^2$ )	-	-
UM 461	15	20.8 $\pm$ 0.8	23.4 $\pm$ 3.8	70.7 $\pm$ 1.2	-	$\leq 0.83$	-	-

*Continued on next page*

**Table 3.1.** Line fluxes of the DGS galaxies.

Source Name	Extraction <sup>(a)</sup>	Observed Spectral Line						
		[C II] 157 $\mu$ m	[O I] 63 $\mu$ m	[O III] 88 $\mu$ m	[O I] 145 $\mu$ m	[N II] 122 $\mu$ m	[N II] 205 $\mu$ m	[N III] 57 $\mu$ m
VII Zw 403	25	$1.14 \pm 0.02$ ( $\times 10^2$ )	$41.8 \pm 5.2$	$61.3 \pm 2.8$	$\leq 2.51$	$\leq 2.92$	-	-
<i>Extended, partially mapped sources</i>								
IC 10-1 <sup>(b)</sup>	n.a.	$3.44 \times 10^{-7}$	$1.78 \times 10^{-7}$	$7.99 \times 10^{-7}$	$1.51 \times 10^{-8}$	$6.13 \times 10^{-9}$	-	-
IC 10-2	n.a.	$2.38 \times 10^{-7}$	$1.36 \times 10^{-7}$	$8.00 \times 10^{-7}$	$1.09 \times 10^{-8}$	$3.45 \times 10^{-9}$	-	-
IC 10-3	n.a.	$4.58 \times 10^{-8}$	$1.01 \times 10^{-8}$	$3.29 \times 10^{-8}$	-	-	-	-
LMC-30Dor-1	n.a.	$2.32 \times 10^{-6}$	$3.35 \times 10^{-6}$	$2.02 \times 10^{-5}$	$3.27 \times 10^{-7}$	$5.10 \times 10^{-8}$	-	-
LMC-30Dor-2	n.a.	$1.13 \times 10^{-6}$	$1.44 \times 10^{-6}$	$1.40 \times 10^{-5}$	$1.52 \times 10^{-7}$	$2.15 \times 10^{-8}$	-	-
LMC-N11A	n.a.	$7.75 \times 10^{-7}$	$3.07 \times 10^{-7}$	-	-	-	-	-
LMC-N11B	n.a.	$9.17 \times 10^{-7}$	$1.88 \times 10^{-6}$	$2.41 \times 10^{-6}$	$1.06 \times 10^{-7}$	$1.43 \times 10^{-8}$	$\leq 6.30 \times 10^{-9}$	$1.97 \times 10^{-7}$
LMC-N11C-1	n.a.	$4.52 \times 10^{-7}$	$3.81 \times 10^{-7}$	$1.82 \times 10^{-6}$	-	-	-	-
LMC-N11C-2	n.a.	$4.97 \times 10^{-7}$	$2.83 \times 10^{-7}$	$1.72 \times 10^{-6}$	-	-	-	-
LMC-N11I	n.a.	$2.23 \times 10^{-7}$	$2.59 \times 10^{-7}$	$1.16 \times 10^{-7}$	-	-	-	-
LMC-N158	n.a.	$1.01 \times 10^{-6}$	$9.43 \times 10^{-7}$	$2.72 \times 10^{-6}$	-	-	-	-
LMC-N159-1	n.a.	$1.22 \times 10^{-6}$	$1.29 \times 10^{-6}$	$5.01 \times 10^{-6}$	$2.03 \times 10^{-7}$	$2.38 \times 10^{-8}$	$\leq 5.52 \times 10^{-9}$	-
LMC-N159-2	n.a.	$7.85 \times 10^{-7}$	$5.18 \times 10^{-7}$	$3.87 \times 10^{-6}$	$7.26 \times 10^{-8}$	$2.33 \times 10^{-8}$	$\leq 5.03 \times 10^{-9}$	-
LMC-N159-3	n.a.	$1.13 \times 10^{-6}$	$1.38 \times 10^{-6}$	$4.99 \times 10^{-6}$	$1.82 \times 10^{-7}$	-	-	-
LMC-N159S	n.a.	$9.63 \times 10^{-8}$	$3.17 \times 10^{-8}$	-	-	-	-	-
LMC-N160-1	n.a.	$1.30 \times 10^{-6}$	$3.17 \times 10^{-6}$	$9.52 \times 10^{-6}$	$3.65 \times 10^{-7}$	-	-	-
LMC-N160-2	n.a.	$1.34 \times 10^{-6}$	$1.78 \times 10^{-6}$	$1.40 \times 10^{-6}$	$2.82 \times 10^{-7}$	-	-	-
SMC-N66	n.a.	$1.80 \times 10^{-7}$	$4.73 \times 10^{-7}$	$6.59 \times 10^{-7}$	-	-	-	-
NGC 4449-1	n.a.	$2.14 \times 10^{-7}$	$1.21 \times 10^{-7}$	$1.64 \times 10^{-7}$	$5.49 \times 10^{-9}$	$\leq 2.90 \times 10^{-9}$	-	-
NGC 4449-2	n.a.	$1.58 \times 10^{-7}$	$6.88 \times 10^{-8}$	$2.59 \times 10^{-7}$	$4.06 \times 10^{-9}$	$\leq 2.96 \times 10^{-9}$	-	-
NGC 6822-HV	n.a.	$1.50 \times 10^{-7}$	$1.14 \times 10^{-7}$	$5.37 \times 10^{-7}$	$8.29 \times 10^{-9}$	$1.12 \times 10^{-9}$	-	-
NGC 6822-HIV	n.a.	$3.84 \times 10^{-8}$	$1.51 \times 10^{-8}$	$1.47 \times 10^{-8}$	-	-	-	-
NGC 6822-HX	n.a.	$4.63 \times 10^{-8}$	$2.70 \times 10^{-8}$	$1.80 \times 10^{-7}$	-	-	-	-

**Table 3.1.** Fluxes are in  $10^{-18}$  W m $^{-2}$  for compact and fully mapped extended galaxies, and surface brightness in W m $^{-2}$  sr $^{-1}$  for partially mapped extended galaxies.

Beam sizes are 9.5 at 57, 63, and 88 $\mu$ m, 10'' at 122 $\mu$ m, 11'' at 145 $\mu$ m, 11.5'' at 157 $\mu$ m, and 14.5'' at 205 $\mu$ m.

(a) Extraction method. Indicated as *pt* for point-like sources, or with the radius (in '') used for the aperture extraction. Where two radii are reported, the second corresponds to the aperture used for the [CII] line, which is often more spatially extended than the other lines. It is not applicable (*n.a.*) for the most extended regions where the surface brightness is given (in W m $^{-2}$  sr $^{-1}$ ).

(b) For the most extended galaxies, we indicate the surface brightness over one or several positions of each region mapped. Thus, the source name is appended by the position number (-n). The peak position is shown by a dark cross, and the extra positions by an orange cross on the spectral maps of these sources (in Appendix B).

The symbol # indicate that the flux is a lower limit as the source of emission is at the edge of the PACS array (not centered). We are probably missing less than 50% of the total flux.

The symbol \* indicate galaxies with extended emission that is not fully covered by our PACS observations. We are probably missing less than 20% of the total flux.

## 3.2 Correlation diagrams and ISM properties

The *Herschel* dataset provides unique information on ISM properties. In this section, we present and analyse the correlations between several FIR tracers to identify empirical trends in the sample, and to try to link observational trends to global parameters (Figures 3.2 to 3.14). FIR line ratios are important diagnostics of the gas conditions, as detailed in Section 1.2.4.

### 3.2.1 Method

#### What are the interesting correlations?

We choose to analyse the PACS observations of the dwarf galaxies with two main parameters: the ratio of 60/100 $\mu$ m, and  $L_{\text{TIR}}$ .

The ratio of *IRAS* broad band data of 60/100 $\mu$ m (or 70/100 $\mu$ m) is a direct probe of the physical conditions. It is an indicator of the dust temperature (and grain charging) as the SED of compact H II regions peaks at shorter wavelength, hence having higher 60/100 $\mu$ m ratios. On the other hand, SEDs of PDRs or diffuse gas peak at longer wavelengths. The ratio of 60/100 $\mu$ m thus points out the relative contribution of H II regions and PDRs.

Moreover,  $L_{\text{TIR}}$  is an indirect probe of the star formation activity. The relation of [C II] and other gas tracers with  $L_{\text{TIR}}$  has been studied in a variety of objects (e.g. Stacey et al. 1991, 2010; Malhotra et al. 1997; Luhman et al. 2003; Pierini et al. 2003; Boselli et al. 2002a; de Looze et al. 2011). In starburst galaxies, line-to-TIR ratios are indicators of the effect of the UV field on the gas, independently of galaxy spectral type. The FIR lines of [O III], [N III], and [N II] are tracers of the ionised gas, while the [O I] and [C II] lines are usually tracers of the neutral gas. [O I] normally dominates the cooling in dense PDRs, and [C II] in more diffuse neutral or ionised gas (Section 1.2.4). More specifically, the ratio of the [C II]157 and [O I] lines to  $L_{\text{TIR}}$  is a measure of the photoelectric efficiency, provided the main heating source for the [C II] line is photoelectric effect (i.e. that it is associated with neutral gas). The photoelectric efficiency can be defined as  $\epsilon_{PE} = \frac{\Gamma_{gas}}{\Gamma_{dust}}$ , where  $\Gamma_{gas}$  and  $\Gamma_{dust}$  are respectively the gas and dust heating rates. Thus  $\epsilon_{PE}$  measures the fraction of energy in the dust heating that is transferred to the gas heating. The photoelectric effect (see Section 1.2.2) acts on dust grains and PAHs, with  $\epsilon_{PE}$  typically  $\leq 1\%$ , with higher  $\epsilon_{PE}$  for small grains and PAHs, and lower  $\epsilon_{PE}$  for charged grains (Bakes & Tielens 1994).  $L_{\text{TIR}}$  include all contribution from the dust emission. While dust grains are heated by photons, their cooling is done by thermal radiation in the FIR, dominating the TIR luminosity. The cooling by PAHs is also taken into account in  $L_{\text{TIR}}$  as they emit photons in the MIR via vibrational and bending transitions. Hence  $L_{\text{TIR}}$  is commonly used as the proxy for the gas heating (e.g. Rubin et al. 2009).

#### Preparing the datasets

We compute  $L_{\text{TIR}}$  for all the galaxies of the DGS sample. For the unresolved or fully mapped galaxies of the DGS, we use SED integrated values from Rémy et al. (2012), which are total  $L_{\text{TIR}}$ . For the most extended objects of the DGS, we have only partial PACS spectroscopy coverage of the galaxy or star-forming region, and the area mapped in the PACS lines is, in most cases, different from one spectral line to the other. Therefore, we create TIR maps based on the Galliano models (e.g. Galliano et al. 2008), and, to compute line-to-TIR ratios, for each PACS line, we integrate  $L_{\text{TIR}}$  over the area mapped for the line. For those extended objects (IC 10, NGC 4449, NGC 6822, and the Magellanic Clouds), figures

in Section 3.2.4 hence do not show total values, but values in part of the galaxy or in the most active regions. A pixel-by-pixel comparison with the PACS tracers will be investigated in future work. These maps are convolved to the largest beam of  $12''$  corresponding to the PACS  $160\mu\text{m}$  beam. For UM 311, we also create a TIR map and use an aperture of the same size as for the line flux extraction.

Besides comparing line ratios and  $L_{\text{TIR}}$  within the dwarf galaxy sample, we also compare them to more metal-rich galaxies to study the effects of metallicity on these line diagnostics. Brauher et al. (2008) present an *ISO* extragalactic survey of FIR fine-structure lines that we compare to our DGS sample. The Brauher et al. sample contains a larger variety of galaxies, extending to more metal-rich galaxies, starbursts, and AGNs. The DGS sample extends the analysis of Brauher et al. (2008) to lower TIR luminosities, as the Brauher et al. sample is composed mostly of bright objects. As  $L_{\text{TIR}}$  is not yet compiled from integrated SEDs for the Brauher et al. dataset, as we do with the DGS sample (above), we use a rough estimate of  $L_{\text{TIR}}$  for these galaxies. First, we derive  $L_{\text{FIR}}$  with the Helou et al. (1988) formula using *IRAS* 60 and  $100\mu\text{m}$ , and then we multiply by a factor of 3.5 to get  $L_{\text{TIR}}$ . This factor 3.5 is the median scaling between the FIR luminosity from the Helou et al. (1988) formula and the integrated SED TIR luminosities derived for the dwarfs (Rémy et al. 2012). Although this may not be strictly accurate, this approximation is sufficient to empirically compare the two datasets.  $L_{\text{TIR}}$  is usually estimated as  $2 \times L_{\text{FIR}}$  (Hunter et al. 2001). However, using a factor of 3.5 instead of 2 will not change dramatically the position of the Brauher et al. sample in the following plots, and hence should not alter our conclusions.

In the figures presented in the next sections, the DGS galaxies are represented by filled circles color-coded by metallicity (dark is metal-poor and light is more metal-rich). We overplot the galaxies from Brauher et al. (2008) in red dots, and those of the Brauher et al. sample with subsolar metallicities in blue dots. Only their data for unresolved sources, and with clear detections ( $>3\sigma$ ) are shown.

Median values and ranges of the PACS lines ratios and line-to-TIR ratios are summarized in Table 3.2. We indicate values for the complete sample (unresolved+extended objects), for the compact objects only (all but the LMC, SMC regions, NGC 4449, NGC 6822, and IC 10), and for the Brauher et al. dataset.

### 3.2.2 Lack of trend with metallicity: Figure 3.2

Figure 3.2 shows ratios of PACS lines-to-TIR luminosity versus metallicity. The  $[\text{C II}]$  intensity (*top right* panel) increases with metallicity, which can be interpreted as a brightness effect (or effect of  $L - Z$ ; Section 1.1.3): more metal-rich objects are brighter. When normalizing the line intensity by the TIR intensity, this effect is removed.

On the low metallicity end, ratios of  $[\text{C II}]/L_{\text{TIR}}$  and  $[\text{O III}]/L_{\text{TIR}}$  are spread over an order of magnitude.  $[\text{C II}]/L_{\text{TIR}}$  range from 0.04% to 0.7%,  $[\text{O III}]/L_{\text{TIR}}$  range from 0.1% to 3.2%, while  $[\text{O I}]/L_{\text{TIR}}$  span a slightly narrower range, from 0.06% to 0.4%. For low metallicity and faint sources, the  $L_{\text{TIR}}$  determination is sometimes less accurate due to non-detections in the *Herschel* photometer bands. On the high metallicity end, ratios of line-to-TIR seem to be higher, although the scatter is significant. The ratios are particularly high for the individual regions of the LMC. The PACS observations of the extended galaxies were indeed designed to map the most active regions, hence this is a bias towards excitation by the young massive stars resulting in bright FIR lines, while the dust still emits significantly further from the



**Table 3.2.** PACS line and line-to-TIR median ratios of the DGS galaxies.

	Full DGS sample		Selected DGS <sup>(a)</sup>	Brauher et al. sample
<i>PACS line ratio</i> <sup>(b)</sup>	min – max	median	median	median
[O I]63/[C II] .....	0.15 – 2.63	0.64 ± 0.01	0.60 ± 0.05	0.72 ± 0.08
[O III]/[C II] .....	0.38 – 12.4	2.06 ± 0.04	1.54 ± 0.14	0.54 ± 0.07
[O I]145/[O I]63 .....	0.05 – 0.16	0.080 ± 0.002	0.069 ± 0.006	0.063 ± 0.009
[O III]/[O I]63 .....	0.45 – 12.5	3.14 ± 0.06	2.82 ± 0.18	0.74 ± 0.09
[O III]/[N II]122 .....	21.0 – 651	130 ± 5	62.1 ± 8.9	3.27 ± 0.70
[N III]/[N II]122 .....	3.92 – 13.8	8.12 ± 0.77	8.12 ± 1.42	1.91 ± 0.60
[N II]122/[C II] .....	0.0072 – 0.041	0.018 ± 0.001	0.016 ± 0.002	0.12 ± 0.02
[N III]/[O III] .....	0.073 – 0.24	0.14 ± 0.01	0.14 ± 0.01	1.08 ± 0.11
<i>Line-to-TIR ratio [in %]</i> <sup>(c)</sup>				
[C II]/TIR .....	0.035 – 0.71	0.23 ± 0.02	0.20 ± 0.02	0.087 ± 0.005
[O I]63/TIR .....	0.061 – 0.43	0.13 ± 0.01	0.11 ± 0.01	0.065 ± 0.005
[O III]/TIR .....	0.13 – 3.16	0.37 ± 0.03	0.35 ± 0.04	0.051 ± 0.004
[O I]145/TIR .....	0.0044 – 0.023	0.0085 ± 0.0008	0.0075 ± 0.0009	0.0039 ± 0.0006
[N II]122/TIR .....	0.0025 – 0.018	0.0048 ± 0.0005	0.0044 ± 0.0007	0.0095 ± 0.0022
[N III]/TIR .....	0.020 – 0.041	0.030 ± 0.006	0.041 ± 0.006	0.024 ± 0.004
([C II]+[O I]63)/TIR .....	0.10 – 0.97	0.38 ± 0.03	0.33 ± 0.04	0.17 ± 0.02
([C II]+[O I]63+[O III])/TIR	0.23 – 3.69	0.78 ± 0.06	0.73 ± 0.07	0.22 ± 0.03

Only clear detections ( $>3\sigma$ ) are considered when deriving the median ratios.

(a) this includes all unresolved and fully mapped sources, i.e., all objects from the DGS sample, except the LMC, SMC regions, NGC 4449, NGC 6822, and IC 10.

(b) line ratios are derived with integrated line fluxes for unresolved or fully mapped galaxies, or considering the surface brightness over the peak of emission for the most extended sources (as given in Table 3.1).

(c) line/TIR ratios are derived with integrated line fluxes and  $L_{\text{TIR}}$  for unresolved or fully mapped galaxies, or integrating the line flux and TIR emission over the area mapped for the line for the most extended sources (as explained in Section 3.2.1).

### 3.2.3 PACS line ratios

Figures 3.3 to 3.9 show ratios of the DGS and Brauher FIR lines with  $L_{\text{TIR}}$  and with the FIR colors 60/100 $\mu\text{m}$ .

#### • [O III]88 / [C II]157 : Figure 3.3

The [O III] 88 $\mu\text{m}$  line is found to be very bright in the DGS galaxies and is the brightest line in most cases. This is true – not only locally in extended sources where the peaks of emission are  $\sim 10$  times brighter than the [C II] 157 $\mu\text{m}$  line (e.g. 30Dor) – even integrated over full galaxies. The [C II] line is the second brightest FIR line. In compact objects, [C II] often shows a larger spatial extent than the other lines, hinting perhaps towards an important contribution from a diffuse phase. Values of [O III]88/[C II]157 span more than an order of magnitude, from 0.4 to 12, and [O III] is on average 2.1 times [C II]. This is surprising, at first, as it requires 35 eV photons to create a  $\text{O}^{++}$  ion while the [C II] is more easily excited (I.P. of  $\text{C}^0 = 11.26$  eV). Bright [O III] is likely related to the starbursting nature of the dwarfs in the DGS, as observed in dwarf irregular galaxies (Hunter et al. 2001), which may

host stars with higher effective temperatures than normal galaxies. In the extended sources, [O III] is detected over large spatial scales (e.g. N11B in the LMC; see [Lebouteiller et al. 2012](#)) indicating the presence of low density channels where the UV photons can travel far to excite the gas.

The [O III]88/[C II]157 ratio decreases slightly with increasing  $L_{\text{TIR}}$  (Figure 3.3). This is because [O III]88/TIR (Fig. 3.14) decreases more steeply with  $L_{\text{TIR}}$  than [C II]157/TIR (Fig. 3.10). As explained in Sect. 3.2.4, both the lower dust content and UV field dilution are responsible for these relations, [O III] being more sensitive to the extent of the hard UV photons.

For the Brauher et al. galaxies, [O III]88/[C II]157 tends to increase with increasing  $60/100\mu\text{m}$ , which is not obvious for the dwarfs. [Brauher et al. \(2008\)](#) explain the increase in [O III]/TIR with higher  $60/100\mu\text{m}$  in normal galaxies as warmer colors are typically seen in compact H II regions, while the contribution of the compact H II regions to the [C II]157 line is negligible, hence resulting in increasing [O III]88/[C II]157 with increasing  $60/100\mu\text{m}$ . However, we argue that both [O III] and [C II] can also arise from diffuse gas, not only from dense H II regions/PDRs, and thus, the interpretation of [O III] and [C II] with  $60/100\mu\text{m}$  is not straightforward. [O III] is found spatially extended in the LMC and SMC regions (e.g. [Lebouteiller et al. 2012](#)), probing diffuse high-excitation gas. For the C<sup>+</sup> to originate in the ionised gas, low densities ( $n_{\text{crit}} \sim 50 \text{ cm}^{-3}$ ) are required, and low ionisation also, as carbon would otherwise be doubly ionised. C<sup>++</sup> has an excitation potential of 24.4 eV, lower than that of O<sup>++</sup>. Moreover, in low metallicity galaxies with high  $60/100\mu\text{m}$  ratios, the structure of the ISM phases may be more extreme, harboring very compact phases of low filling factor as well as a large volume filling factor of diffuse phase. Therefore, both the [O III] and [C II] lines could originate from low density high-excitation and low-excitation gas, which are not directly traced by the  $60/100\mu\text{m}$  colors.

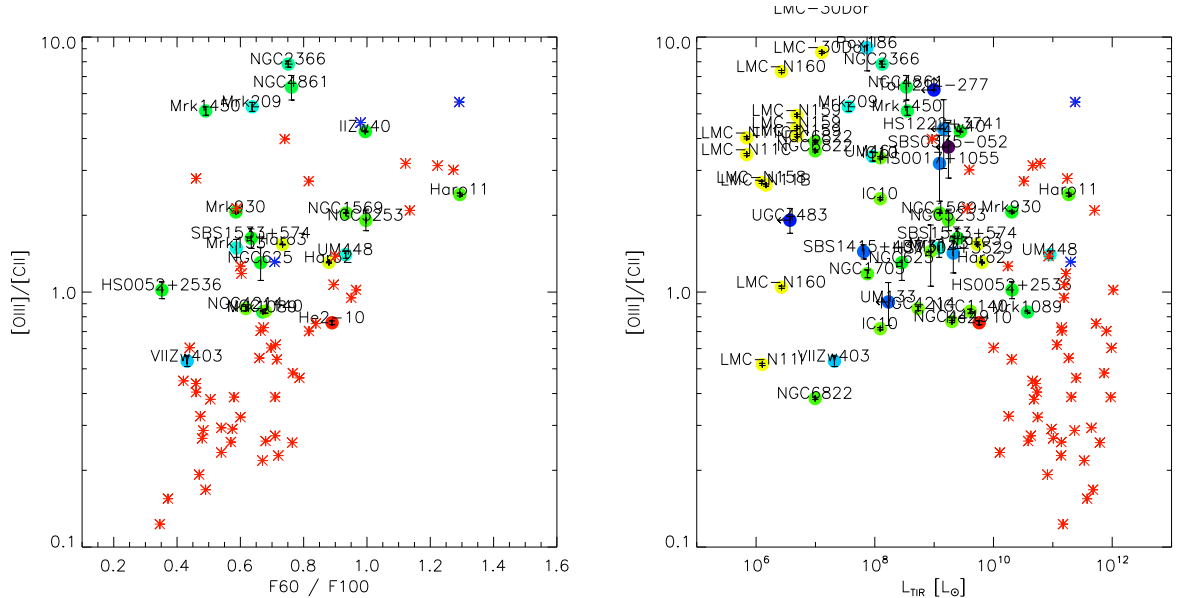


**Figure 3.3.** PACS line ratios: [O III]/[C II] versus  $60/100\mu\text{m}$  and  $L_{\text{TIR}}$ . The DGS galaxies are represented by filled circles color-coded by metallicity: dark is metal-poor ( $\sim 1/30 Z_{\odot}$ ), and light is more metal-rich (close to solar metallicity). We overplot the galaxies from [Brauher et al. \(2008\)](#) in red dots, and those few galaxies of the Brauher et al. sample with subsolar metallicities in blue dots.



- $[O\text{ I}]63 / [C\text{ II}]157$  : **Figure 3.4**

$[O\text{ I}]63$  usually dominates the cooling in resolved PDRs (e.g. the Orion Bar, Tielens et al. 1993; Bernard-Salas et al. 2012), and we find that it is often brighter than  $[C\text{ II}]$  on peaks of extended sources (e.g. N66 in the SMC). Integrated over the galaxy, it is found on average fainter than  $[C\text{ II}]$ , with  $[O\text{ I}]63/[C\text{ II}]157 \sim 0.64$ . The ratio of DGS galaxies falls in the range observed by Brauher et al., although located in the lower range of their observed  $[O\text{ I}]63/[C\text{ II}]$  values.

We see an increase of  $[O\text{ I}]63/[C\text{ II}]157$  with FIR color for the dwarfs, which is less pronounced than in Brauher et al. (Figure 3.4). Models indicate that this ratio globally increases with density and radiation field (Kaufman et al. 2006), as the critical density and excitation energy of  $[O\text{ I}]63$  are higher than for  $[C\text{ II}]$ , and therefore higher ratios are expected in compact H II regions (Malhotra et al. 2001). The relatively low ratios of  $[O\text{ I}]63/[C\text{ II}]157$  observed in dwarfs could be due to (1) optical depth effects on the  $[O\text{ I}] 63\mu\text{m}$  line, which becomes significantly optically thick for  $A_V \geq 5$  (Abel et al. 2007); and/or to (2) a low-density origin, from the ionised or neutral gas, of the  $[C\text{ II}]$  emission. As a function of  $L_{\text{TIR}}$ , the  $[O\text{ I}]63/[C\text{ II}]157$  ratios of the DGS and Brauher et al. samples are not showing any clear trend, but, instead, show a large scatter, over more than an order of magnitude, with values between 0.2 and 2.6 for the dwarfs. Both  $[O\text{ I}]63/\text{TIR}$  and  $[C\text{ II}]/\text{TIR}$  decrease similarly with increasing  $L_{\text{TIR}}$ , hence cancelling out any correlation of  $[O\text{ I}]63/[C\text{ II}]157$  with  $L_{\text{TIR}}$ . We notice that  $[O\text{ I}]63/[C\text{ II}]157$  values are relatively high in the LMC regions, which is explained by the fact that we have zoomed in on the star-forming sites, where the high densities and radiation favor emission from  $[O\text{ I}]$  rather than  $[C\text{ II}]$ , and we are also missing some extended  $[C\text{ II}]$  emission compared to global values.

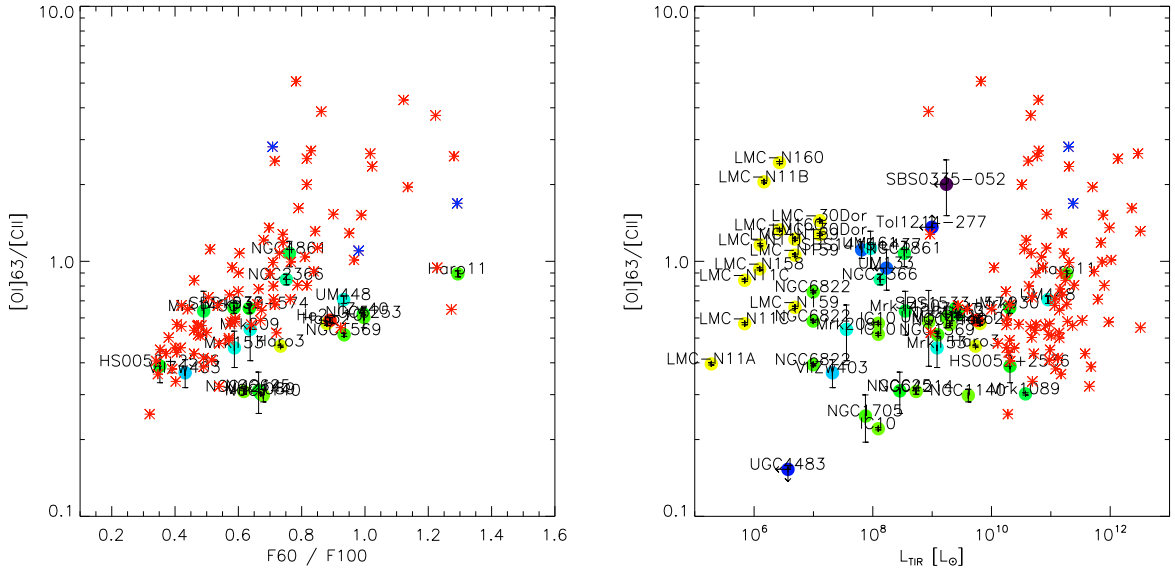


**Figure 3.4.** PACS line ratios:  $[O\text{ I}]63/[C\text{ II}]$  versus  $60/100\mu\text{m}$  and  $L_{\text{TIR}}$ . Same color-coding as in Fig. 3.3.

- $[O\text{ III}]88 / [O\text{ I}]63$  : **Figure 3.5**

As mentioned previously,  $[O\text{ III}]$  is the brightest FIR line in the dwarf galaxies, and  $[O\text{ I}]63$  is a dominant coolant of the PDR, but, on average, fainter than  $[C\text{ II}]$  compared to what is

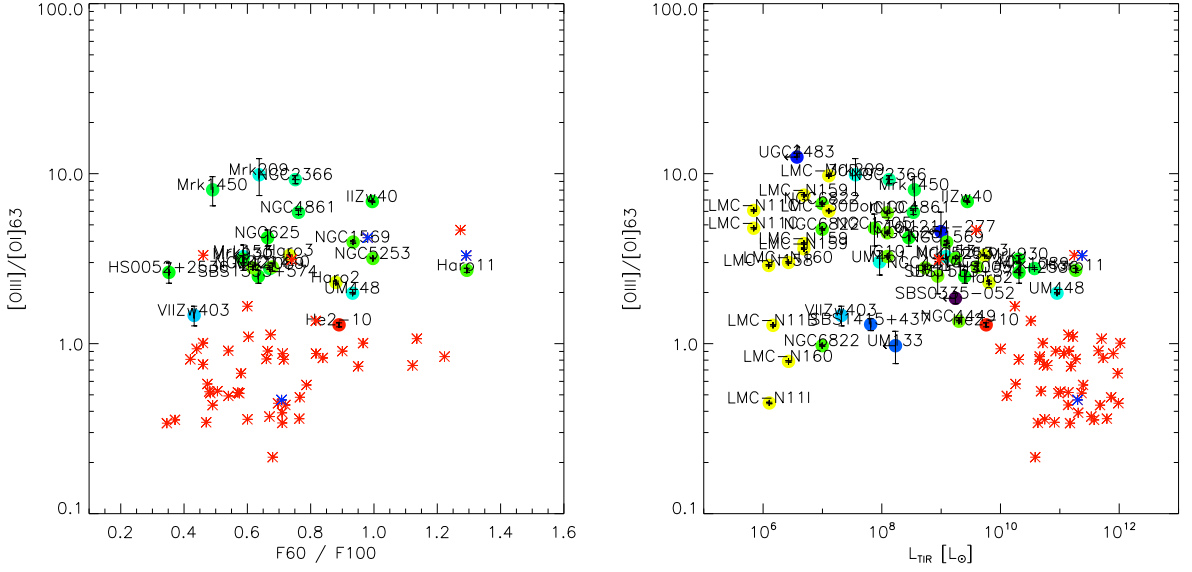


**Figure 3.5.** PACS line ratios:  $[\text{O III}]/[\text{O I}]63$  versus  $60/100\mu\text{m}$  and  $L_{\text{TIR}}$ . Same color-coding as in Fig. 3.3.

observed in more metal-rich galaxies by Brauher et al. (2008). As a result, the  $[\text{O III}]/[\text{O I}]63$  values are very high in dwarf galaxies, and fill a different parameter space than the Brauher et al. galaxies (Figure 3.5). High  $[\text{O III}]88/[\text{O I}]63$  ratios have been observed in earlier studies of dwarf irregular galaxies by Hunter et al. (2001). The range in values spans from 0.5 to  $\sim 10$  for the dwarfs, with average  $[\text{O III}]88/[\text{O I}]63$  ratio of 3.1, while most of the more metal-rich galaxies, from Brauher et al., have ratios  $\leq 1$ . However, these high  $L_{\text{TIR}}$  sources may be suffering from the same deficit which has been seen for  $[\text{C II}]$  (e.g. Graciá-Carpio et al. 2011a). For all galaxies, this  $[\text{O III}]88/[\text{O I}]63$  ratio is uncorrelated with  $60/100\mu\text{m}$  and decreases with  $L_{\text{TIR}}$  (Figure 3.5). We note that the obvious decoupling of the  $[\text{O III}]/[\text{O I}]63$  ratio and the  $60/100\mu\text{m}$  ratio may be a strong indication that the bulk of the  $[\text{O III}]$  emission is not directly linked to the dense highly ionised gas and its surrounding dense PDRs, but arises from a diffuse more extended phase.

The  $[\text{O III}]/[\text{O I}]63$  ratio may be used as an indicator of the filling factor of the ionised gas, traced by  $[\text{O III}]$ , relative to the filling factor of the PDR, traced by  $[\text{O I}]63$ . The dwarf galaxies, with high  $[\text{O III}]/[\text{O I}]63$  ratios, are probably mostly filled with ionised gas (with densities likely below  $n_{\text{crit},[\text{O III}]88\mu\text{m}} \sim 510 \text{ cm}^{-3}$ ), and very low filling factor of PDRs. This is also a result from the Haro 11 study in Cormier et al. (2012a).

#### • $[\text{O I}]145 / [\text{O I}]63$ : Figure 3.6

The  $[\text{O I}] 145\mu\text{m}$  line is always fainter than the  $[\text{O I}] 63\mu\text{m}$  line for all galaxies. Ratios of  $[\text{O I}]145/63$  range from 0.04 up to 0.16, with an average of 0.08 for the dwarf galaxies. The range of  $[\text{O I}]145/63$  values is tight and in the range of values found by Brauher et al. for the more metal-rich galaxies. This ratio is sensitive to the density and temperature of the gas, increasing with increasing temperature and decreasing density (Tielens & Hollenbach 1985).

In Figure 3.6, there is no obvious dependence of the  $[\text{O I}]145/63$  ratio on the  $60/100\mu\text{m}$  ratio or  $L_{\text{TIR}}$ . There are less data points compared to Fig. 3.4, 3.3, and 3.5 because the  $[\text{O I}] 145\mu\text{m}$  line is fainter and therefore was observed for fewer galaxies with *ISO* and *Herschel*. Optical depth effects for the  $[\text{O I}] 63\mu\text{m}$  line are invoked in Malhotra et al. (2001) and Hunter

et al. (2001) to account for high  $[\text{O I}]145/[\text{O I}]63$  values ( $>0.1$ ). Although our values of  $[\text{O I}]145/63$  are moderate, values higher than  $\sim 0.1$  are indeed difficult to reconcile with PDR models in the optically thin limit (Röllig et al. 2006b; Kaufman et al. 2006), and may be explained by  $[\text{O I}] 63\mu\text{m}$  optical depth effects.

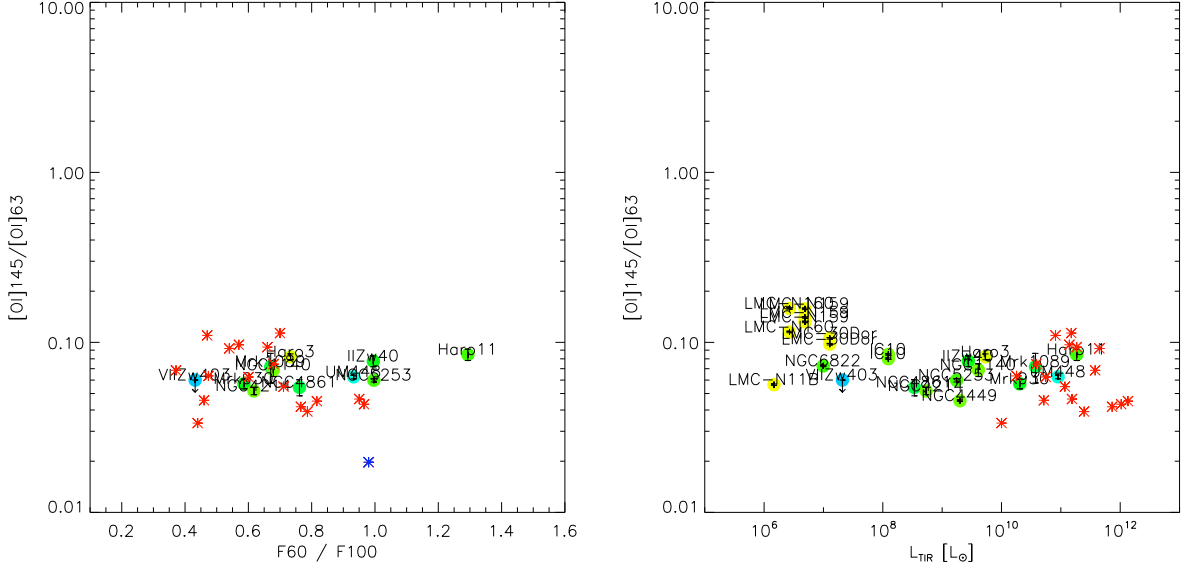


**Figure 3.6.** PACS line ratios:  $[\text{O I}]145/[\text{O I}]63$  versus  $60/100\mu\text{m}$  and  $L_{\text{TIR}}$ . Same color-coding as in Fig. 3.3.

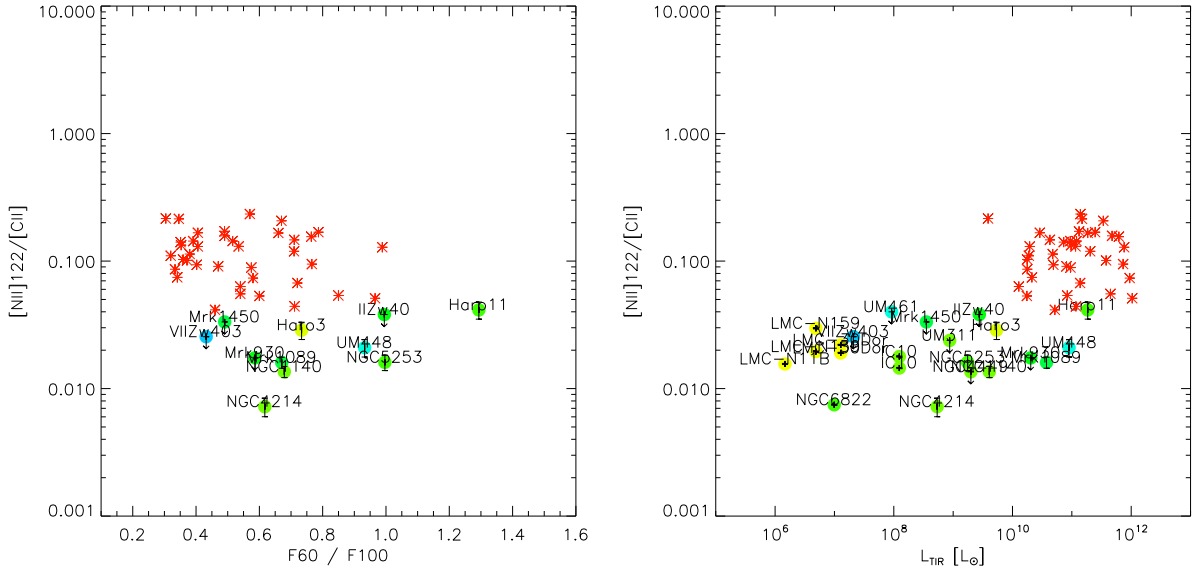


**Figure 3.7.** PACS line ratios:  $[\text{N II}]122/[\text{C II}]$  versus  $60/100\mu\text{m}$  and  $L_{\text{TIR}}$ . Same color-coding as in Fig. 3.3.

•  $[\text{N II}]122 / [\text{C II}]157$  : **Figure 3.7**

The  $[\text{N II}] 122\mu\text{m}$  line is only detected in 9 sources of the DGS out of 16 attempted observations as this line is relatively faint. Values of  $[\text{N II}]122/[\text{C II}]157$  range between

0.007 and 0.04 for the dwarfs, with an average value of 0.02, and are typically an order of magnitude lower than in the Brauher et al. galaxies (Figure 3.7), which is a result of globally lower  $[\text{N II}]122/L_{\text{TIR}}$  and higher  $[\text{C II}]157/L_{\text{TIR}}$  in dwarfs (Fig. 3.10).  $[\text{N II}]122$  emission is expected to be significant in regions of low density and rather low ionisation. High ionisation would, instead, favor the presence of  $\text{N}^{++}$  rather than  $\text{N}^+$ , which seems to be the case for the dwarf galaxies from Figure 3.9.

We do not see clear correlations of  $[\text{N II}]122/[\text{C II}]157$  with  $60/100\mu\text{m}$  and  $L_{\text{TIR}}$  in Figure 3.7. It is remarkable how the dwarf galaxies fill a completely different parameter space than the more metal rich galaxies from the Brauher et al. sample. The  $[\text{N II}]122/[\text{C II}]157$  ratio is relatively constant in the Brauher et al. galaxies, with average value 0.11, compared to 0.02 in the dwarfs. Brauher et al. (2008) suggest that a significant fraction of  $[\text{C II}]$  originates in H II regions where  $[\text{N II}]$  comes from. Our lower  $[\text{N II}]122/[\text{C II}]157$  values would favor the idea of a non-H II region contribution from the neutral and/or ionised diffuse ( $n_{\text{H}} < 50 \text{ cm}^{-3}$ ) gas to the  $[\text{C II}]$  line. Indeed, from Oberst et al. (2006) and Figure 1.4 in Section 1.2.4, we know that low  $[\text{N II}]122/[\text{C II}]157$  ratios ( $< 0.1$ ) require excitation sources other than the ionised gas. The  $[\text{N II}]122/[\text{C II}]157$  ratio could be used as an indicator of the  $[\text{C II}]$  excitation, which is mostly the ionised gas for high  $[\text{N II}]122/[\text{C II}]157$  ratios, and PDRs for low ratios. Haro 11, with  $[\text{N II}]122/[\text{C II}]157 = 0.04$ , has the highest ratio for the DGS galaxies. We have found that, for Haro 11, the diffuse ionised gas contributes to  $\sim 40\%$  to its  $[\text{C II}]$  emission. Thus Haro 11 nicely separates the two samples. On the other hand, when zooming in on N11B in the LMC, the  $[\text{C II}]$  is associated with the PDRs (Lebouteiller et al. 2012), and the  $[\text{N II}]122/[\text{C II}]157$  is lower,  $\simeq 0.02$ .

#### • $[\text{O III}]88 / [\text{N II}]122$ : Figure 3.8

As a result of the previous points, the  $[\text{O III}]88/[\text{N II}]122$  ratio is indeed very high in dwarfs. It ranges from  $\sim 20$  to 650, with average value 130. The  $[\text{O III}]88/[\text{N II}]122$  ratio decreases with increasing  $L_{\text{TIR}}$  and is not correlated with  $60/100\mu\text{m}$  (Figure 3.8).  $[\text{O III}]$  and  $[\text{N II}] 122\mu\text{m}$  have similar critical densities ( $\sim 300\text{--}500 \text{ cm}^{-3}$ ), but different excitation potentials (35.5 and 14.5 eV respectively). The harder radiation fields present in dwarf galaxies hence favor the excitation of  $[\text{O III}]$  (and  $[\text{N III}]$ ) rather than  $[\text{N II}]$ . The fact that  $[\text{O III}]$  and  $[\text{N II}] 122\mu\text{m}$  behave similarly with FIR colors may indicate an important contribution of low density ionised gas to these lines, in addition to the compact H II regions.

#### • $[\text{N III}]57 / [\text{N II}]122$ : Figure 3.9

We have 4 DGS sources observed in  $[\text{N III}] 57\mu\text{m}$  and 3 of them have both  $[\text{N III}]$  and  $[\text{N II}]122$  detections. With so few data points, no trend of  $[\text{N III}]57/[\text{N II}]122$  with  $60/100\mu\text{m}$  or  $L_{\text{TIR}}$  can be identified. Nevertheless, the  $[\text{N III}]57/[\text{N II}]122$  ratios are high in dwarfs, with an average value of 8.1, at the higher end of the ratio values of the few metal-rich galaxies presented by Brauher et al. (2008). This ratio is an indicator of the effective stellar temperature (Rubin et al. 1994), as it requires 14.5 eV to create  $\text{N}^+$ , and 29.6 eV to create  $\text{N}^{++}$ . Again, with hard radiation fields and lower dust attenuation throughout the galaxy, high ratios of  $[\text{N III}]57/[\text{N II}]122$  are expected in dwarfs.

### 3.2.4 Relation of FIR fine-structure lines with $L_{\text{TIR}}$ , star formation indicator

In Figures 3.10 to 3.14, we show ratios of PACS line -to-  $L_{\text{TIR}}$  versus  $60/100\mu\text{m}$  and  $L_{\text{TIR}}$ .

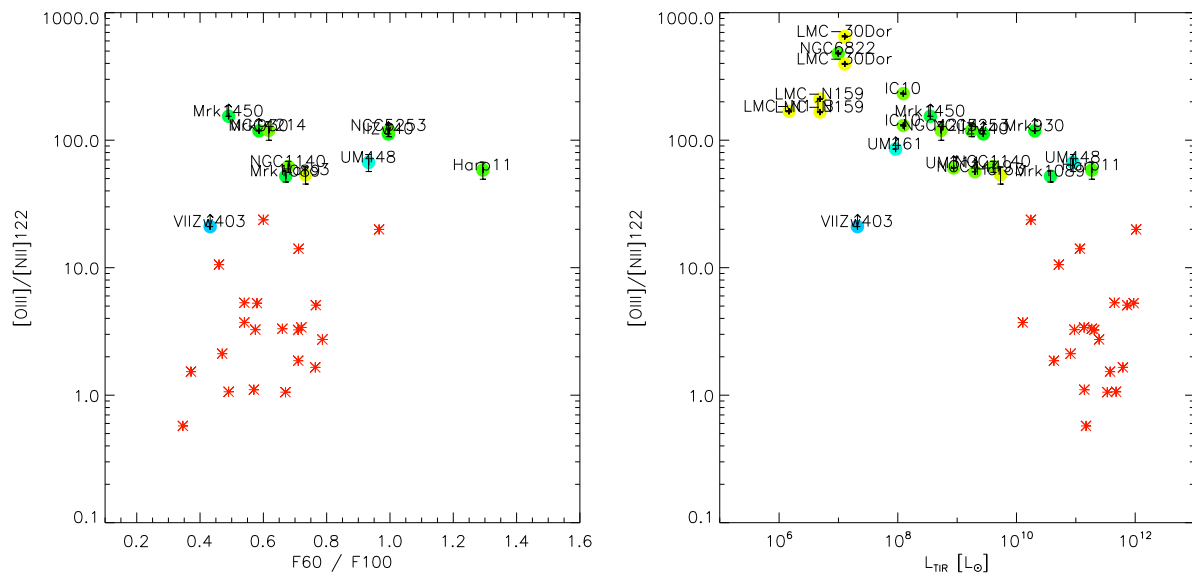


**Figure 3.8.** PACS line ratios:  $[\text{O III}]/[\text{N II}]_{122}$  versus  $60/100\mu\text{m}$  and  $L_{\text{TIR}}$ . Same color-coding as in Fig. 3.3.

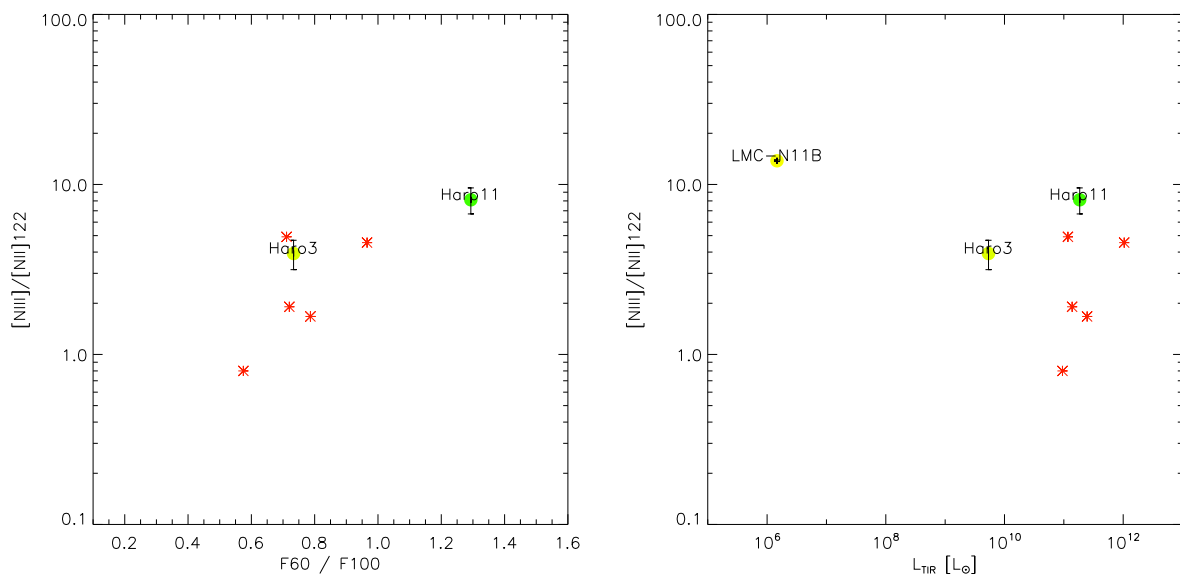


**Figure 3.9.** PACS line ratios:  $[\text{N III}]/[\text{N II}]_{122}$  versus  $60/100\mu\text{m}$  and  $L_{\text{TIR}}$ . Same color-coding as in Fig. 3.3.

• *[C II]157 / TIR and [O I]63 / TIR : Figure 3.10 and Figure 3.11*

The ratio of  $[C II]/TIR$  spans more than an order of magnitude in the DGS galaxies, from 0.07 to 0.5%, with an average value of 0.2%. This ratio is at the high end of the range observed by Brauher et al. (2008) and Malhotra et al. (2001). Globally higher  $[C II]$  emission and lower  $L_{TIR}$  are observed in irregulars compared to spirals (Hunter et al. 2001). The large spread in the  $[C II]/TIR$  values (Fig. 3.10), compared to  $[O I]63/TIR$  (Fig. 3.11) and  $([O I]63+[C II])/TIR$  (Fig. 3.13), may hint towards different origins of the  $[C II]$  lines or different conditions of the phases emitting  $[C II]$ , or may just be a bias since fewer galaxies were observed in  $[O I]63$ .

The dwarfs seem to extend the correlation, observed in Brauher et al., of  $[C II]157/TIR$  decreasing with increasing  $L_{TIR}$  (Figure 3.10).  $[C II]157/TIR$  values decrease by about an order of magnitude over 6 orders of magnitude in  $L_{TIR}$ .  $[C II]157/TIR$  may also be decreasing with increasing  $60/100\mu m$  for the DGS galaxies, but not as steeply as the Brauher et al. galaxies.

The ratio of  $[O I]63/TIR$  does not vary significantly among the dwarfs with average value of 0.1%, and is in the range observed by Brauher et al.. There is no clear trend between  $[O I]63/TIR$  and  $60/100\mu m$ , but  $[O I]63/TIR$  decreases with increasing  $L_{TIR}$  (Figure 3.11). Similar conclusions can be drawn for the  $[O I] 145\mu m$  line which has average  $[O I]145/TIR$  ratio value of 0.09% (Figure 3.12).

As a result, the ratio of  $([C II]157+[O I]63)/TIR$  decreases with increasing  $L_{TIR}$  and  $60/100\mu m$  (Figure 3.13), perhaps not as steeply as in Brauher et al. or Malhotra et al. (2001). The average value of  $([C II]157+[O I]63)/TIR$  is 0.4%.

The interpretation of these observed trends is not straightforward since several factors act and compete in the emission of the cooling lines and of  $L_{TIR}$ . These factors generally include cloud physical conditions, mixing of gas phases, geometry, dust properties, and photoelectric efficiency. They probably all play a role in the line-to-TIR ratios observed in the dwarf galaxies since these values are integrated over full-size galaxies. The different origin of the FIR lines and TIR emission are mostly responsible for the dispersions in the  $[C II]/TIR$  and  $[O I]/TIR$  ratios, and the photoelectric efficiency to a second order.

We notice that the line-to-TIR ratios are globally higher for the individual star-forming regions of the LMC than for the global values (integrated over full-size galaxies). When ignoring the ratio values in the LMC regions, the decreasing trends of  $[C II]157/TIR$  and  $[O I]/TIR$  with  $L_{TIR}$  are not as strong, and the distributions of the compact galaxies look flatter. This demonstrates the effect of physical size scales on the observed ratios. Ratios are higher when zooming in on the star-forming regions, and high ratios for the compact objects may therefore indicate that  $H II$  regions clearly dominate the overall emission of the galaxy. We briefly discuss photoelectric efficiency in the following section.

• *Photoelectric efficiency  $\epsilon_{PE}$ :*

At the high TIR luminosity end (ULIRGs), a clear deficit of  $[C II]157/TIR$  (Luhman et al. 2003), and FIR lines in general (Graciá-Carpio et al. 2011b), is observed. A recent study of spatially resolved PACS observations of the Seyfert 1 galaxy NGC 1097 by Croxall et al. (2012) shows variations in the  $[C II]/TIR$  and  $[O I]/TIR$  with  $70/100\mu m$  colors.

Several hypothesis to explain this deficit include: 1) more efficient dust screening at high ionisation parameter (Luhman et al. 2003; Abel et al. 2009); 2) less efficient photoelectric heating due to charged small dust grains under intense radiation fields (Malhotra et al. 2001;

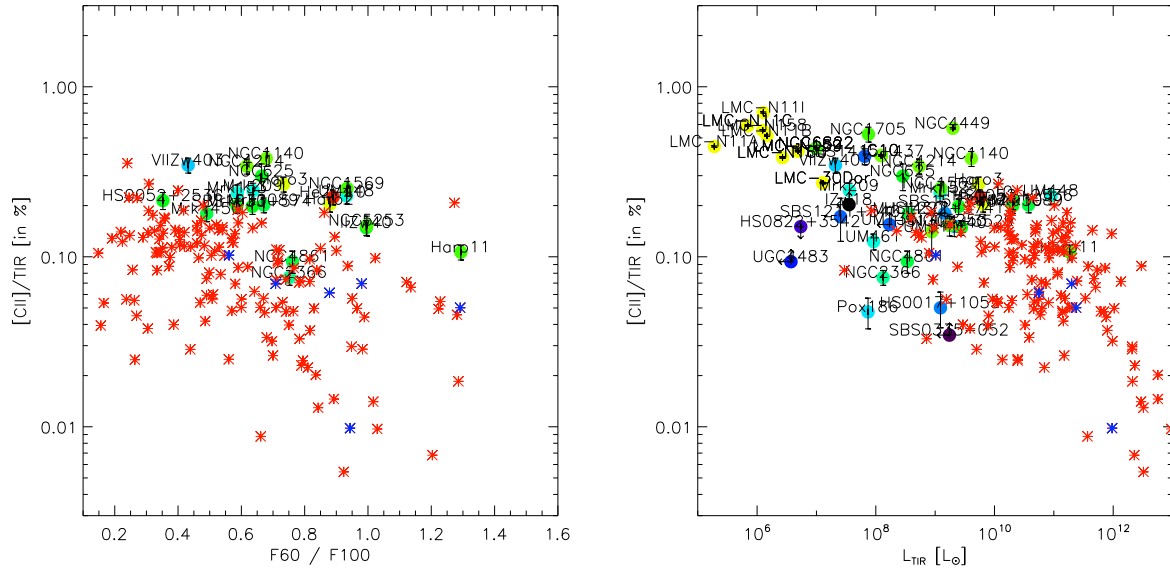


**Figure 3.10.** PACS line -to- TIR ratio:  $[\text{C II}]\lambda 157 / \text{TIR}$  versus  $60/100\mu\text{m}$  and  $L_{\text{TIR}}$ . Same color-coding as in Fig. 3.3.

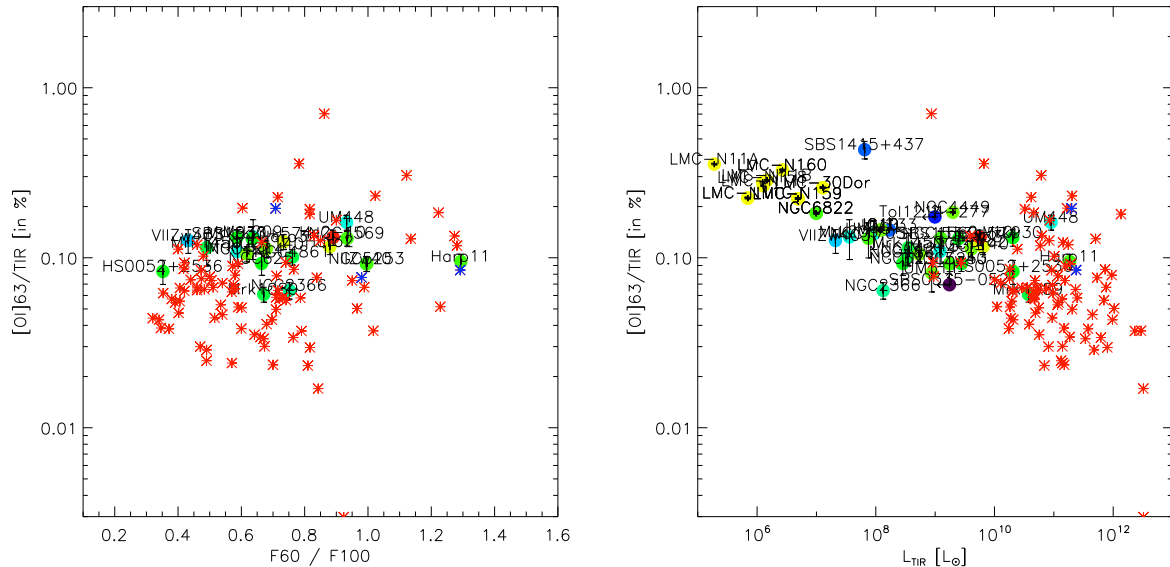


**Figure 3.11.** PACS line -to- TIR ratio:  $[\text{O I}]63 / \text{TIR}$  versus  $60/100\mu\text{m}$  and  $L_{\text{TIR}}$ . Same color-coding as in Fig. 3.3.

Croxall et al. 2012); 3) less efficient photoelectric heating due to a decrease in the PAH abundance under hard radiation fields (Rubin et al. 2009; Madden et al. 2006); 4) dust optical depth effects (Papadopoulos et al. 2010; Rangwala et al. 2011).

Star-forming dwarf galaxies exhibit generally lower dust abundances due to their lower metallicity, high ionisation parameters (e.g. [Dopita & Evans 1986](#)), and reduced PAH abundances due to the hard radiation fields ([Madden et al. 2006](#)). Hence options 2) and 3), valid for the dwarfs, would, without further investigation into the dust properties, indicate lower photoelectric efficiencies in dwarf galaxies. This would contradict the observed high



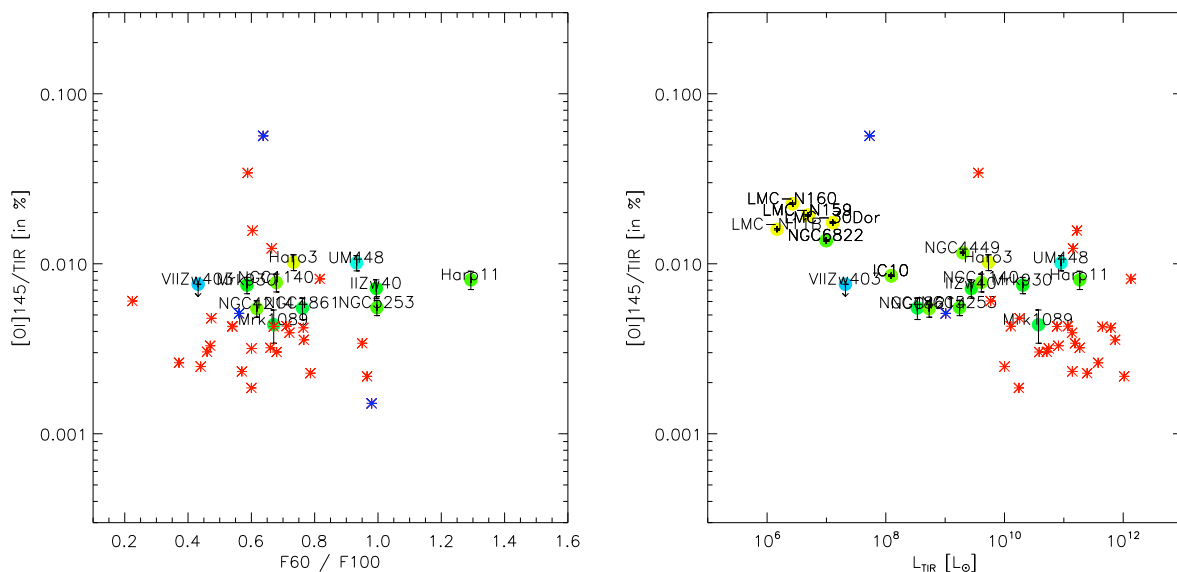


**Figure 3.12.** PACS line -to- TIR ratio:  $[\text{O I}]_{145} / \text{TIR}$  versus  $60/100\mu\text{m}$  and  $L_{\text{TIR}}$ . Same color-coding as in Fig. 3.3.

[C II]/TIR (Fig. 3.10) and average [O I]/TIR ratios (Fig. 3.11). However, dwarf galaxies also exhibit enhanced small grain abundances (e.g. Galliano et al. 2003) which contribute to the photoelectric heating. Because of the lower dust content, the mean free path of UV photons is larger, resulting in a UV field dilution over larger spatial scales, which may result in less grain charging, and thus cancel the effects of 1), and 2). Hence, we do not observe a deficit of the [C II]/TIR and [O I]/TIR ratios with  $L_{\text{TIR}}$  or 60/100 $\mu\text{m}$  colors for the dwarfs, but relatively *efficient* photoelectric effect. It would be interesting to quantify the balance between small grain charging and abundance, in the resulting photoelectric efficiency. The ([C II]+[O I]63)/TIR ratios (Fig. 3.13) tend to flatten out to 1% at low luminosity (constant heating efficiency). The emission lines are not enhanced. This could indicate a ceiling on the photoelectric efficiency, or a non-active contribution of the dust emission to  $L_{\text{TIR}}$ .

The heating efficiency, measured by  $([\text{C II}]157 + [\text{O I}]63)/\text{TIR}$ , is a direct function of  $G_0/n_H$  (Tielens & Hollenbach 1985; Kaufman et al. 2006). With increasing  $60/100\mu\text{m}$ , the warmer dust is located in compact regions close to the stars, associated with dense PDRs. Hence both  $G_0$  and  $n_H$  increase, while  $G_0/n_H$  can stay constant, leading to enhanced  $[\text{O I}]63/\text{TIR}$ , lower  $[\text{C II}]157/\text{TIR}$ , and constant  $([\text{C II}]157 + [\text{O I}]63)/\text{TIR}$ , according to models (e.g. Kaufman et al. 2006). This is indeed what we see in Figure 3.10 with  $[\text{C II}]157/\text{TIR}$  decreasing with increasing  $60/100\mu\text{m}$ . And this is also why we have  $[\text{O I}]63/[\text{C II}]$  increasing with  $60/100\mu\text{m}$  (Figure 3.4). However, we do not see an enhancement of  $[\text{O I}]63/\text{TIR}$  (or  $[\text{O I}]145/\text{TIR}$ ) with increasing  $60/100\mu\text{m}$ . The dwarfs rather show a flat and narrow distribution of  $[\text{O I}]/\text{TIR}$ . This may have two explanations: 1) that the  $[\text{O I}] 63\mu\text{m}$  line becomes optically thick at high  $A_V$  in the dense PDR, or 2) that the covering factor of the dense PDR clouds decreases with increasing  $60/100\mu\text{m}$ . The fact that the  $[\text{O I}] 145\mu\text{m}$  line would become optically thick for column densities greater than that for  $[\text{O I}]63$ , and that  $[\text{O I}]145$  and  $[\text{O I}]63$  behave similarly with  $L_{\text{TIR}}$  and  $60/100\mu\text{m}$ , may rather favor the second option. This would, in turn, decrease the fraction of  $[\text{C II}]$  originating from the PDR envelope at high  $60/100\mu\text{m}$ . However, in the case of low filling factor PDRs, low density neutral/ionised gas may fill the major part of the ISM volume, where  $[\text{C II}]$  would dominate the cooling (compared to  $[\text{O I}]$ ). This may be

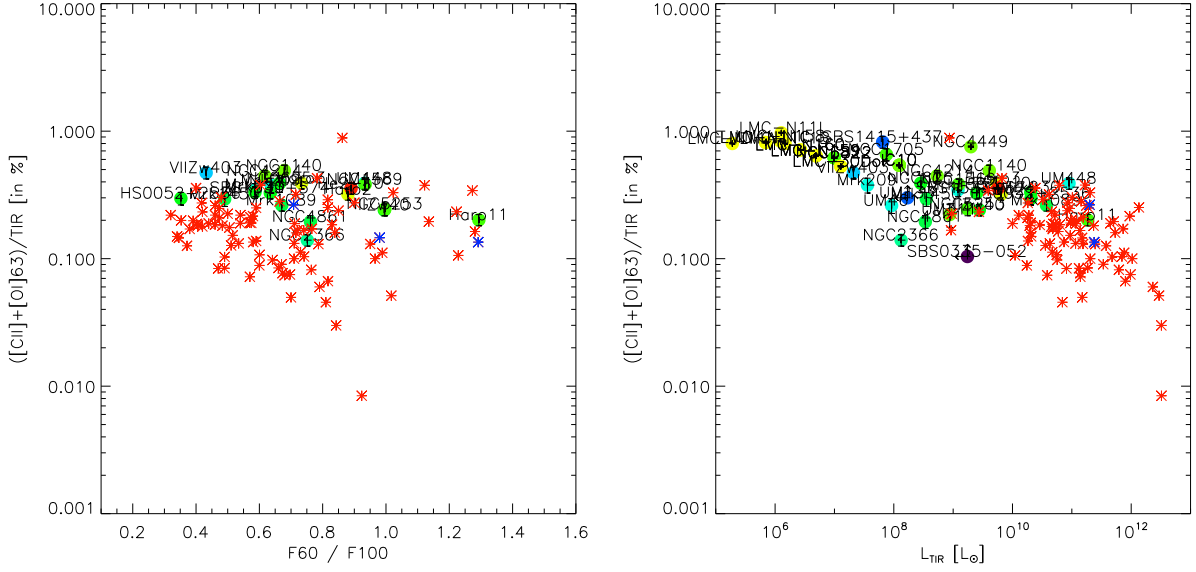


**Figure 3.13.** PACS line -to- TIR ratio:  $([\text{C II}]157 + [\text{O I}]63) / \text{TIR}$  versus  $60/100\mu\text{m}$  and  $L_{\text{TIR}}$ . Same color-coding as in Fig. 3.3.

the reason why  $[\text{C II}]157/\text{TIR}$  does not go down with  $L_{\text{TIR}}$  as quickly as the Brauher et al. galaxies.

If  $L_{\text{TIR}}$  encompasses all the dust emission from large, small grains and PAHs, it is dominated by the large grains in thermal equilibrium, hiding the relative role of small grains and PAHs in the gas heating. What the true dust sources heating the gas in dwarf galaxies actually are, is not clear. Leboutteiller et al. (2012) examine both spatial distributions of  $([\text{C II}]157 + [\text{O I}]63)$  over TIR and PAH emission in the star-forming region N11B of the LMC, and find that PAHs dominate the gas heating with  $\epsilon_{\text{PE,PAH}} \simeq 7\%$ . Extracting the relative emission from PAHs and small dust grains from dust models should place constraints on their contributions to the gas heating.

#### • $[\text{O III}]88 / \text{TIR}$ : Figure 3.14

$[\text{O III}]88/\text{TIR}$  values span an order of magnitude, from 0.1 to 3.2 (in the region 30-Dor of the LMC), with average value of 0.4%. The dwarf galaxies are at the high end of the Brauher et al. sample (Figure 3.14). While the Brauher et al. sample roughly spans two orders of magnitude in both  $L_{\text{TIR}}$  and  $[\text{O III}]88/\text{TIR}$  axes, the dwarf sample spans an order of magnitude in  $[\text{O III}]88/\text{TIR}$  for 5 orders of magnitude in  $L_{\text{TIR}}$ . This demonstrates that the  $[\text{O III}]$  and TIR emission are related.

The  $[\text{O III}]88/\text{TIR}$  ratio clearly decreases with increasing  $L_{\text{TIR}}$ , as observed in Brauher et al., the dwarfs extending the trend observed in normal galaxies to lower luminosities. This relation is explained by the combination of high stellar effective temperature on galaxy-wide scales, resulting in high  $[\text{O III}]$  emission, and lower dust extinction with lower  $L_{\text{TIR}}$ , which in turn allows UV photons to excite  $\text{O}^{++}$  on larger spatial scales. When ignoring the extended sources (LMC regions), this decreasing trend of  $[\text{O III}]88/\text{TIR}$  with increasing  $L_{\text{TIR}}$  is still present. This indicates that  $[\text{O III}]$  is more affected by the extent of the hard UV photons on galaxy-wide scales.

On the other hand,  $[\text{O III}]88/\text{TIR}$  is not particularly correlated with  $60/100\mu\text{m}$  in dwarfs,

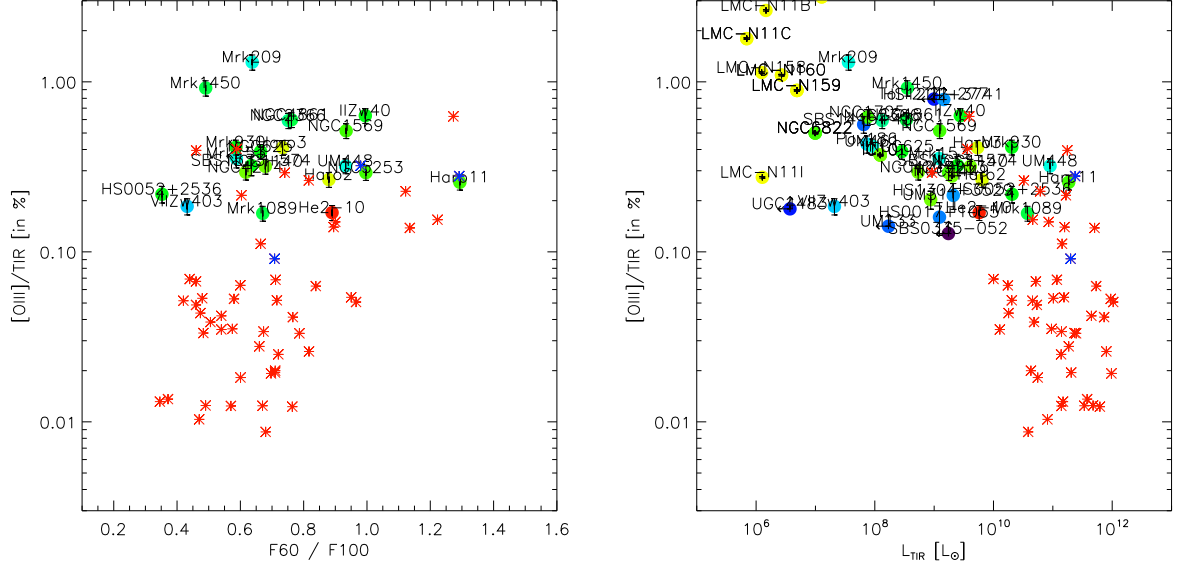


**Figure 3.14.** PACS line -to- TIR ratio:  $[O\ III]88 / TIR$  versus  $60/100\mu m$  and  $L_{TIR}$ . Same color-coding as in Fig. 3.3.

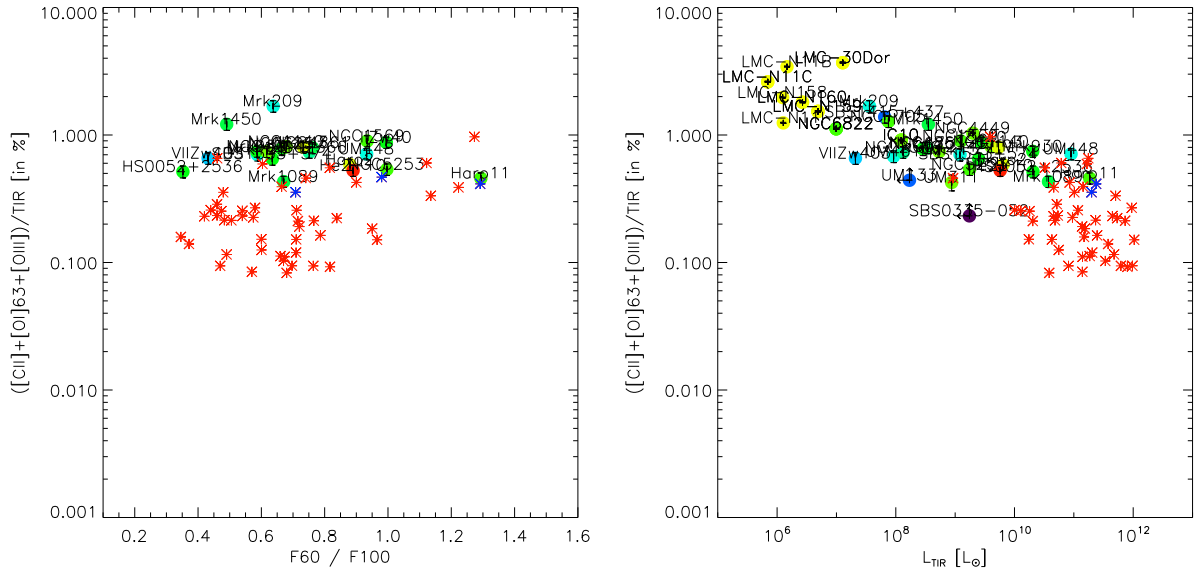


**Figure 3.15.** PACS line -to- TIR ratio:  $([C\ II]157+[O\ I]63+[O\ III]88) / TIR$  versus  $60/100\mu m$  and  $L_{TIR}$ . Same color-coding as in Fig. 3.3.

while Brauher et al. find an increase of  $[\text{O III}]88/\text{TIR}$  with  $60/100\mu\text{m}$ . They attribute this increase in warmer galaxies to a higher density of H II regions. As discussed in the  $[\text{O III}]88/[\text{C II}]157$  paragraph (Section 3.2.3),  $[\text{O III}]$  may also originate from low density ionised gas, hence flattening the relation between  $[\text{O III}]88/\text{TIR}$  and  $60/100\mu\text{m}$  in dwarfs. The  $[\text{O III}]$  emission in the low luminosity dwarf galaxies probably has a different overall origin (from more diffuse ionised gas), compared to the high luminosity galaxies where the dense H II regions contribute most.

•  $([\text{C II}]+[\text{O I}]63+[\text{O III}]) / \text{TIR} : \text{Figure 3.15}$

The ratio of  $([\text{C II}]+[\text{O I}]63+[\text{O III}])/\text{TIR}$  spans values from 0.2 to 3.7, with average of 0.8 (Figure 3.15). This ratio does not obviously correlate with FIR colors, but clearly decreases with increasing  $L_{\text{TIR}}$ , the DGS galaxies extending trends observed in the Brauher et al. sample. In the most luminous massive galaxies, this is interpreted as a deficit of the FIR fine-structure lines (e.g. Graciá-Carpio et al. 2011a). The sum of  $[\text{C II}]+[\text{O I}]63+[\text{O III}]$  may be regarded as the budget of the gas cooling, and  $L_{\text{TIR}}$  as the total dust cooling. Note that since this includes the  $[\text{O III}]$ , this ratio should not be considered as a proxy for the photoelectric efficiency. The observed trend of decreasing line emission with increasing  $L_{\text{TIR}}$  may be due to the gas cooling decreasing in importance throughout a given galaxy, or, alternatively, can be explained as an inactive phase which increases in importance in more massive galaxies. In the latter case, the decrease of  $([\text{C II}]+[\text{O I}]63+[\text{O III}])/\text{TIR}$  with increasing  $L_{\text{TIR}}$  may reflect the existence of an ISM phase in the most massive galaxies with much less line cooling. The lower ratio would be the result of mixing this inactive phase and an active phase with very significant line contribution. This inactive phase may represent a much larger volume of gas which is not excited enough to give rise to  $[\text{O III}]$  emission (due to dust-bounded H II regions). Alternatively, a medium where dust is heated by field stars without exhibiting a significant PDR would give rise to a much lower  $[\text{C II}]$  and  $[\text{O I}]63$  to  $L_{\text{TIR}}$  ratio.

### 3.2.5 Conclusions

A quantitative approach will be conducted to confirm the described behaviors and scatter in the correlations seen in the FIR line ratios. These general trends have implications on the ISM properties of dwarf galaxies, although modeling of individual galaxies is required to recover detailed gas conditions (temperature, density). The FIR lines are globally bright relative to the TIR luminosity, together accounting for a few percent of  $L_{\text{TIR}}$  – always brighter than the more metal-rich galaxies. This indicates that the gas cooling line intensities are *enhanced on galaxy-wide scales*. When zooming on the active regions of the LMC, line-to-TIR ratios appear globally higher than for galaxy-integrated values. This confirms that the dwarf galaxies are dominated by emission from their star-forming regions even on galaxy scales. In terms of ISM structure, the high  $[\text{C II}]/\text{TIR}$  and  $[\text{O III}]/\text{TIR}$  ratios highlight a leaky structure with a large volume filling factor of low density gas and UV photons escaping from dense H II regions and travelling far from the H II regions. However different ISM structure/filling factors may be responsible for the large spread in the  $[\text{C II}]/\text{TIR}$  values. When compared to the Brauher et al. sample, it is surprising how the dwarf galaxies sometimes occupy a completely different parameter space than the more metal-rich galaxies. The line ratios can be interpreted in terms of excitation of the different FIR lines. In particular, the very high  $[\text{O III}]/[\text{N II}]122$  found for the dwarfs is a clear indication of prominent high excitation regions. The low  $[\text{N II}]122/[\text{C II}]$ , relatively low  $[\text{O I}]63/[\text{C II}]$ , and high  $[\text{O III}]/[\text{C II}]$  ratios could be

used to investigate the [C II] excitation, as the [C II] line which can arise in the diffuse ionised, diffuse neutral, or dense neutral phases. In order to really disentangle between the possible origins of the [C II] line, spatial information, to localise the origin and constrain possible optical depth effects, and/or [N II]205 data would be very valuable.

This results in a vivid picture for the ISM of dwarf galaxies, of clumpy PDRs bathing in a diffuse ionised/neutral gas. Resolving the structures, as is possible in the Magellanic clouds and few Local Group galaxies (e.g. IC 10), is essential to confirm this.

### 3.3 A look into the ISM of the nearby Magellanic-type dwarf galaxy NGC 4214

The first study of my thesis concerns the *Herschel* spectroscopic data of the dwarf galaxy NGC 4214. The observations and results are presented in the A&A *Herschel* Special Issue letter, “The effects of star formation on the low-metallicity ISM: NGC 4214 mapped with *Herschel*/PACS spectroscopy”, [Cormier et al. \(2010\)](#), and can be found at the end of this Chapter (Section 3.3.5).

#### 3.3.1 Properties of the Local Group galaxy, NGC 4214

NGC 4214 is one of the closest dwarf galaxies, at a distance of 2.9 Mpc, and has a metallicity value of  $1/3 Z_{\odot}$ . It presents an intricate irregular morphology with a star formation nucleus in the center of an extended H I cloud showing a spiral structure. The central part of NGC 4214 hosts two main star-forming complexes noted as NGC 4214-I and NGC 4214-II (Fig. 3.16, left). NGC 4214-I is composed of a super star cluster (3-3.5 Myrs) and several star clusters with O stars and Wolf-Rayet stars. There is an H $\alpha$  cavity where most of the H $\alpha$  emission originates. NGC 4214-II is composed of several OB associations with WR stars as well, and an H $\alpha$  peak. It is more compact, filled, and younger than NGC 4214-I which is larger and evacuated in its central part ([MacKenty et al. 2000](#)). Its SFR is around  $0.066 M_{\odot} \text{ yr}^{-1}$  and has a high star-formation efficiency of 8%. A third region, NGC 4214-III, north-west of the center, also shows a prominent peak of CO emission with little evidence of star formation activity.

#### 3.3.2 *Herschel*/PACS spectral maps

NGC 4214 was observed with *Herschel* during the Science Demonstration phase of the mission in December 2009. The 3 star-forming regions were covered. It was one of the first object ever mapped with the PACS spectrometer. The dataset obtained is very complete, with maps of the [C II]  $157\mu\text{m}$ , [O III]  $88\mu\text{m}$ , [N III]  $57\mu\text{m}$ , [O I]  $63\mu\text{m}$ , [O I]  $145\mu\text{m}$ , [N II]  $122\mu\text{m}$ , and [N II]  $205\mu\text{m}$  lines, which can be found in Section 3.3.5 and Appendix B (p. 171).

#### 3.3.3 Conditions in the 3 star-forming regions

##### [C II]-to-CO map

One of the results of [Cormier et al. \(2010\)](#) is the very different distribution of the [C II] and CO(1-0) lines throughout the 3 regions. We found that [C II] correlates with both the dense neutral and diffuse gas. While [C II] peaks on NGC 4214-I and NGC 4214-II, it also

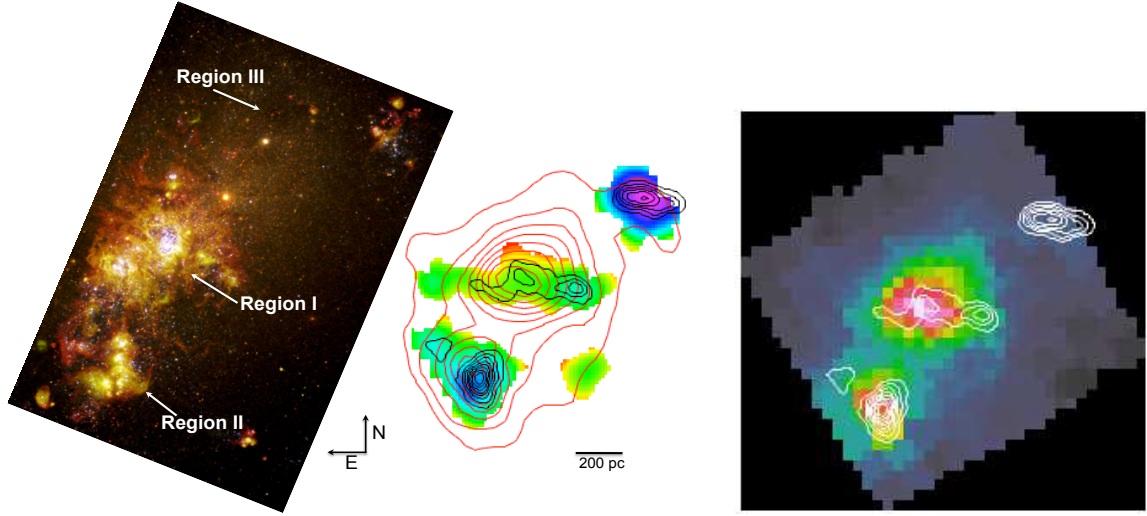


**Figure 3.16.** *Left:* Hubble Heritage image of NGC 4214 ( $D = 2.9$  Mpc). *Middle:*  $[\text{C II}]$   $157\mu\text{m}$ -to-  $\text{CO}(1-0)$  ratio map with  $\text{CO}(1-0)$  contours in black and  $[\text{C II}]$  in red. The CO map was obtained with OVRO (Walter et al. 2001) and  $[\text{C II}]$  with the *Herschel*/PACS spectrometer. Ratios of  $[\text{C II}]/\text{CO}$  vary from 4 500 up to  $10^5$ . *Right:*  $[\text{C II}]$   $157\mu\text{m}$   $1.6' \times 1.6'$  map of NGC 4214 with PACS, with resolution  $\sim 150$  pc.  $\text{CO}(1-0)$  contours are overlaid in white.

extends to the quiescent NGC 4214-III. There is CO emission in the 3 regions as well. CO is bright in NGC 4214-III with little  $[\text{C II}]$ . In NGC 4214-I, the CO and  $[\text{C II}]$  peaks do not coincide.  $[\text{C II}]$  peaks near the super star cluster, which seems to have blown out molecular gas.

Figure 3.16 (*right*) shows the  $[\text{C II}]$  map with  $\text{CO}(1-0)$  contours from Walter et al. (2001). These regions, captured at different stages of evolution, exhibit very different  $[\text{C II}]$ -to-CO ratios (Fig. 3.16, *middle*), often used as a star formation tracer in galaxies (e.g. Stacey et al. 1991, 2010).  $[\text{C II}]$ -to-CO ratios are  $\sim 75\,000$  in NGC 4214-I,  $23\,000$  in NGC 4214-II, and  $5\,000$  in NGC 4214-III; while they range typically from 2 000 to 4 000 for normal or dusty starburst galaxies (Stacey et al. 1991).

### Different SEDs

With *Spitzer*/IRAC, MIPS and IRS measurements, we have produced individual SEDs of the 3 separate regions (Fig. 3.17). The dust modelling is described in Galametz et al. (2009). The MIR and FIR lines are also added to present the full SED.

All SEDs have prominent PAHs and a peak around  $40\mu\text{m}$ . NGC 4214-I and NGC 4214-II are brighter. The total IR luminosity was measured from the individual SEDs. We derive  $L_{\text{TIR}} = 8.6 \times 10^7$  and  $4.5 \times 10^7 L_{\odot}$  while for NGC 4214-III,  $L_{\text{TIR}} = 5.2 \times 10^6 L_{\odot}$ . The thermal emission from grains is broader in NGC 4214-I and NGC 4214-II with more emission in the MIR compared to NGC 4214-III. This indicates that they are not homogeneous but may harbor a range of radiation fields/densities with a more compact component than NGC 4214-III which agrees better with diffuse models.

The SEDs also reveal a wide diversity of behaviour of the high excitation vs. low excitation lines. NGC 4214-I and NGC 4214-II have prominent FIR and MIR lines. In particular, the  $[\text{C II}]$  and  $[\text{O III}]$  lines dominate the infrared line emission. In contrast, NGC 4214-III shows low levels of high excitation ionic lines. Only the  $[\text{C II}]$  line is very prominent on the SED.

The SEDs of NGC 4214-I and NGC 4214-II are representative of typical compact H II



regions while that of NGC 4214-III represents a more quiescent region.

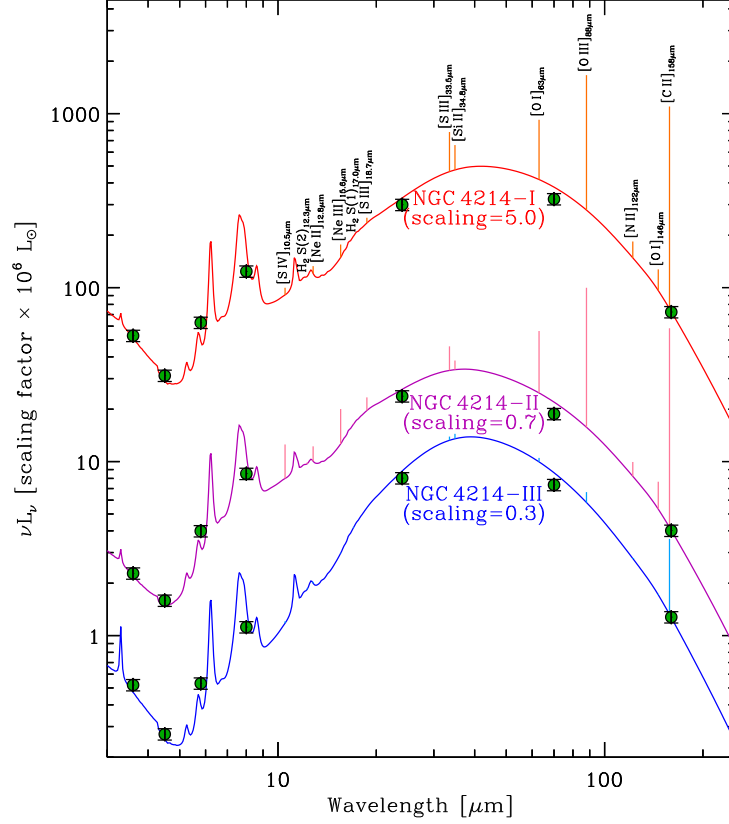


**Figure 3.17.** SEDs of the three star-forming regions in NGC 4214. For clarity, the luminosities have been multiplied by the scaling factor indicated below each SED. The black circles with error bars are the integrated *Spitzer* broadband observations. The solid line is a phenomenological SED model (Galametz et al. 2009), fit to the broadband observations. The green dots are the synthetic photometry of the model. The vertical lines on top of the SED represent the observed integrated line luminosity.

### PDR properties

We investigate the physical conditions of the star-forming regions NGC 4214-I and NGC 4214-II in which several PDR lines are detected. For that purpose, we compare observed line ratios of [C II]/[O I] and [C II]/CO to model predictions of the spherical PDR model KOSMA- $\tau$  (Röllig et al. 2006b). It provides grids of predicted line ratios for the main PDR lines ([C II], [O I], C I, CO) as a function of radiation field and cloud density, for a range of metallicities and clump mass. Section 4.1.2 briefly gives details on the KOSMA- $\tau$  model and its advantages compared to other PDR models.

Figure 3.18 shows the observed line ratios with modeled radiation field and density in contours. The shaded box indicates the approximate solution for each region. For NGC 4214-I, we find  $G_0 \sim 2 \times 10^2$  ( $\chi_{\text{Draine}}$ ) and  $n_{\text{H}} \sim 6 \times 10^3 \text{ cm}^{-3}$ . For NGC 4214-II, we find  $G_0 \sim 3 \times 10^2$  ( $\chi_{\text{Draine}}$ ) and  $n_{\text{H}} \sim 10^4 \text{ cm}^{-3}$ .

Such approach was already done in Cormier et al. (2010) using the PDR TOOLBOX (Kaufman et al. 2006). While the web interface of the PDR TOOLBOX provides more line diagnostics, in particular of the TIR intensity, which can be used as a diagnostic on the



heating efficiency, it is limited to solar (and supersolar) metallicities and to a plane-parallel slab geometry. Both limitations have a significant impact on the  $[\text{C II}]/\text{CO}$  predictions due to the different cloud structure at low metallicity. KOSMA- $\tau$  on the other hand, uses a spherical geometry, better adapted to the low metallicity PDR/molecular cloud geometry (see Sect. 1.3 and Sect. 4.1.2). This is why the  $[\text{C II}]/\text{CO}$  ratios predicted by the PDR TOOLBOX do not coincide with the PDR solution values, but the KOSMA- $\tau$  models are more successful in explaining the high  $[\text{C II}]/\text{CO}$ .

The other PDR parameter values from the PDR TOOLBOX agree with those from KOSMA- $\tau$ . They are indicative of a relatively moderate gas density and radiation field, resulting from the mixing of media with various conditions, as we do not resolve the cloud structure in the individual star-forming regions.

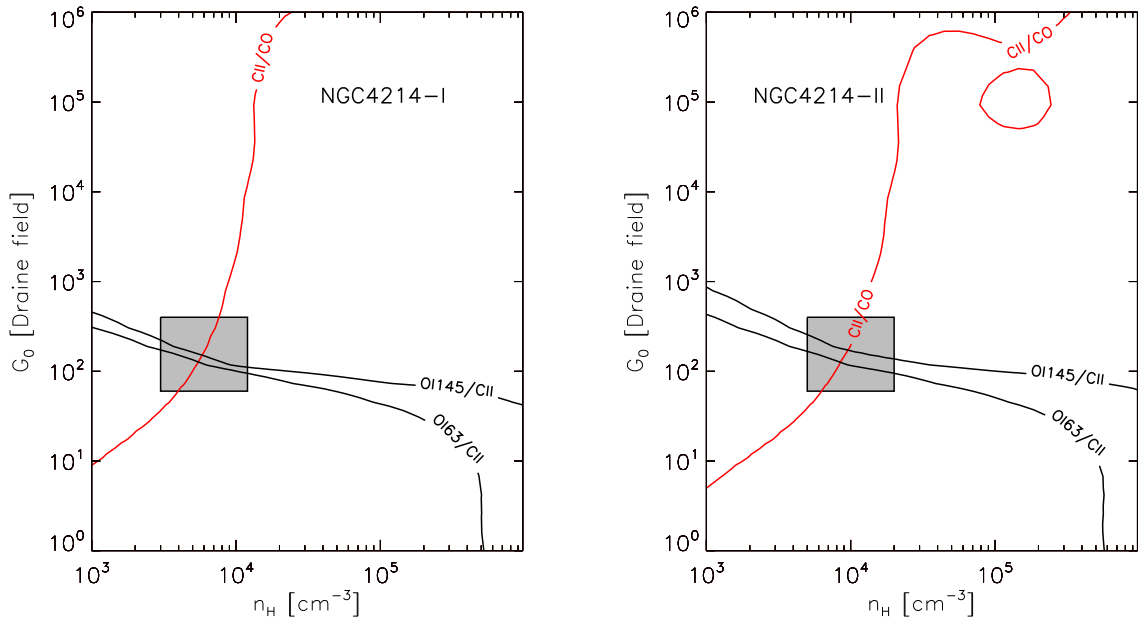


**Figure 3.18.** Contour plots of PDR line ratios in radiation field and density space from the PDR model KOSMA- $\tau$  (Röllig et al. 2006b). Observed ratios correspond to the dark and red solid lines. The shaded box indicates the range of solutions for the PDR conditions.

### 3.3.4 Need for higher spatial/spectral resolution

One of the limitations of this study is the lack of spatial resolution. Although the 3 star-forming regions are clearly separated by PACS on *Herschel*, we have no spatial information concerning their internal structure due to the large beam size of PACS (11.5'') and poor spectral resolution (instrument FWHM of 240 km s<sup>-1</sup>). To analyse the data in more detail, and in particular the connection between the H II region and PDR/molecular cloud, we require structural information, i.e. better spatial or spectral resolution.

The high spectral resolution is now accessible with e.g. the instrument GREAT onboard *SOFIA*. By spectrally resolving the line we can access the dynamics and ISM structure along the line of sight. In combination with existing CO and H I high-resolution data, we can characterize the physical properties of these regions, determine the origin of the  $[\text{C II}]$  emission, and dissect the molecular cloud structures. More details on the science opened by *SOFIA* for dwarf galaxies can be found in Chapter 6.

### 3.3.5 Paper published in A&A, 2010, 518, 57

The study carried out in this Letter for the Science Demonstration phase of the mission presents *Herschel*/PACS spectral observations of 6 FIR fine-structure lines in the Magellanic-type galaxy NGC 4214. The maps cover a central area ( $1.6' \times 1.6'$ ) of the galaxy where the star formation takes place. The FIR lines are bright, together accounting for  $\sim 2\%$  of  $L_{\text{TIR}}$ . We compare the spatial distribution of the different cooling lines in the 3 star-forming knots. While the [C II] emission is extended, and its overall intensity highest, over the peaks of star formation, [O III] is two times brighter and traces well the source of ionisation. The [C II] distribution is somewhat different than that of ancillary CO(1-0) data, with [C II]/CO(1-0) as high as 70 000, indicating strong photodissociation. Preliminary PDR modeling using the PDR TOOLBOX is presented, for coarse constraints on the physical conditions. Both spatial resolution and more precise modeling are needed for a more accurate picture of the ISM properties of NGC 4214.

## LETTER TO THE EDITOR

**The effects of star formation on the low-metallicity ISM:  
NGC 4214 mapped with *Herschel*\*/PACS spectroscopy**D. Cormier<sup>1</sup>, S. C. Madden<sup>1</sup>, S. Hony<sup>1</sup>, A. Contursi<sup>2</sup>, A. Poglitsch<sup>2</sup>, F. Galliano<sup>1</sup>, E. Sturm<sup>2</sup>, V. Doublier<sup>2</sup>,  
H. Feuchtgruber<sup>2</sup>, M. Galametz<sup>1</sup>, N. Geis<sup>2</sup>, J. de Jong<sup>2</sup>, K. Okumura<sup>1</sup>, P. Panuzzo<sup>1</sup>, and M. Sauvage<sup>1</sup><sup>1</sup> Laboratoire AIM, CEA/DSM - CNRS - Université Paris Diderot, Irfu/Service d'Astrophysique, CEA Saclay,  
91191 Gif-sur-Yvette, France  
e-mail: [diane.cormier@cea.fr](mailto:diane.cormier@cea.fr)<sup>2</sup> Max-Planck-Institut fuer extraterrestrische Physik, Postfach 1312, 85741 Garching, Germany

Received 31 March 2010 / Accepted 29 April 2010

**ABSTRACT**

We present *Herschel*/PACS spectroscopic maps of the dwarf galaxy NGC 4214 observed in 6 far infrared fine-structure lines: [C II] 158  $\mu\text{m}$ , [O III] 88  $\mu\text{m}$ , [O I] 63  $\mu\text{m}$ , [O I] 146  $\mu\text{m}$ , [N II] 122  $\mu\text{m}$ , and [N II] 205  $\mu\text{m}$ . The maps are sampled to the full telescope spatial resolution and reveal unprecedented detail on  $\sim 150$  pc size scales. We detect [C II] emission over the whole mapped area, [O III] being the most luminous FIR line. The ratio of [O III]/[C II] peaks at about 2 toward the sites of massive star formation, higher than ratios seen in dusty starburst galaxies. The [C II]/CO ratios are 20 000 to 70 000 toward the 2 massive clusters, which are at least an order of magnitude larger than spiral or dusty starbursts, and cannot be reconciled with single-slab PDR models. Toward the 2 massive star-forming regions, we find that  $L_{[\text{CII}]}$  is 0.5 to 0.8% of the  $L_{\text{TIR}}$ . All of the lines together contribute up to 2% of  $L_{\text{TIR}}$ . These extreme findings are a consequence of the lower metallicity and young, massive-star formation commonly found in dwarf galaxies. These conditions promote large-scale photodissociation into the molecular reservoir, which is evident in the FIR line ratios. This illustrates the necessity to move to multiphase models applicable to star-forming clusters or galaxies as a whole.

**Key words.** galaxies: ISM – galaxies: individual: NGC 4214 – ISM: line and bands – photon-dominated region (PDR) – galaxies: dwarf

**1. Introduction**

As building blocks of larger galaxies, dwarf galaxies in the early universe presumably played an important role in the evolution of galaxies we see today. Understanding how stars form and evolve under low metallicity conditions and the process of subsequent enrichment of the interstellar medium (ISM) will help us constrain possible scenarios of galaxy formation and evolution. The Local Group dwarf galaxies provide laboratories to study in detail the effects of the lower metal abundance on the process of star formation and the feedback on the ISM.

To examine the interplay between massive star formation and low metallicity ISM, we have mapped the far infrared (FIR) fine structure lines in the Local Group Magellanic-type irregular galaxy, NGC 4214, as part of the *Herschel* key proposal, SHINING (P.I. E. Sturm). NGC 4214 harbors 2 main star-forming complexes containing hundreds of O stars as well as a super star cluster (SSC). Our aim here is to characterise the physical conditions and the structure of the different phases of the ISM in NGC 4214. The proximity of NGC 4214 (2.9 Mpc, [Maíz-Apellániz et al. 2002](#)) and its low-metallicity ( $\log(\text{O}/\text{H}) + 12 = 8.2$ , [Kobulnicky & Skillman 1996](#)) make it a choice target. The PACS spectrometer onboard the *Herschel* Space Observatory allows us to zoom into the low-metallicity

photodissociation regions (PDRs) and their surroundings, tracing physical properties from 125 to 165 pc size scales.

The tools for this study are the FIR fine-structure lines arising from some of the most abundant species C, O, and N, which provide the most important cooling channels in the neutral and diffuse ionized ISM of galaxies. These lines trace H II regions and PDRs, which are neutral atomic and molecular regions where penetrating FUV photons ( $6 \text{ eV} < h\nu < 13.6 \text{ eV}$ ) dominate the energy balance and the chemical composition of the gas. Most of the ISM in galaxies is contained in PDRs. The FIR lines in combination with PDR models ([Tielens & Hollenbach 1985](#); [Wolfire et al. 1990](#); [Ferland et al. 1998](#); [Kaufman et al. 1999](#); [Abel et al. 2005](#); [Röllig et al. 2006](#)) can unveil the structure of these regions, which depends on both the strength of the FUV radiation field density ( $G_0$ ) illuminating the cloud and the hydrogen density ( $n_{\text{H}}$ ).

**2. Observations and data reduction**

We mapped the 6 FIR fine-structure lines, [C II] 158, [O III] 88, [O I] 63, [O I] 146, [N II] 122, and [N II] 205  $\mu\text{m}$ , using the PACS spectrometer ([Poglitsch et al. 2010](#)) on *Herschel* ([Pilbratt et al. 2010](#)). The PACS array consists of  $5 \times 5$  spatial pixels of  $9.4''$  size offering a total field-of-view of  $47''$  on the sky. Each spatial pixel covers 16 spectral elements with a spectral resolution ranging from 100 to 300  $\text{km s}^{-1}$ . The lines are not spectrally resolved for NGC 4214. The 6 lines were observed in raster mapping mode over a total of 15h during the science demonstration phase. The [O III] 88  $\mu\text{m}$  and [O I] 63  $\mu\text{m}$  (“blue”) were mapped

\* *Herschel* is an ESA space observatory with science instruments provided by European-led Principal Investigator consortia and with important participation from NASA.

A&amp;A 518, L57 (2010)

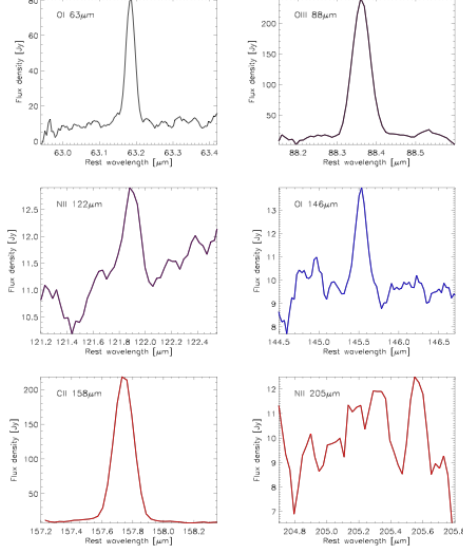


**Fig. 1.** Individual PACS spectral lines added up over the central raster. The lines are not spectrally resolved.

with  $5 \times 5$  rasters and the other lines (“red”) with  $3 \times 3$  rasters, all centered on 12h15m39.08s,+36d19m35.9s (J2000). Each raster pointing is separated by approximately half of the array ( $22''$ ,  $24''$ ) in the “red” range and approximately one third of the array ( $14.5''$ ,  $16''$ ) in the “blue” range, giving homogeneous coverage of the galaxy and a total field of view of  $1.6' \times 1.6'$ . We selected the chop-nod mode with a chop throw of  $6'$  off the source.

The data were reduced with the PACS spectrometer pipeline of the *Herschel* interactive processing environment (HIPE) v3.0.455. We show the 6 individual lines in Fig. 1. We fitted a spline plus Gaussian to the line and baseline and measured the  $1\sigma$  noise of the residual. In this way, we estimate the overall noise in the maps to be 0.17, 0.42, 0.27, 0.07, 0.06, and 0.30 Jy/pix for the [C II] 158  $\mu$ m, [O III] 88  $\mu$ m, [O I] 63  $\mu$ m, [O I] 146  $\mu$ m, [N II] 122  $\mu$ m, and [N II] 205  $\mu$ m lines, respectively. We applied a flat field correction and divided by calibration correction factors of 1.1 (“red”) and 1.3 (“blue”) to obtain the final reduced maps.

The rasters are combined by a drizzle scheme to produce final maps with  $4''$  grid pixel size for the [O III] and [O I] 63  $\mu$ m lines, and  $6''$  for the other lines. To compare the lines and create ratio maps, we scaled all maps down to the coarser resolution of  $6''$ . We analyze separately the whole map as well as three specific regions corresponding to NGC 4214-I (center), NGC 4214-II (southeast), and NGC 4214-III (northwest). These are represented by the red circles in Fig. 2a. Regions I and II are centered on the [C II] peaks, with radii encompassing most of the emission (at the level of  $\sim 50\%$  of the peak), while region III was chosen by taking into account the peak of the CO emission as well as the brightest counterpart of the [C II] emission ( $S/N \gtrsim 15$ ), which is truncated by the map edge.

### 3. Results

The *Herschel*/PACS maps clearly resolve the two star-forming regions NGC 4214-I and NGC 4214-II, where most of the emission originates. The [N II] 122  $\mu$ m emission is rather faint and the

**Table 1.** FIR line ratios.

NGC 4214	total	I	II	III
RA [J2000]	12 15 39.1	12 15 39.1	12 15 40.5	12 15 36.7
Dec [J2000]	+36 19 35.9	+36 19 35.9	+36 19 05.9	+36 20 01.0
Aperture ( $''$ )	—	18	12	9
Quantity	Line ratios			
$f_{\text{[OIII]}}/f_{\text{[CII]}}$	0.996 (0.009)	1.40 (0.007)	1.71 (0.014)	0.264 (0.053)
$f_{\text{[O I]146}}/f_{\text{[O I]63}}$	0.058 (0.015)	0.060 (0.011)	0.072 (0.023)	— (0.095)
$f_{\text{[O I]63}}/f_{\text{[CII]}}$	0.445 (0.007)	0.474 (0.004)	0.560 (0.008)	0.438 (0.035)
$f_{\text{[O I]146}}/f_{\text{[CII]}}$	0.026 (0.007)	0.028 (0.005)	0.040 (0.013)	— (0.042)
$L_{\text{TIR}} [10^7 L_{\odot}]$	37.7	8.60	4.52	0.522
$10^{-3} L_{\text{[O I]63}} + L_{\text{[CII]}} / L_{\text{TIR}}$	2.77	8.11	6.50	11.1
$10^{-3} L_{\text{[CII]}} / L_{\text{TIR}}$	5.30	7.93	5.71	7.70
$10^3 L_{\text{[CII]}} / L_{\text{CO}}$	33.8	75.0	22.9	4.73

[N II] 205  $\mu$ m is not detected. The most prominent lines are the [C II] 158  $\mu$ m, [O III] 88  $\mu$ m, [O I] 63  $\mu$ m, and, to a lesser extent, the [O I] 146  $\mu$ m and [N II] 122  $\mu$ m lines. The emission from the [C II] line is the most extended of all of the lines (Fig. 2a) and covers the entire map. The total [C II] luminosity in the PACS map is  $2.0 \times 10^6 L_{\odot}$  with about 50% of the emission originating in the two bright star-forming sites and 50% in the surrounding medium. The [C II] 158  $\mu$ m line is known to be one of the most important tracers of physical conditions in PDRs because it is so luminous and has a low critical density for collisional excitation.

Comparing the [C II] and [O I] 63  $\mu$ m line emission, we find that the latter is a factor of two weaker integrated over the mapped region. These two lines show a very similar distribution (Fig. 2b), both peaking at the 2 star-forming sites and spanning a small range of ratios. These ratios vary by less than a factor of two across the entire map. The [C II] line, in principle, may originate in the PDR and the diffuse media alike. The observed resemblance between the [O I] 63  $\mu$ m and [C II] maps (Fig. 2b) suggests that the [C II] is dominated by the PDR component (see also Sect. 3.1).

The [O I] 146  $\mu$ m line is fainter than the [O I] 63  $\mu$ m line, and is barely detected in the outer regions of the map. Toward the 2 peaks, and in total, the ratios of the two [O I] lines are about 0.06 (Table 1), and do not vary much across the map. These ratios are insensitive to density since their critical densities are not very different. For moderate densities ( $n < 10^5 \text{ cm}^{-3}$ ), this ratio is more indicative of the gas temperature.

The [O III] 88  $\mu$ m line is the brightest of all lines observed in NGC 4214 (Fig. 2c). A comparison of the [O III] line map with the *HST* optical images of NGC 4214 (Úbeda et al. 2007), illustrates that it coincides with the star formation sites and exhibits a peak toward the position of the SSC in NGC 4214-I, thus tracing the ionization source. High ratios of [O III] to [C II] observed here (Table 1) are not commonly seen in dusty starbursts or spiral galaxies (Negishi et al. 2001; Malhotra et al. 2001), an example being M82 with a ratio of  $\sim 0.7$ . However, high ratios have been observed in the *ISO* observations of dwarf galaxies and may be explained by hot stars surrounded by optically thick PDRs (Hunter et al. 2001). The [O III] / [C II] ratio map of NGC 4214 (Fig. 2d) exhibits peaks in intensity toward the 2 star-forming sites but drops off rapidly away from the peaks. We note that the peaks of the [O III] / [C II] ratio map appear to be offset from those of the [C II] by  $\sim 6''$ , which is larger than the expected relative pointing uncertainty (on the order of several arcsecs).



D. Cormier et al.: The effects of star formation on the low-metallicity ISM

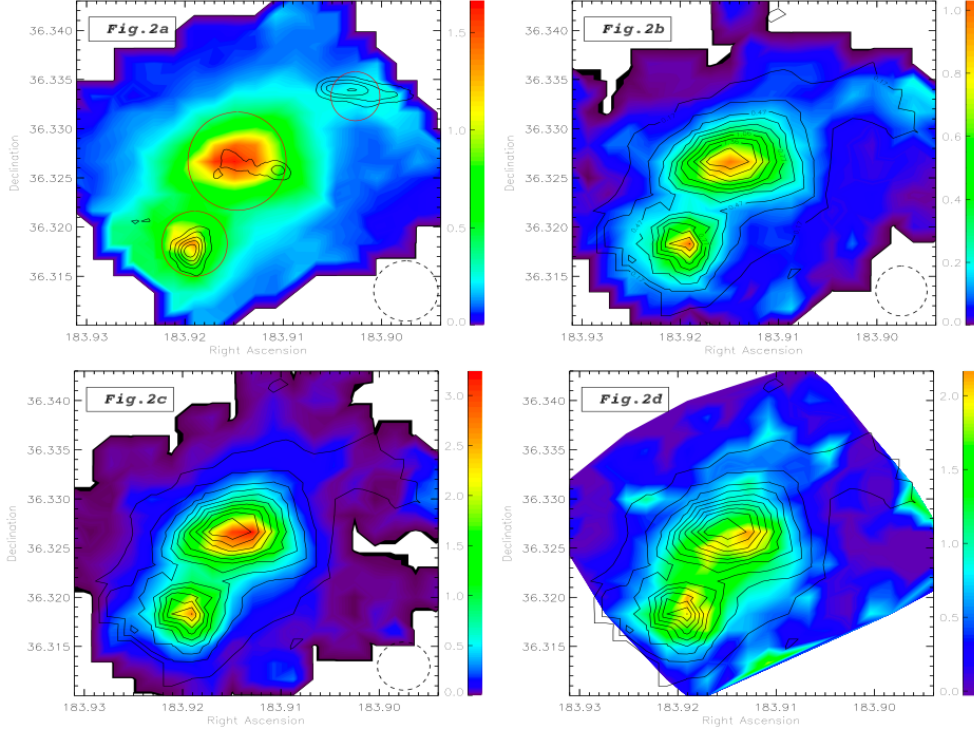


**Fig. 2.** PACS spectral maps of NGC 4214. **a)** PACS map of the [C II] 158  $\mu\text{m}$  line with CO(1–0) contours (Walter et al. 2001). The total field of view is  $1.6' \times 1.6'$  with a grid resolution of  $6''$ . The red circles show the positions and sizes of the 3 regions we study in more detail: NGC 4214-I (center –  $36''$  diameter), NGC 4214-II (southeast –  $24''$ ), and NGC 4214-III (northwest –  $18''$ ). The dotted circle on the lower right corner represents the PACS beam size of  $9.4'' \times 9.1''$  at  $62 \mu\text{m}$ ,  $9.6'' \times 8.8''$  at  $90 \mu\text{m}$ , and  $11.8'' \times 11.0''$  at  $154 \mu\text{m}$ . **b)** PACS map of the [O I] 63  $\mu\text{m}$  line with [C II] 158  $\mu\text{m}$  contours. **c)** PACS map of the [O III] 88  $\mu\text{m}$  line with [C II] 158  $\mu\text{m}$  contours. **d)** Ratio map of [O III] 88  $\mu\text{m}$ /[C II] with [C II] contours. Units for the color bars are  $10^{-16} \text{ W m}^{-2} \text{ grid pix}^{-1}$ . The [C II] contours begin at  $0.17 \times 10^{-16} \text{ W m}^{-2}$  (above  $15\sigma$ ) and are linearly spaced up to the peak of  $1.66 \times 10^{-16} \text{ W m}^{-2}$ .

The shift in the [O III] / [C II] peak, corresponding to a shift of  $\sim 80 \text{ pc}$ , if real, implies that the ratio peak coincides with the SSC peak, the probable source of the ionization. Since  $\text{O}^{++}$  has an ionization potential of  $35.1 \text{ eV}$ , [O III] traces the highly ionized medium around early O stars and is thus more confined than the [C II] emission. This is consistent with the AKARI findings that the [O III] 88  $\mu\text{m}$  line traces excitation sources even more accurately than the radio continuum (Okada et al. 2010).

We show the CO contours from Walter et al. (2001) in Fig. 2a. There is a striking distinction between the three different regions in terms of [C II]/CO (Table 1). NGC 4214-III probably hosts little star formation, which explains its paucity in excited FIR line emission compared to its molecular reservoir. However, even the two main regions of active star formation exhibit very different [C II]/CO ratios. One explanation of these high [C II]/CO ratios is the presence of small clumps of CO embedded in large PDR envelopes. Applying this interpretation to these observations would imply that the star formation in the central region of NGC 4214-I has (already) affected (photodissociated) most of the surrounding molecular reservoir, while many of the molecular clouds in the south eastern region are relatively unscathed. It is interesting to remark that NGC 4214-II has a younger stellar population than NGC 4214-I (Úbeda et al. 2007).

Using *Spitzer* data, we estimate the total infrared luminosity ( $L_{\text{TIR}}$ ) over the area mapped with PACS, following

Dale & Helou (2002) (see Table 1). The [C II] line alone accounts for  $\sim 0.5\%$  of the  $L_{\text{TIR}}$ <sup>1</sup>, which is at the high end of the range of normal galaxies and starburst galaxies (Stacey et al. 1991; Negishi et al. 2001) and more typical of the elevated ratios seen in dwarf galaxies (Madden 2000; Hunter et al. 2001). Toward the two bright star-forming regions,  $L_{[\text{CII}]} / L_{\text{TIR}}$  is similar to 30 Dor in the LMC (Poglitsch et al. 1995; Rubin et al. 2009). Likewise,  $L_{[\text{OIII}]} / L_{\text{TIR}}$  either toward these 2 prominent star-forming regions or over the entire galaxy is an order of magnitude higher than what Negishi et al. (2001) find for normal and starburst galaxies. The FIR lines of the 2 star-forming regions contribute all together up to about 2% of their TIR flux.

### 3.1. Origin of the [C II] line

Before we can consider PDR model solutions to the observations, we consider the origin of the  $\text{C}^+$  line, which is most often used as a diagnostic of PDR conditions because it is a primary coolant in PDRs. However, since the ionization potential of carbon ( $11.3 \text{ eV}$ ) is less than that of hydrogen,  $\text{C}^+$  can exist in both the ionized and neutral gas. In galactic nuclei, most of the [C II] emission arises from the PDRs (Stacey et al. 1991;

<sup>1</sup> To compare ratios using  $L_{\text{FIR}}$  in the literature, for dwarf galaxies (Hunter et al. 2001),  $L_{\text{TIR}}$  is approximately a factor of 2 greater than  $L_{\text{FIR}}$ , as defined by IRAS 60 and  $100 \mu\text{m}$  fluxes (Helou et al. 1988).

A&amp;A 518, L57 (2010)

Negishi et al. 2001). With an ionization potential of 14.53 eV, the  $N^+$  emission originates only from the H II regions. Therefore we use the [N II] line to correct for a possible contribution of the ionized gas to the  $C^+$  line.

The [N II] 205  $\mu$ m line was not confidently detected and could not be analyzed but the [N II] 122  $\mu$ m line is detected in the two star-forming regions. We see evidence of [N II] 122  $\mu$ m emission over the central  $3 \times 3$  pixels in each region and average them to obtain a higher signal-to-noise ratio and measure the intensity of the line in these two regions. The observed ratios of the [N II] 122  $\mu$ m/[C II] 158  $\mu$ m are 0.04 and 0.03 in NGC 4214-I and NGC 4214-II, respectively. Following Malhotra et al. (2001), we estimate a maximum contribution of the ionized medium to the [C II] emission to be a factor of 11 times the flux of the [N II] 122  $\mu$ m. Therefore, at least 60% of the [C II] emission originates in PDRs. To bound the physical conditions in NGC 4214, we model the PDR (see Sect. 3.2) assuming that all [C II] emission is from PDRs and that only 60% originates in PDRs.

### 3.2. Results from PDR models

As a first diagnostic of PDR properties, we use the model of Kaufman et al. (1999) by means of the web interface of the PDR Toolbox<sup>2</sup>. This model, which assumes solar metallicity, calculates the intensity of the main PDR lines as a function of the physical conditions, which are the incident radiation field ( $G_0$ ) and the density ( $n_H$ ). We can compare our observed line intensities to the model predictions to narrow down the range of the physical conditions.

We use [O I] 63  $\mu$ m/[C II], [O I] 146  $\mu$ m/[C II], [O I] 146  $\mu$ m/[O I] 63  $\mu$ m, and the ([C II]+[O I] 63  $\mu$ m)/ $I_{TIR}$  and [C II]/CO (Table 1). The ratio ([C II]+[O I] 63  $\mu$ m)/ $I_{TIR}$  is interesting because it relates the “total” cooling of the gas to the total cooling by the dust, so measures the efficiency of the dust to heat the gas (photoelectric efficiency). The observed [C II]/CO ratio disagrees significantly with those predicted by the best-fit solution for all the other line ratios. This has been noted before for other low metallicity PDRs (see Sect. 3.3) and may be a geometry or low metallicity effect not taken into account in the model. Using all the above line ratios except [C II]/CO, the maximum values found for NGC 4214-I are  $G_0^3 \sim 800$  and  $n_H \sim 2000$ . For NGC 4214-II, we find that  $G_0 \sim 1000$  and  $n_H \sim 3000$ . The solution for the third region NGC 4214-III infers a lower incident radiation field ( $G_0 \lesssim 100$ ). The quoted values above take into account the contribution to the [C II] intensity of the ionized medium between 0 and 40%. In all cases, these PDR parameters are indicative of a relatively moderate gas density and radiation field.

### 3.3. [C II]-to-CO ratio

We measure [C II]/CO intensity ratios of 70 000 and 20 000 for NGC 4214-I and II, respectively (Table 1). These values are at least an order of magnitude higher than those inferred for spiral or starburst galaxies (Stacey et al. 1991; Negishi et al. 2001) but in closer agreement with those of dwarf galaxies (Poglitsch et al. 1995; Madden et al. 1997; Hunter et al. 2001). NGC 4214-I has a [C II]/CO similar to 30 Dor (Poglitsch et al. 1995; Rubin et al. 2009). This high ratio could be explained by the paucity of dust; less dust shielding allows the photodissociating FUV photons to penetrate deeper into the cloud, reducing the size of

the CO cores while leaving a large [C II]-emitting envelope. This envelope may well contain self-shielded molecular hydrogen. If this were true, the [C II] would be a more accurate tracer of the molecular reservoirs in low metallicity environments than CO.

## 4. Conclusion

These observations of NGC 4214 with *Herschel*/PACS have enabled us to spatially resolve the FIR fine-structure lines in the low metallicity dwarf galaxy NGC 4214. A very striking result from the mapping is the brightness of the [C II] 158  $\mu$ m, [O I] 63  $\mu$ m, and the [O III] 88  $\mu$ m lines. The [C II] alone corresponds to 0.5% of the total infrared luminosity. The combined luminosity of the FIR lines reaches 2% of the  $L_{TIR}$ . The [O III] 88  $\mu$ m line is more confined to star-forming regions and the [O III]/[C II] reaches almost a factor of 2 close to the SSC in NGC 4214-I.

The [C II]/CO ratios are also exceptionally high (20 000–70 000). These extreme ratios are indicative of an ISM that is strongly affected by photodissociation and reflect the combined effects of low metallicity ISM and intense star formation. It should be borne in mind that, when comparing with models, the models predict line ratios for a single, homogeneous PDR. In reality, we observe a multiphase medium that probably harbors many extremely different PDR conditions. Therefore, this preliminary comparison indicates the need for more complete (complex) models to be able to derive accurate physical quantities.

*Acknowledgements.* We would like to thank the referee for suggestions that improved this letter. Many thanks to Fabian Walter for sharing his valuable CO data with us, and Leonardo Úbeda for his HST images for us to compare with. We are also extremely grateful for the help of the PACS ICC and *Herschel* Science Centre. PACS has been developed by a consortium of institutes led by MPE (Germany) and including UVIE (Austria); KU Leuven, CSL, IMEC (Belgium); CEA, LAM (France); MPIA (Germany); INAF-IFSI/OAA/OAP/OAT, LENS, SISSA (Italy); IAC (Spain). This development has been supported by the funding agencies BMVIT (Austria), ESA-PRODEX (Belgium), CEA/CNRS (France), DLR (Germany), ASI/INAF (Italy), and CICYT/MCYT (Spain).

## References

- Abel, N. P., Ferland, G. J., Shaw, G., & van Hoof, P. A. M. 2005, *ApJS*, 161, 65
- Dale, D. A., & Helou, G. 2002, *ApJ*, 576, 159
- Ferland, G. J., Korista, K. T., Verner, D. A., et al. 1998, *PASP*, 110, 761
- Helou, G., Khan, I. R., Malek, L., & Boehmer, L. 1988, *ApJS*, 68, 151
- Hunter, D. A., Kaufman, M., Hollenbach, D. J., et al. 2001, *ApJ*, 553, 121
- Kaufman, M. J., Wolfire, M. G., Hollenbach, D. J., & Luhman, M. L. 1999, *ApJ*, 527, 795
- Kobulnicky, H. A., & Skillman, E. D. 1996, *ApJ*, 471, 211
- Madden, S. C. 2000, *New Astron. Rev.*, 44, 249
- Madden, S. C., Poglitsch, A., Geis, N., Stacey, G. J., & Townes, C. H. 1997, *ApJ*, 483, 200
- Maíz-Apellániz, J., Cieza, L., & MacKenty, J. W. 2002, *AJ*, 123, 1307
- Malhotra, S., Kaufman, M. J., Hollenbach, D., et al. 2001, *ApJ*, 561, 766
- Negishi, T., Onaka, T., Chan, K., & Roellig, T. L. 2001, *A&A*, 375, 566
- Okada, Y., Kawada, M., Murakami, N., et al. 2010, *A&A*, 514, A13
- Pilbratt, G. L., et al. 2010, *A&A*, 518, L1
- Poglitsch, A., Krabbe, A., Madden, S. C., et al. 1995, *ApJ*, 454, 293
- Poglitsch, A., et al. 2010, *A&A*, 518, L2
- Röllig, M., Ossenkopf, V., Jeyakumar, S., Stutzki, J., & Sternberg, A. 2006, *A&A*, 451, 917
- Rubin, D., Hony, S., Madden, S. C., et al. 2009, *A&A*, 494, 647
- Stacey, G. J., Geis, N., Genzel, R., et al. 1991, *ApJ*, 373, 423
- Tielens, A. G. G. M., & Hollenbach, D. 1985, *ApJ*, 291, 722
- Úbeda, L., Maíz-Apellániz, J., & MacKenty, J. W. 2007, *AJ*, 133, 917
- Walter, F., Taylor, C. L., Hüttemeister, S., Scoville, N., & McIntyre, V. 2001, *AJ*, 121, 727
- Wolfire, M. G., Tielens, A. G. G. M., & Hollenbach, D. 1990, *ApJ*, 358, 116

<sup>2</sup> <http://dustem.astro.umd.edu/pdrt/index.html>

<sup>3</sup> In units of Habing field:  $1.6 \times 10^{-3}$  erg cm<sup>-2</sup> s<sup>-1</sup>.

## Chapter 4

# Modeling the Interstellar Medium of Dwarf Galaxies

### Contents

---

<b>4.1</b>	<b>Modeling State of the Art . . . . .</b>	<b>88</b>
4.1.1	From LTE to radiative transfer . . . . .	88
4.1.2	Existing PDR models and specific use . . . . .	91
<b>4.2</b>	<b>A multi-phase picture of the Interstellar Medium of Haro 11 . . . . .</b>	<b>93</b>
4.2.1	Description of the method . . . . .	93
4.2.2	Paper accepted in A&A, August 28 2012 . . . . .	96

---



## 4.1 Modeling State of the Art

### 4.1.1 From LTE to radiative transfer

#### Radiative transfer formalism

The intention of modeling line observations is not to describe the exact structure of the emitting regions, which is anyway unknown for the majority of our dwarf galaxies, except e.g. the Magellanic Clouds (the distance from the exciting star to the cloud, and the size of the cloud can be the limiting factors in resolved cases), but rather to uncover the physical conditions of the gas.

Observed spectra are the result of the transport of radiation through the emitting cloud with depth-dependent physical conditions. These conditions (essentially the gas temperature and density) are governed by local processes that set the ionisation distribution, level populations, the electron/gas temperature, and hence the energy balance. The gas kinetic temperature is determined by the balance between heating and cooling processes. The important heating and cooling processes in each ISM phase are outlined in Section 1.2, including ionisation, recombination, and collisional processes. The level of ionisation is set by the balance of ionisation and recombination processes.

The radiation is continuously absorbed, emitted, and scattered through the medium. Considering the specific intensity,  $I_\nu$ , the general form of the radiative transfer equation is:

$$\frac{dI_\nu}{ds} = -(\alpha_\nu + \sigma_\nu)I_\nu + j_\nu + \sigma_\nu J_\nu, \text{ and } J_\nu = \frac{1}{4\pi} \int I_\nu d\Omega \quad (4.1)$$

where  $j_\nu$  is the emission coefficient,  $\alpha_\nu$  is the absorption coefficient, related to the cross section of the particle,  $\sigma_\nu$  is the scattering coefficient.  $J_\nu$  is the mean intensity of the radiation field, averaged over all directions. *Ignoring scattering* ( $\sigma_\nu = 0$ ), the coefficients are combined in the source function  $S_\nu = j_\nu/\alpha_\nu$ , taken as the locally produced emission. For local emission between two levels  $u$  (upper) and  $l$  (lower), those emission and absorption coefficients are directly related to the Einstein coefficients of spontaneous emission,  $A_{ul}$ , and absorption and stimulated emission,  $B_{ul}$ , via:

$$\begin{aligned} j_\nu &= \frac{h\nu}{4\pi} n_u A_{ul} \Phi_\nu, \\ \alpha_\nu &= \frac{h\nu}{4\pi} (n_l B_{lu} - n_u B_{ul}) \Phi_\nu \\ \text{hence, } S_\nu &= \frac{n_u A_{ul}}{n_l B_{lu} - n_u B_{ul}} \end{aligned}$$

$n_u$  and  $n_l$  are the densities of atoms in the upper and lower levels.  $\phi_\nu$  is the line profile, assumed to be the same for emission and absorption. Given the optical depth  $\tau_\nu = \int \alpha_\nu ds$ , formal solutions of the radiative transfer equation are of the form:

$$I_\nu(\tau_\nu) = I_\nu(0)e^{-\tau_\nu} + \int S_\nu \tau'_\nu e^{-(\tau_\nu - \tau'_\nu)} d\tau'_\nu \quad (4.2)$$

with  $I_\nu(0)$  the background radiation. Solving for the radiative transfer often comes down to solving for the source function  $S_\nu$ .

The energy transfer, from the source of excitation to the observed side of the region, gives the predicted line intensities. General methods assume the region to be a slab or sphere, and

divide it in zones, with a small step for the conditions not to vary significantly. The position in the cloud can be tracked with  $\tau_{depth}$  or  $A_V$ , which increase as a function of depth into the cloud, as the impact of the source radiation becomes weaker.

Radiation affects level populations, resulting in a coupling of radiative transfer and statistical equilibrium. For a two-level system with levels  $u$  and  $l$  in a steady-state regime, the statistical equilibrium equations can be written as:

$$\frac{dn_u}{dt} = \frac{dn_l}{dt} = 0 \Rightarrow n_u(B_{ul}\bar{J} + C_{ul}) = n_l(A_{lu} + B_{lu}\bar{J} + C_{lu}), \text{ and } \bar{J} = \int J_\nu \Phi_\nu d\nu, \quad (4.3)$$

where  $n_u$  and  $n_l$  are the densities of atoms in the upper and lower levels.  $C_{ul}$  is the collisional rate coefficients. This relates the radiative and collisional processes that populate level  $u$  that are balanced by the processes that depopulate level  $l$ . This two-level system is a limiting case to a more general steady-state condition where all excitation processes balance all de-excitation processes.

## Methods

Several tools, with gradients in complexity, are available to interpret emission line observations. The coupled equations describing statistical equilibrium and radiative transfer, make the radiative transfer problem cumbersome to solve for. One can make assumptions to get around this, to simplify the problem and find a simple solution.

A first common approximation is to assume Local Thermodynamic Equilibrium (LTE), in which excitation temperature,  $T_{ex}$ , and kinetic temperature,  $T_{kin}$ , are equal. The Planck function describes the radiation field of a black-body expressed as:

$$B_\nu(T) = \frac{2h\nu^3}{c^2} \frac{1}{e^{h\nu/kT} - 1} \quad (4.4)$$

$h$  is the Planck constant and  $k$  the Boltzmann constant. In LTE, the state of the gas depends only on the temperature and density. The gas is described by a single temperature with  $\bar{J} = S_\nu = B_\nu(T)$ . Statistical distribution of particles in thermal equilibrium is described, for a two-level system with levels  $u$  and  $l$ , by the Boltzmann distribution:

$$\frac{n_u}{n_l} = \frac{g_u}{g_l} e^{\frac{-h\nu_{ul}}{kT_{ex}}} = \frac{g_u}{g_l} e^{\frac{-(E_u - E_l)}{kT_{ex}}}, \quad (4.5)$$

where  $g_u$  and  $g_l$  are the statistical weights of the upper and lower levels, and  $T_{ex}$  is the excitation temperature governing the population between levels  $u$  and  $l$ . More generally, relative to the total number of particles, the level population of level  $u$  is thus simplified to:

$$N_u/N_{tot} = g_u \exp(-E_u/kT_{ex}) Z(T_{ex}) \quad (4.6)$$

$N_u$  and  $N_{tot}$  are the column densities of the level  $u$  and of all levels (total), and  $Z(T)$  is the partition function equal to  $Z(T) = \sum_u g_u \exp(-E_u/kT)$ . There is detailed balance in the collisional processes and radiative processes. Hence, when few lines are observed, a single temperature directly solves for the column density. When observing more lines, one can build a rotation diagram (see Section 5.3.1 for more details) and solve simultaneously for  $T_{ex}$  and  $N_{tot}$ , where excitation and kinetic temperatures can depart (especially true at low densities).

The LTE approach often holds at high densities where collisional excitations/de-excitations

dominate. The local optical depths are large and photons do not escape, hence the radiation field approaches locally  $B_\nu(T)$ . However, under several typical conditions, the LTE approximation can be too crude to yield accurate predictions.

A second common step to simplify the radiative transfer problem, is to include absorption and optical depth effects, which are important for collisional excitation/de-excitation, in, e.g., the escape probability method. Such methods are more satisfactory in optically thick regimes. This is introduced in an approach to a molecular cloud analysis by Goldreich & Kwan (1974), and is now widely used in codes such as RADEX (van der Tak et al. 2007a; code publicly available) for simple molecular lines modeling (see Section 5.2.3). Escape probability,  $\beta(\tau)$ , is based on the fact that photons produced locally can only be absorbed locally. The gas is thus described with  $\bar{J} = S_\nu(1 - \beta)$ , which decouples statistical equilibrium from radiative transfer equations. Einstein coefficients  $A_{ul}$  and  $B_{ul}$  enter in the statistical equilibrium.

The escape probability,  $\beta$ , is a function of  $\tau$  given, for an expanding sphere, as:  $\beta = \frac{1-e^{-\tau}}{\tau}$ . In that case, the Doppler shift between particles at the center and particles at outer radii reduces the probability of an absorption in the expanding sphere. The sphere is transparent for photons emitted at the center and thus decouples radiation from matter. This is the Sobolev approximation (Sobolev & Gaposchkin 1960) or Large Velocity Gradient (LVG).

The optical depth is expressed as:

$$\tau = \frac{c^3}{8\pi\nu_{ul}} \frac{A_{ul}N_{tot}}{V_D} \left[ n_l \frac{g_u}{g_l} - n_u \right], \quad (4.7)$$

where  $V_D$  is the Doppler width.

Once solving for the radiative transfer and level population, one can get to the observed line intensities, by subtracting the background contribution measured outside the line ( $I_\nu^{background}$ ) from the total contribution to the observed line intensity ( $I_\nu^{total}$ ):

$$\Delta I_\nu = I_\nu^{total} - I_\nu^{background} = (B_\nu(T_{ex}) - I_\nu^{background})(1 - e^{-\tau_0}) = \frac{2k\nu^2 T_R}{c^2}, \quad (4.8)$$

where  $T_R$  is the radiation temperature, the temperature for which the Planck function, expressed in the Rayleigh-Jeans limit ( $h\nu \ll kT$ ), would give the observed intensity  $\Delta I_\nu$ .

More sophisticated methods, such as full radiative transfer or spectral synthesis codes, leave the local approximation and consider quantities as a function of cloud depth. These methods rely on complete atomic and molecular databases, including knowledge of energy levels, transition probabilities, collision strengths, excitation, absorption rates, opacities, etc.

A choice of initial conditions and geometry need to be specified. We detail these parameters further in the next section. At each step into the cloud, the chemistry, level populations, thermal balance, and radiative transfer are solved. A steady state cloud is usually assumed. Since these steps are dependent on each other, iterations are necessary. This is particularly the case for the radiative transfer in models with finite geometry and backward radiation. Integrated and emergent properties can then be derived. Physical quantities are presumed to vary smoothly in the cloud, and adaptative steps can be used for discontinuities. Detailed chemistries (gas-phase and grain-surface) with formation and destruction of species, as well as ionisation balance, are taken into account. Levels of reactions (mainly involving two species) or heating and cooling processes can differ between various codes. The inclusion of

grains and PAHs is essential for the heating (photoelectric effect, essentially), the extinction (absorption and scattering coefficients) and subsequent radiative transfer, and the chemistry as hosts of molecule formation.

For the physics and chemistry in the H II region, CLOUDY and MAPPINGS-III are often used. MAPPINGS-III is a shock and photoionisation code available through a library of models (Allen et al. 2008). Beyond the H II region, the radiative transfer affects the PDR/molecular cloud (see Section 1.2). PDR codes compute the structure, state, and conditions of neutral atomic/molecular interstellar clouds. PDR physics and chemistry are often treated separately from the photoionisation region (except, e.g. CLOUDY). Examples of PDR models (including CLOUDY) are outlined in the next section. Meijerink & Spaans (2005) present grids of PDR and XDR models for PDR and molecular lines. RATRAN (Hogerheijde & van der Tak 2000), which employs a Monte Carlo method, is also useful for molecular lines.

#### 4.1.2 Existing PDR models and specific use

Several PDR codes are widely used by the community. Those that I have used for my thesis are the following: CLOUDY, PDR TOOLBOX, KOSMA- $\tau$ , and the MEUDON code. A PDR benchmark study is presented in Röllig et al. (2007) to compare code results, with a specific focus on the C<sup>+</sup>/C/CO transition and H<sub>2</sub> formation.

The main parameters to set in a PDR model are:

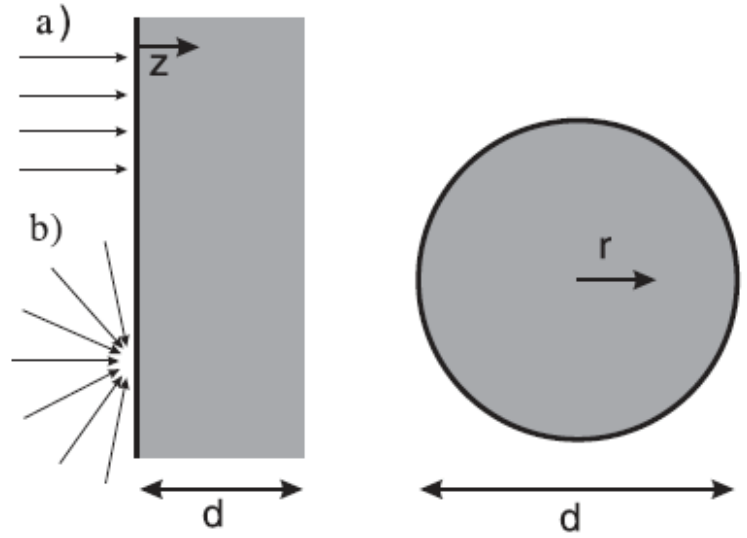
- the radiation field (shape and strength);
- the gas and grain abundances;
- the gas density  $n_H$ ;
- the cloud geometry;
- the velocity structure (thermal and possibly turbulent);
- a stopping criterion;

One or several parameters can be fixed depending on the code used. Other free parameters can also be specified (e.g. type and size distribution of grains, additional exciting sources...). Two types of geometries are usually used: spherical cloud or plane-parallel slab, with internal/external, isotropic/uni-directed illumination (see Figure 4.1).

#### PDR Toolbox

The PDR TOOLBOX was developed by Michael Kaufman and the code is described in Kaufman et al. (1999, 2006). Model grids and a line ratio fitting program are available through the web interface <http://dustem.astro.umd.edu/pdrt/index.html>. Contour plots in  $G_0 - n_H$  space are available for many PDR lines: [C II], [O I], [Si II], [Fe II], [C I], H<sub>2</sub>, CO, as well as  $L_{TIR}$ . Standard parameters with plane-parallel geometry are used for those grids (abundances, grain properties fixed with metallicity 1  $Z_\odot$  or 3  $Z_\odot$ , turbulent Doppler velocity of 1.5 km s<sup>-1</sup> added). The radiation field is a scaling of the Galactic interstellar radiation field.

**Figure 4.1.** Possible cloud geometries in PDR models: plane-parallel or spherical cloud with isotropic (a)/uni-directed (b) illumination from one or both sides or the cloud; taken from Röllig et al. (2007).



### Meudon PDR code

The code is described in Le Petit et al. (2006). Model grids are available through the web interface <http://pdr.obspm.fr/PDRcode.html> but the code is also publicly available for download. The geometry is a plane parallel slab, either finite or semi-infinite depending on the radiation field configuration. Detailed micro-physical processes are taken into account, especially in the  $H_2$  treatment. The incident radiation field can be defined by the interstellar radiation field (isotropic), and/or an input stellar spectrum (uni-directed), on both sides of the cloud. The gas density can be constant, user-defined with an input profile, or governed by the ideal gas law in the isobaric case. The MEUDON PDR code is suited for both diffuse and dark cloud modeling.

### Kosma- $\tau$

The KOSMA- $\tau$  model is described in Röllig et al. (2006a). One of the specificities of this model is that it simulates a clump geometry with spherical clouds illuminated by an external isotropic radiation. Model grids are available through the web interface <http://hera.ph1.uni-koeln.de/~pdr/> with predictions of line ratios of [C II], [O I], [C I], and CO. These are computed in a 4-parameter space: radiation field, cloud density, metallicity, and clump mass. The radiation field is a scaling of the Galactic interstellar radiation field. All other parameters are otherwise fixed.

### Cloudy

CLOUDY is described in Ferland et al. (1998) and Abel et al. (2005). Model grids of H II and PDR lines are shown in Abel et al. (2005). The code is available for download <http://www.nublado.org/>. CLOUDY is a very versatile photoionisation and PDR code. The geometry is 1D spherical but can be made effectively plane-parallel (with a large radius from the illuminating source to the cloud compared to the cloud thickness). Open and closed geometries are possible by changing the covering factor of the cloud (in which case part of the input radiation is directly transmitted to the observer). For a sphere, the illumination is internal and isotropic. The radiation field can be scaled to the Galactic interstellar radiation field (isotropic), or a stellar spectrum (uni-directed with a chosen illumination angle) from

a stellar library or STARBURST99 (Leitherer et al. 2010), AGN continuum, a user-defined spectrum, etc., with as many energy sources entered as needed (at the same position relative to the cloud). Similarly, the density can be constant, user-defined with an input profile, or govern by the ideal gas law in the isobaric or isothermal case. With such flexibility, CLOUDY is suited for many kinds of environments, extreme to more quiescent, H II regions, planetary nebulae, PDRs, diffuse clouds, etc. It is often used to model extragalactic objects, as in, e.g., Abel et al. (2009); Graciá-Carpio et al. (2011a); Lebouteiller et al. (2012).

The main advantage of CLOUDY is that it treats both the ionised and neutral gas, and the radiative transfer between the two phases. For example, to interpret PDR lines, and particularly [C II] which can arise not only from the PDR that is usually pressured, but also from the diffuse ionised gas, it is necessary to correct for this possible contribution from the ionised gas using e.g. CLOUDY. Since our dataset of *Herschel* lines contain both ionised and neutral gas tracers, we have chosen to use CLOUDY for the ISM modeling of dwarf galaxies for that purpose.

## 4.2 A multi-phase picture of the Interstellar Medium of Haro 11

### 4.2.1 Description of the method

In order to relate the *Herschel* observations of the dwarf galaxies to the state of the gas in a more accurate way than analysing empirical trends as done in Section 3.2, we have decided to make use of PDR models. The application of a PDR model to observations in a self-consistent way is a long process given the degrees of freedom in setting the input parameters of the model. To test the limits of our full dataset, we have modeled one galaxy of the DGS: Haro 11, using 17 MIR and FIR fine-structure lines.

The choice of Haro 11 is based on the fact that it is the most luminous galaxy of the DGS ( $L_{\text{TIR}} \sim 2 \times 10^{11} L_{\odot}$ ), 7 lines were observed with PACS and 6 well detected (see Appendix B, p. 169), and there are exhaustive ancillary data (UV, optical, and IR) available, including high S/N *Spitzer*/IRS spectra that give us the MIR fine-structure and molecular lines, which allow together for a multi-wavelength and multi-phase approach.

The aim of this work is to model the suite of 17 *Spitzer*/MIR and *Herschel*/FIR lines which are little affected by dust extinction and hence less sensitive to geometrical assumptions. As those lines originate from both the ionised and the neutral ISM phases, we have chosen to use the code CLOUDY to treat both the photoionisation and the PDR regions. The analysis is presented in the A&A paper, “*A multiphase picture of the interstellar medium of Haro 11: a model of the infrared emission*”, Cormier et al. (2012a), that can be found in Section 4.2.2.

### Cloud conditions with Cloudy

Contrary to the other codes for which the radiation field illuminating the PDR needs to be input (FUV field), the radiation field in CLOUDY is directly constrained from the stellar population, which is well studied (and usually better known). The radiative transfer through the ionised phase (in the Strömgren sphere) then sets the radiation field at the illuminated front of the PDR (ionisation front).

The choice of initial conditions (stellar library, abundances, grain properties) is detailed in the paper (Section 3.3). Since Haro 11 is not resolved in the MIR-FIR, we are only interested in the integrated properties and thus work in luminosity convention (for which a distance of



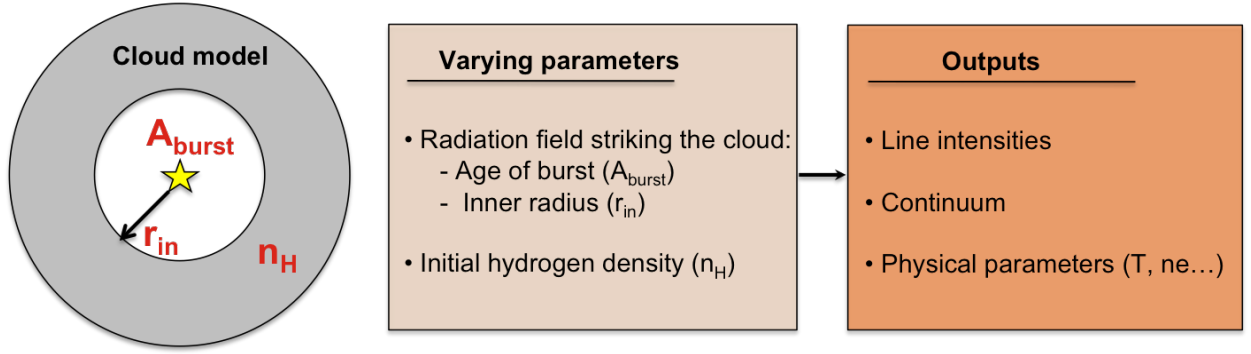


**Figure 4.2.** Varying input and output parameters of the CLOUDY models.

the energy source to the cloud  $r_{\text{in}}$  is needed) rather than intensity convention. *The originality of the approach is that we construct a self-consistent multi-phase model that fully describes Haro 11. The parameters are specific to this galaxy (and will not apply to other galaxies). We do not simply reproduce line ratios, but also absolute line intensities (for which the energy budget needs to be correctly taken into account).*

For Haro 11 this source of energy is a starburst. The hardness of the radiation field is given by the stellar spectrum, and its strength by an input total luminosity (taken as  $L_{\text{TIR}}$ ). Figure 4.3 shows stellar spectra of instantaneous bursts with different ages obtained from STARBURST99 and of single stellar temperatures from the Castelli & Kurucz (2004) library. The choice of the age of the burst is important in setting the hardness of the radiation field and match the emission of high excitation potential species such as [O IV] or [Ne III].

The geometry is chosen to be spherical although it results effectively in a plane-parallel geometry given the large radii  $r_{\text{in}}$  found (Section 3.4 of the paper). A 3D grid of models is run to find a solution, with a  $\chi^2$  minimisation fitting method, for the density ( $n_{\text{H}}$ ) and radiation field (through the age of the burst  $A_{\text{burst}}$  and  $r_{\text{in}}$ ) as illustrated in Figure 4.2.

The models are run in pressure equilibrium as observed at the H II region/PDR connection.

### Temperature-density profiles

As the radiative transfer is computed from the illuminated face of the cloud, where the ionising photons create the H II region, into the cloud, hydrogen is successively in the ionised ( $H^+$ ), atomic ( $H^0$ ), and molecular ( $H_2$ ) state. The hydrogen fractions as a function of cloud depth (traced by  $A_V$  here) are shown in Figure 4.4 (*top* panel). The model was stopped at  $A_V$  of 10 mag so that photons also traverse the molecular phase.

The gas density  $n_{\text{H}}$  is set to an initial value at the inner edge of the cloud and then evolves through the cloud with the electron temperature,  $T_e$ , following the ideal gas law:

$$P_{\text{tot}} = P_{\text{gas}} = n_{\text{H}} k T_e, \quad (4.9)$$

where  $P_{\text{tot}}$  is kept constant in pressure equilibrium. Additional sources of energy, such as magnetic fields (Section 6.3 of the paper) or turbulence (Section 5.3.2) that we explore in the models, can be added in the equation as pressure terms with the thermal pressure, hence impacting on the density profile.

The density and temperature profiles through the cloud are shown in Figure 4.4. As the temperature decreases inside the cloud, the density increases, with a noticeable jump at the



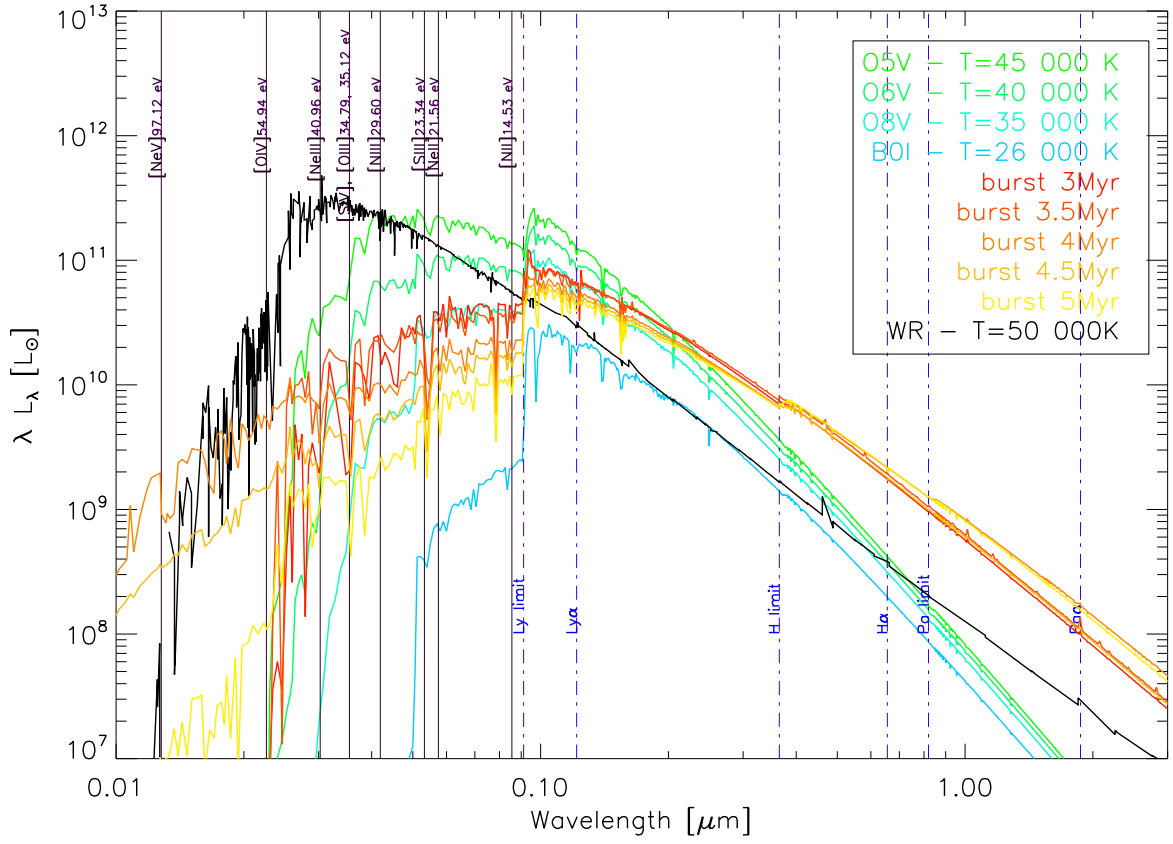


**Figure 4.3.** Stellar spectra of instantaneous bursts with ages 3 to 5 Myr (yellow and red colors) obtained from STARBURST99 and of single stellar temperatures with  $T_{eff}$  from 26 000 to 45 000 K (blue and green colors) from the [Castelli & Kurucz \(2004\)](#) library. A Wolf-Rayet spectrum is overlaid in dark for comparison. Purple vertical lines indicate the excitation potentials of observed species.

ionisation front (transition from the H II region to the PDR with hydrogen recombination) and with a smoother transition from the PDR to the molecular phase. Depth-dependant profiles can be inserted in CLOUDY, but we do not have the necessary constraints to do that. Choosing density profiles can be important particularly in the molecular phase where pressure equilibrium does not hold and turbulence effects may dominate (see Section 5.3.2).

#### 4.2.2 Paper accepted in A&A, August 28 2012

In this paper, we investigate the ISM physical conditions and structure of the low metallicity starburst galaxy Haro 11 by building a multi-phase picture of the full galaxy with CLOUDY. This is the first time that a galaxy is modeled with such complexity and completeness, using new *Herschel* FIR fine-structure lines, the *Spitzer* MIR lines, and the dust continuum, to constrain properties of the different phases. The global picture of the ISM is described by small filling factor dense star-forming regions, bathing in an extended diffuse medium, in which a fraction of the high energy photons permeate.

We present observations of the MIR fine-structure lines from *Spitzer* and the FIR lines from *Herschel*. They are important coolants of the ISM, accounting for  $\sim 1\%$  of  $L_{\text{TIR}}$ . These lines are modeled with CLOUDY with a combination of 3 components. The main model is composed of a compact H II region in pressure equilibrium with a dense PDR and accounts for most of the observed lines ([Ne III], [S IV], [S III], [N III], [O I], etc.). We also find the need for a more diffuse low-ionisation medium to account for the observed [N II], [Ne II], and [C II] emission; and possibly of a diffuse high-ionisation medium for the observed [O III] emission. We discuss the influence of magnetic fields on the density profile, and implications on the predicted intensities in the PDR. Interestingly, only 10 to 50% of the [C II] emission in this model is associated with the PDR, and the rest arises from the diffuse medium. In terms of structure, the diffuse medium has a volume filling factor  $\geq 90\%$ , the H II region of  $\sim 0.2\%$ , and the PDR  $< 0.01\%$ . Most of the gas mass is also concentrated in the diffuse medium, with a total mass of  $3 \times 10^7 M_{\odot}$  for the H II region,  $10^8 M_{\odot}$  for the PDR, and  $7 \times 10^8 M_{\odot}$  for the diffuse medium. The global SED, from the UV to the mm wavelength range, is marginally reproduced, and differences are largely explained by the geometrical assumptions of the models. We discuss that point further in Section 6.1.2.

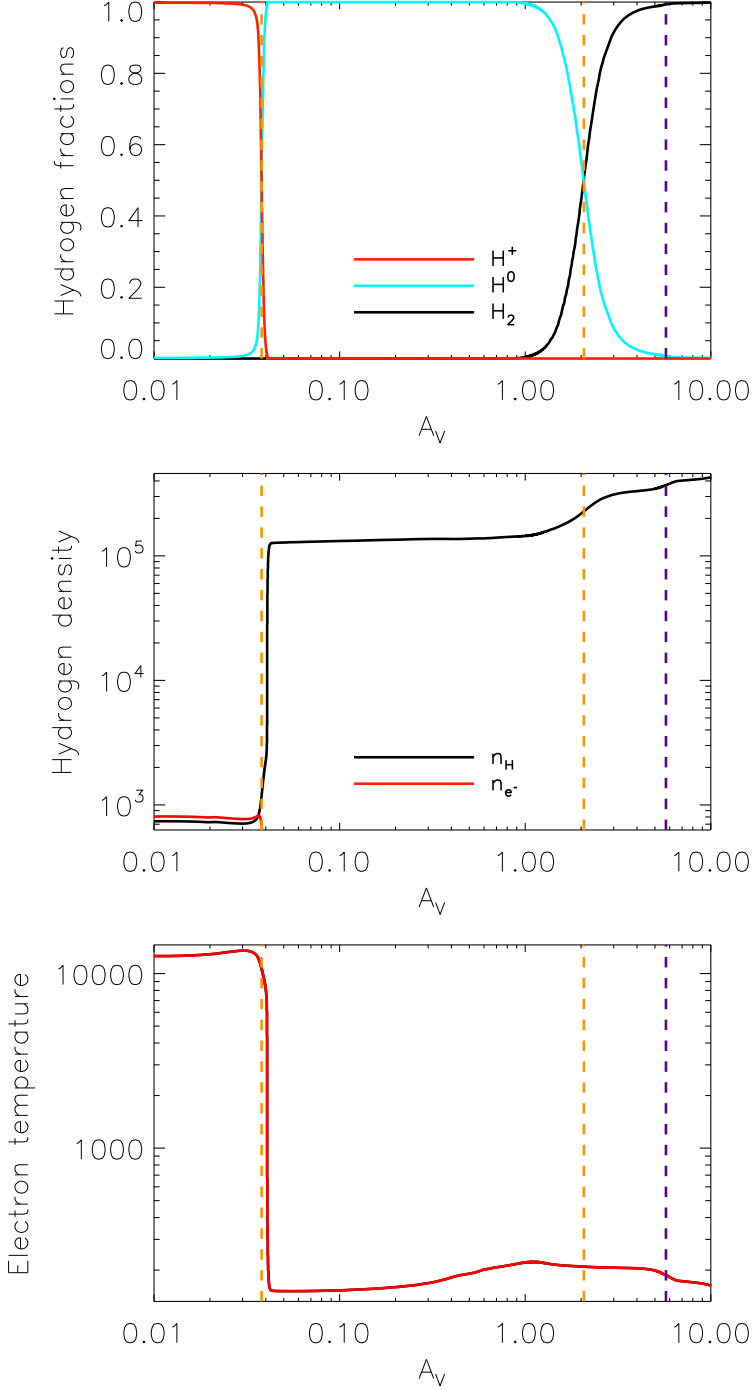


**Figure 4.4.** *Top:* Hydrogen fraction as a function of cloud depth. Ionised fraction ( $H^+$ ) is represented in red, atomic fraction ( $H^0$ ) in blue, and molecular fraction ( $H_2$ ) in black. *Middle:* Density profile through the cloud. The gas density ( $n_H$ ) is in dark color, and the electron density ( $n_{e^-}$ ) in red. *Bottom:* Electron temperature profile through the cloud. For all panels, the vertical orange dashed line indicates the transition from one phase to the other (fraction 0.5 for each). The vertical purple dashed line indicate the start of CO formation. This is the area where hydrogen is molecular and CO has not yet formed, i.e. between  $A_V$  of  $\sim 2$  and 6 mag, and where the dark gas resides. The model is stopped at an  $A_V$  of 10 mag.

# The nature of the interstellar medium of the starburst low-metallicity galaxy Haro 11: a multi-phase model of the infrared emission <sup>★</sup>

D. Cormier<sup>1</sup>, V. Lebouteiller<sup>1</sup>, S. C. Madden<sup>1</sup>, N. Abel<sup>2</sup>, S. Hony<sup>1</sup>, F. Galliano<sup>1</sup>, M. Baes<sup>3</sup>, M. J. Barlow<sup>6</sup>, A. Cooray<sup>4</sup>, I. De Looze<sup>3</sup>, M. Galametz<sup>5</sup>, O. Ł. Karczewski<sup>6</sup>, T. J. Parkin<sup>7</sup>, A. Rémy<sup>1</sup>, M. Sauvage<sup>1</sup>, L. Spinoglio<sup>8</sup>, C. D. Wilson<sup>7</sup>, and R. Wu<sup>1</sup>

<sup>1</sup> Laboratoire AIM, CEA/DSM - CNRS - Université Paris Diderot, Irfu/Service d'Astrophysique, CEA Saclay, 91191 Gif-sur-Yvette, France e-mail: diane.cormier@cea.fr

<sup>2</sup> University of Cincinnati, Clermont College, Batavia, OH, 45103, USA

<sup>3</sup> Sterrenkundig Observatorium, Universiteit Gent, Krijgslaan 281 S9, B-9000 Gent, Belgium

<sup>4</sup> Department of Physics & Astronomy, University of California, Irvine, CA 92697, USA

<sup>5</sup> Institute of Astronomy, University of Cambridge, Madingley Road, Cambridge, CB3 0HA, UK

<sup>6</sup> Department of Physics and Astronomy, University College London, Gower Street, London WC1E 6BT, UK

<sup>7</sup> Dept. of Physics & Astronomy, McMaster University, Hamilton, Ontario, L8S 4M1, Canada

<sup>8</sup> Istituto di Fisica dello Spazio Interplanetario, INAF, Via del Fosso del Cavaliere 100, I-00133 Roma, Italy

Preprint online version: October 18, 2012

## Abstract

**Context.** The low metallicity interstellar medium (ISM) is profoundly different from that of normal systems, being clumpy with low dust abundance and little CO-traced molecular gas. Yet many dwarf galaxies in the nearby universe are actively forming stars. As the complex ISM phases are spatially mixed with each other, detailed modeling is needed to understand the gas emission and subsequent composition and structure of the ISM.

**Aims.** Our goal is to describe the multi-phase ISM of the infrared bright low-metallicity galaxy Haro 11, dissecting the photoionised and photodissociated gas components.

**Methods.** We present observations of the mid-infrared and far-infrared fine-structure cooling lines obtained with the *Spitzer*/IRS and *Herschel*/PACS spectrometers. We use the spectral synthesis code Cloudy to methodically model the ionised and neutral gas from which these lines originate.

**Results.** We find that the mid- and far-infrared lines account for  $\sim 1\%$  of the total infrared luminosity  $L_{\text{TIR}}$ , acting as major coolants of the gas. Haro 11 is undergoing a phase of intense star formation, as traced by the brightest line, [O III]  $88\ \mu\text{m}$ , with  $L_{[\text{O III}]} / L_{\text{TIR}} \sim 0.3\%$ , and high ratios of [Ne III]/[Ne II] and [S IV]/[S III]. Due to their different origins, the observed lines require a multi-phase modeling comprising: a compact H II region, dense fragmented photodissociation regions (PDRs), a diffuse extended low-ionisation/neutral gas which has a volume filling factor of at least 90%, and porous warm dust in proximity to the stellar source. For a more realistic picture of the ISM of Haro 11 we would need to model the clumpy source and gas structures. We combine these 4 model components to explain the emission of 17 spectral lines, investigate the global energy balance of the galaxy through its spectral energy distribution, and establish a phase mass inventory. While the ionic emission lines of Haro 11 essentially originate from the dense H II region component, a diffuse low-ionisation gas is needed to explain the [Ne II], [N II], and [C II] line intensities. The [O III]  $88\ \mu\text{m}$  line intensity is not fully reproduced by our model, hinting towards the possible presence of yet another low-density high-ionisation medium. The [O I] emission is consistent with a dense PDR of low covering factor, and we find no evidence for an X-ray dominated component. The PDR component accounts for only 10% of the [C II] emission. Magnetic fields, known to be strong in star-forming regions, may dominate the pressure in the PDR. For example, for field strengths of the order of  $100\ \mu\text{G}$ , up to 50% of the [C II] emission may come from the PDR.

**Key words.** galaxies:ISM – galaxies:individual (Haro 11) – ISM: line and bands – ISM: structure – techniques: spectroscopic – radiative transfer

## 1. Introduction

Star formation in the most pristine environments of the early universe is poorly understood. The closest analogs to chemically unevolved systems are the low metallicity dwarf galaxies of our local universe. But even those well-studied nearby galaxies continue to plague us with fundamental questions on

what triggers and regulates star formation in metal-poor gas-rich conditions. Certainly, from an observational point of view, at all wavelengths, local universe low-metallicity dwarf galaxies show dramatic differences compared to their more metal-rich counterparts (Kunth & Östlin 2000, for a review), in the mid-infrared (MIR), far-infrared (FIR), and submillimeter (submm) wavelength regimes. These include the dearth of Polycyclic Aromatic Hydrocarbons (PAHs), prominent hot MIR-emitting dust, submm excess, and enhanced [C II]  $157\ \mu\text{m}$ /CO(1-0) ratios (e.g. Madden 2008; Madden et al. 2012a).

<sup>★</sup> *Herschel* is an ESA space observatory with science instruments provided by European-led Principal Investigator consortia and with important participation from NASA.

What physical properties, local as well as global, within the dwarf galaxies are we witnessing with these observational signatures? How do we turn these signatures into a realistic view of star formation under early universe conditions? How do basic local parameters, such as radiation field, density, compactness, filling factors, metallicity, etc. figure in the picture we have of star-forming dwarf galaxies? Much of the ambiguity surrounding these questions is due to the lack of understanding the precise role of critical diagnostics and of spatial resolution in the most nearby objects, especially in the FIR/submm, resulting in a mixture of different interstellar medium (ISM) phases in the integrated view of galaxies.

Low metallicity star-forming dwarf galaxies host young massive stellar clusters (e.g. Turner et al. 2000; Beck et al. 2000; Johnson & Kobulnicky 2003) which produce ultraviolet (UV) photons. The low abundance and prevailing hard radiation field can explain most of the differences observed in dwarf galaxies in destroying large grains and PAHs, in favor of smaller dust grains. The UV photons also photodissociate molecules such as CO, which are unable to adequately self-shield, thus reducing the CO abundance in metal-poor gas (e.g. Wolfire et al. 2010; Narayanan et al. 2012). Thus UV photons play an important role in the heating and the chemistry of the ISM, controlling the structure of H II regions and photodissociation regions (PDRs). While the heating of the gas is mainly due to photoionisation and gas-grain collisions in the H II regions and to the photoelectric effect and cosmic rays in the neutral phase, the cooling is normally dominated by radiative de-excitation of fine-structure lines, readily observed in the MIR and FIR/submm. The behavior of these tracers and their relationship to the star formation properties, have been extensively studied to access physical parameters in terms of the gas temperature, density, and the radiation field (Malhotra et al. 2001; Hunter et al. 2001; Brauher et al. 2008, e.g.). These studies make use of photoionisation and PDR models at the scale of individual clouds (Kaufman et al. 1999; Wolfire et al. 1990; Ferland et al. 1998; Abel et al. 2005; Röllig et al. 2006; Tielens & Hollenbach 1985).

The [C II] 157  $\mu\text{m}$  line is an important FIR diagnostic often put forward as a star formation tracer (Stacey et al. 2010; Boselli et al. 2002; de Looze et al. 2011). It has been observed in many different object types, including dense star-forming regions (Stacey et al. 1991), diffuse ionised and atomic regions (Madden et al. 1993), and high-redshift galaxies (Maiolino et al. 2009; Stacey et al. 2010). Since the [C II] line is well-correlated with the  $^{12}\text{CO}(1-0)$  line and the FIR luminosity (e.g. Stacey et al. 1991; Pierini et al. 2003), it is generally considered that the [C II] line traces massive star formation within the PDR paradigm. [C II] is normally the brightest FIR cooling line, being much brighter than CO, and carrying about 0.1 to ~0.5% of the FIR luminosity in metal-rich star-forming galaxies. In low metallicity dwarf galaxies, where CO(1-0) is not easily detected because of photodissociation (e.g. Schrubba et al. 2012; Leroy et al. 2011), [C II] can be as high as 1% of the  $L_{\text{FIR}}$  and often 5 to 10 times brighter relative to CO than in dustier starburst galaxies (e.g. Poglitsch et al. 1995; Madden et al. 1995; Madden 2000; Hunter et al. 2001; Cormier et al. 2010). The high [C II]/CO(1-0) ratio in low-metallicity systems may be alerting us to the fact that the morphology of their PDRs and H II regions and the relative filling factors of the various phases of dwarf galaxies differ from those of more metal-rich objects (e.g. Madden 2000; Kaufman et al. 2006; Röllig et al. 2006). Even in the nearest neighboring dwarf galaxies, the picture of star formation – and what controls this star formation – is enigmatic.

However, using [C II] alone can lead to ambiguous interpretation, particularly on the origin of the C<sup>+</sup> emission, which can arise from the ionised as well as neutral phases of the ISM. To employ the [C II] line as a valuable star formation tracer, it is necessary to model the different phases on galaxy-wide scales. The challenge rests on the unavoidable fact that on the scale of galaxies, aside from the closest dwarf galaxies such as the LMC (50 kpc,  $1/2 Z_{\odot}$ ), SMC (60 kpc,  $1/5 Z_{\odot}$ ), NGC 6822 (500 kpc,  $1/4 Z_{\odot}$ ), or IC 10 (800 kpc,  $1/3 Z_{\odot}$ ), the phases of the ISM are mixed together in single telescope beams. When using a limited number of diagnostic lines, only a single galactic component can be modeled and average conditions derived, which is otherwise an ensemble of individual PDRs, ionised regions, etc. This requires modeling a comprehensive suite of tracers covering a range of critical densities and excitation potentials to characterise the dense H II regions, the diffuse H II regions, PDRs, etc. self-consistently. This approach allows us to grapple with degeneracies and ambiguities in the interpretation of these tracers. In this way, valuable observational diagnostics can be turned into a more accurate description of the multi-phase configuration of a full galaxy.

The *Herschel* Space Observatory (Pilbratt et al. 2010) has brought the opportunity to obtain a wide range of valuable FIR fine-structure diagnostics never observed before in dwarf galaxies. The Dwarf Galaxy Survey (DGS; P.I. Madden) is surveying the dust and gas of a wide range of low metallicity galaxies in the local universe (Cormier et al. 2010; Galametz et al. 2010; O'Halloran et al. 2010; Madden et al. 2012b; Rémy et al. 2012) using PACS (Poglitsch et al. 2010) and SPIRE (Griffin & et al. 2010). The brightest low-metallicity galaxy of the DGS observed with the PACS spectrometer is Haro 11, an infrared-luminous starburst galaxy with metallicity  $Z = 1/3 Z_{\odot}$ . Haro 11 has the largest dataset obtained with PACS with observations of 7 FIR fine-structure lines: [C II] 157, [O III] 88, [O I] 63, [O I] 145, [N III] 57, [N II] 122, and [N II] 205  $\mu\text{m}$ . It has also been observed with the IRS spectrograph onboard *Spitzer*. Unresolved in the IR, Haro 11 is an ideal candidate to conduct a study modeling an exhaustive set of gas tracers to retrieve information about the structure of the multi-phase low metallicity ISM.

In this paper, we propose a systematic approach to model the multi-phase ISM of Haro 11, focusing on the gas properties of the ionised and neutral ISM phases. We consider a set of 17 *Herschel* and *Spitzer* MIR and FIR ionic and atomic fine-structure cooling lines which trace a wide range of environmental conditions, spanning excitation potentials from 8 to 55 eV. With the spectral synthesis code Cloudy (Ferland et al. 1998), we create a self-consistent model of the dominant ISM components from which these lines originate in order to understand the prevailing mechanisms and physical conditions. In Section 2, we present spectroscopic data from the *Spitzer* and *Herschel* observatories. Section 3 explains the modeling strategy and assumed initial parameters. Section 4, 5, and 6 report the model results and conditions of the ISM components. This study establishes an encompassing picture of the dominant ISM phases in Haro 11 and describes the mass budget of the various phases in our model (Section 7).

### 1.1. Studies of Haro 11

Several studies of Haro 11 have highlighted its peculiarity as a galaxy and challenged our understanding of star formation. Haro 11 – also known as ESO 350-IG38 – is a blue compact dwarf (BCD) galaxy at 84 Mpc, with  $M_B = -20.3$ , and metallicity  $Z \sim 1/3 Z_{\odot}$  (Guseva et al. 2012). It is composed of 3 main

star-forming regions, or knots, described in Vader et al. (1993) and Kunth et al. (2003), with a morphology presumably resulting from a merger event (Östlin et al. 2001). The starbursting nature of Haro 11 is visible in Figure 1 with a dominant bright stellar component and dust lanes in front of knot B. These knots host hundreds of young star clusters and  $\sim 60$  super star clusters (SSC) with ages between 1 and 100 Myr peaking at 3 Myr, and constituting a total stellar mass of  $10^{10} M_{\odot}$  (Adamo et al. 2010). An older stellar population is also present, primarily in knots A and C, as seen in the red colors of the V-K bands, modeled in Micheva et al. (2010) by a metal-poor ( $Z=0.001$ ) stellar population of age around 14 Gyr with standard Salpeter IMF, indicating that the galaxy is not undergoing its first star formation event. Ly $\alpha$  emission (Kunth et al. 1998) and Lyman continuum leakage were investigated using UV and X-ray observations in Bergvall et al. (2006); Hayes et al. (2007); Grimes et al. (2007) and Leitert et al. (2011). In Leitert et al. (2011), they estimated the leakage to be 3%. In particular, the discrepant location of Ly $\alpha$  and H $\alpha$  emission, originating in the ionised gas surrounding the star-forming regions, may be explained by a diffuse ionised ISM in the halo of the galaxy with internal resonant scattering at the surface of clumpy dense neutral clouds (Kunth et al. 2003; Hayes et al. 2007). These properties have resulted in its popularity as a local analogue of the high-redshift Lyman-break galaxies (Overzier et al. 2008), and therefore a must-study case to link nearby star formation to the distant universe and galaxy evolution.

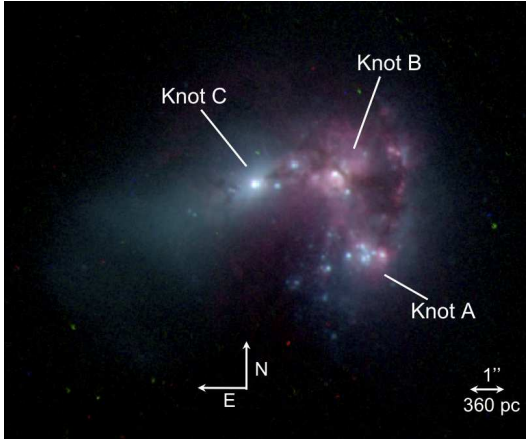


**Figure 1.** HST/ACS 3-color image of Haro 11 with labels for the 3 star-forming knots (blue: F435, green: F550, red: F656N/H $\alpha$ ). Images were downloaded from the Hubble Legacy Archive.

In the IR, Haro 11 is extremely bright compared to other nearby dwarf galaxies. IRAS measurements yielded a FIR luminosity  $L_{\text{FIR}}$  of  $1 \times 10^{11} L_{\odot}$  (Sanders et al. 2003a) from 40 to 400  $\mu\text{m}$  using the Lonsdale et al. (1985) prescription. Its spectral energy distribution (SED) shows a peculiar behavior. It peaks around 40  $\mu\text{m}$ , indicating the prevalence of warm dust, and shows an excess of emission in the submm, as unveiled by APEX/LABOCA and *Herschel*, which is often seen in low metallicity starbursting dwarf galaxies (Galliano et al. 2003, 2005; Galametz et al. 2009, 2011; Rémy et al. 2012). The origin of the excess is not well determined and several hypotheses described in Galametz et al. (2011), including a change of dust emissivity,

spinning dust grains, or a cold dust component, are invoked in current dust models to explain the submm excess. Galametz et al. (2009) present a detailed dust modeling of Haro 11 in which they derive a total dust mass of  $6 \times 10^6 M_{\odot}$  if the submm excess is ignored, and of  $2 \times 10^7 M_{\odot}$  if the submm excess is interpreted as cold dust. Assuming the excess as cold dust ( $T \sim 10$  K) is however difficult to reconcile with the observed dust and gas mass budgets, and the expected lower dust-to-gas mass ratios (DGR; Galametz et al. 2011). Integrating the SED from 3 to 1100  $\mu\text{m}$ , the total IR luminosity  $L_{\text{TIR}}$  is  $1.4 \times 10^{11} L_{\odot}$  (Galametz et al. 2009). We will use this value of  $L_{\text{TIR}}$  throughout this paper.

Spectroscopic observations show bright lines in the FIR with ISO/LWS, while both the H I 21-cm line, and the CO ( $J=1-0$ ) line, the most common tracer of molecular gas in galaxies, are undetected (Bergvall et al. 2000). A detailed study of the neutral gas of the ISM of Haro 11 by Bergvall et al. (2000) investigated the mass budget of the different ISM phases. They establish masses for each phase:  $M(\text{H I}) < 10^8 M_{\odot}$ , with an upper limit on the atomic H I;  $M(\text{PDR})$  of  $2 \times 10^8 M_{\odot}$  using the LWS [C II] observations, the PDR mass being larger than the H I mass; and  $M(\text{H}_2) \sim 10^8 M_{\odot}$  for the molecular gas, using both a scaling of the PDR mass and the CO upper limit converted to  $\text{H}_2$  column density through the CO/ $\text{H}_2$  conversion factor ( $X_{\text{CO}}$ ). They used a Galactic value for  $X_{\text{CO}}$  (Strong et al. 1988):  $X_{\text{CO,gal}} = 2.3 \times 10^{20} \text{ cm}^{-2} (\text{K km s}^{-1})^{-1}$ . Therefore they describe the ISM structure as: very extended PDRs, in which the H I mass resides; a small fraction of the total ISM gas is left in atomic form; and the bulk of the gas, that is normally in neutral state, is ionised by the starburst. Bergvall & Östlin (2002) derive  $M(\text{H II}) \sim 10^9 M_{\odot}$  from H $\alpha$  observations for the ionised gas. These masses are lower than the total stellar mass of  $10^{10} M_{\odot}$  derived in Adamo et al. (2010).

However, important questions remain, particularly on the state of the ionised, neutral atomic, and molecular gas. While evidence for young massive stellar populations and SSCs exist from the optical and IR point of view, evidence for any substantial reservoir of neutral gas, in the form of either atomic or molecular, is non-existent to date. Where is the fuel for the vigorous star formation observed in Haro 11? What is the state of the gas reservoirs in Haro 11, residing in the ionised, neutral, and molecular form? This study, using a wide variety of tracers of neutral and ionised gas, aims for a more complete description of the enigmatic nature of the ISM of Haro 11.

**Table 1.** General properties of Haro 11.

Quantity	Value	Reference
RA (J2000)	00h36'52.5"	NED <sup>(a)</sup>
Dec (J2000)	-33°33'19"	NED
Distance	84 Mpc	NED <sup>(b)</sup>
12+log(O/H)	8.2	Guseva et al. (2012)
Optical size	0.4'x0.5'	NED
$L_{\text{TIR}}^{(c)}$	$1.4 \times 10^{11} L_{\odot}$	Galametz et al. (2009)
$L_{\text{FUV}}$	$2 \times 10^{10} L_{\odot}$	Grimes et al. (2007)
$L_{\text{X-rays}}$	$4.4 \times 10^7 L_{\odot}$	Grimes et al. (2007)
$L_{\text{Ly}\alpha}$	$1.9 \times 10^8 L_{\odot}$	Hayes et al. (2007)
$L_{\text{H}\alpha}$	$8 \times 10^8 L_{\odot}$	Östlin et al. (1999)

(a) NASA/IPAC Extragalactic Database. (b) This distance is derived with a Hubble constant  $H_0 = 73 \text{ km/sec/Mpc}$ . (c)  $L_{\text{TIR}}$  is the integrated SED from 3 to 1100  $\mu\text{m}$ . All luminosities are scaled to the distance chosen in this paper of 84 Mpc.

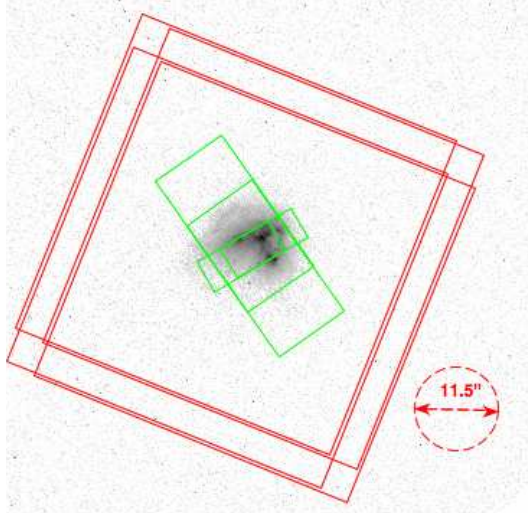


**Figure 2.**  $H\alpha$  image of Haro 11 from the Hubble Legacy Archive. The *Spitzer*/IRS high-resolution slits are overlaid in green and the *Herschel*/PACS array in red. The PACS beamsize at  $150\ \mu\text{m}$  is  $11.5''$ . The IRS low-resolution slits are not shown.

## 2. Observations

### 2.1. *Spitzer* data

Haro 11 was observed with the Infrared Spectrograph (IRS; Houck et al. 2004) on board the *Spitzer* Space Telescope (Werner et al. 2004), on the 17th of July 2004 (P.I.: J. R. Houck). The 4 modules were used, i.e., the 2 high-resolution modules: Short-High SH ( $\approx 10 - 20\ \mu\text{m}$ ) and Long-High LH ( $\approx 19 - 37\ \mu\text{m}$ ) with  $R \sim 600$ , and the 2 low-resolution modules: Short-Low SL ( $\approx 5 - 14\ \mu\text{m}$ ) and Long-Low LL ( $\approx 14 - 37\ \mu\text{m}$ ) with  $R \sim 60 - 120$ . Observations were done in staring mode (AORKey 9007104). Figure 2 shows the slits of the high-resolution module on the sky.

The low-resolution spectra were retrieved from the CASSIS Atlas<sup>1</sup> (Lebouteiller et al. 2011), with a tapered spatial window that scales with wavelength to account for the broader PSF at longer wavelengths. The high-resolution spectra were obtained with SMART v8.2.2 (Lebouteiller et al. 2010; Higdon et al. 2004) from the full-slit extraction of SH and LH and assuming a point-like source calibration. The SL and SH spectra were stitched to LL and LH by applying the same factor 1.13, which is due to the fact that the source is slightly extended for the SL and SH apertures ( $3.7''$  and  $4.7''$  height respectively), while it is point-like for the LL and LH apertures ( $\approx 11''$ ). Another factor of 1.15 was applied to the low-resolution spectra to match the continuum of the high-resolution. The final rest-frame spectrum is displayed in Figure 3 (*top*), with a zoom on individual spectral lines (*bottom*). With a spectral resolution  $\geq 500\ \text{km s}^{-1}$ , the lines are not spectrally resolved.

Line fitting and flux measurements were also done in SMART. A Gaussian and second order polynomial function were fitted to the line and continuum. For total uncertainties, we

added 10% of the line flux due to calibration uncertainties. The resulting fluxes and uncertainties of the most prominent lines are listed in Table 2. The fluxes agree within the uncertainties to those of Wu et al. (2006). The  $[\text{Ne III}]$  line at  $36.0\ \mu\text{m}$  was not observed as it falls out of the IRS spectral range.

### 2.2. *Herschel* data

Haro 11 was observed with the PACS spectrometer (Poglitsch et al. 2010) on the 27th of June 2010, OD 409 of the *Herschel* mission (Pilbratt et al. 2010) as part of the Guaranteed Time Key Program, the Dwarf Galaxy Survey (P.I.: S. C. Madden). The PACS array is composed of  $5 \times 5$  spatial pixels each  $9.4''$  square, covering a total field-of-view of  $47''$ . Haro 11 was mapped with  $2 \times 2$  rasters separated by  $4.5''$  in the 7 following fine-structure spectral lines:  $[\text{C II}]$   $157\ \mu\text{m}$ ,  $[\text{O III}]$   $88\ \mu\text{m}$ ,  $[\text{O I}]$   $145\ \mu\text{m}$  (OBSID 1342199236),  $[\text{O I}]$   $63\ \mu\text{m}$ ,  $[\text{N III}]$   $57\ \mu\text{m}$ ,  $[\text{N I}]$   $122\ \mu\text{m}$  (OBSID 1342199237), and  $[\text{N II}]$   $205\ \mu\text{m}$  (OBSID 1342199238), for a total of 7.2h. The  $[\text{N II}]$   $205\ \mu\text{m}$  line was also re-observed on OD 942 for 1.6h with a single pointing (OBSID 1342234063). The observations were done in chop-nod mode with a chop throw of  $6'$  off the source. The chopped position is free of emission. The beam size is  $9.5''$  at  $60\ \mu\text{m}$ , and  $11.5''$  at  $150\ \mu\text{m}$  (diffraction limited above  $\sim 100\ \mu\text{m}$ ). The spectral resolution is  $\sim 90\ \text{km s}^{-1}$  at  $60\ \mu\text{m}$ ,  $125\ \text{km s}^{-1}$  at  $90\ \mu\text{m}$ ,  $295\ \text{km s}^{-1}$  at  $120\ \mu\text{m}$ , and  $250\ \text{km s}^{-1}$  at  $150\ \mu\text{m}$  (PACS Observer's Manual 2011<sup>2</sup>).

The data were reduced with the *Herschel* Interactive Processing Environment (HIPE) v7.0.1935 (Ott 2010). We used standard scripts of the PACS spectrometer pipeline. The line fitting and map making were done using the software PACSman (Lebouteiller et al. 2012). The signal from each spatial position of the PACS array is fitted with a second order polynomial plus Gaussian for the baseline and line. For total uncertainties, we add 30% of the line flux due to calibration uncertainties (Poglitsch et al. 2010). The rasters are combined by drizzling to produce final reduced maps with pixel size of  $3''$ .

With *Herschel*, all of the lines are well detected, at least in the central pixel of the PACS array, except the  $[\text{N II}]$   $205\ \mu\text{m}$  line. The  $[\text{N II}]$   $205\ \mu\text{m}$  line is located at the edge of the first grating order of the spectrometer and affected by spectral leakage, due to overlapping of the grating orders. It is contaminated by signal from the second grating order around  $100\ \mu\text{m}$ , and is therefore difficult to observe and to calibrate. The line profiles are displayed in Figure 4. The line centers range between  $-30$  and  $+70\ \text{km s}^{-1}$  within the maps of all observed lines, and indicate a rotation around the north-south axis of both the ionised and neutral gas components, slightly tilted compared to the velocity structure of  $H\alpha$  analysed in Östlin et al. (1999). All lines display broad profiles, with a broadening up to  $300\ \text{km s}^{-1}$ , which suggests that both the neutral and ionised gas are coming from several components with different velocities. However, with spectral resolution  $> 100\ \text{km s}^{-1}$ , the lines are well fitted by a single Gaussian and we cannot separate the different velocity components in the spectra. This suggested complex velocity structure is corroborated by studies of optical lines that show broad profiles as well (Kunth et al. 1998; Östlin et al. 1999), and where the neutral gas is shifted compared to the ionised gas, expanding over few kpcs (Kunth et al. 2003). FUSE spectra in Grimes et al. (2007) show absorption lines of the ISM with FWHM  $300\ \text{km s}^{-1}$  and blueshifted by  $80\ \text{km s}^{-1}$ . The higher ionisation lines can be stronger in galactic outflows (Contursi et al. 2012).

<sup>1</sup> The Cornell Atlas of *Spitzer*/IRS Sources (CASSIS) is a product of the Infrared Science Center at Cornell University, supported by NASA and JPL.

<sup>2</sup> available at [http://herschel.esac.esa.int/Docs/PACS/html/pacs\\_om.html](http://herschel.esac.esa.int/Docs/PACS/html/pacs_om.html)



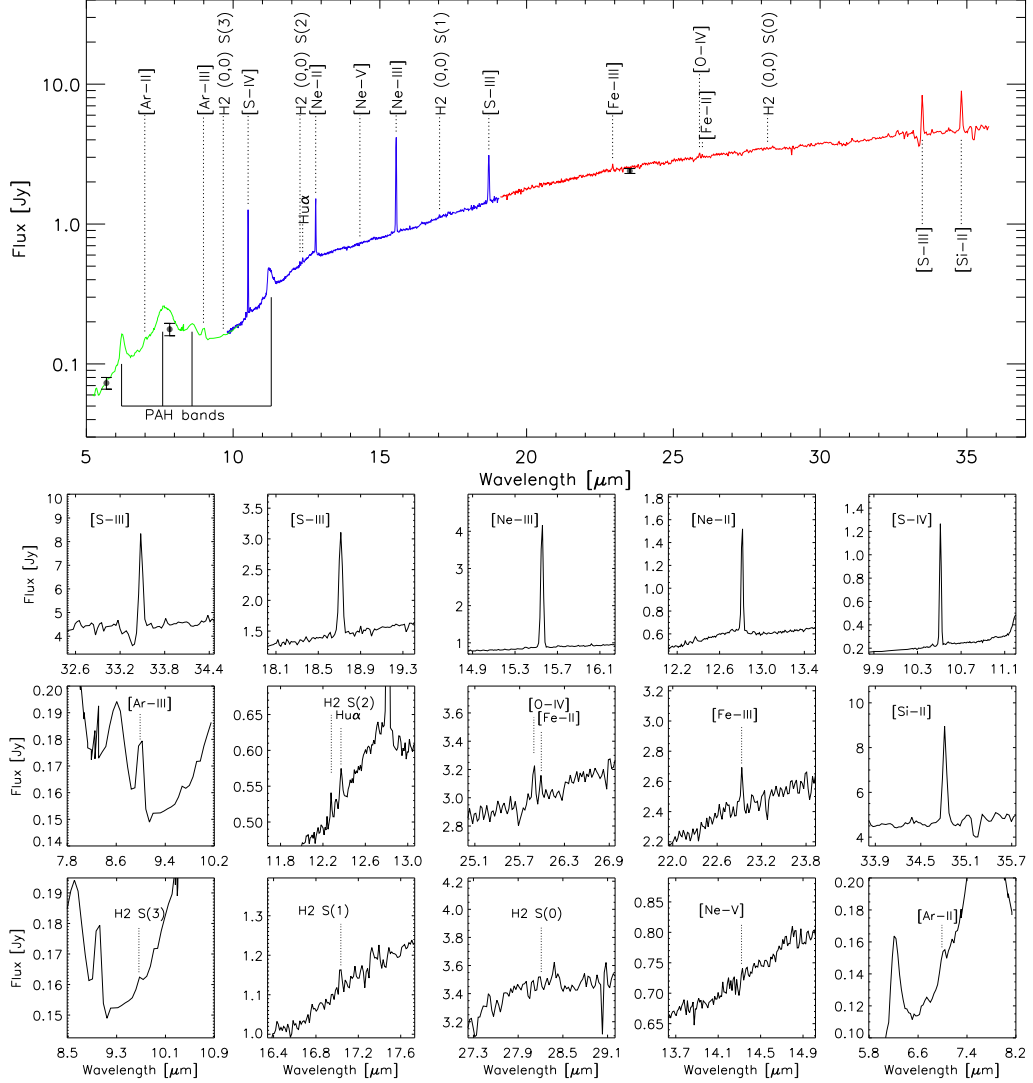


**Figure 3.** *Top:* *Spitzer*/IRS spectrum of Haro 11 in the rest wavelength frame ( $z = 0.0206$ ), SL in green, SH in blue, and LH in red. Emission lines are labeled on top. The IRAC and MIPS photometry is also overlaid (fluxes in Table 3). *Bottom:* Zoom on the individual spectral lines. Fluxes and upper limits are reported in Table 2.

The [C II] line shows a marginally extended emission at  $157 \mu\text{m}$ , peaking at a signal-to-noise ratio of 50 in the center and dropping below detection at the edge of the map. The emission of the other lines is rather compact. The shape of the PACS spectrometer beam is not known well enough to measure an accurate source size if the source were slightly extended. Hence we cannot recover spatial information. To derive total line intensities, we integrated the fluxes over a circular aperture of diameter  $30''$  to encompass all the emission. The line intensities are listed in Table 2. Observations of the [O III], [C II], and [O I]  $63$  and  $145 \mu\text{m}$  lines were also performed with the LWS instrument on-board *ISO* (Bergvall et al. 2000; Brauher et al. 2008; Vasta et al.

2010). The PACS intensities of the [O I]  $63 \mu\text{m}$  and [O III] lines agree within 40% with the LWS observations, although they are found to be lower with PACS. This may be attributed to a beam effect, the LWS beam size being  $\sim 80''$ . However, we find that the [C II] intensity is two times brighter with PACS compared to LWS. To understand this discrepancy, we have reduced the PACS data with different flat-field corrections, as well as with background normalization (PACS Data Reduction Guide). All these methods give the same final [C II] flux as quoted in Table 2 within 10%, ruling out a mis-calibration from PACS. Therefore we attribute the difference between the PACS and LWS fluxes to a calibration problem from the LWS instrument.

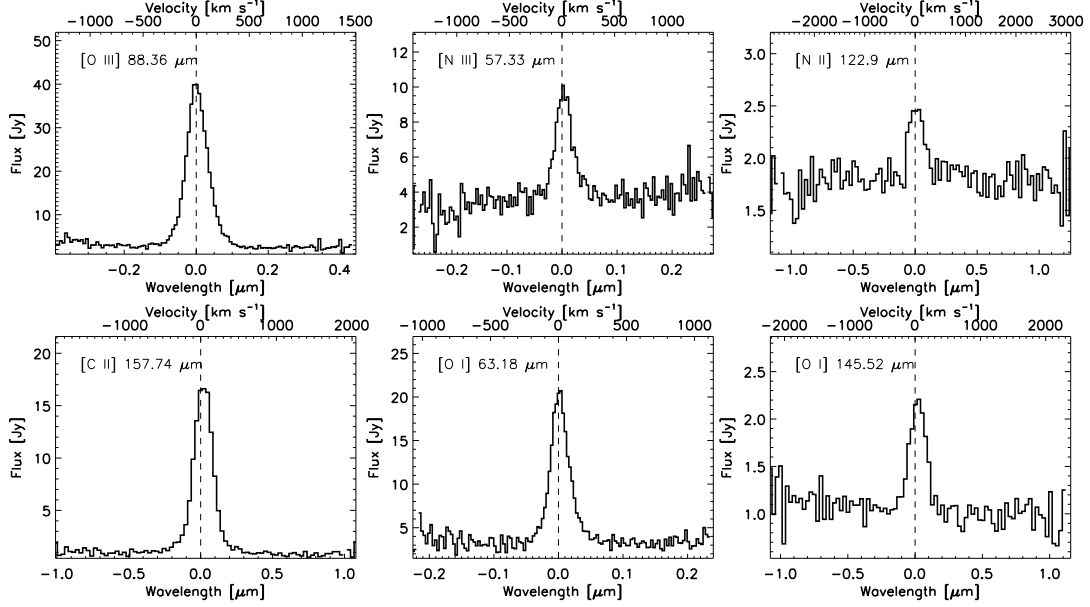


Figure 4. *Herschel*/PACS line profiles from an individual spatial pixel ( $9.4''$ ) centered on the galaxy.

### 2.3. Spectral line description

The IRS and PACS spectra probe the ionised and neutral media. The IRS spectrum shows a wealth of MIR fine-structure lines, the brightest being (in order) [Ne III]  $15.6 \mu\text{m}$ , [Si II]  $34.8 \mu\text{m}$ , [S III]  $18.7$  and  $33.5 \mu\text{m}$ , [S IV]  $10.5 \mu\text{m}$ , and [Ne II]  $12.8 \mu\text{m}$ . PAH features at  $6.2$ ,  $7.7$ ,  $8.6$ ,  $11.2$ , and  $12.8 \mu\text{m}$  are also present. The PACS spectrum also shows bright FIR lines, especially [O III], [C II], [O I]  $63 \mu\text{m}$ , and [N III]. The [O III] line is the brightest of all, with  $[\text{O III}]/[\text{C II}] = 2.4$ . While [C II] is the brightest FIR fine-structure line in normal and dusty starburst galaxies (Brauhar et al. 2008), we find that this is often not the case in low-metallicity dwarf galaxies (Hunter et al. 2001; Cormier et al. 2010, 2012a; Madden et al. 2012b).

The young star-forming nature of this galaxy also agrees with intense [Ne III] ( $41.0 \text{ eV}$ ), [O III] ( $35.1 \text{ eV}$ ), [S IV] ( $34.8 \text{ eV}$ ), and [N III] ( $29.6 \text{ eV}$ ) lines observed, arising from relatively highly ionised regions. [O IV] ( $54.9 \text{ eV}$ ) at  $25.9 \mu\text{m}$ , which requires a relatively hard radiation field (Sect. 6.3), is also detected. The  $[\text{Ne III}]/[\text{Ne II}]$  ratio is  $3.5$ ,  $[\text{S IV}]/[\text{S III}]$  is  $0.9$ , and  $[\text{N III}]/[\text{N II}]$  is  $8$ . These ratios are indicative of a hard radiation field typical of BCDs (Thornley et al. 2000; Madden et al. 2006). While [C II] can come from both the diffuse ionised phase and the neutral phase, [O I] traces only the neutral phase. The  $[\text{O I}] 63 \mu\text{m}/[\text{C II}]$  ratio is  $0.9$ , similar to that found in other dwarf galaxies and dustier galaxies (Hunter et al. 2001; Brauhar et al. 2008). Table 2 lists the ionisation energies of the observed lines, as well as the excitation temperatures and critical densities ( $n_{\text{crit}}$ ) of the transitions with collisions with H and/or  $\text{e}^-$ .

Comparing line luminosities to the TIR luminosity, we find  $L_{[\text{C II}]} / L_{\text{TIR}} = 0.1\%$ ,  $L_{[\text{O III}]} / L_{\text{TIR}} = 0.3\%$ , and  $L_{[\text{O I}]} / L_{\text{TIR}} = 0.1\%$ . Altogether, the FIR lines represent  $0.6\%$  of the TIR luminosity;

and when adding the MIR lines, they represent  $1.2\%$  of  $L_{\text{TIR}}$ . Together these lines are responsible for most of the gas cooling of the ISM. Such line-to-TIR ratios are typical of star-forming galaxies (Malhotra et al. 2001; Brauhar et al. 2008)<sup>3</sup>. Similar  $L_{[\text{C II}]} / L_{\text{TIR}}$  ratios are found in several high-redshift galaxies (Maiolino et al. 2009; Stacey et al. 2010). Croxall et al. (2012) find  $L_{[\text{C II}]} / L_{\text{TIR}} \sim 0.5\%$  and  $L_{[\text{O I}]} / L_{\text{TIR}} \sim 0.1\%$  in spatially resolved regions of the nearby spiral galaxy NGC 4559. There is observational evidence that  $L_{[\text{C II}]} / L_{\text{TIR}}$  tends to decrease in galaxies with warmer FIR-color,  $f_{\nu}(60 \mu\text{m})/f_{\nu}(100 \mu\text{m})$ . Among other effects, this may be attributed to a less efficient photoelectric heating due to charged grains (Malhotra et al. 2001; Croxall et al. 2012), or to a UV-photon screening from large amounts of dust as in ultra-luminous IR galaxies (ULIRGs) (Abel et al. 2009; Graciá-Carpio et al. 2011). With observed FIR-color  $\sim 1$ , Haro 11 falls within the large spread of  $L_{[\text{C II}]} / L_{\text{TIR}}$  values and is not particularly [C II] deficient nor [C II] excessive, as often seen in low metallicity galaxies (Madden et al. 2012b).

### 2.4. Photometry data

For the discussion on the SED of Haro 11 in Section 7.1, we use broad-band data available from the X-ray to the radio regime, to assess how the models perform in reproducing the continuum emission. The photometry is taken from NED. In addition, we use the *Spitzer*/MIPS photometry from Bendo et al. (2012), the *Herschel*/PACS and SPIRE photometry from Rémy et al. (2012), and the *Spitzer*/IRAC and LABOCA  $870 \mu\text{m}$  photometry from Galametz et al. (2009). All fluxes are summarized in Table 3.

<sup>3</sup> Note that they use  $L_{\text{FIR}}$ , determined from *IRAS* fluxes with the Helou et al. (1988) formula, and that  $L_{\text{TIR}}$  estimated as  $2 \times L_{\text{FIR}}$  (Hunter et al. 2001) can be different from the true  $L_{\text{TIR}}$  when including submm observations.

**Table 2.** *Spitzer* and *Herschel* line fluxes.

Line	Wavelength ( $\mu\text{m}$ )	Flux <sup>(a)</sup> ( $10^{-16} \text{ W m}^{-2}$ )	Uncertainty ( $10^{-16} \text{ W m}^{-2}$ )	Excit. potential <sup>(b)</sup> (eV)	Excit. temperature <sup>(c)</sup> (K)	Critical density <sup>(d)</sup> ( $\text{cm}^{-3}$ )
<i>Spitzer</i> /IRS						
[S iv]	10.51	5.37	0.66	34.79	1 369	$5 \times 10^4$ [e]
[Ne ii]	12.81	3.53	0.43	21.56	1 123	$7 \times 10^5$ [e]
[Ne iii]	15.56	12.3	1.5	40.96	925	$3 \times 10^5$ [e]
[S iii]	18.71	5.79	0.72	23.34	769	$2 \times 10^4$ [e]
[S iii]	33.48	5.85	0.69	"	430	$7 \times 10^3$ [e]
[Si ii]	34.82	6.21	0.75	8.15	413	$3 \times 10^5$ [H], $1 \times 10^3$ [e]
Humphreys $\alpha$	12.37	0.208	0.045	13.60	1 163	-
H <sub>2</sub> (0,0) S(0)	28.22	< 0.62	-	4.48	510	$7 \times 10^2$ [H]
H <sub>2</sub> (0,0) S(1)	17.03	0.168	0.055	"	1015	$2 \times 10^4$ [H]
H <sub>2</sub> (0,0) S(2)	12.28	0.101	0.013	"	1682	$2 \times 10^5$ [H]
H <sub>2</sub> (0,0) S(3)	9.66	0.121	0.018	"	2504	$9 \times 10^5$ [H]
[Fe iii]	22.93	0.54	0.20	16.19	627	$1 \times 10^5$ [e]
[O iv]	25.89	0.49	0.18	54.94	555	$1 \times 10^4$ [e]
[Fe ii]	25.99	< 0.25	-	7.90	554	$2 \times 10^6$ [H], $1 \times 10^4$ [e]
[Ar iii]	8.99	0.99	0.33	27.63	2 060	$3 \times 10^5$ [e]
[Ar ii]	6.99	0.60	0.15	15.76	1 600	$4 \times 10^5$ [e]
[Ne v]	14.32	< 0.080	-	97.12	592	$3 \times 10^4$ [e]
<i>Herschel</i> /PACS						
[C ii]	157.74	7.4	2.2	11.26	91	$3 \times 10^3$ [H], 50 [e]
[O iii]	88.36	18.0	5.4	35.12	163	$5 \times 10^2$ [e]
[O i]	63.18	6.7	2.0	-	228	$5 \times 10^5$ [H]
[O i]	145.52	0.56	0.17	-	99	$1 \times 10^5$ [H]
[N iii]	57.32	2.50	0.78	29.60	251	$3 \times 10^3$ [e]
[N ii]	121.9	0.31	0.10	14.53	118	$3 \times 10^2$ [e]
[N ii]	205.18	< 0.29	-	"	70	45 [e]

The *ISO*/LWS fluxes can be found in Bergvall et al. (2000), Brauher et al. (2008), and Vasta et al. (2010).

(a) Upper limits are given as the  $3\text{-}\sigma$  uncertainty from the line fit.

(b) Excitation potential. Energy to create an ion. For H<sub>2</sub>, it is the energy to photodissociate the molecule.

(c) Excitation temperature. Temperature  $T = \Delta E/k$  required to populate the transition level.

(d) Critical density  $n_{\text{crit}}$  noted [H] for collisions with hydrogen atoms ( $T=100$  K and  $T=300$  K for the H<sub>2</sub> lines), [e] with electrons ( $T=10\,000$  K). Values are from Malhotra et al. (2001), Giveon et al. (2002), and Kaufman et al. (2006).

sion of most of the spectral lines. Derived physical conditions are presented in Section 4.

### 3. Modeling strategy

#### 3.1. Identification of the model components

We aim to model the IR emission from all 17 detected lines (except the MIR H<sub>2</sub> lines which will be modeled in a coming paper) listed in Table 2 to understand the conditions of the various media and the dominant processes at work in this low-metallicity starburst. The ISM is very heterogeneous, and over the scale of a galaxy, various phases with a wide range of conditions are mixed together.

In our spectral dataset, we notice that Haro 11 is typified by very intense [Ne iii], [Ne ii], [S iii], [S iv], [O iii], and [N iii] lines. These high-excitation lines require a hard radiation field which is naturally encountered in a compact H ii region. Stars in compact H ii regions are young, hence their UV radiation is harder, and SSCs are likely to contain massive stars which contribute to the production of hard photons. Moreover, the high critical densities of these lines (except the [O iii] line) favor their origin at the same location. Therefore, the intensity of these lines demonstrates the importance of the dense H ii region in the global spectrum of Haro 11. Moreover, the *Herschel* observations show bright [O i] and [C ii] lines, which are usual tracers of the neutral gas. In particular, the intensity of the [O i] lines indicates the presence of dense PDRs. These two dense (ionised and neutral) phases will be investigated first since they account for the emis-

With low critical density ( $\sim 300 \text{ cm}^{-3}$ ) and low ionisation potential (14.5 eV), the [N ii] 122  $\mu\text{m}$  line is a tracer of low-excitation diffuse gas rather than the dense H ii region. The intensity of [N ii] demonstrates the need for an additional diffuse low-ionisation component that is investigated in Section 5. Our subsequent modeling also shows that this diffuse phase is the main contributor to the [Ne ii] and [C ii] lines.

Therefore, the three main phases that we identify as necessary model components to account for the observed emission lines are: 1) a dense ionised phase (Sect. 4.1), 2) PDR (Sect. 4.2), 3) a diffuse low-ionisation medium (Sect. 5).

In addition, we discuss the possible presence of other model components that may influence the line predictions. The detection of the high-excitation [O iv] line is the driver of a discussion on the role of X-rays and XDRs in Section 6.3. The [O iii] line, which is the brightest of all MIR-FIR lines, has high excitation potential (35.1 eV) and low critical density ( $\sim 500 \text{ cm}^{-3}$ ). Although it is accounted for by the dense H ii model, it may originate as well from diffuse high-excitation medium that we do not model but briefly discuss in Section 6.2. Finally, we investigate the influence of magnetic fields on the cloud density profile and their impact on the PDR predictions in Section 6.1.

**Table 3.** Photometry data.

Instrument	Wavelength	Flux (Jy)	Uncertainty (Jy)	Reference
Chandra	2-10 keV	9.17e-09	1.03e-09	(1)
Chandra	0.5-2 keV	3.21e-08	0.43e-08	(1)
ROSAT	0.1-2 keV	4.41e-08	0.55e-08	(2)
FUSE	1150 Å	2.30e-03	0.33e-03	(3)
GALEX	1530 Å	3.63e-03	7e-05	(4)
GALEX	2315 Å	4.37e-03	4e-05	(4)
Cousins	0.439 $\mu$ m	8.03e-03	0.69e-03	(5)
Cousins	0.639 $\mu$ m	0.012	0.001	(5)
2MASS	1.25 $\mu$ m	0.013	0.001	(6)
2MASS	1.64 $\mu$ m	0.013	0.001	(6)
2MASS	2.17 $\mu$ m	0.014	0.001	(6)
IRAC	3.6 $\mu$ m	0.023	0.002	(7)
IRAC	4.5 $\mu$ m	0.029	0.003	(7)
IRAC	5.8 $\mu$ m	0.073	0.007	(7)
IRAC	8 $\mu$ m	0.177	0.018	(7)
IRAS	12 $\mu$ m	0.52	0.02	(8)
MIPS	24 $\mu$ m	2.51	0.03	(9)
IRAS	25 $\mu$ m	2.49	0.03	(8)
IRAS	60 $\mu$ m	6.88	0.04	(8)
MIPS	70 $\mu$ m	4.91	0.49	(9)
PACS	70 $\mu$ m	6.08	0.18	(10)
IRAS	100 $\mu$ m	5.04	0.03	(8)
PACS	100 $\mu$ m	4.97	0.15	(10)
MIPS	160 $\mu$ m	2.01	0.24	(9)
PACS	160 $\mu$ m	2.43	0.12	(10)
SPIRE	250 $\mu$ m	0.633	0.042	(10)
SPIRE	350 $\mu$ m	0.231	0.013	(10)
SPIRE	500 $\mu$ m	0.092	0.008	(10)
LABOCA	870 $\mu$ m	0.040	0.006	(7)

(1) Hayes et al. (2007); (2) Tajer et al. (2005); (3) Grimes et al. (2009); (4) Iglesias-Páramo et al. (2006); (5) Lauberts & Valentijn (1989); (6) Jarrett et al. (2000); (7) Galametz et al. (2009); (8) Sanders et al. (2003b); (9) Bendo et al. (2012); (10) Rémy et al. (2012).

### 3.2. Method

We use the 1D spectral synthesis code Cloudy v10.00, last described by Ferland et al. (1998), which includes photoionisation and photodissociation treatment (Abel et al. 2005), to model the multiple phases from which the emission lines originate. Since Haro 11 is not resolved in most of the *Spitzer* and *Herschel* bands, we have no spatial constraints. Thus, the model is reduced to a central source of energy surrounded by a spherical cloud. In the case of Haro 11, this central source is a starburst. The dense ionised gas that is closest to the central source with respect to the other phases that we model separately will yield the best constraints on the properties of the stellar cluster that is powering the model. Therefore we first derive the best fit model concentrating on the dense H II region diagnostics, which are the [Ne II] 12.8  $\mu$ m, [Ne III] 15.6  $\mu$ m, [S IV] 10.5  $\mu$ m, [S III] 18.7  $\mu$ m and 33.5  $\mu$ m, and the [N III] 57  $\mu$ m lines. Moreover, the interpretation of these ionic lines is less ambiguous than, for example, the [C II] line. Following this step, we will assess what this model predicts for the PDR phase.

The starburst ionises the inner edge of the cloud, where the H II region begins, and the radiative transfer is computed step by step progressively into the cloud. The distance from the source to the inner edge of the cloud is the inner radius ( $r_{\text{in}}$ ). Depending on where the calculation is stopped, the ionised, atomic, and molecular phases can be treated as the model is computed within one Cloudy model. Here we stop the models until the molecular

fraction  $\text{H}_2/\text{H}$  reaches 50% such that both the ionised and PDR phases are computed within the same model. We opt to impose pressure equilibrium throughout the models. This is particularly important for the density profile between different phases. We will come back to this assumption in Sect. 4.2.

#### 3.2.1. Parameter grid of the dense H II region

We vary the following 3 physical parameters in order to calculate our model grid: the age of the burst ( $A_{\text{burst}}$ ), the initial hydrogen density at the inner edge of the cloud ( $n_{\text{H}}$ ), and  $r_{\text{in}}$ , where the calculation starts (see Fig. 5 for an illustration). The age is varied from 2.4 to 5.0 Myr (Sect. 4.1.2),  $r_{\text{in}}$  from  $10^{20.0}$  to  $10^{22.0}$  cm (or 30 pc to 3 kpc, Sect. 4.1.3), and  $n_{\text{H}}$  from  $10^1$  to  $10^4$   $\text{cm}^{-3}$  (Sect. 4.1.1). The step size for  $A_{\text{burst}}$  is 0.2 Myr (linear step), and for  $r_{\text{in}}$  and  $n_{\text{H}}$ , we use 0.2 step sizes on a logarithmic scale.

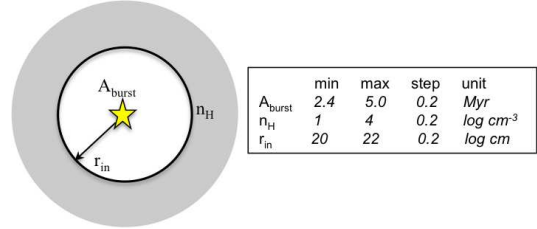


**Figure 5.** Geometry of the Cloudy model with the three free parameter that we vary in the grid: the age of the burst ( $A_{\text{burst}}$ ), inner radius ( $r_{\text{in}}$ ), and initial hydrogen density ( $n_{\text{H}}$ ). Parameter boundaries and step sizes are also indicated.

#### 3.2.2. $\chi^2$ evaluation

In order to find a solution for this ionised phase, we aim first to reproduce as best as possible the intensities of the ionic lines. For each individual model, the goodness of the fit is evaluated by computing the reduced  $\chi^2$ . The  $\chi^2$  is measured from a set of selected lines. The lines we consider to constrain the fit are the following: [Ne II] 12.8  $\mu$ m, [Ne III] 15.6  $\mu$ m, [S IV] 10.5  $\mu$ m, [S III] 18.7  $\mu$ m, and 33.5  $\mu$ m, because they are the brightest and relatively well understood, as well as the [N III] 57  $\mu$ m line from PACS which is also bright and expected to arise from the same medium. With 6 observations and 3 free parameters to fit, the degree of freedom is  $N = n_{\text{obs}} - n_{\text{param}} = 3$ . Best fit models are determined by minimising the reduced  $\chi^2$ . There are several lines that originate in part from the dense ionised gas that we do not consider when calculating the  $\chi^2$ , although we do discuss how the model predictions of these lines compare to the observations. We do not consider the high-excitation [O IV] line because it is faint and can be excited by several mechanisms (see Sect. 6.3). We do not include the [O III] and [N II] lines here as constraints for the dense H II region because our subsequent modeling shows that a fraction of these lines arises from a low density ionised medium which we consider in a later step (see Sect. 5).

### 3.3. Setting the input fixed parameters

#### 3.3.1. Incident radiation field

We use Starburst99 v6.0.2 (Leitherer et al. 2010) to reproduce the incident, wavelength-dependent radiation field density of

Haro 11. Following the UV-optical studies by Hayes et al. (2007) and Grimes et al. (2007), we assume a Salpeter IMF from 0.1 to 100  $M_{\odot}$  and stellar tracks from Padova AGB with metallicity  $Z = 0.004$ . According to Adamo et al. (2010), the stellar population of Haro 11 is very young. The present starburst started less than 40 Myr ago, and shows a formation peak at about 3.5 Myr. Knot B is dominated by a young starburst of 3.5 Myr, and knot C contains an older starburst of 9.5 Myr (Fig. 1). Therefore, we select the stellar spectrum of an instantaneous burst of a few Myr, letting the age of the burst be a free parameter, varying from 2.4 to 5.0 Myr. We also add to this the spectrum of an instantaneous burst of 9.5 Myr to account for the slightly older stellar population. We keep this age fixed since the ionising part of the stellar spectrum does not vary significantly for ages larger than 5 Myr, and will therefore not significantly affect the model predictions of the ionised gas. This starburst spectrum dictates the shape of the input energy source in Cloudy. The incident radiation field on the cloud is shown in purple in Figure 12. For the input luminosity of the central source, we take the total observed infrared luminosity of Haro 11:  $L_{\text{TIR}} = 1.4 \times 10^{11} L_{\odot}$ . This approximation assumes an energy balance between the UV and IR domains, i.e. that all of the UV photons are reprocessed in the IR by the gas and the dust. The emergent SED (bottom panel of Fig. 12) shows that this approximation is reasonable since only 20% of the total emergent luminosity is emitted in the UV-optical, and 80% in the IR. We discuss in more details the energy balance in Sect 7.1.

Haro 11 is detected in X-rays (e.g. Grimes et al. 2007). Previous studies on X-ray observations indicate the presence of soft ( $L_{0.5-2\text{keV}} = 1.9 \times 10^8 L_{\odot}$ ) and hard ( $L_{2-10\text{keV}} = 2.6 \times 10^8 L_{\odot}$ ) X-rays. Therefore we add to the input SED an X-ray component that reproduces the shape of the observed X-ray spectrum and of total luminosity  $5 \times 10^8 L_{\odot}$ . The effects of the X-rays in the models are discussed in Section 6.3.

### 3.3.2. Elemental abundances

The elemental abundances directly impact on the predicted line intensities. To match the observed abundances in Haro 11 as closely as possible, we use the abundances in the literature. Abundances of oxygen, nitrogen, neon, sulphur, and argon were obtained in knots B and C of Haro 11 by Guseva et al. (2012) using VLT/X-shooter observations in the optical. In particular, they find an oxygen abundance  $12+\log(\text{O}/\text{H})$  of 8.1 in knot B and 8.3 in knot C, giving a O/H twice as large as the value  $12+\log(\text{O}/\text{H})=7.9$  previously found by Bergvall & Östlin (2002), altering the determination of the metallicity from  $\sim 1/6$  to  $1/3 Z_{\odot}$ . We use the abundances in Guseva et al. (2012), averaged over the two knots, which have similar luminosities, for our calculations. Uncertainties on these abundances are 10%. For neon and sulphur, Guseva et al. (2012) find similar values to those found in Wu et al. (2008), derived from *Spitzer* data. The relatively high neon abundance is typical of BCDs (Izotov & Thuan 1999). For nitrogen, such high abundance is observed in a few BCDs (e.g. Thuan et al. 1996; Izotov & Thuan 1998; Pustilnik et al. 2004), and can be explained by the presence of Wolf-Rayet stars (Bergvall & Östlin 2002), which inject matter enriched in N and C into the ISM. For the other elements, we use gas-phase relative abundances typical of H II regions, based on an average of the abundances in the Orion Nebula determined by Baldwin et al. (1991); Rubin et al. (1991); Osterbrock et al. (1992); Rubin et al. (1993), and scaling them to the metallicity of Haro 11. The resulting carbon abundance is  $\log(\text{C}/\text{O}) = -0.15$ , which is relatively high compared to Izotov & Thuan (1999), where  $\log(\text{C}/\text{O}) \sim -0.5$ . However, Bergvall et al. (2006) find

that the ratio of C and O column densities is  $\sim -0.3$  (log) from the analysis of absorption lines in IUE and FUSE data. Such high value may indicate an enrichment in C and agrees with our adopted carbon abundance (assuming Orion-like C/O) within the uncertainties. For silicon, its abundance Si/O is low in the Orion abundance set compared to that usually found in BCDs, therefore we use the average abundance of  $\log(\text{Si}/\text{O}) = -1.5$  from Izotov & Thuan (1999). We consider the uncertainty on these theoretical abundances to be of a factor of 2. Table 4 summarizes the elemental abundances (and uncertainties) we use in Cloudy. The lack of measured abundances for the other elements limits their use to constrain the models (e.g. Fe, Si).

**Table 4.** Elemental abundances set in Cloudy.

Gas-phase composition	Abundance (uncertainty) in log
O/H	-3.79 (0.14)
N/H	-4.64 (0.12)
Ne/H	-4.44 (0.07)
S/H	-5.57 (0.10)
Ar/H	-6.20 (0.13)
C/H	-3.92 (0.3)
Si/H	-5.80 (0.3)
Fe/H	-5.92 (0.3)
Grain composition	Mass fraction
Carbonaceous	36%
Silicate	60%
PAH	4%
Dust-to-Gas mass ratio	$2.64 \times 10^{-3}$

Abundances of oxygen, nitrogen, neon, sulphur, and argon are from Guseva et al. (2012), silicon from Izotov & Thuan (1999), and the others are average abundances of the Orion Nebula determined by Baldwin et al. (1991); Rubin et al. (1991); Osterbrock et al. (1992); Rubin et al. (1993), scaled to the metallicity of Haro 11.

The main elemental composition O:C:Si:Fe in the grains is 4:9:1:1.

### 3.3.3. Dust properties

It is important to accurately set the dust properties for two reasons: (1) dust plays an important role in heating the gas through the photoelectric effect, which depends on the dust abundance and grain size distribution, and (2) the radiative transfer is strongly influenced by the properties of the grains. We first tried using the standard MRN grain size distribution (Mathis, Rumpl, & Nordsieck 1977), which failed to reproduce the observed dust emission in the MIR, falling below the photometry data by more than an order of magnitude. The MRN distribution underpredicts the number of small grains (minimum grain radius of 5 nm) and is usually not appropriate for modeling the MIR emission in galaxies. Standard dust models such as Draine & Li (2001) and Zubko et al. (2004) do include more small grains than the standard MRN model. Dust modeling of dwarf galaxies (e.g. Galliano et al. 2003, 2005; Galametz et al. 2011) also demonstrates the need for an increased abundance of smaller grains. Therefore, in Cloudy, we use the MRN distribution extended down to 1.1 nm to account for the very small grains. Other grain size distributions have been used to model the IR emission of galaxies, such as grain shattering distributions (Dopita et al. 2005), that we discuss in Section 7.1.2. We also use PAHs as described in Abel et al. (2008). Both grains and PAH abundances are scaled to the metallicity of Haro 11 ( $1/3 Z_{\odot}$ ), fixing the dust-to-gas mass ratio (D/G) to  $2.64 \times 10^{-3}$  ( $\sim 1/400$ , the

Galactic D/G is  $\sim 1/150$ ). This yields a ratio of visual extinction to hydrogen column density,  $A_V/N(H)$ , of  $10^{-22} \text{ mag cm}^{-2}$ .

### 3.4. Limitations of the approach

Our first limitation lies on the geometry of our modeling that we aim to constrain as much as possible with diagnostics from a large set of spectral lines. Some of the derived parameters of the compact H II region are strongly dependent on the (simple) geometry we impose on the model, which we will see is a recurring theme throughout the paper. The parameters that are best constrained, irrespective of the geometry, are the electron density, temperature and mass of ionised gas. As found in Section 4.1.3, the geometrically thin ionised gas shell, in combination with the large inner radius ( $\sim 1 \text{ kpc}$ ) that describes the model solution of the dense H II region, seems physically implausible. Despite the geometry of the model, we refer to it with the term compact since this model component represents what is observationally described as a compact H II region. This is a direct result of assuming a single region with a single central source. Although we are aware that the knots B and C of Haro 11 are spatially separated in the optical, we do not have the spatial resolution in the *Spitzer* and *Herschel* observations to treat them separately. If, for example, we were to construct a model as the sum of several regions – as seems reasonable when perusing the optical images – the inner radius of each region would have to decrease in order to obtain a similar effective  $U$  parameter, while the shell thickness would increase in order to obtain the same gas mass, thus evolving towards a model with a more geometrically thick layout. It is impossible to obtain reliable and reproducible results using such a complex model, without better observational constraints on the actual source distribution, i.e. spatially resolved spectroscopy. In this paper we focus on the derived parameters that are least sensitive on the actual assumed geometry. In Section 7.1, we discuss the spectral energy distribution resulting from the combination of models of the various phases in terms of energy balance, but we do not pretend to accurately fit the total SED because of these geometry issues.

Our second limitation lies in the evaluation of the goodness of the fits. It is mainly weighted by the elemental abundance uncertainties, which can be up to a factor of 2, and by the observational uncertainties (up to 40%). Therefore, when comparing the model predictions to observed intensities, we aim for a match within a factor of 2.

## 4. A model of the H II region and PDR: $\mathcal{C}$

### 4.1. The compact H II region

The results of the computed grid are displayed in Figure 6. It shows the intensity predictions of the compact model labeled  $\mathcal{C}$  for each ionic line as a function of density,  $n_H$ , and inner radius,  $r_{in}$ , for a starburst age of 3.7 Myr (age of the best fit model, see Sect. 4.1.2). In this section, we discuss the influence of each grid parameter on the model predictions and possible solution values. These parameters are linked via the quantity  $U$ , which is the ionisation parameter, defined as the dimensionless ratio of the incident ionising photon surface density to the hydrogen density  $n_H$ :  $U = \frac{Q(H)}{4\pi r_{in}^2 n_H c}$ , where  $Q(H)$  is the rate of hydrogen-ionising photons striking the illuminated face and  $c$  is the velocity of light.  $U$  describes how many ionising photons arrive per atom.

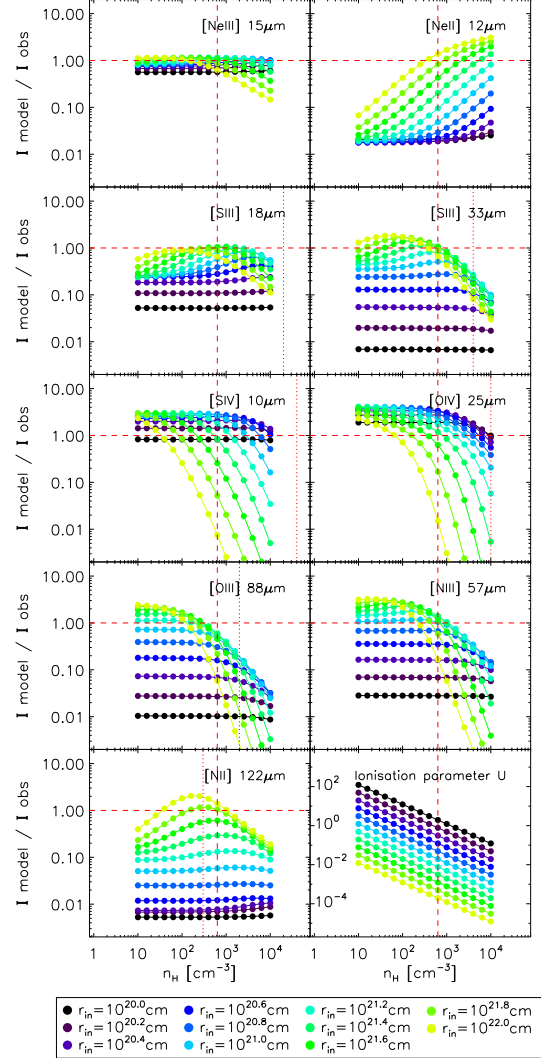


**Figure 6.** Predicted intensities for model  $\mathcal{C}$  ( $I_{model}$ ) normalised by their observed value ( $I_{obs}$ ) for all ionic lines considered, as a function of  $n_H$  and  $r_{in}$  for a given starburst age (of 3.7 Myr). The vertical dashed line shows the best fit model density  $n_H = 10^{2.8} \text{ cm}^{-3}$ , and the vertical dotted line the critical density of the ionic specie, if within the range displayed. The best fit inner radius is  $r_{in} = 10^{21.4} \text{ cm}$  (green symbols).

#### 4.1.1. The density of the gas

In general terms the predicted line intensities are dependent on the gas density through both the critical density of each atom, and the ionisation parameter,  $U$ . Line intensities increase with increasing gas density until the critical density of a fine-structure line is reached. Above such critical density, the de-excitation process is dominated by collisions rather than radiative decay. Therefore the maximum gas density is well determined by the critical density of the brightest line tracers. The gas density also plays an important role in determining the population of the dif-

ferent ionisation stages. The ionisation parameter,  $U$ , is inversely proportional to the density (bottom right panel of Fig. 6).

We find that the minimum  $\chi^2$  occurs for a solution with a density around  $10^{2.8} \text{ cm}^{-3}$  (dashed vertical line in Fig. 6). This derived gas density compares well with density diagnostics proposed in the literature, for example, based on the ratio of the [S III] lines at 18.7 and  $33.5 \mu\text{m}$  (Houck et al. 1984). This ratio is sensitive to the density since these lines originate from the same ion but with significantly different critical densities (Table 2). From Abel et al. (2005) and requiring  $\frac{[\text{S III}] 18 \mu\text{m}}{[\text{S III}] 33 \mu\text{m}} \sim 1.0$ , we obtain a density of the ionised gas of  $n_{\text{H}} = 10^{2.7} \text{ cm}^{-3}$ . The value of the electron density predicted by the diagnostic plot in Houck et al. (1984) is also around  $10^{2.8} \text{ cm}^{-3}$ . Following the method from Kingsburgh & Barlow (1992, 1994) who use the programs *EQUIB* and *RATIO* (developed at UCL by I. D. Howarth and modified by S. Adams), we also find  $n_{\text{H}} \sim 10^{2.8} \text{ cm}^{-3}$ .

#### 4.1.2. The age of the burst

The spectrum of the starburst (intensity and shape) changes drastically with time in the age range considered here. The age of the burst sets the hardness of the incident radiation field. Figure 7 shows line ratios of [Ne III]/[Ne II], [O IV]/[Ne III], [O III]/[N III], [O III]/[S IV], and [S IV]/[S III]  $18 \mu\text{m}$  as a function of burst age. The observed ratios agree with an age of burst of 3.5–5 Myr. These values are also in agreement with the age of 3.5 Myr for the brightest knot B and 9 Myr for knot C, and a mixture of very young and older bursts, found in Adamo et al. (2010). After 5 Myr, the ionising part of the burst spectrum decreases, the high ionisation lines start to disappear, and in particular the [Ne III]/[Ne II] ratio drops off (bottom panel of Fig. 7). This is why we do not compute models with  $A_{\text{burst}} > 5 \text{ Myr}$  in our grid. The best fit on the neon lines favours a relatively young burst, of about 3 Myr. However, the emission of the highest excitation potential [O IV] line (54.9 eV) is rather favoured by models with ages between 3.7 and 4.7 Myr. Indeed this time frame corresponds to the time needed for the onset of Wolf-Rayet stars. A burst age of 4.7 Myr is also a good match to the [Ne III]/[Ne II] ratio, although it does not agree with the intensity of the [S IV] line, which is one of the lines that has the highest weight in the  $\chi^2$ . The best single solution model in that case has an age of burst of 3.7 Myr.

#### 4.1.3. The inner radius

All lines are sensitive to the inner radius  $r_{\text{in}}$ . Its choice has no direct influence on the hardness of the radiation field, but rather on its intensity. With increasing radius, the total input luminosity is distributed over a larger surface, decreasing the number of ionising photons per surface area, and therefore the ionisation rate.  $U$  decreases as the inverse square of the radius. Intensities of species with a high ionisation potential, such as [O IV], decrease with increasing  $r_{\text{in}}$ , and the inverse is observed for low ionisation species such as [N II]. For  $r_{\text{in}} < 10^{21.0} \text{ cm}$ , atoms are preferably present in high ionisation states. Models with such small  $r_{\text{in}}$  often predict too much [O IV] and [S IV], and not enough [Ne II] and [S III]. [Ne III] and [S IV] intensities are constant at low  $r_{\text{in}}$  and then drop with increasing  $r_{\text{in}}$ . [S III], [N III] and [O III] intensities increase with low  $r_{\text{in}}$  ( $< 10^{21.5} \text{ cm}$ ) because of an ionisation balance between  $\text{S}^{2+}$ ,  $\text{N}^{2+}$ ,  $\text{O}^{2+}$  and  $\text{S}^{3+}$ ,  $\text{N}^{3+}$ ,  $\text{O}^{3+}$ . Then their intensities drop with increasing  $r_{\text{in}}$ . The opposite effect is observed for the lower ionisation state species such as [Ne II] and [N II] which increase with  $r_{\text{in}}$ .

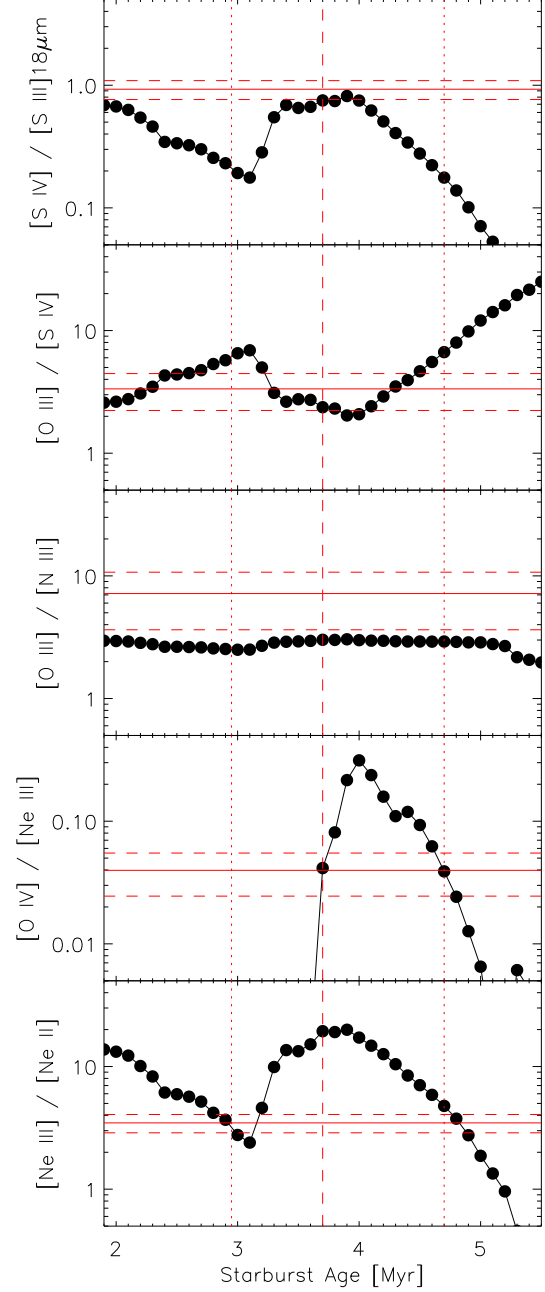


**Figure 7.** Model predicted intensity ratios as a function of burst age  $A_{\text{burst}}$ , for a hydrogen density of  $10^{2.8} \text{ cm}^{-3}$ , and inner radius of  $10^{21.4} \text{ cm}$ . The true burst age of these models is an average of  $A_{\text{burst}}$  and the older stellar population of 9.5 Myr, although the latter has a negligible influence on the high-ionisation lines considered here. The horizontal solid lines represent the observed ratios and the dashed lines the uncertainties on the ratios. The vertical dashed line shows the solution burst age of 3.7 Myr, and the vertical dotted lines the age of 3 Myr and 4.7 Myr that would better match the [Ne III]/[Ne II] ratio.



The observations are best matched for an inner radius of  $10^{21.4}$  cm (800 pc). At that distance, the model cloud is a very thin shell of large radius, at the center of which resides the central starburst. The resulting geometry is plane-parallel. This is not a realistic geometry, as discussed in Sect. 3.4, but we do not aim to model the spatial structures in Haro 11.

#### 4.1.4. Parameters of the best fit model $\mathcal{C}_{HII}$

We have minimised the  $\chi^2$  to find the parameters of the best fit model for the compact H II region described above. Figure 8 shows contour plots of the reduced  $\chi^2$  computed for our grid of models. Contour levels at 1- $\sigma$ , 3- $\sigma$ , and 5- $\sigma$  from the minimum  $\chi^2$  are displayed in orange. The intensities of the spectral lines included in the fit are best reproduced with the parameters:  $n_H = 10^{2.8} \text{ cm}^{-3}$ ,  $A_{\text{burst}} = 3.7 \text{ Myr}$ , and  $r_{\text{in}} = 10^{21.4} \text{ cm}$ . The ionisation parameter is  $U = 10^{-2.5}$ . The reduced  $\chi^2$  of this model solution, which has the minimum  $\chi^2$ , is 1.48. This value is close to 1, indicating that this model describes the data well, with a probability of  $\sim 70\%$ . For clarity throughout the following Sections, we will refer to this model solution of the compact H II region as  $\mathcal{C}_{HII}$ .

With  $\mathcal{C}_{HII}$ , the strongest MIR line, [Ne III], is reproduced within 15%, as well as the [O IV] line. The two [S III] lines are achieved within 5% and their ratio within 1%. The modeled [S IV] and [Ar III] lines deviate by 20%. The [N III] line is reproduced within 40%. The [Ne II] line, however, is under-predicted by a factor of 5 by  $\mathcal{C}_{HII}$ .

We then compare the line intensities predicted by  $\mathcal{C}_{HII}$  to the PACS lines, [O III] and [N II]  $122 \mu\text{m}$ , which were not used to constrain the model fit since they can originate from less dense ionised gas. We find that [O III] is under-predicted by a factor of 2, which is within our expectations, while the [N II]  $122 \mu\text{m}$  is under-predicted by a factor of 4. The dense H II region is not the primary source of [N II]. The prediction for the [N II]  $205 \mu\text{m}$  line falls below its derived upper limit.

We discuss the origin of the [Ne II] and [N II] lines from diffuse low-ionisation gas in Sect. 5 and the possible origin of the [O III] emission from diffuse high-ionisation gas in Sect. 5.

We also find that  $\mathcal{C}_{HII}$  contributes very little to the [O I] emission (3%), as expected since the atomic oxygen is a tracer of the neutral gas.  $\mathcal{C}_{HII}$  shows very little contribution to the [C II] (<1%) and [Si II] (11%) lines as well. The energy required to create  $\text{C}^{++}$  ions is 24.4 eV, close to that of  $\text{S}^{++}$ , therefore when the radiation field is sufficiently hard, as is the case inside the H II region, C is doubly rather than singly ionised.

#### 4.2. The dense photodissociation regions: $\mathcal{C}_{PDR}$

We subsequently investigate the properties of the neutral gas and compare model predictions to the [C II] and [O I] 63 and  $145 \mu\text{m}$  lines. To this end, we extend  $\mathcal{C}_{HII}$  into the atomic phase and the outer envelope of the molecular phase, until the molecular fraction  $\text{H}_2/\text{H}$  reaches 99%. The modeled shell is fully covered by the gas. The ionised cloud, with average density of  $10^{2.8} \text{ cm}^{-3}$ , transitions from the H II region into a dense PDR, which is where the [O I] originates. This transition between these two phases in a constant pressure model translates into a jump of the gas density at the ionisation front. With this model, the average density of the PDR is  $10^{5.1} \text{ cm}^{-3}$ . The radiation field striking the PDR is:  $G_0 = 3.5 \times 10^3$  Habing unit ( $1.6 \times 10^{-3} \text{ ergs cm}^{-2} \text{ s}^{-1}$ ). The heating of the gas in the PDR is dominated by grain photoelectric heating (85%), and there is a second order contribution from

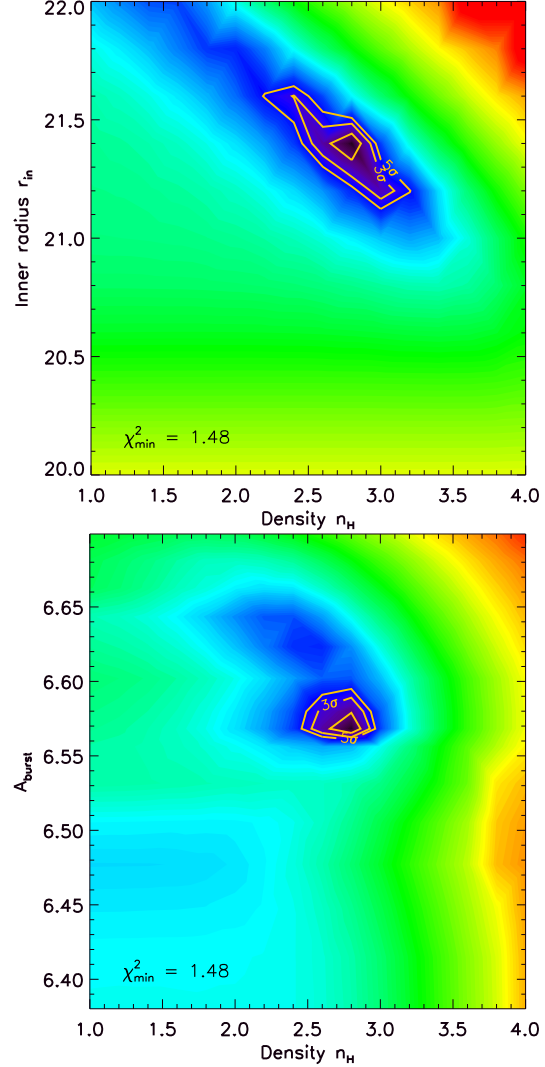


**Figure 8.** Contour plots of the  $\chi^2$  values of the 3D grid (log scale). The parameters are given in logarithmic values. Units are  $\text{cm}^{-3}$  for the density, yr for the burst age, and cm for the inner radius. The minimum reduced  $\chi^2$  found for  $\mathcal{C}_{HII}$  is  $\chi^2_{\text{min}} = 1.48$ . Contour levels at 1- $\sigma$ , 3- $\sigma$ , and 5- $\sigma$  from the minimum  $\chi^2$  are displayed in orange. There are 5 other models within 3- $\sigma$  of  $\chi^2_{\text{min}}$ . The red color on the plots correspond to  $>1000\text{-}\sigma$  level. *Top:*  $\chi^2$  contours in the  $n_H$ - $r_{\text{in}}$  plane, for  $A_{\text{burst}} = 3.7 \text{ Myr}$  (or 6.57 in log). *Bottom:*  $\chi^2$  contours in the  $n_H$ - $A_{\text{burst}}$  plane, for  $r_{\text{in}} = 10^{21.4} \text{ cm}$ .

collisions with  $\text{H}^0$ , He, and  $\text{H}_2$ . The cooling is done by radiative de-excitation mainly of the [O I]  $63 \mu\text{m}$  (65%), [Si II] (20%), [C II]  $157 \mu\text{m}$  and [O I]  $145 \mu\text{m}$  (<7% each) lines. At such low  $A_V < 1$ , the [O I] lines are optically thin.

The [O I] 63 and  $145 \mu\text{m}$  absolute intensities are overestimated by a factor of 10, while their ratio is reproduced within 15% by this dense PDR component. Along with the [O I]  $63 \mu\text{m}$

line, [C II] 157  $\mu\text{m}$  and [Si II] 35  $\mu\text{m}$  are the brightest PDR lines. While the [Si II] line intensity is over-predicted by a factor of 2 by the dense model, the [C II] line agrees with the observation within 10%.

The consistent over-prediction of the two [O I] lines may be explained by the fact that, in reality, the dense PDR does not cover the full dense H II region. Assuming that all of the [O I] arises from a single dense phase (and not the diffuse gas, see Sect. 5.3), we reduce the covering factor of the dense PDR to only 10%, which is a proxy for dense clumps (Hunter et al. 2001; Groves et al. 2008). The PDR model with a covering factor of 1/10 matches the observed [O I] emission, but under-estimates the [C II] emission by an order of magnitude. The main conclusion from this is that the dense PDR component cannot account for the bulk of the [C II] emission observed in Haro 11, but only for 10%. This mismatch for the [C II] is due to the relatively low critical density of [C II] ( $2 \times 10^3 \text{ cm}^{-3}$ ) compared to the high density reached in the PDR ( $n_{\text{PDR}} = 10^{5.1} \text{ cm}^{-3}$ ), generated by the pressure equilibrium and the drop of gas temperature between the ionised and neutral phases. Indeed, Cloudy PDR models with constant densities of  $\sim 10^{3.5} \text{ cm}^{-3}$  and a covering factor of unity would reproduce the absolute intensity of the two [O I] lines simultaneously, and yet under-predict the [C II] by a factor of 2. Moreover, the H I mass of such models would exceed the upper limit of  $10^8 M_{\odot}$  found by Bergvall et al. (2000).

The small fraction of [C II] that originates from the dense PDR is at odds with the finding of Bergvall et al. (2000), who estimate that more than 80% of the observed [C II] in Haro 11 comes from the neutral gas. They use stellar clusters of  $T_{\text{eff}} \sim 35\,000\text{--}40\,000 \text{ K}$  to account for the [O III] 88  $\mu\text{m}$  emission, which contributes less than 20% to the [C II] emission, and they assume that the rest of the [C II] (>80%) is associated with PDRs. Then, they find  $n_{\text{PDR}} = 2 \times 10^3 \text{ cm}^{-3}$  using the Kaufman et al. (1999) model, which assumes a constant density. The much higher density that we find is compatible with the findings of Vasta et al. (2010) who analysed ISO observations with PDR models for several dwarf galaxies, including Haro 11, and find PDR densities between  $10^4$  and  $9 \times 10^4 \text{ cm}^{-3}$ , and  $G_0$  between 60 and  $8 \times 10^2$  Habing. They also estimate that 10 to 60% of [C II] comes from the ionised gas, which is in agreement with the diffuse ionised model contribution to the [C II] line that we discuss in Sect. 5.3.

We have also explored the influence of cloud geometry on the line predictions by using the PDR model Kosma- $\tau$  (Röllig et al. 2006), in which the illumination of the cloud is external, simulating a spherical cloud structure. At corresponding values of  $n_{\text{H}}$  ( $10^{5.1} \text{ cm}^{-3}$ ) and  $G_0$  ( $3.5 \times 10^3$  Habing) found with Cloudy, Kosma- $\tau$  predicts ratios of [O I] 145  $\mu\text{m}$ /[C II]  $\sim 1$  and [O I] 145/63  $\mu\text{m}$   $\sim 0.05$ . The [O I] 145  $\mu\text{m}$ /[C II] model ratios are over-predicted, as found with Cloudy, compared to our observed value of 0.08. However, if we attribute only 10% of the [C II] emission to the PDR, then [O I] 145  $\mu\text{m}$ /[C II]<sub>PDR</sub>  $\sim 0.1$  from Kosma- $\tau$ , which is in line with our observations. The spherical geometry affects both [O I] and [C II] lines similarly to first order, and is not the primary reason for the discrepancy between observed and predicted [C II] intensities.

We prefer to impose the pressure equilibrium between the compact H II region and the dense PDR, because this gives physical insight into the presence of dense but fragmented PDRs (e.g. Hunter et al. 2001). Although the pressure equilibrium assumption is not valid on large scales (nor is the assumption of a constant density) and, in particular, is expected to break in molecular clouds, here we do not model the molecular phase. We are interested in the interface between the dense H II region

and the PDR, the presence for which there is observational evidence. This model solution of the dense PDR with covering factor of 10% is noted  $\mathcal{C}_{\text{PDR}}$ . Next, we will discuss possible ways to lower the density in the PDR to account for the [C II] emission, by either combining a high density with a low density model (Sect. 5.3), representative of the multi-phase ISM of galaxies, or by including a magnetic field (Sect. 6.1).

## 5. A model for the diffuse medium: $\mathcal{D}$

### 5.1. Need for a softer radiation field

The major discrepancies between observations and model predictions in the ionised gas are seen for the [Ne II] 12.6  $\mu\text{m}$  and [N II] 122  $\mu\text{m}$  lines, which are both under-predicted by a factor of  $\sim 5$  in the dense H II region model  $\mathcal{C}_{\text{HII}}$ , which is not unexpected. With excitation potentials of 14.5 and 21.6 eV respectively, emission of  $\text{N}^+$  and  $\text{Ne}^+$  originates only from the ionised gas, from both the dense H II region and the diffuse medium. For [N II] 122  $\mu\text{m}$ ,  $\mathcal{C}_{\text{HII}}$  does not reproduce the observed value even when varying the 3 free parameters. Only  $r_{\text{in}} > 10^{21.8} \text{ cm}$  may agree (bottom left panel of Fig. 6). The contribution of the compact H II region to this line is thus marginal; mostly because the radiation field produced by the young starburst is too hard and favors the ionisation of  $\text{N}^{++}$  rather than  $\text{N}^+$ . For the [Ne II] line, a small change in the age of the burst would impact on its prediction, as discussed in Sect. 4.1.2. For the same values of density and inner radius, a model of age 3 Myr (instead of 3.7 Myr) would agree better with the observed intensity of [Ne II]. For a burst age of 3.7 Myr, higher densities ( $n_{\text{H}} > 10^3 \text{ cm}^{-3}$ ) and inner radii ( $r_{\text{in}} > 10^{21.6} \text{ cm}$ ) are required to reproduce the observed [Ne II] (top right panel of Fig. 6). However, such values of  $n_{\text{H}}$  and  $r_{\text{in}}$  would no longer agree with the other ionic lines. In order to reconcile the modeled [Ne II] and [N II] with their observations, a component with softer radiation field is required. This highlights the fact that one component is not enough the account for the emission of all the observed lines due to the presence of several phases in the ISM of galaxies with different properties. Our physical picture of the ISM of dwarf galaxies is of a highly permeable medium, where some of the ionising photons from the central starburst escape the H II region and travel large distances. This means that in dwarf galaxies, larger effective volumes can be maintained in an ionised state, compared to those of dusty starbursts.

To model this additional ionised component we have tried three different methods: (1) set the cloud further away (higher  $r_{\text{in}}$ ) under the same starburst conditions, and allowing the density to be a free parameter, (2) stop  $\mathcal{C}_{\text{HII}}$  before it reaches the ionisation front and take the output spectrum as the input spectrum of a lower density medium, (3) opt for a softer radiation field by including a scaled local interstellar radiation field. However, all of these methods fail to reproduce the observed line intensities. Either the radiation is still too hard (case (1) and (2) when stopping too early), or too soft (case (3) and (2) when stopping too close to the ionisation front).

The radiation field that works best to explain the observed [Ne II] and [N II] lines is a representative stellar SED from the Kurucz library of relatively low temperature (see next subsection). This is supported by the fact that more evolved stars producing low energy photons are present in Haro 11 (Micheva et al. 2010) but not accounted for in the compact model  $\mathcal{C}$  ( $\mathcal{C}_{\text{HII}} + \mathcal{C}_{\text{PDR}}$ ). This older population affects mainly the emission of [N II], [Ne II], and to a lesser extent [S III].

### 5.2. Properties of the model $\mathcal{D}$

We ran constant density models of diffuse ionised gas, stopped at the ionisation front, with stellar temperature between 20 000 and 40 000 K. The best fit to the [N II] 122  $\mu$ m and [Ne II] emission is obtained for a stellar temperature of 35 000 K. Figure 9 shows how the [N II], [Ne II], [S III], and [C II] lines vary with density for several values of  $r_{\text{in}}$ . We refer the reader to the Sections 4.1.1 and 4.1.3 for an interpretation of the behavior of the lines. The range of possible solutions for the [N II] 122  $\mu$ m emission are densities below  $10^3 \text{ cm}^{-3}$  and  $r_{\text{in}}$  higher than  $10^{21.0} \text{ cm}$ . [Ne II] also agrees well with these conditions. At  $T_{\text{eff}}$  of 35 000 K, [S III] also emits, but remains below its observed value. Very little [N III], [Ne III], [O III], and [S IV] are produced in this diffuse component, and no [O IV]. Although [N II] 122  $\mu$ m has a relatively low critical density, the density of the  $\text{N}^+$  emitting medium is usually well constrained by the [N II] 205  $\mu$ m line. Unfortunately, the [N II] 205  $\mu$ m line is difficult to observe with PACS because of spectral leakage (see Sect. 2.2). The upper limit on the [N II] 205  $\mu$ m line sets an upper limit on the ratio [N II] 205/122  $\mu$ m of 0.75 which corresponds to a lower limit on the density of the “diffuse” gas component of  $10 \text{ cm}^{-3}$  (e.g. Rubin et al. 1994; Oberst et al. 2006). The [N II] 122  $\mu$ m line critical density sets an upper limit of  $10^3 \text{ cm}^{-3}$ . Models with densities between 10 and  $10^3 \text{ cm}^{-3}$  work equally well for the “diffuse” medium in accounting for the [N II] 122  $\mu$ m and [Ne II] emission.

### 5.3. [C II] contribution from the model $\mathcal{D}$

Since  $\mathcal{C}_{\text{PDR}}$  predicts very little [C II] 157  $\mu$ m, we expect a significant contribution of the diffuse medium to the  $\text{C}^+$  emission.  $\text{C}^+$  is usually found in the surface layers of far-UV illuminated PDRs (Stacey et al. 1991; Negishi et al. 2001), but it can also come from the ionised gas, with a contribution up to 50% (Madden et al. 1993; Carral et al. 1994; Heiles 1994; Abel et al. 2005). With ionisation potentials lower than that of hydrogen, both  $\text{C}^+$  and  $\text{Si}^+$  can be produced by low energy photons or excited by collisions with electrons or hydrogen atoms, depending on the degree of ionisation from the emitting medium.

Figure 9 shows the predicted [C II] line intensities from the diffuse medium with a stellar temperature of 35 000 K, as a function of gas density. The contribution of the diffuse phase (ionised+neutral) is in filled circles, and the contribution of the ionised phase only shown by open circles. Calculations are stopped when molecules start to form and the fraction of  $\text{H}_2/\text{H}$  reaches 10%. At low  $n_{\text{H}}$ , the empty and filled circles are very close: a large fraction of the [C II] can arise from the ionised phase, until [C II] is collisionally de-excited by  $e^-$  ( $n_{\text{crit}} = 50 \text{ cm}^{-3}$ ), and emits mostly in the neutral phase, its intensity then increasing with density. At  $r_{\text{in}} = 10^{22.2} \text{ cm}$ , the [C II] predictions decrease for  $n_{\text{H}} > 10^2 \text{ cm}^{-3}$ , because the atomic phase is very thin as the material is cold and enters quickly into the molecular phase where the models stop. We disregard these models which do not predict enough [C II]. The range of possible solutions for the [C II] 157  $\mu$ m emission are  $r_{\text{in}}$  higher than  $10^{21.4} \text{ cm}$ , and are degenerate in  $n_{\text{H}}$ . We can set a low-density case where  $n_{\text{H}} = 10 \text{ cm}^{-3}$  – for example. Then  $r_{\text{in}} = 10^{21.8} \text{ cm}$  is the best fit, and [C II] comes mostly from the ionised phase, accounting for ~45% of the observed value. We also consider a high-density case where  $n_{\text{H}} = 10^3 \text{ cm}^{-3}$ , and  $r_{\text{in}} = 10^{21.8} \text{ cm}$ . In this case, [C II] is mostly emitted in the neutral phase, accounting for ~40% of the observed value. Both models fill a larger volume than the compact model  $\mathcal{C}$ .

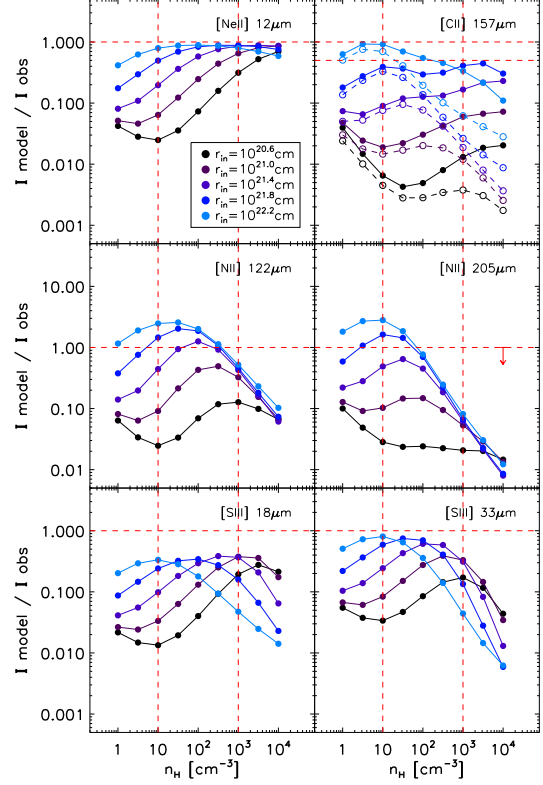


**Figure 9.** Predictions for the model  $\mathcal{D}$  of the [Ne II], [C II], [N II], and [S III] line intensities ( $I_{\text{model}}$ ), normalised by their observed value ( $I_{\text{obs}}$ ) as a function of density  $n_{\text{H}}$ . Models are for a diffuse ionised/neutral gas, with constant density, stellar temperature of 35 000 K, and are stopped when molecules start to form. The [S III], [Ne II] and [N II] lines emit in the ionised phase. The contribution of the ionised phase to the [C II] line is indicated with open circles. The vertical dashed lines indicate density values of the diffuse models  $\mathcal{D}_l$  ( $n_{\text{H}} = 10 \text{ cm}^{-3}$ ) and  $\mathcal{D}_h$  ( $n_{\text{H}} = 10^3 \text{ cm}^{-3}$ ) defined in Sect. 5.3.

#### 5.3.1. Constraint from the H I 21-cm line

The H I 21-cm mass upper limit of  $10^8 M_{\odot}$  from Bergvall et al. (2000) is an important gas diagnostic of the diffuse atomic gas and brings a strong constraint that we can use to differentiate between the low-density and high-density case models. The H I mass from  $\mathcal{C}_{\text{PDR}}$  is  $10^7 M_{\odot}$ . While the models from Fig. 9 were stopped at a fraction of  $\text{H}_2/\text{H}$  reaching 10% to compute entirely the ionised and atomic phases, most of those models exceed the H I mass upper limit. By stopping those models when the upper limit on the H I mass is reached, we find that the low-density case model contribution to the [C II] line is unchanged since it comes from the ionised phase, while the high-density case model contributes to only ~20% of the [C II] line intensity, since the atomic phase is stopped at lower  $A_V$  than previously computed.

For the rest of this study, we refer to the low-density case model as  $\mathcal{D}_l$ , and to the high-density case model as  $\mathcal{D}_h$ . We cannot exclude the presence of a diffuse neutral gas, but in all cases, there is a prominent contribution to the [C II] from the ionised gas. We estimate that ~40% originates in  $\mathcal{D}_l$ ; the rest coming

from  $\mathcal{C}_{PDR}$  and little from  $\mathcal{D}_h$ . Moreover, the diffuse models do not contribute more than 15% to the [O I] lines, which are reliable tracers of the PDR.

## 6. Influence from other possible components

### 6.1. Magnetic fields

Magnetic fields impact the model solution, dominating the pressure deep into the cloud, and they are expected to be important in star-forming regions (Shaw et al. 2009). Robishaw et al. (2008) found magnetic fields on the order of a few mG in ULIRGs, from OH Zeeman splitting. In local dwarf irregular galaxies, magnetic fields are found to be weak, of a few  $\mu\text{G}$  to 50  $\mu\text{G}$  in more extreme cases (e.g. NGC 1569, NGC 4214; Chyży et al. 2011; Kepley et al. 2010, 2011). No study on magnetic fields has been conducted for Haro 11, so we did not include them in our grid calculation. Nevertheless, in view of the fact that we have found that the density of the dense PDR plays a determining role in the predicted line fluxes, we investigate the influence of adding a magnetic field  $B_{\text{mag}}$  of strength 1  $\mu\text{G}$  to 3 mG to the solution model  $\mathcal{C}$  described in Sect 4.

The magnetic field ( $B_{\text{mag}}$ ) is expressed as a pressure term ( $P_{\text{mag}}$ ) through the cloud by the following equation:

$$P_{\text{mag}} = \frac{B_{\text{mag}}^2}{8\pi} \text{ and } B_{\text{mag}}(r) = B_{\text{mag}}(0) \left( \frac{n_H(r)}{n_H(0)} \right)^\kappa, \text{ where } \kappa = 2/3(1)$$

where  $r$  is the depth of the cloud,  $B_{\text{mag}}(0)$  and  $n_H(0)$  are the initial values of the magnetic field and hydrogen density. This density–magnetic field relationship from Crutcher (1999) corresponds to the case where gravity dominates over magnetic support in the cloud collapse, and the magnetic flux is conserved. Figure 10 shows the predicted [C II] and [O I] intensities with increasing  $B_{\text{mag}}$ . For low values of  $B_{\text{mag}}$ , thermal pressure, expressed as  $P_{\text{gas}} \propto n_H T_{\text{gas}}$ , dominates and the densities in the PDR are high, with strong emission of [O I], as seen previously. With increasing  $B_{\text{mag}}$ , magnetic pressure starts to dominate over gas pressure and the transition into the PDR is smooth, resulting in lower densities in the PDR, and less emission of [O I]. The [C II]/[O I] ratio increases with increasing  $B_{\text{mag}}$ . The [C II] prediction falls between a factor of 0.5 and 1 of its observed value for all models. Values of  $B_{\text{mag}}$  up to  $10^{-3.75}$  G predict enough [O I] emission. For  $B_{\text{mag}} > 10^{-3.75}$  G, the models under-predict the intensity of the PDR lines, which would require extra input power, although we are still within the errors (factor of 2).

However, when lowering the density, the size of the PDR layer increases, and the H I mass as well. With no magnetic field, we find  $M(\text{H I}) = 10^7 M_\odot$  with a covering factor of  $\sim 10\%$ . For  $B_{\text{mag}} > 10^{-4}$  G, we find  $M(\text{H I}) > 2 \times 10^8 M_\odot$  for a covering factor of unity. By increasing the magnetic field strength, we go from a picture of small dense clumps to a more diffuse extended medium, which again does not agree with the observational upper limit on the H I mass. Moreover, high field strengths ( $> 100 \mu\text{G}$ ) may be found in the cores of star formation, but are unlikely to hold on galaxy-wide scales. Models with  $B_{\text{mag}} > 10^{-4}$  G are therefore discarded and appear in the shaded grey area on Fig. 10. The model with  $B_{\text{mag}}$  of  $10^{-4}$  G is noted  $\mathcal{C}_B$ . Then, if we consider that all of the [O I] 145  $\mu\text{m}$  emission originates in the PDR, we can consequently scale the [C II] intensity and we estimate the contribution of the PDR to the [C II] line to be from 10% up to at most 50% in strong magnetic field cases.

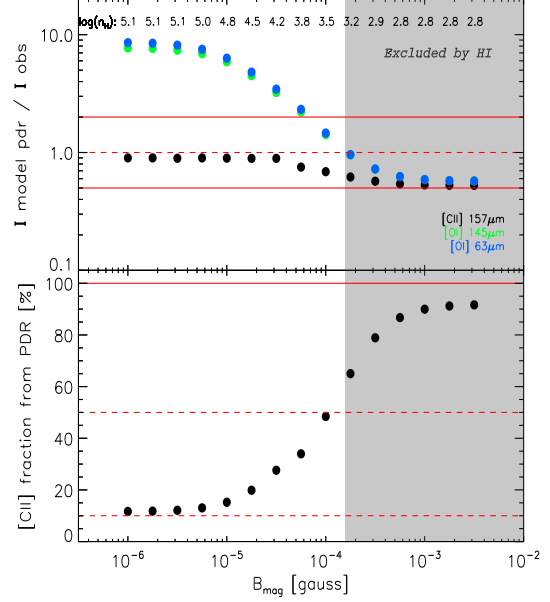


**Figure 10.** Influence of the magnetic field on the PDR lines. *Top:* Model predictions of the [C II] and [O I] intensities ( $I_{\text{model}}$ ) normalised by their observed value ( $I_{\text{obs}}$ ) as a function of magnetic strength  $B_{\text{mag}}$ . The effective density in the PDR is indicated for each  $B_{\text{mag}}$  value. *Bottom:* Fraction of [C II] coming from the PDR, scaled to the [O I] 145  $\mu\text{m}$  prediction, assuming that all of it originates in the PDR. Models in the shaded area are not valid with respect to the upper limit on the H I column density.

### 6.2. Origin of the [O III] 88 $\mu\text{m}$ line

Although emission from the [O III] 88  $\mu\text{m}$  line is expected in starburst galaxies, recent *Herschel* observations show that it is exceptionally bright in dwarf galaxies (Madden et al. 2012b). In Haro 11, it is the brightest of all MIR and FIR lines. With an excitation potential of 35.1 eV and critical density,  $n_{\text{crit}} = 5 \times 10^2 \text{ cm}^{-3}$ , this line is expected to originate from a high ionisation and relatively low density medium. Effective temperatures,  $T_{\text{eff}} > 40\,000 \text{ K}$ , are usually needed to explain the bright [O III] emission in star-forming irregular galaxies (Hunter et al. 2001). When considering both models  $\mathcal{C}_{\text{HII}}$  and  $\mathcal{D}$ , we find a good match between model predictions and observations for all ionic lines considered, although the [O III] 88  $\mu\text{m}$  line is under-predicted by the models by a factor of  $\sim 2$ .  $\mathcal{C}_{\text{HII}}$  accounts for 60% of the [O III] 88  $\mu\text{m}$  emission, and  $\mathcal{D}$  does not predict any [O III] emission; the ionising photons are not energetic enough. This factor of 2 is within the uncertainties of this study, however we discuss the possible origin of the [O III] 88  $\mu\text{m}$  line from a highly ionised more diffuse medium. Although the [O III] emission is explained by  $\mathcal{C}_{\text{HII}}$  in the extreme case of Haro 11, this may not be the case in other metal-poor dwarf galaxies.

In the star-forming region N11-B of the Large Magellanic Cloud, Leboutteiller et al. (2012) find bright [O III] 88  $\mu\text{m}$  emission that originates from spatially extended high-excitation diffuse ionised gas, and can be modeled by O stars distributed across the region. In the case of Haro 11, the density in  $\mathcal{C}_{\text{HII}}$  is too high to fully reproduce the observed [O III] 88  $\mu\text{m}$  emission. As shown in Fig. 6, lowering the density in  $\mathcal{C}_{\text{HII}}$  to densities

$\leq 10^2 \text{ cm}^{-3}$  would better reproduce the observed [O III] 88  $\mu\text{m}$  intensity.

Given the two components that we have modeled  $\mathcal{C}_{\text{HII}}$  and  $\mathcal{D}$ , we may consider a picture in which  $\mathcal{C}_{\text{HII}}$  does not have a covering factor of unity, but is actually porous. This would allow some fraction of the ionising photons to escape the compact H II region and travel further away in a lower density medium. Such a configuration could explain the [O III] 88  $\mu\text{m}$  emission, but would also lead to over-predicting several lines. In particular, in our case, predicted intensities of the [S IV], [O IV], and [N III] lines would be a factor of  $\sim 2$  higher than their observed values.

### 6.3. Origin of the [O IV] line and X-rays

With an ionisation potential of 54.9 eV, [O IV] can only be excited by high energy sources. Its origin has been discussed in Lutz et al. (1998); Schaerer & Stasińska (1999). It can come from AGN activity (X-rays), very hot sources or shocks. In this Section, we explore the role of X-ray photons and/or shocks. In dwarf starbursting galaxies, a hot and young stellar population is usually responsible for the [O IV] emission. This has been confirmed by ISO observations of the dwarf galaxies II Zw 40 and NGC 5253 (Schaerer & Stasińska 1999). Signatures of Wolf-Rayet stars in the optical and P Cygni profiles in the far-UV (O VI lines), revealing the presence of O supergiants and a very young burst in Haro 11, were reported by Bergvall et al. (2006) and Grimes et al. (2007). In the case of Haro 11, we find that the young starburst containing Wolf-Rayet stars can indeed account for the [O IV] 25.9  $\mu\text{m}$  line intensity. The luminosity of the [O IV] line is  $\sim 0.006\%$  of  $L_{\text{TIR}}$ . Spinoglio et al. (2012) have compared the IR/submm emission lines to the IR luminosity in local samples of AGNs and starburst galaxies. They showed that the [O IV] line is weaker in starburst galaxies, about one order of magnitude less intense than in AGNs, and that starbursts follow the relation  $L_{[\text{O IV}]} \sim 10^{-4} L_{\text{TIR}}$  in the high IR luminosity range, which is consistent with that observed in Haro 11. The [Ne V] (97.1 eV) at 14.3  $\mu\text{m}$  is not detected in the *Spitzer*/IRS spectrum. The upper limit in Table 2 is consistent with our model prediction. Its absence confirms the fact that there is no AGN activity nor intense hard X-ray emission in Haro 11. The X-ray component discussed in Sect. 3.3.1 in our model has little effect on the intensities of the ionic lines. Around the parameters of  $\mathcal{C}_{\text{HII}}$ , adding X-rays to the radiation field increases the intensity of the [O IV] 25.9  $\mu\text{m}$  line by only  $\sim 1\%$ . In the PDR, the X-rays have a moderate effect. They contribute up to 5% to the [C II] intensity, and  $\sim 10\%$  to the [O I] intensities. X-rays play a second order role and the physics of the neutral gas is dominated by the FUV photons (PDR), not the X-rays (XDR).

Shocks are also not our preferred explanation for the [O IV] emission. O'Halloran et al. (2008) find that the emission of the [Fe II] 26.0  $\mu\text{m}$  line in low metallicity BCDs may be shock-derived or can result from a larger abundance of iron in the gas-phase as it is less depleted onto dust grains at low metallicity. However, the [Fe II] 26.0  $\mu\text{m}$  line is barely detected in Haro 11. The observed ratio of [Fe III]/[Fe II] is  $\sim 0.005$ , which also tends to rule out shocks as a major heating process here.

## 7. Multi-phase build-up of Haro 11

We summarize the contributions of the different ISM phases that, when put together, account for the global MIR and FIR fine-structure line emission observed in Haro 11 (Figure 11). The panel on the *left* is an illustration of this multi-phase build-up: the central starburst is surrounded by our main model  $\mathcal{C}$  composed

of a compact H II region  $\mathcal{C}_{\text{HII}}$  (red), with adjacent dense PDRs  $\mathcal{C}_{\text{PDR}}$  (blue). The volume around this compact nucleus is filled by diffuse ionised/neutral gas  $\mathcal{D}$  (yellow). We also add a low filling factor component of warm dust close to the starburst (black dots), the need for which we discuss (Sect. 7.1). This scheme is the global picture (not to scale) that results from this modeling study. We remind the reader that the models  $\mathcal{C}$  and  $\mathcal{D}$  were computed separately. The panel on the *right* is a histogram indicating the contribution of each model to the line intensities, with identical color-coding. All 17 lines considered are reproduced by the 3 models  $\mathcal{C}_{\text{HII}}$ ,  $\mathcal{C}_{\text{PDR}}$ , and  $\mathcal{D}$  within a factor of 2. The model parameters of these phases and line predictions are also listed in Table 5. In view of the results from Sect. 5.3 and 6.1, in which the upper limit on the H I mass limits the contribution from the diffuse neutral medium and from magnetic fields, the models  $\mathcal{D}_h$  and  $\mathcal{C}_B$  are not taken into account for our final build-up of the ISM of Haro 11. The models we combine are:

- a compact H II region that dominates the emission of the ionic lines  $\mathcal{C}_{\text{HII}}$ ,
- a dense PDR of coverage  $\sim 10\%$   $\mathcal{C}_{\text{PDR}}$ ,
- a diffuse low-ionisation medium  $\mathcal{D}_l$ .

We analyse results from this build-up in terms of dust emission, extinction, and mass budget.

### 7.1. The global SED

The proposed geometry also implies a prediction for the dust emission coming from the different ISM phases of Haro 11. We compare the predicted SED of the multi-phase build-up with the observations of Haro 11 in Figure 12. The goal here is not to fit in detail the dust emission but rather to reproduce the global shape of the SED because it is sensitive to the temperature of the dust, which is one of the main predictions of the multi-phase model. The SED of the compact model  $\mathcal{C}$  (both  $\mathcal{C}_{\text{HII}}$  and  $\mathcal{C}_{\text{PDR}}$ ) peaks at  $\sim 40 \mu\text{m}$  (Fig. 12), as in the observed SED. In particular,  $\mathcal{C}_{\text{PDR}}$  is too dense to explain the FIR shape of the SED, which corroborates the presence of a more diffuse component. Indeed, the diffuse component  $\mathcal{D}_l$  matches the temperature of Haro 11 in the FIR, although the longest wavelengths, beyond 250  $\mu\text{m}$ , are still under-predicted. Perhaps the most surprising result is that the multi-phase model fails completely to reproduce the UV-optical extinction and the MIR emission, despite the choice of a lower cut in the grain sizes (Sect. 3.3.3). We discuss these two points in Sect. 7.1.1 and Sect. 7.1.2.

#### 7.1.1. Energy balance

In the UV-optical wavelength range, the total outward luminosity (Fig. 12: bottom panel, black line) is 80% greater than the observed luminosity. Has the input energy in the UV-optical wavelength range been overestimated? We are confident about the shape of the input starburst spectrum since the spectral line ratios depend on the hardness of the radiation field and are well fitted by our models. Additional confidence draws from the right amount of input energy as the level of the NIR photometry, unaffected by the little extinction present in Haro 11, is well matched.

The SED reflects the global energy balance of Haro 11 and shows that a fraction of the total input energy injected in the UV-optical wavelength range is not absorbed. The models  $\mathcal{C}_{\text{HII}}$  and  $\mathcal{D}_l$  are responsible for the over-prediction in the UV-optical. We find the average extinction of the model to be  $A_V = 0.15 \text{ mag}$ . The spectrum is dominated by emission from the ionised model



**Table 5.** Model parameters and line predictions.

Quantity	Model						
	$\mathcal{C}_{HII}$	+	$\mathcal{C}_{PDR}$	$\mathcal{G}_l$	$\mathcal{G}_h$	Warm dust	Total <sup>(a)</sup>
Energy source	Starburst 3.7 Myr			Star 35 000 K	Star 35 000 K	Starburst 3.7 Myr	
$n_H$ [cm <sup>-3</sup> ]	10 <sup>2.8</sup>		10 <sup>5.1</sup> ( 10 <sup>3.4</sup> )	10 <sup>1.0</sup>	10 <sup>3.0</sup>	10 <sup>1.5</sup>	
$r_m$ [cm]	10 <sup>21.4</sup>		10 <sup>21.4</sup>	10 <sup>21.8</sup>	10 <sup>21.8</sup>	10 <sup>19.8</sup>	
I([S iv] 10.5)/ $I_{obs}$ <sup>(b)</sup>	0.84 (0.29)	-	-	-	-	-	0.84
I([Ne ii] 12.8)/ $I_{obs}$	0.20 (0.10)	-	0.53	0.89	-	-	0.73
I([Ne iii] 15.6)/ $I_{obs}$	1.13 (0.61)	-	-	-	-	-	1.13
I([S iii] 18.7)/ $I_{obs}$	1.03 (0.50)	-	0.26	0.16	-	-	1.29
I([S iii] 33.5)/ $I_{obs}$	1.04 (0.63)	-	0.61	0.14	-	-	1.65
I([Si ii] 34.8)/ $I_{obs}$	0.11 (0.07)	0.24 (0.37)	0.04	0.24	-	-	0.39
I(Hu $\alpha$ 12.4)/ $I_{obs}$	1.28 (0.61)	-	0.37	0.63	-	-	1.65
I([Fe iii] 22.9)/ $I_{obs}$	0.49 (0.27)	-	0.44	0.50	-	-	0.93
I([O iv] 25.9)/ $I_{obs}$	1.18 (0.74)	-	-	-	0.10	-	1.28
I([Ar iii] 8.99)/ $I_{obs}$	1.49 (0.51)	-	0.08	0.06	-	-	1.57
I([Ar ii] 6.99)/ $I_{obs}$	0.12 (0.08)	-	0.75	1.49	-	-	0.87
I([C ii] 157)/ $I_{obs}$	0.01 (0.01)	0.07 (0.49)	0.40	0.19	-	-	0.48
I([O iii] 88)/ $I_{obs}$	0.59 (0.44)	-	0.02	-	-	-	0.61
I([O ii] 63)/ $I_{obs}$	0.03 (0.02)	1.11 (1.03)	-	0.08	-	-	1.14
I([O ii] 145)/ $I_{obs}$	0.03 (0.02)	0.95 (1.00)	-	0.07	-	-	0.98
I([N iii] 57)/ $I_{obs}$	1.41 (0.99)	-	0.13	-	-	-	1.44
I([N ii] 122)/ $I_{obs}$	0.29 (0.23)	-	1.46	0.46	-	-	1.75

(a) The total is taken as the sum of models  $\mathcal{C}$ ,  $\mathcal{G}_l$  and warm dust, which is what we consider for the final build-up in Sect. 7; although  $\mathcal{G}_h$  and  $\mathcal{C}_B$  may also alter the line predictions.

(b) Ratio of the predicted intensity of the model over the observed intensity ( $I_{obs}$ ). Ratio values below 1% are not indicated.

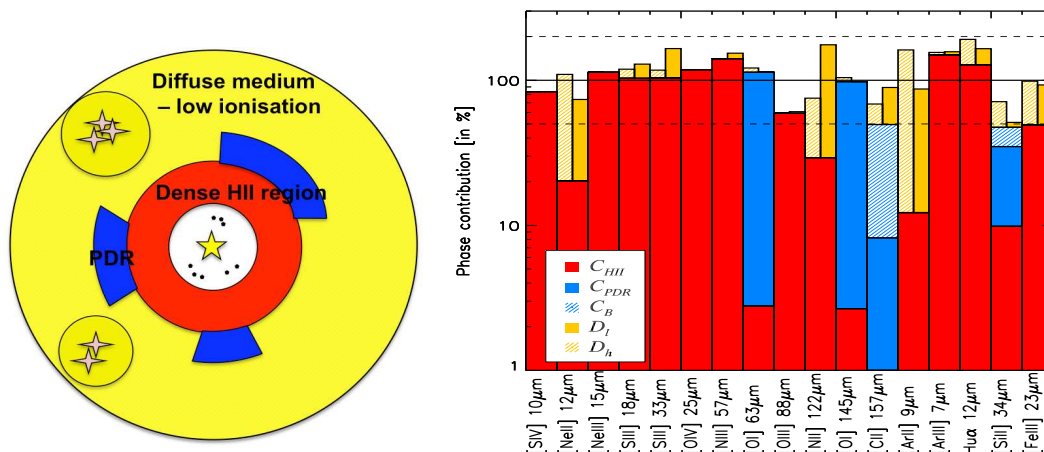


**Figure 11.** *Left:* Multi-phase build-up of the ISM of Haro 11, composed of a compact H II region ( $\mathcal{C}_{\text{HII}}$ ) in red, a dense fragmented PDR ( $\mathcal{C}_{\text{PDR}}$ ) in blue, a diffuse medium of lower ionisation ( $\mathcal{D}$ ) in yellow, and warm dust in the inner region (represented as dots close to the starburst). *Right:* Diagram of the contribution of each individual ISM phase to the global emission of the MIR and FIR lines. Red color corresponds to  $\mathcal{C}_{\text{HII}}$ , blue to  $\mathcal{C}_{\text{PDR}}$ , with possible enhancement in the [C II] and [Si II] lines when considering magnetic fields (hashed blue,  $\mathcal{C}_B$ ), and yellow from the diffuse ionised medium ( $\mathcal{D}$ ), also with possible contribution from a diffuse neutral phase (hashed yellow,  $\mathcal{D}_n$ ).

components:  $\mathcal{C}_{HII}$ , of which 90% of the radiation escapes since the PDR covers only 10%, and  $\mathcal{Q}_i$ . These models are computed separately and work as MIR-FIR emission line diagnostics, very little affected by dust attenuation, but we neglect their interaction. We can estimate the reddening needed to match the level of the model spectrum to the observed data points. Using the extinction law of Calzetti et al. (2000), with  $R_V = 3.3$  set by the model, we find  $A_V = 0.9$  mag, hence  $A_B = 1.2$  mag and  $E(B - V) = 0.3$  mag. The reddened spectrum appears in dashed dark line on Fig. 12 (*bottom*). From UV continuum mea-

surements and  $H\alpha/H\beta$  ratio, Bergvall & Östlin (2002) estimate  $A_B = 0.7$  mag. The optical image (Fig. 1) shows a dust lane passing in front of knot B, where the extinction is known to be higher (Adamo et al. 2010; Guseva et al. 2012). Adamo et al. (2010) find that  $E(B - V)$  is 0.4 towards knot B and 0.1 towards knot C.

On the contrary, in the MIR (5 to 40  $\mu\text{m}$ ), the predicted luminosity is two times lower than the observed luminosity. This emission in the MIR can be attributed to warm dust that we model in the following Section.

This suggests an interpretation in terms of geometry of the galaxy, in which a large number of ionising photons can travel far, but in the end, the different media (compact and diffuse) are well mixed together, yielding a significant dust column along most lines of sight. In particular, the warm dust component that we add close to the central starburst and emits in the MIR is likely responsible for the absorption of the UV-optical part of the  $\mathcal{C}_{HII}$  spectrum which is the primary contributor to the total spectrum in this range.

### 7.1.2. Warm dust component

To account for the observed warm dust that our models do not produce in the MIR range (Fig 12, *top* panel), we have examined two possible solutions that do not change the intrinsic properties of the dust grains (which are little known):

1) change the dust distribution for a postshock distribution (Jones et al. 1996), where grains are affected by shocks, with preferential destruction of large grains, resulting in an enhancement of small grains with respect to large grains. This grain shattering results in a distribution with steeper slope and lower cut-off sizes. This distribution is successfully applied to model IR SEDs of LIRGs in Dopita et al. (2011). Galliano et al. (2003) used this distribution, that may have been generated by supernova shocks, to model the dust in the dwarf galaxy NGC 1569. However we have been unable to satisfactorily fit the SED by changing the grain properties.

2) add a warm dust component close to the central starburst. In this way we add to our picture a porous layer of dust particles close to the central starburst, which is not inconceivable for compact H II regions. Models from Groves et al. (2008) show that the observed warm dust emission arises from hot dust embedded within the H II region. This is also supported by spatially resolved observations of nearby galaxies. Calzetti et al. (2005) find that the 8  $\mu$ m and 24  $\mu$ m emission originate within the H II regions.

We adopt a warm dust component, at a distance of  $r_{in} = 10^{19.8}$  cm, with density  $n_H = 10^{1.5}$  cm $^{-3}$  and covering factor 15% (orange spectrum on Fig 12). These parameters are chosen to reproduce the level of the SED in the MIR. In these conditions grains can easily survive. *This component has little or no effect on the discussed emission lines* because of its compactness. The photons are predominantly absorbed by the dust, not the gas, and dust collisions are responsible for the cooling. This warm dust component may be regarded as an equivalent of an ultra-compact H II region (Dopita et al. 2003), or the hot spots described in Siebenmorgen & Krügel (2007). This component takes away 15% of the input luminosity from the H II region model. The amount of necessary energy and the hardness of the radiation field can be adjusted by modifying simultaneously the input luminosity, covering factor, and the inner radius in the code. Integrating the spectrum from 3 to 1100  $\mu$ m gives  $L_{TIR} = 1.7 \times 10^{11} L_{\odot}$ , very close to the inferred dust-model value of  $1.4 \times 10^{11} L_{\odot}$  from Galametz et al. (2009); Rémy et al. (2012).

This warm dust model matches the continuum level in the NIR-MIR, but produces a silicate feature in emission at 9.7  $\mu$ m, which is not seen in the *Spitzer*/IRS spectrum. This discrepancy is likely due to the fact that we have modeled the compact and diffuse phases of the ISM independently. Foreground dust from the other components may in turn extinguish the silicate seen in emission. Another factor at play is the adopted abundance of silicate grains. Quantitative surveys with *Spitzer* of AGB carbon and silicate dust production rates in the Magellanic Clouds find

that carbon dust injection rates dominate over those of silicate (Matsuura et al. 2009; Boyer et al. 2012). There may be a small effect from foreground cold dust from the molecular phase of Haro 11 that we do not model, which would have low filling factor and high  $A_V$ .

### 7.1.3. FIR-mm wavelength range

The mismatch between the observed and predicted SED beyond 250  $\mu$ m (Fig. 12) may be attributed to colder dust in the molecular phase. With no molecular gas constraint, we cannot include a cold molecular phase in our modeling. However, as a first approximation on the required dust properties, we can continue  $\mathcal{C}_{PDR}$  to higher  $A_V$  and stop the model when it matches the submm temperature. This way, we estimate that the missing emission requires high  $A_V \sim 40$  mag and agrees with a grain temperature of  $\sim 25$  K, which would fit the SPIRE data to 500  $\mu$ m but still under-predict the LABOCA 870  $\mu$ m data (see Fig. A.1 in Appendix A). The latter is rather related to the submm excess introduced in Sect. 1.1. This excess is modeled by a cold dust component in Galametz et al. (2009).

### 7.2. Optical lines

Several optical lines, including H $\alpha$ , H $\beta$ , [O III] 5007 Å, have been observed towards the central visual peak in Bergvall & Östlin (2002). Because of the small aperture of the observations,  $4'' \times 4''$ , an absolute flux comparison cannot be made, except for H $\alpha$  which was fully mapped in Östlin et al. (1999) with the ESO 3.6 m telescope. More recent observations were also performed with the VLT/X-shooter, in the wavelength range 3 000-24 000 Å, by Guseva et al. (2012). In particular, they observed, in a slit of size  $\sim 1'' \times 11''$ , the H $\alpha$ , H $\beta$ , [O III] 3727 Å, [O III] 4959 and 5007 Å, [S II] 6716 and 6731 Å, [S III] 9069 and 9535 Å lines, in both knots B and C of Haro 11. From these observations, they determined the metallicity of Haro 11 and element abundances. Optical lines are affected by dust extinction, and comparison of the model predictions to the observations is very dependent on the adopted geometry. With Cloudy, we can compare the intrinsic emission predicted by our model to the extinction-corrected observations.

The ratio of the optical lines listed above to H $\beta$  are all well reproduced by our Cloudy models, within 40%, with contribution from both the H II region and the diffuse medium (Table 6). The only line which poses a problem is [S II], which is overestimated by a factor of 3 at 6716 Å, and 1.5 at 6731 Å. The Cloudy ratio of the two [S II] lines is thus 0.9. The Cloudy models of Guseva et al. (2012) also over-predict the [S II] lines by a factor of 2, but reproduce their observed ratio of 1.5. This ratio is sensitive to the electron density of the medium probed, which in their case is a density of 10 cm $^{-3}$ . We find that our diffuse ionised model with density 10 cm $^{-3}$  does predict a [S II] line ratio of 1.5. Concerning H $\alpha$ , we compare its absolute flux and find that it emits from both the H II region and the diffuse medium, with a total predicted luminosity of  $7 \times 10^8 L_{\odot}$ , close to the observed value of Östlin et al. (1999),  $L_{H\alpha} = 8 \times 10^8 L_{\odot}$ .

### 7.3. Mass budget

The gas mass of each ISM component can be calculated using the density profile in the cloud and integrating over the volume



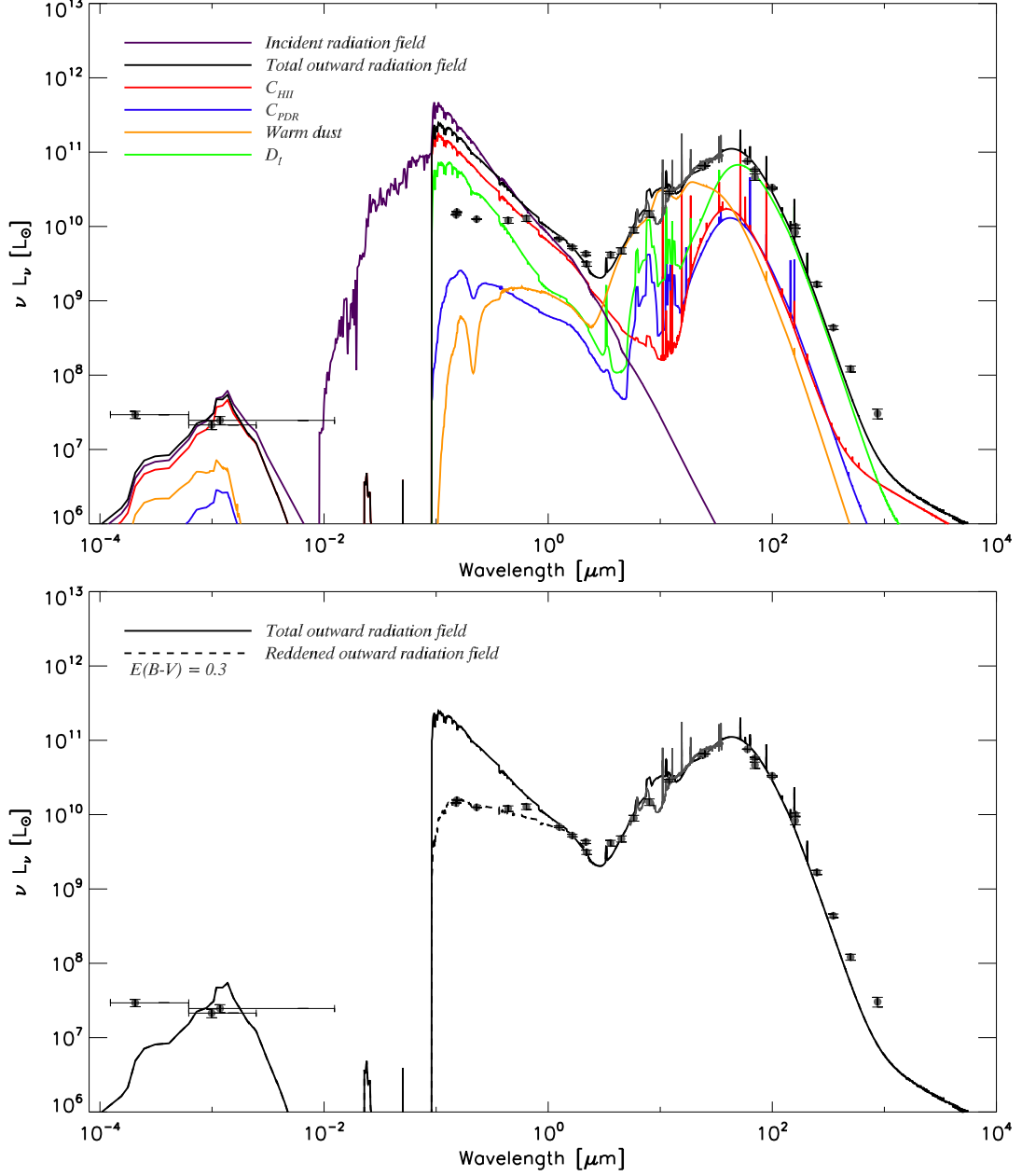


**Figure 12.** *Top:* Spectral energy distribution (SED) of the incident radiation field striking the cloud and outward radiation from each component modeled by Cloudy. The dark spectrum is the total outward radiation resulting from multi-phase build-up, and arriving to the observer. Photometry data from NED, Bendo et al. (2012), Galametz et al. (2009), and Rémy et al. (2012), and the IRS spectrum are overlaid in grey. *Bottom:* Spectral energy distribution of the total outward radiation field and the reddened outward radiation field in dashed dark line.

of each slice inside the cloud. We then multiply the gas mass by 1.36 to account for helium, and use the D/G mass ratio of the model ( $2.64 \times 10^{-3}$ ) to derive the dust mass. The masses of

each component are summarized in Table 7. We find a mass of ionised gas ( $\mathcal{C}_{\text{HII}} + \mathcal{D}_I$ ) of  $5.8 \times 10^8 M_\odot$ , and a mass of neutral gas ( $\mathcal{C}_{\text{PDR}} + \mathcal{D}_I$ ) of  $2.4 \times 10^8 M_\odot$ . This neutral gas mass accounts for

**Table 6.** Optical line predictions.

Line	I/I(H $\beta$ )			
	Observations <sup>(a)</sup>	$\mathcal{C}_{HII}$	$\mathcal{I}_I$	Total Model <sup>(b)</sup>
[O II] 3727 Å	2.3	1.4	3.5	2.3
H $\beta$ 4861 Å	1.0	1.0	1.0	1.0
[O III] 4959 Å	1.1	1.7	0.08	1.5
[O III] 5007 Å	3.4	5.2	0.03	4.5
H $\alpha$ 6563 Å	2.9	2.6	2.0	2.9
[N II] 6583 Å	0.53	0.32	0.79	0.52
[S II] 6716 Å	0.22	0.07	0.03	0.07
[S II] 6731 Å	0.12	0.08	0.02	0.08
[S III] 9069 Å	0.15	0.17	0.13	0.19
[S III] 9532 Å	0.41	0.42	0.32	0.47

(a) Ratio of the observed line intensity over H $\beta$  from Guseva et al. (2012). The fluxes are extinction-corrected and averaged over the two knots B and C. (b) Ratio of the intrinsic line intensity over H $\beta$  predicted by Cloudy.

the H I mass as well as the mass of H<sub>2</sub> formed in PDR envelopes before the CO formation. This H<sub>2</sub> layer not traced by CO is referred as the “dark gas” (Wolfire et al. 2010). The PDR-H<sub>2</sub> mass is  $\sim 10^8 M_\odot$  and comes from  $\mathcal{C}_{PDR}$ , while the H I mass comes essentially from the diffuse model  $\mathcal{I}_I$  with M(H I)  $\sim 10^8 M_\odot$  fixed by its upper limit. As expected, the ionised phase is dominant in Haro 11. The ionised gas and PDR masses are similar to that of Bergvall et al. (2000). We derive a total dust mass of  $2.1 \times 10^6 M_\odot$ , comparable to the value  $6 \times 10^6 M_\odot$  of Galametz et al. (2009).

These dust and gas mass inventories do not include modeling of the cold CO-cloud. The missing FIR emission discussed in Sect 7.1.3 results in a dust mass of  $\sim 2 \times 10^6 M_\odot$ , which does not include the observed submm excess. When modeling the dust submm excess as cold dust, Galametz et al. (2009) find a total dust mass of  $2 \times 10^7 M_\odot$ , which would result in a higher D/G mass ratio ( $\sim 1/50$ ) compared to our current gas modeling. A significant fraction of ISM mass would therefore not accounted for by our models, part of which should sit in the molecular phase that we have not modeled. CO(1-0) is to date undetected (Bergvall et al. 2000). The state of a reservoir of warm molecular gas is addressed in a forthcoming paper (Cormier et al. 2012b). We would like to emphasize that the determination of the cold dust mass is very sensitive to the model and geometry adopted. Both the cool dust interpretation of the submm excess and the model accounting for the missing FIR emission (Sect 7.1.3) are, without further onstraints on the cold phase, ad hoc means to fit the dust SED. In particular, the cold dust interpretation of the submm excess has little physical support as it is unlikely to encounter such very large columns of (cold shielded) dust in dwarf galaxies, and because the submm excess does not seem to correlate spatially with the densest ISM phases (Galliano et al. 2011).

## 8. Conclusion

We have presented *Spitzer*/IRS and *Herschel*/PACS spectroscopic observations of the MIR-FIR fine-structure cooling lines in the starburst low-metallicity galaxy Haro 11. Investigating the nature of the different gas phases in this galaxy, we have modeled the ISM phases of Haro 11 step by step with the spectral synthesis code Cloudy. The main results can be summarized as follows:

**Table 7.** Mass budget in solar mass  $M_\odot$ .

Model	M(H II)	M(PDR) <sup>(a)</sup>	M <sub>dust</sub>
$\mathcal{C}_{HII}$	$3.0 \times 10^7$	-	$7.2 \times 10^4$
$\mathcal{C}_{PDR}$	-	$1.2 \times 10^8$	$3.2 \times 10^5$
$\mathcal{I}_I$	$5.5 \times 10^8$	$1.2 \times 10^8$	$1.7 \times 10^6$
Warm dust	-	-	$8.5 \times 10^3$
Total	$5.8 \times 10^8$	$2.4 \times 10^8$	$2.1 \times 10^6$
Literature	$\sim 10^9$ <sup>(b)</sup>	$2 \times 10^8$ <sup>(c)</sup>	$\sim 6 \times 10^6$ <sup>(d)</sup>

(a) M(PDR) is the sum of the H I mass and the H<sub>2</sub> mass in the PDR envelope untraced by CO. (b) Bergvall & Östlin (2002). (c) Bergvall et al. (2000), where they also report M(H I)  $< 10^8 M_\odot$ . (d) This is the dust mass without including the cold component of 10 K from Galametz et al. (2009). Their total dust mass is  $2 \times 10^7 M_\odot$ .

1. The IRS and PACS spectra show very bright MIR and FIR fine-structure cooling lines, the brightest of all being the [O III] 88  $\mu$ m line. The galaxy is undergoing young active star formation, as traced by the [O III] 88  $\mu$ m line (35.1 eV), which is about 3 times brighter than the classical neutral gas tracers [C II] 157  $\mu$ m and [O I] 63  $\mu$ m. High line ratios of [Ne III]/[Ne II], [S IV]/[S III], and [N III]/[N II] also trace the hard radiation field. We find  $L_{[C II]}/L_{TIR} = 0.1\%$ ,  $(L_{[C II]} + L_{[O I]})/L_{TIR} = 0.2\%$ , and altogether, the MIR and FIR lines represent 1.2% of  $L_{TIR}$ .
2. We model our exhaustive dataset of 17 fine-structure lines with Cloudy and find the need to describe Haro 11 with these component phases:
  - a dense H II region, illuminated by a young starburst, from which most of the ionic lines originate,
  - adjacent dense PDR of low ( $\sim 10\%$ ) covering factor,
  - an extended diffuse low-ionised/neutral medium,
  - a porous warm dust component close to the stars that accounts for the elevated MIR continuum.
3. Emission from the [N II] 122  $\mu$ m and [Ne II] lines cannot be reconciled with the compact H II region but are rather associated with a more diffuse low-ionisation medium.
4. We find that 10% of the [C II] emission is associated with the dense PDR, and up to 50% when lowering the density. About 50% of the [C II] arises from a more diffuse ionised medium. The low extinction and low metallicity of Haro 11 make its ISM more leaky, and the emitting region of [C II] larger. The [O I] emission is fully associated with the PDR. The observed [C II] luminosity is comparable to that of the [O I] 63  $\mu$ m line. In the dense component we derive  $L_{[C II]}/L_{TIR} \sim 0.05\%$  and  $(L_{[C II]} + L_{[O I]})/L_{TIR} \sim 1\%$ , which is a common measure of the gas heating efficiency in the neutral gas, and in the diffuse component we find  $L_{[C II]}/L_{TIR} \sim 0.1\%$ .
5. The only line that we do not completely reconcile with our model is the [O III] 88  $\mu$ m. Our compact H II region model accounts for 50% of the emission of [O III]. Our preferred explanation for the intense [O III] emission is the presence of yet another additional diffuse component, filling the volume around the porous H II region, and where the gas is heated by escaping UV photons.
6. We estimate the mass from each modeled phase. We find a mass of ionised gas of  $6 \times 10^8 M_\odot$ , a PDR mass of  $2 \times 10^8 M_\odot$ , and a dust mass (without submm constraints, because of the submm excess) of  $3 \times 10^6 M_\odot$ . The ionised gas mass is larger than the atomic gas mass.
7. Finally, in terms of structure, the ISM of Haro 11 appears to be mostly filled with extended diffuse gas. Our simple pic-

ture can reproduce the observations by a galaxy with a filling factor of diffuse neutral and ionised gas of at least 90%, a dense H II region component of filling factor  $\sim 0.2\%$ , and a PDR component of filling factor  $< 0.01\%$ . A radiative transfer model which takes into account clumpy source and gas structures would provide a more realistic picture of Haro 11.

**Acknowledgements.** The authors would like to thank Albrecht Poglitsch and Alessandra Contursi for their help with the PACS data. Part of this work has been made possible by financial support from the CNRS/INSU programme PCMI. PACS has been developed by a consortium of institutes led by MPE (Germany) and including UVIE (Austria); KU Leuven, CSL, IMEC (Belgium); CEA, LAM (France); MPIA (Germany); INAF-IFSI/OAA/OAP/OAT, LENS, SISSA (Italy); IAC (Spain). This development has been supported by the funding agencies BMVIT (Austria), ESA-PRODEX (Belgium), CEA/CNES (France), DLR (Germany), ASI/INAF (Italy), and CICYT/MCYT (Spain). This research has made use of the NASA/IPAC Extragalactic Database (NED) which is operated by the Jet Propulsion Laboratory, California Institute of Technology, under contract with the National Aeronautics and Space Administration. Based on observations made with the NASA/ESA Hubble Space Telescope, and obtained from the Hubble Legacy Archive, which is a collaboration between the Space Telescope Science Institute (STScI/NASA), the Space Telescope European Coordinating Facility (ST-ECF/ESA) and the Canadian Astronomy Data Centre (CAD/CNRC/CSA).

## References

- Abel, N. P., Dudley, C., Fischer, J., Satyapal, S., & van Hoof, P. A. M. 2009, *ApJ*, 701, 1147
- Abel, N. P., Ferland, G. J., Shaw, G., & van Hoof, P. A. M. 2005, *ApJS*, 161, 65
- Abel, N. P., van Hoof, P. A. M., Shaw, G., Ferland, G. J., & Elwert, T. 2008, *ApJ*, 686, 1125
- Adamo, A., Östlin, G., Zackrisson, E., et al. 2010, *MNRAS*, 407, 870
- Baldwin, J. A., Ferland, G. J., Martin, P. G., et al. 1991, *ApJ*, 374, 580
- Beck, S. C., Turner, J. L., & Kovo, O. 2000, *AJ*, 120, 244
- Bendo, G. J., Galliano, F., & Madden, S. C. 2012, *ArXiv e-prints*
- Bergvall, N., Masegosa, J., Östlin, G., & Cernicharo, J. 2000, *A&A*, 359, 41
- Bergvall, N. & Östlin, G. 2002, *A&A*, 390, 891
- Bergvall, N., Zackrisson, E., Andersson, B.-G., et al. 2006, *A&A*, 448, 513
- Boselli, A., Gavazzi, G., Lequeux, J., & Pierini, D. 2002, *A&A*, 385, 454
- Boyer, M. L., Srinivasan, S., Riebel, D., et al. 2012, *ApJ*, 748, 40
- Brauer, J. R., Dale, D. A., & Helou, G. 2008, *ApJS*, 178, 280
- Calzetti, D., Armus, L., Bohlin, R. C., et al. 2000, *ApJ*, 533, 682
- Calzetti, D., Kennicutt, Jr., R. C., Bianchi, L., et al. 2005, *ApJ*, 633, 871
- Carral, P., Hollenbach, D. J., Lord, S. D., et al. 1994, *ApJ*, 423, 223
- Chyży, K. T., Weżgowiec, M., Beck, R., & Bomans, D. J. 2011, *A&A*, 529, A94
- Contursi, A. et al. 2012, submitted
- Cormier, D., Madden, S. C., Hony, S., et al. 2010, *A&A*, 518, L57
- Cormier, D. et al. 2012a, in preparation
- Cormier, D. et al. 2012b, in preparation
- Croxall, K. V., Smith, J. D., Wolfire, M. G., et al. 2012, *ApJ*, 747, 81
- Crutcher, R. M. 1999, *ApJ*, 520, 706
- de Looze, I., Baes, M., Bendo, G. J., Cortese, L., & Fritz, J. 2011, *MNRAS*, 416, 2712
- Dopita, M. A., Armus, L., Kewley, L. J., et al. 2011, *Ap&SS*, 333, 225
- Dopita, M. A., Groves, B. A., Fischera, J., et al. 2005, *ApJ*, 619, 755
- Dopita, M. A., Groves, B. A., Sutherland, R. S., & Kewley, L. J. 2003, *ApJ*, 583, 727
- Draine, B. T. & Li, A. 2001, *ApJ*, 551, 807
- Ferland, G. J., Korista, K. T., Verner, D. A., et al. 1998, *PASP*, 110, 761
- Galametz, M., Madden, S. C., Galliano, F., et al. 2009, *A&A*, 508, 645
- Galametz, M., Madden, S. C., Galliano, F., et al. 2011, *A&A*, 532, A56
- Galametz, M., Madden, S. C., Galliano, F., et al. 2010, *A&A*, 518, L55
- Galliano, F., Hony, S., Bernard, J.-P., et al. 2011, *A&A*, 536, A88
- Galliano, F., Madden, S. C., Jones, A. P., Wilson, C. D., & Bernard, J.-P. 2005, *A&A*, 434, 867
- Galliano, F., Madden, S. C., Jones, A. P., et al. 2003, *A&A*, 407, 159
- Giveon, U., Sternberg, A., Lutz, D., Feuchtgruber, H., & Pauldrach, A. W. A. 2002, *ApJ*, 566, 880
- Graciá-Carpio, J., Sturm, E., Hailey-Dunsheath, S., et al. 2011, *ApJ*, 728, L7
- Griffith, M. J. et al. 2010, *A&A*, 518, L3
- Grimes, J. P., Heckman, T., Aloisi, A., et al. 2009, *ApJS*, 181, 272
- Grimes, J. P., Heckman, T., Strickland, D., et al. 2007, *ApJ*, 668, 891
- Groves, B., Dopita, M. A., Sutherland, R. S., et al. 2008, *ApJS*, 176, 438
- Guseva, N. G., Izotov, Y. I., Fricke, K. J., & Henkel, C. 2012, *ArXiv e-prints*
- Hayes, M., Östlin, G., Atek, H., et al. 2007, *MNRAS*, 382, 1465
- Heiles, C. 1994, *ApJ*, 436, 720
- Helou, G., Khan, I. R., Malek, L., & Boehmer, L. 1988, *ApJS*, 68, 151
- Higdon, S. J. U., Devost, D., Higdon, J. L., et al. 2004, *PASP*, 116, 975
- Houck, J. R., Roellig, T. L., Van Cleve, J., et al. 2004, in *Society of Photo-Optical Instrumentation Engineers (SPIE) Conference Series*, Vol. 5487, *Society of Photo-Optical Instrumentation Engineers (SPIE) Conference Series*, ed. J. C. Mather, 62–76
- Houck, J. R., Shure, M. A., Gull, G. E., & Herter, T. 1984, *ApJ*, 287, L11
- Hunter, D. A., Kaufman, M., Hollenbach, D. J., et al. 2001, *ApJ*, 553, 121
- Iglesias-Páramo, J., Buat, V., Takeuchi, T. T., et al. 2006, *ApJS*, 164, 38
- Izotov, Y. I. & Thuan, T. X. 1998, *ApJ*, 500, 188
- Izotov, Y. I. & Thuan, T. X. 1999, *ApJ*, 511, 639
- Jarrett, T. H., Chester, T., Cutri, R., et al. 2000, *AJ*, 119, 2498
- Johnson, K. E. & Kobulnicky, H. A. 2003, *ApJ*, 597, 923
- Jones, A. P., Tielens, A. G. G. M., & Hollenbach, D. J. 1996, *ApJ*, 469, 740
- Kaufman, M. J., Wolfire, M. G., & Hollenbach, D. J. 2006, *ApJ*, 644, 283
- Kaufman, M. J., Wolfire, M. G., Hollenbach, D. J., & Luhman, M. L. 1999, *ApJ*, 527, 795
- Kepley, A. A., Mühle, S., Everett, J., et al. 2010, *ApJ*, 712, 536
- Kepley, A. A., Zweibel, E. G., Wilcots, E. M., Johnson, K. E., & Robshaw, T. 2011, *ApJ*, 736, 139
- Kingsburgh, R. L. & Barlow, M. J. 1992, *MNRAS*, 257, 317
- Kingsburgh, R. L. & Barlow, M. J. 1994, *MNRAS*, 271, 257
- Kunth, D., Leitherer, C., Mas-Hesse, J. M., Östlin, G., & Petrosian, A. 2003, *ApJ*, 597, 263
- Kunth, D., Mas-Hesse, J. M., Terlevich, E., et al. 1998, *A&A*, 334, 11
- Kunth, D. & Östlin, G. 2000, *A&A Rev.*, 10, 1
- Lauberts, A. & Valentijn, E. A. 1989, *The surface photometry catalogue of the ESO-Uppsala galaxies*
- Lebouteiller, V., Barry, D. J., Spoon, H. W. W., et al. 2011, *ApJS*, 196, 8
- Lebouteiller, V., Bernard-Salas, J., Sloan, G. C., & Barry, D. J. 2010, *PASP*, 122, 231
- Lebouteiller, V. et al. 2012, submitted to *A&A*
- Leitert, E., Bergvall, N., Piskunov, N., & Andersson, B.-G. 2011, *A&A*, 532, A107
- Leitherer, C., Ortiz Otálvaro, P. A., Bresolin, F., et al. 2010, *ApJS*, 189, 309
- Leroy, A. K., Bolatto, A., Gordon, K., et al. 2011, *ApJ*, 737, 12
- Lonsdale, C. J., Helou, G., Good, J. C., & Rice, W. L. 1985
- Lutz, D., Kunze, D., Spoon, H. W. W., & Thornley, M. D. 1998, *A&A*, 333, L75
- Madden, S. C. 2000, *New Astronomy Review*, 44, 249
- Madden, S. C. 2008, in *EAS Publications Series*, Vol. 31, *EAS Publications Series*, ed. C. Kramer, S. Aalto, & R. Simon, 123–128
- Madden, S. C., Galliano, F., Jones, A. P., & Sauvage, M. 2006, *A&A*, 446, 877
- Madden, S. C., Geis, N., Genzel, R., et al. 1993, *ApJ*, 407, 579
- Madden, S. C., Geis, N., Townes, C. H., et al. 1995, in *Astronomical Society of the Pacific Conference Series*, Vol. 73, *From Gas to Stars to Dust*, ed. M. R. Haas, J. A. Davidson, & E. F. Erickson, 181–184
- Madden, S. C., Remy, A., Galliano, F., et al. 2012a, *ArXiv e-prints*
- Madden, S. C. et al. 2012b, in preparation
- Maiolino, R., Caselli, P., Nagao, T., et al. 2009, *A&A*, 500, L1
- Malhotra, S., Kaufman, M. J., Hollenbach, D., et al. 2001, *ApJ*, 561, 766
- Mathis, J. S., Rumpl, W., & Nordsieck, K. H. 1977, *ApJ*, 217, 425
- Matsuura, M., Barlow, M. J., Zijlstra, A. A., et al. 2009, *MNRAS*, 396, 918
- Micheva, G., Zackrisson, E., Östlin, G., Bergvall, N., & Pursimo, T. 2010, *MNRAS*, 405, 1203
- Narayanan, D., Krumholz, M. R., Ostriker, E. C., & Hernquist, L. 2012, *MNRAS*, 421, 3127
- Negishi, T., Onaka, T., Chan, K., & Roellig, T. L. 2001, *A&A*, 375, 566
- Oberst, T. E., Parshley, S. C., Stacey, G. J., et al. 2006, *ApJ*, 652, L125
- O'Halloran, B., Galametz, M., Madden, S. C., et al. 2010, *A&A*, 518, L58
- O'Halloran, B., Madden, S. C., & Abel, N. P. 2008, *ApJ*, 681, 1205
- Osterbrock, D. E., Tran, H. D., & Veilleux, S. 1992, *ApJ*, 389, 305
- Östlin, G., Amram, P., Bergvall, N., et al. 2001, *A&A*, 374, 800
- Östlin, G., Amram, P., Masegosa, J., Bergvall, N., & Boulesteix, J. 1999, *A&AS*, 137, 419
- Ott, S. 2010, in *Astronomical Society of the Pacific Conference Series*, Vol. 434, *Astronomical Data Analysis Software and Systems XIX*, ed. Y. Mizumoto, K.-I. Morita, & M. Ohishi, 139
- Overzier, R. A., Heckman, T. M., Kauffmann, G., et al. 2008, *ApJ*, 677, 37
- Pierini, D., Leech, K. J., & Völk, H. J. 2003, *A&A*, 397, 871
- Pilbratt, G. L., Riedinger, J. R., Passvogel, T., et al. 2010, *A&A*, 518, L1+
- Poglitsch, A., Krabbe, A., Madden, S. C., et al. 1995, *ApJ*, 454, 293
- Poglitsch, A., Waelkens, C., Geis, N., et al. 2010, *A&A*, 518, L2+
- Pustilnik, S., Kniazev, A., Pramskij, A., et al. 2004, *A&A*, 419, 469
- Rémy, A. et al. 2012, in preparation
- Robshaw, T., Quataert, E., & Heiles, C. 2008, *ApJ*, 680, 981
- Röllig, M., Ossenkopf, V., Jeyakumar, S., Stutzki, J., & Sternberg, A. 2006, *A&A*, 451, 917

- Rubin, R. H., Dufour, R. J., & Walter, D. K. 1993, *ApJ*, 413, 242  
 Rubin, R. H., Simpson, J. P., Haas, M. R., & Erickson, E. F. 1991, *ApJ*, 374, 564  
 Rubin, R. H., Simpson, J. P., Lord, S. D., et al. 1994, *ApJ*, 420, 772  
 Sanders, D. B., Mazzarella, J. M., Kim, D., Surace, J. A., & Soifer, B. T. 2003a, *AJ*, 126, 1607  
 Sanders, D. B., Mazzarella, J. M., Kim, D.-C., Surace, J. A., & Soifer, B. T. 2003b, *AJ*, 126, 1607  
 Schaerer, D. & Stasińska, G. 1999, *A&A*, 345, L17  
 Schruha, A., Leroy, A. K., Walter, F., et al. 2012, *ArXiv e-prints*  
 Shaw, G., Ferland, G. J., Henney, W. J., et al. 2009, *ApJ*, 701, 677  
 Siebenmorgen, R. & Krügel, E. 2007, *A&A*, 461, 445  
 Spinoglio, L., Dasyra, K. M., Franceschini, A., et al. 2012, *ApJ*, 745, 171  
 Stacey, G. J., Geis, N., Genzel, R., et al. 1991, *ApJ*, 373, 423  
 Stacey, G. J., Hailey-Dunsheath, S., Ferkinhoff, C., et al. 2010, *ApJ*, 724, 957  
 Strong, A. W., Bloemen, J. B. G. M., Dame, T. M., et al. 1988, *A&A*, 207, 1  
 Tajer, M., Trinchieri, G., Wolter, A., et al. 2005, *A&A*, 435, 799  
 Thornley, M. D., Schreiber, N. M. F., Lutz, D., et al. 2000, *ApJ*, 539, 641  
 Thuan, T. X., Izotov, Y. I., & Lipovetsky, V. A. 1996, *ApJ*, 463, 120  
 Tielens, A. G. G. M. & Hollenbach, D. 1985, *ApJ*, 291, 722  
 Turner, J. L., Beck, S. C., & Ho, P. T. P. 2000, *ApJ*, 532, L109  
 Vader, J. P., Frogel, J. A., Terndrup, D. M., & Heisler, C. A. 1993, *AJ*, 106, 1743  
 Vasta, M., Barlow, M. J., Viti, S., Yates, J. A., & Bell, T. A. 2010, *MNRAS*, 404, 1910  
 Werner, M. W., Roellig, T. L., Low, F. J., et al. 2004, *ApJS*, 154, 1  
 Wolfire, M. G., Hollenbach, D., & McKee, C. F. 2010, *ApJ*, 716, 1191  
 Wolfire, M. G., Tielens, A. G. G. M., & Hollenbach, D. 1990, *ApJ*, 358, 116  
 Wu, Y., Bernard-Salas, J., Charmandaris, V., et al. 2008, *ApJ*, 673, 193  
 Wu, Y., Charmandaris, V., Hao, L., et al. 2006, *ApJ*, 639, 157  
 Zubko, V., Dwek, E., & Arendt, R. G. 2004, *ApJS*, 152, 211

#### Appendix A: SED including the cold molecular component

We model the SED beyond  $250\ \mu\text{m}$  by stopping the dense PDR model  $\mathcal{C}_{PDR}$  at larger  $A_V$  so that it predicts cold dust emission and matches the *Herschel*/SPIRE observations (as discussed in Sect. 7.1.3). The resulting SED is shown in Fig. A.1.

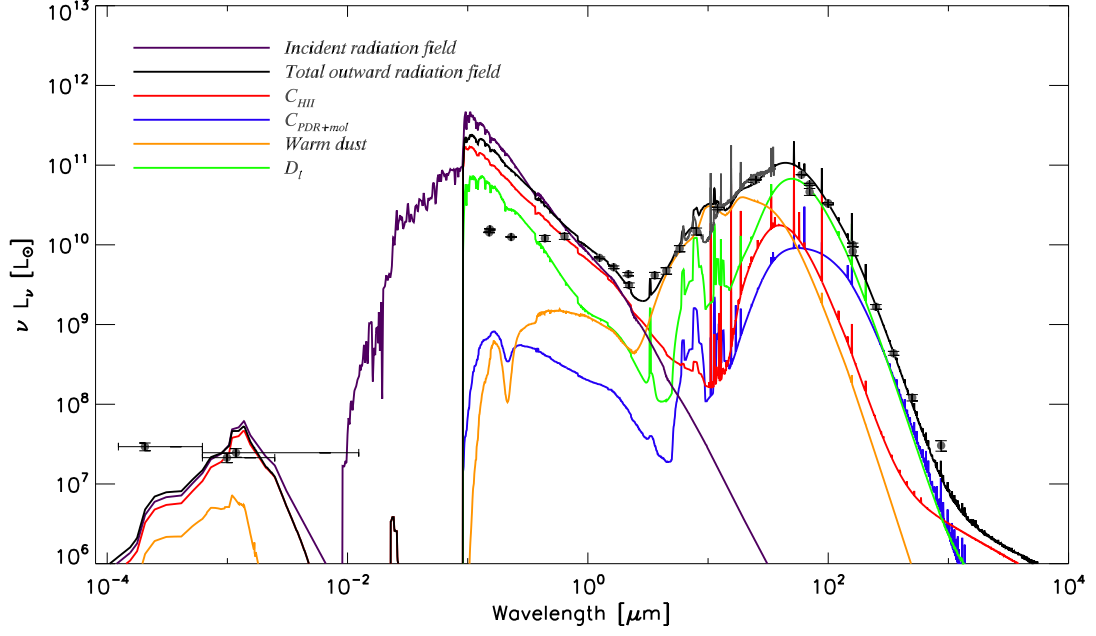


**Figure A.1.** Same as Fig. 12 (*top* panel) except that the PDR component is continued to higher  $A_V$  in the molecular regime to match the observed submm photometry data. The covering factor of this molecular component is of  $\sim 5\%$ .

## Chapter 5

# Probing the cold Interstellar Medium of Dwarf Galaxies

### Contents

---

<b>5.1</b>	<b>Ground-based CO observations . . . . .</b>	<b>122</b>
5.1.1	A few tools for Radio Astronomy . . . . .	122
5.1.2	Sample selection . . . . .	124
5.1.3	Mopra observations . . . . .	128
5.1.4	APEX observations . . . . .	129
5.1.5	IRAM observations . . . . .	130
<b>5.2</b>	<b>Empirical diagnostics . . . . .</b>	<b>130</b>
5.2.1	Line ratios . . . . .	130
5.2.2	Molecular gas mass . . . . .	133
5.2.3	RADEX model . . . . .	134
<b>5.3</b>	<b>Detailed modeling of Haro 11 . . . . .</b>	<b>135</b>
5.3.1	Rotational diagrams of the H <sub>2</sub> molecule . . . . .	135
5.3.2	Full radiative transfer modeling . . . . .	136
<b>5.4</b>	<b>Star formation and total gas reservoir . . . . .</b>	<b>140</b>
5.4.1	Star formation tracers . . . . .	140
5.4.2	Which gas phase is fuelling the star formation? . . . . .	141
5.4.3	Gas depletion times . . . . .	143
<b>5.5</b>	<b>Conclusions on the molecular gas reservoir . . . . .</b>	<b>144</b>

---

The work presented in this Chapter is part of a paper in preparation which investigates the molecular gas content in a sample of 6 dwarf galaxies from the DGS, for which we obtained new CO data. We determine the physical conditions of the molecular clouds, and link the total gas reservoir to the star formation activity via the Schmidt-Kennicutt law. The first section aims to give a brief overview of radio data acquisition, and compare the general characteristics of the different antennas used for this study.

## 5.1 Ground-based CO observations

### 5.1.1 A few tools for Radio Astronomy

#### Temperature formalism

In radio astronomy, flux density ( $S_\nu$ ) and intensity ( $I$ ) are referred to as antenna temperature ( $T_a$ ) and brightness temperature ( $T_{mb}$ ). The choice of temperature unit is to enable the comparison to thermal noise from the receiver electronics. The signal from the source is measured through  $T_a$ :  $S_\nu = 2 k T_a / A_e$ , where  $A_e$  is the antenna effective cross section. The intensity is then equal to the flux by the unit solid angle ( $\Omega$ ). The solid angle depends on the size of the source. For compact sources, the solid angle is determined by the angular size of the source,  $\theta_s$ :  $\Omega = 1.13 \theta_s^2$ . For extended sources, the solid angle is determined by the antenna solid angle,  $\Omega_A$ , which, for a Gaussian shaped main beam of size  $\theta_b$  or  $\theta_{FWHM}$ , gives:  $\Omega = \Omega_A = \lambda^2 / A_e = 1.13 \theta_{FWHM}^2$ . The source is approximated by a black-body, which, in the Rayleigh-Jeans regime of the Planck function ( $h\nu \ll kT$ ), gives the source brightness:  $B_\nu = 2 k T_{mb} / \lambda^2$  [in W m<sup>-2</sup> Hz<sup>-1</sup> sr<sup>-1</sup>] and  $F_\nu = 10^{26} \times 2 k T_{mb} \Omega / \lambda^2$  [in Jy].

Then the conversion from main beam temperature to final intensity,  $I$ , is straightforward:

$$I = 10^{26} \times T_{mb} \times \Delta V \times \frac{2k}{c^3} \times \Omega \times \nu^3 \text{ [in W m}^{-2}\text{]} \quad (5.1)$$

The aperture efficiency  $\eta_a$  is defined by the ratio of effective aperture to geometric aperture ( $A_g$ ):  $\eta_a = A_e / A_g = \frac{4A_e}{\pi D^2}$ , where  $D$  is the antenna diameter. It is taken into account in the Kelvin-to-Jansky [ $K/Jy$ ] conversion:

$$\begin{aligned} \text{from Eq. 5.1, } [Jy] &= [K] \times \frac{2k\Omega\nu^2}{c^2}, \text{ hence,} \\ [K/Jy] &= \frac{\lambda^2}{2k\Omega} = \frac{A_e}{2k} = \eta_a \frac{\pi D^2}{8k}. \end{aligned} \quad (5.2)$$

Instead of  $T_a$ , the output from the instrument is often given as  $T'_a$ , the antenna temperature corrected for atmospheric losses, or as  $T_a^*$ , also further corrected for forward scattering. The mean beam efficiency,  $\eta_{mb} = \Omega_{mb} / \Omega_A = T'_a / T_{mb}$ , indicates the fraction of the power that is concentrated in the main beam.

The source brightness temperature,  $T_s$ , is actually dependant on the source size, which is usually unresolved for compact objects:  $T_s = T_{mb} \frac{(\theta_s^2 + \theta_b^2)}{\theta_s^2}$ . Full beam, instead of main beam parameters, apply for extended sources.

#### Single-dish specifications

The data presented in this Chapter belong to 3 proposals which make use of 3 single-dish antennas:



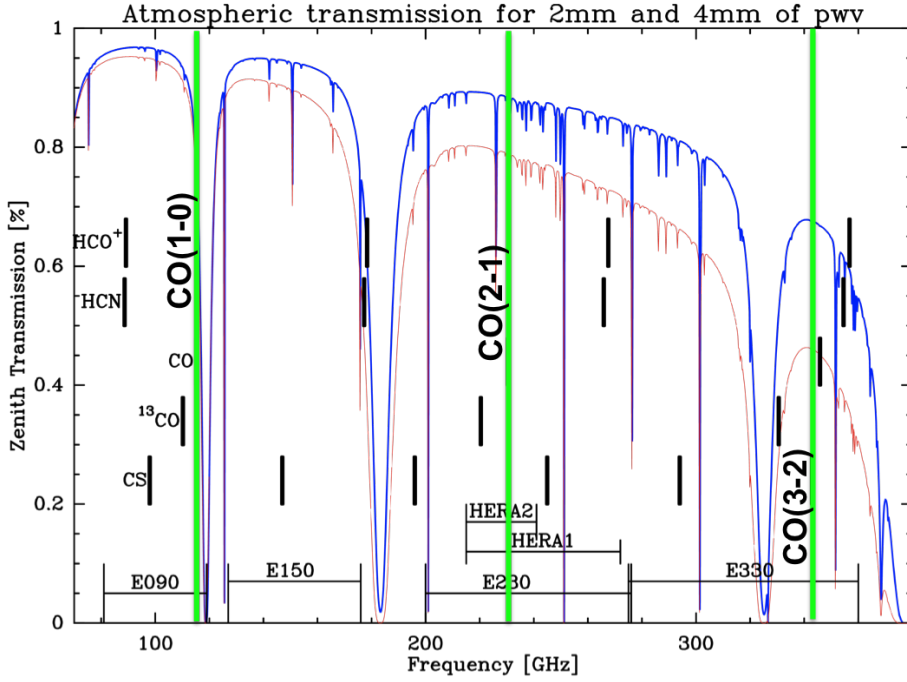


**Figure 5.1.** Atmospheric transmission from the IRAM website (<http://www.iram.es/IRAMES/mainWiki/EmirforAstronomers>). The location of the low-J CO lines are indicated in green. For these lines, small redshifts favor better atmospheric transmissions.

- “Probing the molecular gas in dwarf galaxies” (P.I. D. Cormier), 94.7h with *ATNF*/Mopra;
- “Getting a handle of the molecular gas reservoirs in low metallicity dwarf galaxies observed by Herschel” (P.I. D. Cormier), 34.2h with *APEX*/SHeFI;
- “Low-metallicity star formation: where is the molecular gas?” (P.I. V. Leboutellier), 25.2h with *IRAM*/30-m;

While the *APEX* facility is run in service mode, I have acquired the data of the 2 other programs on-site. General characteristics of these antennas are summarized in Table 5.1.

Mopra is a 22-m antenna located near Coonabarabran, Australia. It is part of the Australia Telescope National Facility (ATNF) and operated by the CSIRO. It has three monolithic microwave integrated circuit (MMIC) receivers, working from 20 to 115 GHz. The 3-mm band is used in wideband mode for continuous coverage of 8.3 GHz (4 sub-bands of 2 GHz each).

SHeFI is the “Swedish Heterodyne Facility Instrument”, built in collaboration with the Chalmers University and Onsala Space Observatory in Sweden. It is mounted on *APEX*, the Atacama Pathfinder EXperiment, located on the site of Llano Chajnantor, Chile, and in collaboration with the MPIfR, OSO, and ESO. It is equipped with four wideband heterodyne receivers, working from 230 to 1 300 GHz. The receivers operate in single sideband, with an intermediate frequency (IF) range of 4-8 GHz.

The 30-m telescope at Pico Veleta near Granada, Spain, is operated by *IRAM*, along with the Plateau de Bure in the Alps near Grenoble, France. The EMIR heterodyne receiver mounted on the 30-m has four bands working from 80 to 360 GHz, with the possibility of using two bands simultaneously, e.g., E0 and E2. EMIR operates in dual sideband, with instantaneous bandwidth of 8 GHz (2 sub-bands of 4 GHz each) per sideband and polarization (i.e. total IF range of 32-GHz).

**Table 5.1.** Radio antennas general specifications.

Antenna	Observed Line	Rest Frequency (GHz)	Receiver	$\theta_{\text{FWHM}}$ ( $''$ )	$\eta_{mb}^{(a)}$	$S/Ta^{*(b)}$ (Jy/K)	Spectral resolution (km s $^{-1}$ )
<i>ATNF/Mopra</i>	$^{12}\text{CO}$ (J $\rightarrow$ 1-0)	115.27	3-mm	33	0.42	30	0.7
<i>IRAM/30m</i>	$^{12}\text{CO}$ (J $\rightarrow$ 1-0)	115.27	EMIR-0	21.3	0.77	6.3	0.5
	$^{12}\text{CO}$ (J $\rightarrow$ 2-1)	230.54	EMIR-2	10.7	0.75	10.5	2.6
<i>APEX/SHeFI</i>	$^{12}\text{CO}$ (J $\rightarrow$ 2-1)	230.54	APEX-1	26	0.75	39	0.08
	$^{12}\text{CO}$ (J $\rightarrow$ 3-2)	345.80	APEX-2	17	0.73	41	0.07

(a) Main beam efficiency.

(b) Point source sensitivity.

### 5.1.2 Sample selection

Due to the faintness of CO and the instrumental sensitivity limitations, studies of CO in dwarf galaxies have essentially focused on Local Group galaxies, such as the Magellanic Clouds, IC 10, NGC 6822, M 33, as well as spiral and irregular dwarfs from the HERACLES survey (Leroy et al. 2009b; Schruba et al. 2012). Detections of the low-J CO lines in BCDs are sparse. From the DGS, only II Zw 40 ( $Z \sim 1/6 Z_{\odot}$ ), Haro 2, Haro 3 ( $Z \sim 1/2 Z_{\odot}$ ), and He 2-10, have been observed in more than one CO transitions (Sage et al. 1992; Meier et al. 2001; Kobulnicky et al. 1995; Bayet et al. 2004).

To complement the CO dataset, we have observed CO in 6 additional dwarf galaxies from the DGS: Haro 11, Mrk 930, Mrk 1089, NGC 625, NGC 4861, and UM 311. These are the brightest IR galaxies of the DGS that lack CO data. This selection is essentially limited by instrument sensitivity. Mrk 930, NGC 4861, and UM 311 had no CO transitions observed at all. CO(1-0) observations were attempted in Haro 11 by Bergvall et al. (2000) without success. Therefore, we observed Haro 11 and UM 311 in the 3 transitions CO(1-0), CO(2-1), and CO(3-2); and Mrk 930 and NGC 4861 in CO(1-0) and CO(2-1). Data of CO(1-0) already existed for Mrk 1089 (Leon et al. 1998), and of CO(2-1) and CO(3-2) for NGC 625 (John Cannon, private communication). Thus for these two galaxies we observed the complementary CO transitions. NGC 625 was observed with 4x1 pointings, while the other galaxies are more compact and required single pointings.

*Haro 11* – is a blue compact galaxy at 92 Mpc, with metallicity  $Z \sim 1/3 Z_{\odot}$  (see Chapter 4). It is composed of 3 main star-forming regions, or knots, described in Vader et al. (1993) and Kunth et al. (2003), with a morphology presumably resulting from a merger event (Östlin et al. 2001). (Adamo et al. 2010). Haro 11 hosts extreme starburst conditions with  $L_{\text{TIR}} = 2 \times 10^{11} L_{\odot}$  (Rémy et al. 2012), and a star formation rate  $\sim 25 M_{\odot} \text{ yr}^{-1}$  (Grimes et al. 2007). Undetected in H I and CO(1-0) (Bergvall et al. 2000), it shows bright MIR and FIR lines, with luminosity  $\sim 1\%$  of  $L_{\text{TIR}}$ , modeled in Cormier et al. (2012a) (see Chapter 4 and Appendix B, p. 169).

*Mrk 1089* – is part of the Hickson Group 31 (Hickson 1982). It is an irregular starburst (HCG 31C) at 57 Mpc and with metallicity  $\sim 1/5 Z_{\odot}$ , in interaction with the galaxy NGC 1741 (HCG 31A). Although the two galaxies are not separated in the MIR-FIR bands, we still refer to Mrk 1089 as in Galametz et al. (2009), since it dominates the emission in these bands and is the only one detected in CO (Leon et al. 1998).

*Mrk 930* – is a blue compact galaxy located at 78 Mpc with metallicity  $\sim 1/4 Z_{\odot}$ . It is also classified as a WR galaxy (Izotov & Thuan 1998), with WR signatures indicating that it is undergoing a young burst episode. It exhibits an intricate morphology with several sites of active star formation, with a star cluster age peaking at 4 Myr (Adamo et al. 2011) and

global SFR  $\sim 6 \text{ M}_{\odot} \text{ yr}^{-1}$ .

*NGC 4861* – is a starburst irregular galaxy with a cometary shape, located at 7.5 Mpc ( $Z \sim 1/5 \text{ } Z_{\odot}$ ). It is classified as a SB(s)m galaxy but shows no evidence for spiral structure (Wilcots et al. 1996). It hosts several knots of star formation, dominated by the south-west region I Zw 49 (where our CO observations point), as seen from H $\alpha$  (van Eymeren et al. 2009). The H $\alpha$  and H I distributions coincide in the center, but the H I extends to form a larger envelope.

*NGC 625* – is an irregular elongated dwarf galaxy in the Sculptor Group, located at 4 Mpc, with metallicity  $\sim 1/4 \text{ } Z_{\odot}$ . It is undergoing an extended starburst  $\geq 50 \text{ Myr}$ , with star formation rate  $0.05 \text{ M}_{\odot} \text{ yr}^{-1}$  (Skillman et al. 2003), which resulted in an outflow visible in H I (Cannon et al. 2004, 2005). It is detected in CO(2-1) and CO(3-2) towards the main dust concentration (John Cannon, private communication).

*UM 311* – is one of a group of 3 compact H II galaxies at a distance of 23 Mpc and with metallicity  $\sim 1/3 \text{ } Z_{\odot}$ , located between the pair of spiral galaxies NGC 450 and UGC 807. It is bright in H $\alpha$  (Guseva et al. 1998) and H I (Smoker et al. 2000). The individual sources of the group are separated by  $\sim 15''$  and are not resolved in the FIR photometry, although UM 311 dominates the emission. In the following work, reference to UM 311 encompasses the 3 sources of the group. The  $L_{\text{TIR}}$  of the group is  $5 \times 10^9 \text{ L}_{\odot}$ .

Global properties of these galaxies are summarized in Table 5.2.

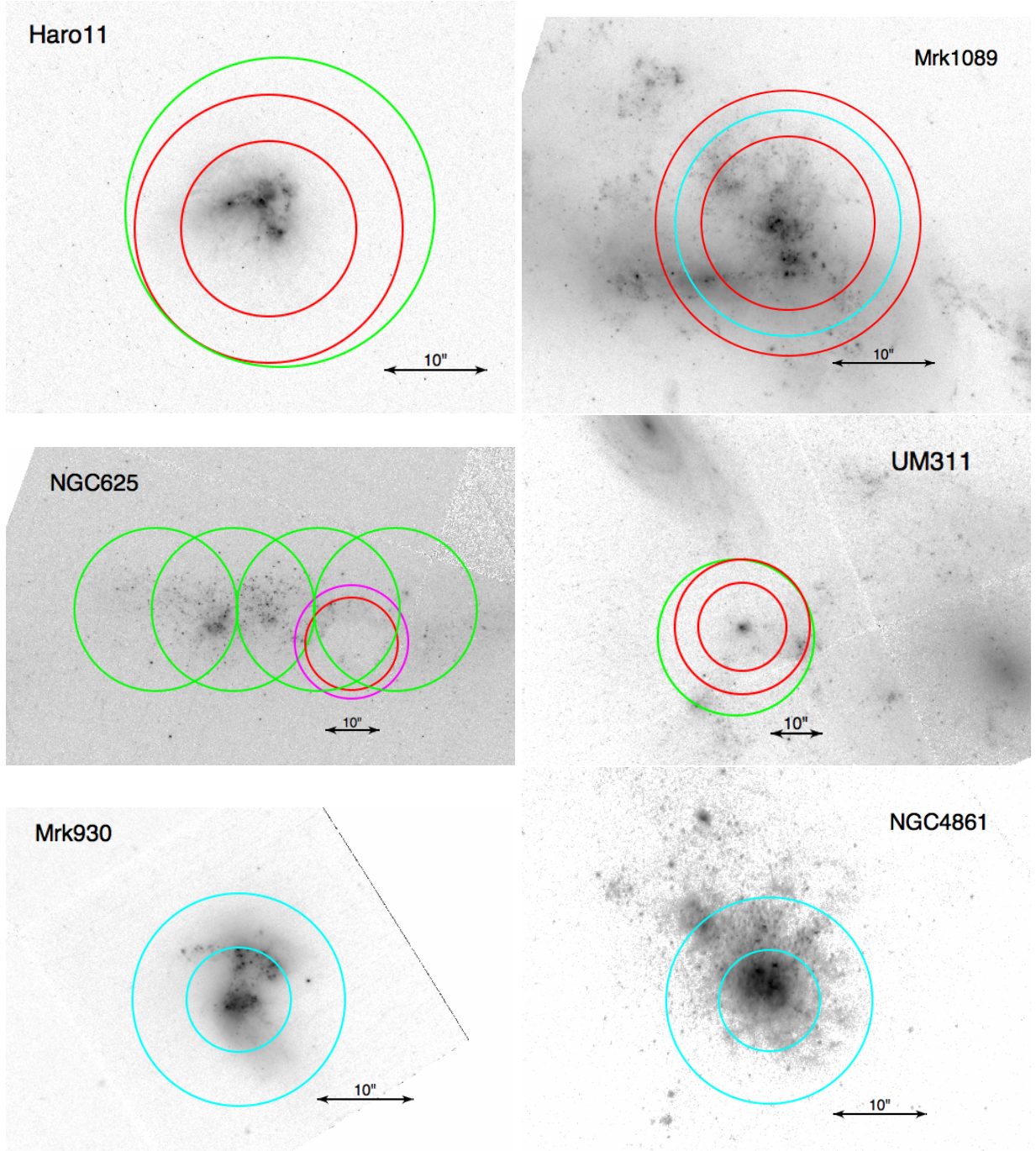


**Figure 5.2.** *HST* broadband images of the 6 galaxies surveyed in CO. The antenna beams are overlaid: *Mopra* in green (33''), *APEX* in red (26'', 17''), *IRAM* in blue (21'', 11''), and the *JCMT* in magenta (22'') for NGC 625.

**Table 5.2.** General properties of the dwarf subsample.

Galaxy	Coordinates (J2000)	Dist. (Mpc)	Optical size (arcmin <sup>2</sup> )	Metallicity 12+log(O/H)	$M_B$ (mag)	$M_{H\ I}$ ( $10^9 M_\odot$ )	$L_{TIR}$ ( $10^9 L_\odot$ )	$L_{H\alpha}$ ( $10^7 L_\odot$ )	$L_{FUV}$ ( $10^9 L_\odot$ )	SFR ( $M_\odot \text{ yr}^{-1}$ )
Haro 11	00h36'52.5" -33°33'19"	92	0.4x0.5	8.2	-20.6	<0.1	185	92	22	32
Mrk 1089	05h01'37.8" -04°15'28"	57	0.6x0.2	8.0	-20.5	15	37.4	23	-	6.4
Mrk 930	23h31'58.3" +28°56'50"	78	0.4x0.4	8.06	-	3.0	20.3	23	-	3.5
NGC 4861	01h15'34.0" -00°51'32"	7.5	4.0x1.5	8.0	-16.8	0.48	0.340	0.04	0.46	0.06
NGC 625	01h35'04.6" -41°26'10"	3.9	5.8x1.9	8.1	-16.2	0.13	0.285	0.18	0.11	0.05
UM 311	01h15'34.0" -00°51'32"	24	0.1x0.1	8.3	-19.2	2.5	0.87 <sup>(a)</sup>	0.48	-	0.15

Coordinates and optical sizes are taken from the NASA/IPAC Extragalactic Database.

Distances, metallicities,  $M_B$ , and  $H\ I$  mass are from [Madden et al. \(2012b\)](#) (see references therein).

(a)  $L_{TIR}$  is integrated over an aperture of radius 20" for UM 311, as used in Chapter 3.

For the other galaxies,  $L_{TIR}$  values are integrated SEDs from 3 to 100  $\mu\text{m}$  from [Rémy et al. \(2012\)](#).

SFRs are derived from  $L_{TIR}$  using the [Kennicutt \(1998\)](#) formula. Luminosities and masses are scaled to the quoted distances.

*References for  $L_{H\alpha}$* : Haro 11: [Östlin et al. \(1999\)](#), UM 311: [Terlevich et al. \(1991\)](#), Mrk 930: [Adamo et al. \(2011\)](#), NGC 4861: [Schmitt et al. \(2006\)](#),

Mrk 1089: [Iglesias-Paramo & Vilchez \(1997\)](#), and NGC 625: [Kennicutt et al. \(2008\)](#).

*References for  $L_{FUV}$* : Haro 11: [Grimes et al. \(2007\)](#), NGC 4861: [Gil de Paz et al. \(2007\)](#), and NGC 625: [Lee et al. \(2011\)](#).



### 5.1.3 Mopra observations

#### Observing

We observed the CO (J=1-0) molecule in Haro 11, NGC 625, and Mrk 1089 with the ATNF *Mopra* 22-m telescope from September 13 to 18 2011. Observations consisted of a single pointing for Haro 11 and UM 311, and of a  $4 \times 1$  map with a half-beam step for NGC 625. The size of the beam is  $\sim 30''$ . The position switching observing mode consist of a pattern of 4min: OFF1-ON-ON-OFF2, where OFF1 and OFF2 are two different reference positions in the sky taken  $\geq 1.5'$  away from the source, to remove the contribution from the sky. We observed in wideband mode, scanning a total bandwidth of 8.2 GHz. The temperature of the system is calculated every 20 min. The total integration times were 14.1 h, 10.3 h, and 3.0 h, resulting in a total of 844, 616, and 180 individual spectra (counting both polarisations separately) for Haro 11, UM 311, and NGC 625 respectively. The average system temperatures were 260, 330, and 310 mK.

#### Data reduction

We used our own IDL-written script for the data reduction. We first create a quotient spectrum taking the average of the two reference position spectra before and after the on-source spectrum. The equation for the quotient spectrum with continuum removal is:  $Q = T_{OFF} \times (ON/OFF) - T_{ON}$ . We then fit a spline function to remove the large scale variations and shift the signal to a median level of zero. The data is calibrated using a main beam efficiency of  $\eta_{mb} = 0.42$ . The pointing errors are estimated to be  $\leq 3.5''$ .

Due to the long integration times, the spectra of Haro 11 and UM 311 are strongly affected by  $\sim 30$  MHz baseline ripples. This is a known issue of the *Mopra* antenna, believed to be caused by standing waves in the receiver-subreflector cavity. To counter this effect, we selected 2 different reference positions and applied a defocusing procedure before observing. The defocusing aims to vary the subreflector position during the observing run with a  $\lambda/2$  cycling, so that the standing waves no longer dominate and cancel as the cavity length expands (Balt Indermuehle, private communication). Although the effect of the standing waves might have been reduced by these methods, it is still present in our data. Since its shape changes with frequency, it is difficult to model it properly. A naive filtering of frequencies around 30 MHz might be too crude and remove part of the signal. As a first step, we identify by eye the spectra affected by the ripples. 10% show ripples with strong amplitude, and standard deviation  $> 110$  mK, and 20% with ripples of lower amplitude but clear wave shapes. Flagging out these spectra, we then rebin the data to a spectral resolution of  $10 \text{ km s}^{-1}$ , and do a sigma-weighted average to obtain a final spectrum, with no additional correction. The CO lines are still not detected in Haro 11 and UM 311. We then aim for a better estimate of the rms level and decide as a second step to model the ripples as a set of sinusoids with varying frequency and amplitude. This is done using a defringing tool based on a routine originally developed for removing fringes from *ISO* SWS spectroscopic data (Kester et al. 2003). The routine was modified for our purpose and tuned to specifically search for a maximum of ten significant fringes in the frequency domain of the fringes seen in the deep *Mopra* data. It is applied on all individual spectra. After subtracting the ripples, the noise level is greatly reduced. We also tried filtering out a range of frequencies in Fourier domain, but the former method gives better results. Again, the final spectrum, shown in Fig. 5.3, is obtained with a sigma-weighted average of all spectra.

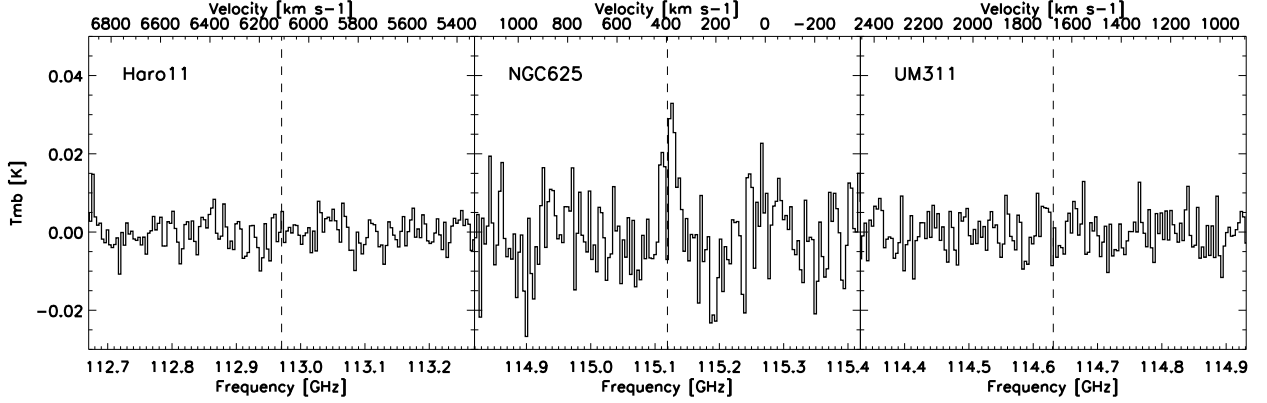


**Figure 5.3.** *Mopra* spectra ( $T_{mb}$ ) of the CO (J=1-0) 115 GHz line in Haro 11 (*left*), NGC 625 (*center*), and UM 311 (*right*). The vertical dashed lines indicate the position of the expected emission lines at the observed frequency. The spectral resolution is  $10 \text{ km s}^{-1}$ .

#### 5.1.4 APEX observations

##### Observing

We observed the CO (J=2-1) and CO (J=3-2) molecules in Haro 11, Mrk 1089, and UM 311 with the *APEX*/SHeFI spectrometer from September 3 to 11 2011. The size of the beam is  $\sim 26''$  at 230 GHz and  $\sim 17''$  at 345 GHz. We integrated on the source (ON+OFF, ON is half that time) for a total time of 82 and 120 min for Haro 11, 79 and 140 min for UM 311, 135 and 110 min for Mrk 1089, for CO (J=2-1) and CO (J=3-2) respectively. Temperatures are corrected for main beam efficiencies of 0.75 and 0.73 at 230 and 345 GHz. The average system temperatures are 150, 248, 156, 214, 153, 208 mK.

##### Data reduction

The data reduction was performed with the “Continuum and Line Analysis Single-dish Software” (CLASS) within the GILDAS software (<http://www.iram.fr/IRAMFR/GILDAS>). The spectra are all averaged together and smoothed to a resolution of  $\sim 10 \text{ km s}^{-1}$ . A 3rd order polynomial is removed for the baseline, and a Gaussian fit is applied to derive the line intensity.

##### Line profiles and velocities

We detect both the CO(2-1) and CO(3-2) lines in the 3 galaxies (Figure 5.4). Line profiles show interesting structure. For all 3 galaxies, the central velocities of the CO lines are lower than those of H I and optical lines (typically  $\text{H}\alpha$ ,  $\text{H}\beta$ ). We overlay the different line centers on the CO spectra (Figure 5.4).

Mrk 1089 has broad CO profiles, with  $\text{FWHM} \sim 110\text{--}150 \text{ km s}^{-1}$ . The signal-to-noise is high enough in Mrk 1089 to clearly distinguish two velocity components, at  $3950 \text{ km s}^{-1}$  and  $4000 \text{ km s}^{-1}$ , which also seem present in the CO(1-0) data from Leon et al. (1998), although the velocity resolution is coarser. At the edges of the *APEX* CO profiles, we may see possible wings, somewhat drowned in the noise. These CO velocities are lower than the central velocities of [C II] ( $4080 \text{ km s}^{-1}$ ), H I ( $4030 \text{ km s}^{-1}$ ) (Williams et al. 1991), or  $\text{H}\alpha$  ( $4070 \text{ km s}^{-1}$ ). The H I velocities show perfect agreement with the ionised gas (Williams



et al. 1991), with velocities ranging between 3970 and 4200 km s<sup>-1</sup> for the entire HCG 31 complex (Mrk 1089 being identified as HCG 31C). The [C II] velocities range between 4030 and 4180 km s<sup>-1</sup>, but the line is not spectrally resolved (PACS FWHM~240 km s<sup>-1</sup>). Although unresolved, several [C II] components may be present, as in the CO profiles, as signatures of this group in interaction.

Haro 11 has CO profiles with a unique visible component, of width ~60 km s<sup>-1</sup>, at central velocity ~6110 km s<sup>-1</sup>. Again, possible emission may be present in the wings of the line, but the S/N is not good enough to clearly identify them. For Haro 11, the H $\alpha$  velocity range between 6230 km s<sup>-1</sup> and 6300 km s<sup>-1</sup>, with average velocity 6260 km s<sup>-1</sup> (Östlin et al. 1999). The [C II] velocities range between 6100 and 6250 km s<sup>-1</sup>, with central velocity 6175 km s<sup>-1</sup>. Interestingly, the PACS lines have broad profiles, indicating complex kinematics, possibly tracing outflows. The line width of [C II] is ~300 km s<sup>-1</sup>, while those of [O III] and [O I] are 280 and 200 km s<sup>-1</sup> respectively, which is much greater than the CO line width of ~60 km s<sup>-1</sup>. This confirms the fact that the [C II] emission, as well as that of the other FIR lines, arise from a larger region than CO.

UM 311 shows narrower CO profiles than the other two galaxies, with line widths of ~45 km s<sup>-1</sup>, and centered at 1680 km s<sup>-1</sup>. For UM 311, the H I central velocity is around 1760 km s<sup>-1</sup> (Smoker et al. 2000), with two line peaks at 1720 and 1800 km s<sup>-1</sup>, and the optical velocity is at 1800 km s<sup>-1</sup> (Terlevich et al. 1991). The [C II] velocities range between 1670 and 1770 km s<sup>-1</sup> for the complex (UM 311 being one of several H II galaxies and located near two spiral galaxies), with velocity 1720 km s<sup>-1</sup> at the position of UM 311. The line profile is not resolved with PACS.

### 5.1.5 IRAM observations

#### Observing

We observed the CO (J→1-0) and CO (J→2-1) molecules in Mrk 930 and NGC 4861 with the *IRAM* 30-m telescope from July 19 to 24 2012. Observations were done in wobbler switching mode, with a throw of 4' for NGC 4861 and 1.5' for Mrk 930, and consist of a single pointing towards the peak of star formation as seen from the [C II] emission. The beam sizes are ~21'' at 115 GHz and ~11'' at 230 GHz. The total integration times (ON+OFF) were 455 and 407min for NGC 4861 and 538 and 548min for Mrk 930, for CO(1-0) and CO(2-1) respectively. The average system temperatures are 362 and 408 mK for NGC 4861 and 190 and 355 mK for Mrk 930. Antenna temperatures are corrected for main beam efficiencies of 0.77 and 0.75 at 115 and 230 GHz. The temperature of the system is calculated every 15min, pointings were done every 1h and focus every 2h on average.

#### Data reduction

The 30-m data is reduced the same way as for the SHeFI data (above) with CLASS.

## 5.2 Empirical diagnostics

### 5.2.1 Line ratios

The similar beam size of the CO(1-0) line at *Mopra* (~30'') and the CO(2-1) line at *APEX* (~26'') make the comparison between these lines independent of source size. However, the

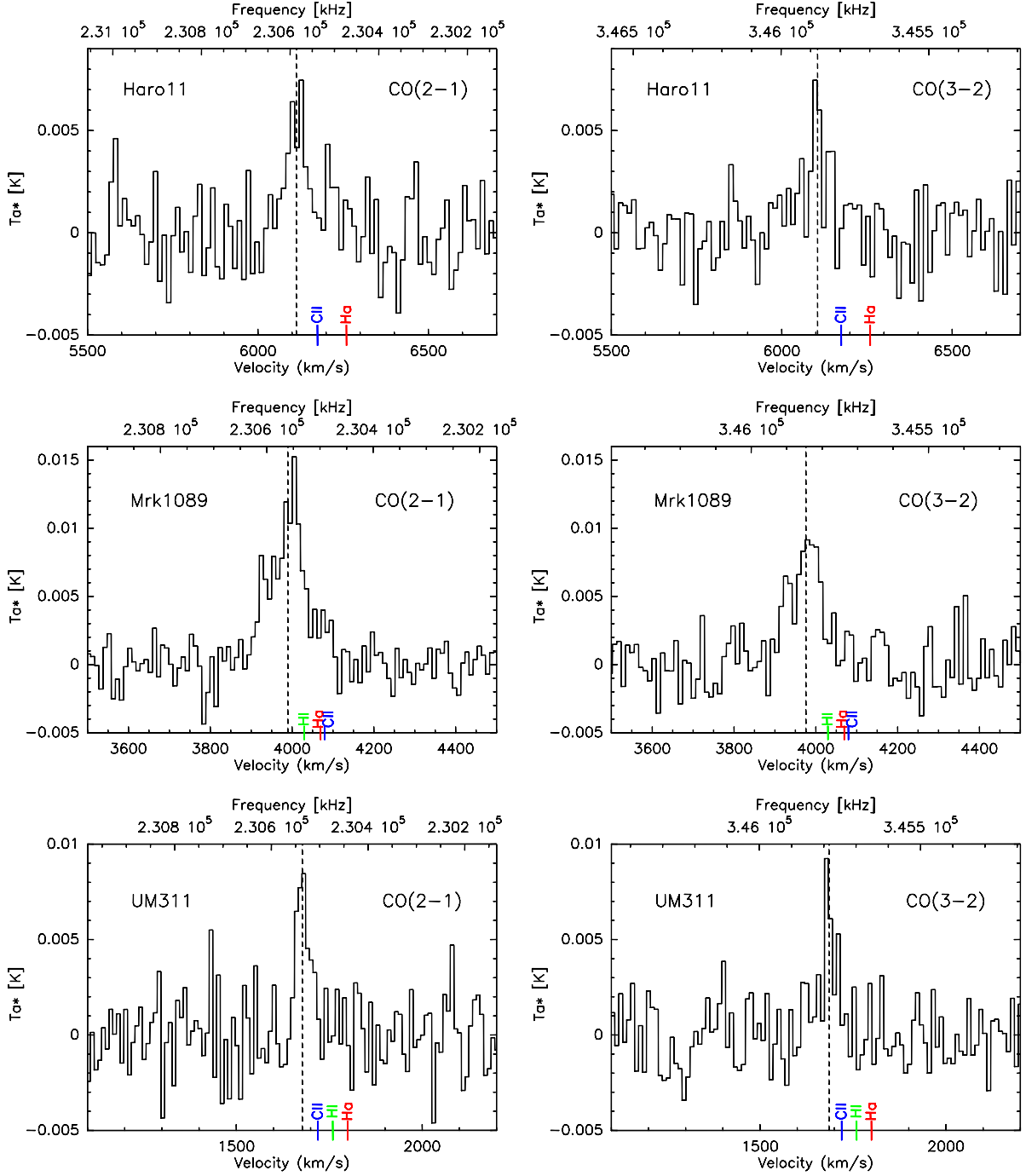


**Figure 5.4.** *APEX* spectra ( $T_a^*$ ) of the CO ( $J=2-1$ ) 230 GHz (*left*) and CO ( $J=3-2$ ) 345 GHz (*right*) lines, in Haro 11, Mrk 1089, and UM 311 (*from top to bottom*). They are put to a common resolution of  $\sim 10 \text{ km s}^{-1}$ . Central velocities of [C II], H I, and H  $\alpha$  are also indicated in blue, green, and red, respectively.

CO(3-2) beam at *APEX* ( $\sim 17''$ ), the CO(2-1) beam at the *JCMT* ( $\sim 20''$ ), and the CO(1-0) and CO(2-1) beams at *IRAM* ( $\sim 22''$  and  $11''$ ) are smaller. Line ratios, here for CO  $J=2-1$  /  $J=1-0$ , are given by:

$$R_{21} = \frac{T_s(2-1)}{T_s(1-0)} = \frac{T_{mb,2-1} \Omega_{21}}{T_{mb,1-0} \Omega_{10}} = \frac{T_{mb,2-1} \times (\theta_{21}^2 + \theta_s^2)}{T_{mb,1-0} \times (\theta_{10}^2 + \theta_s^2)} \quad (5.3)$$

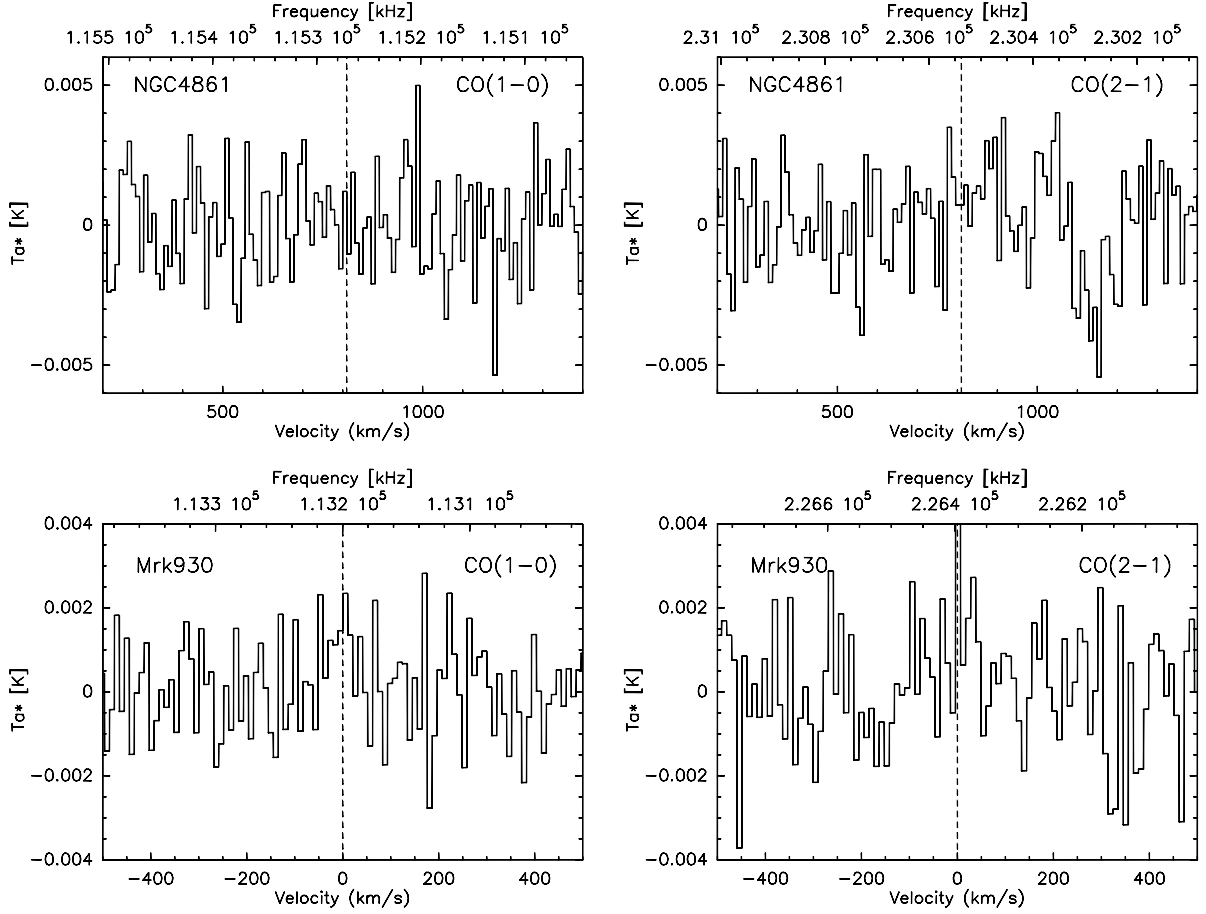


**Figure 5.5.** IRAM spectra ( $T_a^*$ ) of the CO ( $J=1-0$ ) 115 GHz (left) and CO ( $J=2-1$ ) 230 GHz (right) lines, in NGC 4861 (top) and Mrk 930 (bottom). They are put to a common resolution of  $\sim 10 \text{ km s}^{-1}$ .

$\Omega_{21}$  and  $\Omega_{10}$  are the antenna beam solid angles, and  $\theta_{21}$  and  $\theta_{10}$  are the beam sizes, for the CO  $\rightarrow 2-1$  and CO  $\rightarrow 1-0$  transitions. Therefore we derive line ratios in two cases: (1) if the source is point-like ( $\Omega_{\text{source}} \ll \Omega_{\text{beam}}$ ) or (2) if the source is larger than the beam ( $\Omega_{\text{beam}} \ll \Omega_{\text{source}}$ ). The latter case is still valid if the source is not resolved but the CO emission comes from small clumps scattered across the beam and fills the beam (no beam dilution). The line ratios are summarized in Table 5.4.

Overall, the sample does not show unusual line ratios, although there can be significant uncertainties due to the different beam sizes and unknown source size. We find an average CO  $J=3-2 / J=2-1$  ratio of  $\sim 0.4$  in the point-like limit and of  $\sim 0.8$  in the uniform filling limit. Ratios of CO  $J=3-2 / J=1-0$  and CO  $J=2-1 / J=1-0$  are around 0.5 and 0.9 respectively. The lack of firm detections on the CO ( $J=1-0$ ) line render these ratios rather uncertain. CO  $J=2-1 / J=1-0$  ratios of  $\sim 0.8$  are found in spiral disks (Leroy et al. 2008), and similarly ratios of CO  $J=3-2 / J=2-1$  are around 0.8 in Galactic GMCs (Wilson et al. 1999). Wilson et al. (2009) uses an average ratio of CO  $J=3-2 / J=1-0$  of 0.6 to trace the dense gas mass in Virgo Cluster spiral galaxies. Values close to those found in the Galaxy indicate that the CO lines come from the same phase and hence trace the total gas, while higher line ratios indicate warmer and/or denser gas. Sage et al. (1992) find CO  $J=2-1 / J=1-0$  ratios between 0.3 and 0.6 in the point-source limit for a sample of dwarf galaxies, and Meier et al. (2001) derive an average CO  $J=3-2 / J=1-0$  ratio of 0.6. Ratios  $\geq 1$  are found in bright regions of

**Table 5.3.** New CO fluxes.

Galaxy	Line	$\theta_{FWHM}$ ( $''$ )	$T_{mb}$ (mK)	V (km s $^{-1}$ )	$\Delta V$ (km s $^{-1}$ )	$I_{CO}$ (K km s $^{-1}$ )	$L_{CO}$ ( $L_{\odot}$ )	Reference
Haro 11	CO J=1-0	30 <sup>(1)</sup>	< 10.7 <sup>(a)</sup>	-	-	< 0.57	< $5.5 \times 10^3$	this work
	CO J=2-1	26 <sup>(2)</sup>	8.49	6113	56	$0.51 \pm 0.10$	$3.0 \times 10^4$	this work
	CO J=3-2	17 <sup>(2)</sup>	6.49	6105	63	$0.44 \pm 0.10$	$3.7 \times 10^4$	this work
Mrk 1089	CO J=1-0	21 <sup>(3)</sup>	15.7	3987	148	$1.53 \pm 0.30$	$2.8 \times 10^3$	Leon et al. (1998)
	CO J=2-1	26	14.1	3990	111	$1.68 \pm 0.09$	$3.8 \times 10^4$	this work
	CO J=3-2	17	11.5	3976	95	$1.17 \pm 0.12$	$3.8 \times 10^4$	this work
Mrk 930	CO J=1-0	21	2.15	5491	64	$0.14 \pm 0.05$	$5.0 \times 10^2$	this work
	CO J=2-1	11 <sup>(3)</sup>	< 5.60	-	-	< 0.30	< $2.2 \times 10^3$	this work
NGC 4861	CO J=1-0	21	< 7.08	-	-	< 0.37	< $1.2 \times 10^1$	this work
	CO J=2-1	11	< 7.70	-	-	< 0.41	< $2.8 \times 10^1$	this work
NGC 625	CO J=1-0	30	27.1	380	71	$2.02 \pm 0.63$	$3.6 \times 10^1$	this work
	CO J=2-1	22 <sup>(4)</sup>	58.0	390	30	$1.85 \pm 0.50$	$1.2 \times 10^2$	J. Cannon
	CO J=3-2	17	63.6	381	23	$1.55 \pm 0.10$	$2.4 \times 10^2$	ESO Archive <sup>(b)</sup>
UM 311	CO J=1-0	30	< 11.4	-	-	< 0.61	< $4.1 \times 10^2$	this work
	CO J=2-1	26	11.0	1678	41	$0.48 \pm 0.08$	$1.9 \times 10^3$	this work
	CO J=3-2	17	8.62	1686	46	$0.42 \pm 0.08$	$2.4 \times 10^3$	this work

(1) *ATNF*/Mopra, (2): *Apex*/SHeFI, (3): *IRAM*/30-m, (4): *JCMT*/RxA.

(a) The upper limits are  $3\sigma$ .

(b) Program 00.F-0007-2005 (P.I. J. Cannon) at *APEX*.

the Magellanic Clouds (Bolatto et al. 2000, 2003) and are attributed to, on average, small, warmer clumps.

### 5.2.2 Molecular gas mass

The CO data enable us to quantify the  $H_2$  mass via the  $X_{CO}$  factor. While converting from observed CO lines to molecular gas mass is uncertain for low metallicity galaxies (see Chapter 1), we can make first empirical approximations by considering two cases: one where  $X_{CO}$  is equal to the Galactic value  $X_{CO,gal}$ , and one where  $X_{CO}$  scales with  $Z^{-2}$  (noted  $X_{CO,Z}$ ), as found in Schrubba et al. (2012). Although the variation of  $X_{CO}$  with metallicity is still debated, the true  $X_{CO}$  values for our galaxies are likely to be between the two cases considered.

CO is emitted by small filling factor clumps that are not resolved in our observations, hence the source sizes are unknown. For galaxies with *APEX* detections of the CO(3-2) line, we assume the source size to be  $17''$  (CO J=3-2 beam size). For galaxies observed with *IRAM* (Mrk 930 and NGC 4861), we assume the source size to be the CO J=1-0 beam since only the CO(1-0) observations in Mrk 930 is a detection. Now, knowing the source sizes and  $X_{CO}$  factors, we can derive molecular gas masses for the 6 galaxies from their observed CO(1-0) intensities (Table 5.5). Although the  $X_{CO}$  conversion factor is calibrated on the CO (J $\rightarrow$ 1-0) transition, we can also estimate the molecular mass from the CO(2-1) and CO(3-2) observations using the common values of 0.8 and 0.6 for the CO J=2-1 / J=1-0 and CO J=3-2 / J=1-0 ratios (also in Table 5.5).

For Haro 11, if assuming  $X_{CO,gal}$ , we find a molecular gas mass similar to that found in Bergvall et al. (2000), where they estimate  $M(H_2) \leq 10^8 M_{\odot}$  from their CO upper limit. The gas mass would increase significantly if considering a higher  $X_{CO}$ , and that is the case as soon as the metallicity is  $Z \leq 1/2 Z_{\odot}$ . For Mrk 1089, Leon et al. (1998) find  $M(H_2) = 4.4 \times 10^8 M_{\odot}$  from CO J=1-0 observations, with a Galactic conversion factor, and a larger beam. This value

**Table 5.4.** CO line ratios.

Galaxy	3-2 / 1-0	3-2 / 2-1	2-1 / 1-0
Haro 11			
<i>case 1</i>	>0.25	$0.37 \pm 0.11$	>0.67
<i>case 2</i>	>0.76	$0.85 \pm 0.26$	>0.89
Mrk 1089			
<i>case 1</i>	$0.40 \pm 0.14$	$0.30 \pm 0.03$	$1.35 \pm 0.46$
<i>case 2</i>	$0.62 \pm 0.22$	$0.70 \pm 0.08$	$0.88 \pm 0.30$
Mrk 930			
<i>case 1</i>	-	-	<2.02
<i>case 2</i>	-	-	<0.56
NGC 625			
<i>case 1</i>	$0.25 \pm 0.08$	$0.61 \pm 0.17$	$0.41 \pm 0.17$
<i>case 2</i>	$0.77 \pm 0.26$	$0.84 \pm 0.23$	$0.92 \pm 0.39$
UM 311			
<i>case 1</i>	>0.22	$0.37 \pm 0.09$	>0.60
<i>case 2</i>	>0.69	$0.87 \pm 0.22$	>0.79

*case 1*: the source is point-like ( $\Omega_{\text{source}} \ll \Omega_{\text{beam}}$ ),

*case 2*: the source fills the beam ( $\Omega_{\text{beam}} \ll \Omega_{\text{source}}$ ).

is higher than that we derive with  $X_{\text{CO,gal}}$  due to the beam difference, and is below that we derive for a metallicity-scaled  $X_{\text{CO,Z}}$ . We find comparable mass values using the CO J=2-1 and CO J=3-2 lines. There are no other molecular mass estimates for Mrk 930, NGC 625, NGC 4861, and UM 311 in the literature to compare to.

A sensible approach which does not rely on the uncertainties of the  $X_{\text{CO}}$  factor would be to use radiative transfer models to account for both the observed dust and gas and therefore derive more accurately the total gas reservoir. We investigate this question in Section 5.3.2 for Haro 11 with a full radiative transfer modeling.

### 5.2.3 RADEX model

We use the non-LTE code RADEX (van der Tak et al. 2007b), based on the escape probability method (see Section 4.1.1) to analyse the physical conditions of the low-J CO-emitting gas. Initial conditions to run the code are taken as standard (CO molecular data, two collision partners  $\text{H}_2$  and  $\text{e}^-$ , CMB background radiation). We build a 2D grid in gas density ( $n_{\text{H}_2}$ ) – kinetic temperature ( $T_{\text{kin}}$ ) space. The grid is in logarithmic scale, where  $n_{\text{H}_2}$  is varied from 2.0 to 6.0 ( $\log \text{cm}^{-3}$ ) with step 0.1, and  $T_{\text{kin}}$  from 1.0 to 3.0 (log K) with step 0.1.

We draw contour plots of CO line ratios for the 4 galaxies with at least 2 line detections (Figure 5.6). The ratios in the uniform filling case are used. Low-J CO lines are temperature indicators in the high-density and low/moderate temperature regime, which is a result of approaching LTE conditions ( $T_{\text{exc}} \sim T_{\text{kin}}$ ). They are density tracers at low densities and high temperatures, as they are below their critical densities and sub-thermally excited ( $T_{\text{exc}} \leq T_{\text{kin}}$ ).

The behavior of the ratios considered is similar and hence give poor constraints on the physical conditions of the gas. Densities are generally found  $\geq 10^3 \text{ cm}^{-3}$ . Unless one or the other value of gas density or  $T_{\text{kin}}$  are known from other tracers, more detailed modeling is required to narrow down the range of molecular cloud physical conditions.

**Table 5.5.** Observed H<sub>2</sub> masses using  $X_{\text{CO}}$ .

Galaxy	$\frac{X_{\text{CO}}}{X_{\text{CO,gal}}}^{(a)}$	$M_{\text{H}_2} (M_{\odot})$			
		CO (J=1-0)	$R_{21} = 0.8^{(b)}$	$R_{31} = 0.6^{(c)}$	Average
Haro 11	1	$<9.1 \times 10^7$	$1.0 \times 10^8$	$1.2 \times 10^8$	$1.1 \times 10^8$
	10	$<9.1 \times 10^8$	$1.0 \times 10^9$	$1.2 \times 10^9$	$1.1 \times 10^9$
Mrk 1089	1	$1.2 \times 10^8$	$1.3 \times 10^8$	$1.2 \times 10^8$	$1.2 \times 10^8$
	25	$2.9 \times 10^9$	$3.2 \times 10^9$	$3.0 \times 10^9$	$3.0 \times 10^9$
Mrk 930	1	$2.6 \times 10^7$	$<6.5 \times 10^7$	-	$2.6 \times 10^7$
	16	$4.9 \times 10^8$	$<1.2 \times 10^9$	-	$4.9 \times 10^8$
NGC 4861	1	$<6.0 \times 10^5$	$<8.2 \times 10^5$	-	$<8.2 \times 10^5$
	25	$<1.5 \times 10^7$	$<2.1 \times 10^7$	-	$<2.1 \times 10^7$
NGC 625	1	$5.8 \times 10^5$	$6.6 \times 10^5$	$7.4 \times 10^5$	$6.6 \times 10^5$
	16	$9.2 \times 10^6$	$1.1 \times 10^7$	$1.2 \times 10^7$	$1.1 \times 10^7$
UM 311	1	$<6.6 \times 10^6$	$6.6 \times 10^6$	$7.6 \times 10^6$	$7.1 \times 10^6$
	6	$<4.2 \times 10^7$	$4.1 \times 10^7$	$4.8 \times 10^7$	$4.5 \times 10^7$

(a): to bracket the range of molecular gas mass, we use two values of the  $X_{\text{CO}}$  factor:  $X_{\text{CO}} = X_{\text{CO,gal}}$  (lower mass case) and  $X_{\text{CO}} = X_{\text{CO,Z}} \propto Z^{-2}$  (upper mass case).

(b):  $R_{21}$  is the CO J=2-1 / CO J=1-0 ratio.

(c):  $R_{31}$  is the CO J=3-2 / CO J=1-0 ratio.

### 5.3 Detailed modeling of Haro 11

#### 5.3.1 Rotational diagrams of the H<sub>2</sub> molecule

Rotational transitions of the molecular hydrogen are visible in the MIR and originate from a warm gas phase, therefore they place constraints on the PDR properties of star-forming regions (and in particular the mass) rather than the cold molecular phase (e.g, [Kaufman et al. 2006](#)). As a first step in characterizing the conditions of the PDR, we can assume local thermal equilibrium (LTE) and build an excitation diagram to populate the H<sub>2</sub> level transitions and estimate the temperature, column density, and mass of the warm molecular gas.

In the *Spitzer*/IRS spectrum of Haro 11, the S(1) to S(3) lines are detected, while the S(0) line is undetected. The fluxes and upper limits are reported in Table 2 of [Cormier et al. 2012a](#) (see Section 4.2.2). The total luminosity of the three detected lines is  $L_{\text{H}_2} = 8.6 \times 10^6 L_{\odot}$ . We follow the method from [Roussel et al. \(2007\)](#), and assume a single temperature to match the S(1) to S(3) lines. This choice is biased towards higher temperatures (and lower masses) due to the non-detection of the S(0) line, as mentioned in [Roussel et al. \(2007\)](#), and found in [Higdon et al. \(2006\)](#).

The excitation diagram is shown in Figure 5.7. The best fit to the S(1), S(2), and S(3) lines is represented by the dotted dark line and agrees with a temperature of 340 K and column density of  $4 \times 10^{18} \text{ cm}^{-2}$ . The resulting H<sub>2</sub> mass is  $M(\text{H}_2) = 3.5 \times 10^6 M_{\odot}$ . This value may be regarded as a lower limit since the S(0) line is not detected. Fitting the  $1\text{-}\sigma$  limit on the S(0) line and the S(1) line (blue dotted line on Figure 5.7) agrees with a temperature of 100 K, column density of  $1.5 \times 10^{21} \text{ cm}^{-2}$  and  $M(\text{H}_2) = 1.3 \times 10^9 M_{\odot}$ . This is a high limit on the warm molecular gas mass. As for the CO analysis, the source size is taken as the smallest beam size (17'' of the CO(3-2) beam).

For a more complete picture of the conditions in the PDR, we investigate a radiative transfer model in the next section.



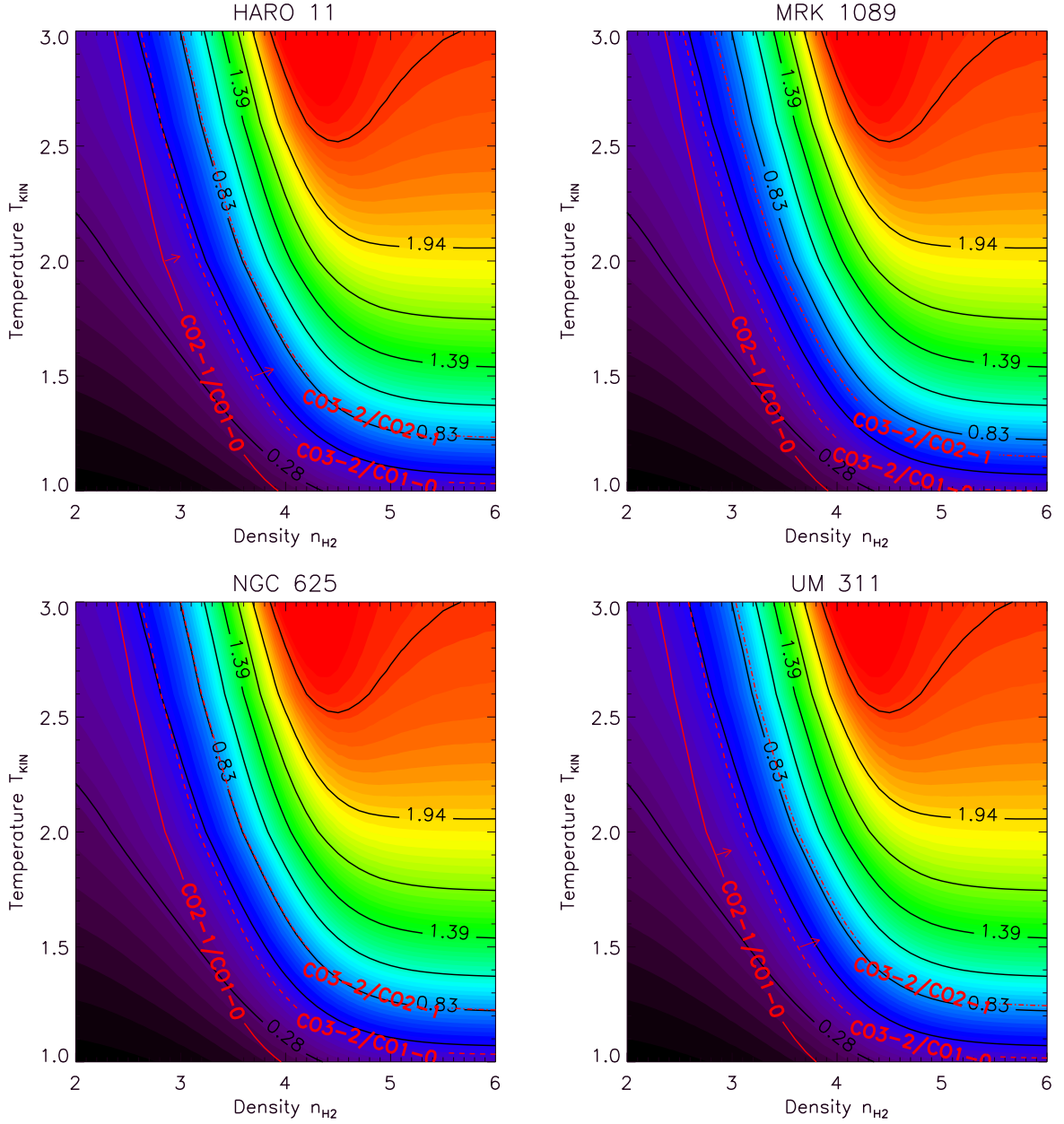


**Figure 5.6.** Contour plots in kinetic temperature ( $T_{kin}$ ) – density ( $n_{H_2}$ ) space (logarithmic scale) made with RADEX. The background colors and dark contours correspond to the model CO J=3-2 / J=2-1 ratio. Observed ratios are indicated in red, with an arrow for lower limits.

### 5.3.2 Full radiative transfer modeling

#### PDR properties

We use the CLOUDY PDR model of Haro 11 described in Section 4.2 of Cormier et al. 2012a (see Section 4.2.2 of this report) to analyse the  $H_2$  emission. This PDR model has parameters  $n_H = 10^{5.1} \text{ cm}^{-3}$ ,  $G_0 = 10^3$  Habing, and a covering factor of  $\sim 10\%$ . With this PDR solution, the model intensities of the three detected  $H_2$  lines are over-predicted by a factor of 10, while the ratios of S(2)/S(1) and S(3)/S(1) are reproduced within 40%. The ratios are well matched and are consistent with the high density of the CLOUDY PDR model. Indeed, the



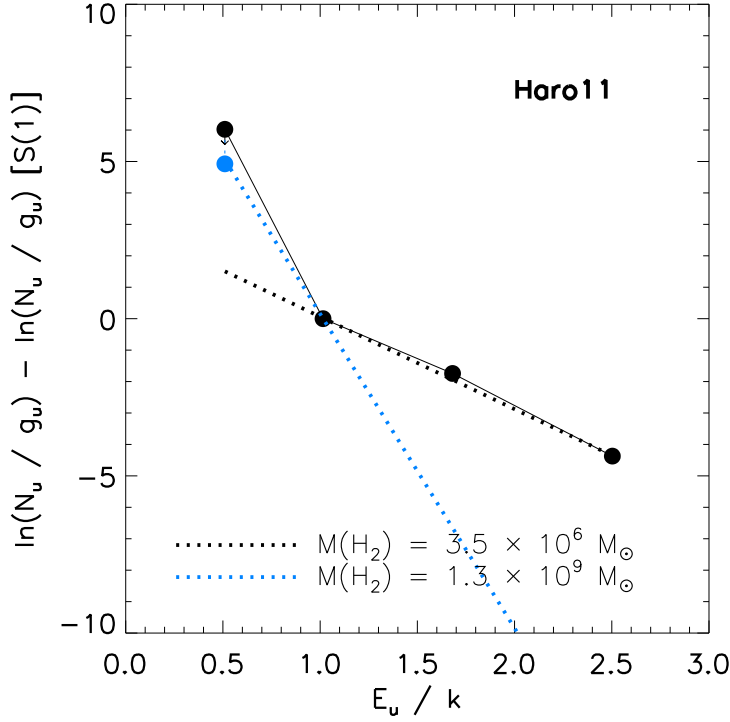


**Figure 5.7.** Excitation diagram of the S(0) to S(3) rotational  $\text{H}_2$  lines. The  $N_u/g_u$  ratios are normalized by the S(1) transition. The observations appear in dark filled circle, and the 1- $\sigma$  limit on the S(0) line in blue circle. The dotted dark line indicates the best fit to the S(1) to S(3) lines. The dotted blue line indicates the fit to the S(0) 1- $\sigma$  limit and the S(1) line.

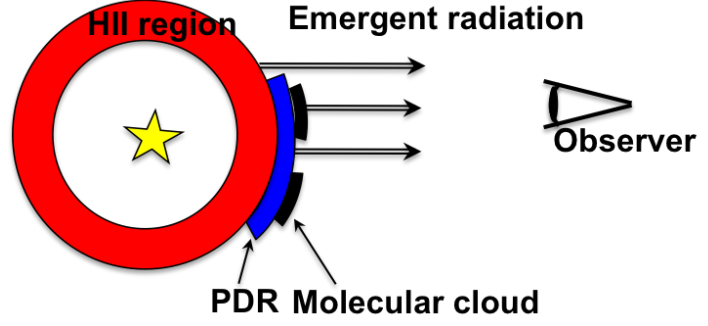
line ratios of  $\text{S}(2)/\text{S}(1) \sim 0.6$  and  $\text{S}(3)/\text{S}(1) \sim 0.7$  agree with high densities  $\geq 10^4 \text{ cm}^{-3}$  from the PDR TOOLBOX (Kaufman et al. 2006).

As discussed in Cormier et al. (2012a), the fact that the observed absolute intensities are not well reproduced by the model but the line ratios are, can have an interpretation in terms of geometry. For the [O I] 63 and  $145 \mu\text{m}$  lines, which are good PDR tracers, we found the need to reduce the covering factor of the PDR model from unity to 10% to reproduce their observed intensities. For the  $\text{H}_2$  lines, even adopting a covering factor of 10% still leads to over-predicting their intensities by a factor of 10 with the model. However, since the  $\text{H}_2$  *Spitzer* lines are emitted in the MIR, the parameter that most influences the  $\text{H}_2$  emission is dust extinction as the IRS lines are attenuated at large  $A_V$  (at least more than the *Herschel* lines up to a certain  $A_V$ ).

While the PDR model from Cormier et al. (2012a) is stopped at  $A_V = 3$  mag, in the next section, we continue the PDR model to larger  $A_V$  to model the CO emission, and we find the need for a covering factor of  $\sim 3\%$  for the molecular cloud. To guide the eye, the geometrical display and contribution of the PDR and molecular phases is illustrated in Figure 5.8. Going to higher  $A_V$  to model the CO lines lowers the emergent predicted intensities of the  $\text{H}_2$  lines if the PDR is geometrically located behind the molecular cloud from the observer. Hence the emergent layer of the PDR has a covering factor of only 7%. This does not change the prediction significantly for the *Herschel* lines analysed in Cormier et al. (2012a), but attenuates significantly the emission of the  $\text{H}_2$  lines behind the molecular cloud. Such considerations are very geometry-dependent and difficult to justify as we have no spatial information on the ISM structures. However, from the *HST* image of Haro 11, we see a dust lane in front of one of the stellar clusters which extinguishes the optical emission and may be the major source of FIR/submm emission. Spatially resolved observations are needed to confirm this picture.

The PDR model is stopped at an  $A_V$  of  $\sim 3$  mag, just before CO starts to form, to quantify

**Figure 5.8.** Schematic of the model geometry. The starburst is surrounded by the cloud, with full coverage of the H II region, and partial coverage of the PDR and molecular cloud layers. The assumed geometry impacts on the emergent radiation from the cloud seen by the observer.



the amount of dark gas untraced by CO (see Section 1.3.2). The total gas mass of the PDR derived is  $M(\text{PDR}) = 1.2 \times 10^8 M_{\odot}$  (Cormier et al. 2012a), and is mainly molecular: 90% is in the form of  $\text{H}_2$  (dark gas component), and only 10% is in the form of H I.

### Molecular cloud properties

To model the molecular cloud ( $A_V \geq$  where CO starts to form) with CLOUDY, we continue the PDR model described above to larger  $A_V$  until the dust column reproduces the FIR emission of the SED ( $A_V \sim 50$ , Cormier et al. 2012a). This way, we assume that the observed CO emission is linked to the densest star-forming cores rather than a more diffuse medium. As discussed in Cormier et al. (2012a), the non-detection of the H I 21-cm line in Haro 11 (Bergvall et al. 2000) excludes the presence of a diffuse extended neutral phase and hence its transition in a diffuse molecular phase.

By doing so, the model predictions do not match the observed CO intensities nor the CO line ratios. The CO intensities and the CO(3-2)/CO(2-1) ratio are globally over-predicted by a factor of 2-3. Again, to reconcile model predictions and observations, one can consider a covering factor of  $\sim 3\%$  for the molecular cloud, instead of 10% for the PDR. The coverage of 5% was used in Cormier et al. (2012a) to match the level of the FIR emission (Section 7.1.3 of the paper). Figure 5.9 (left) shows the CLOUDY model predictions for the CO line luminosities (from CO  $\rightarrow$  1-0 to CO  $\rightarrow$  8-7) as a function of  $A_V$  (models are stopped for  $A_V$  of 50 mag). The observed CO(2-1) and CO(3-2) luminosities are roughly matched by this model and the CO(1-0) model prediction falls below the observed upper limit. The predicted CO(1-0) intensity is actually 3 times lower than the derived upper limit, indicating that telescopes slightly more efficient than *Mopra* (such as *ALMA*) should be able to detect this transition.

Densities in the molecular cloud reach  $10^{5.3} \text{ cm}^{-3}$ . The molecular mass produced by the model is  $4.5 \times 10^8 M_{\odot}$ . This is the mass in the molecular phase associated with CO emission. The molecular mass in the dark gas PDR layer is 25% that of the CO-emitting core, and the total molecular mass in Haro 11 (dark-gas+CO core) is  $5.6 \times 10^8 M_{\odot}$ . The modeled molecular-to-atomic mass ratio is 0.2, and the total model gas mass is  $1.3 \times 10^9 M_{\odot}$ . Thus, the total gas mass to stellar mass ( $10^{10} M_{\odot}$ ) ratio is  $\sim 15\%$ .

The ratio of the two CO lines CO(3-2)/CO(2-1) is still over-predicted by the model by a factor of 2, although this is satisfactory considering the uncertainties of the method. The reason for having high CO model ratios, is that the PDR model assumes thermal pressure equilibrium which prevents the gas to cool to lower temperatures than 100 K as at high density the heating of the gas is mainly due to collisions with  $\text{H}_2$ . The thermal pressure equilibrium which was used to model the physical transition between the H II region and the PDR in Cormier et al. (2012a) is not expected to hold in the molecular regime.

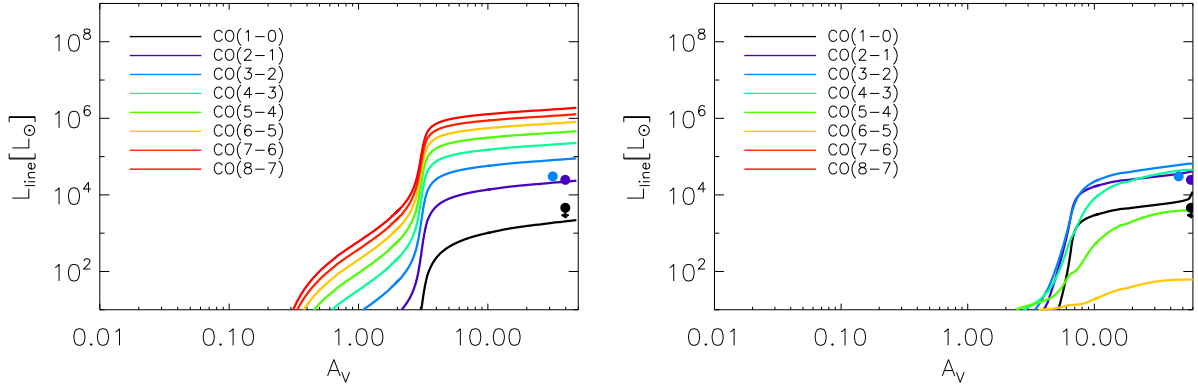


**Figure 5.9.** *Left:* CLOUDY model predictions for the CO line luminosities as a function of  $A_V$ . The model is stopped at  $A_V$  of 50 mag, and the covering factor is set to  $\sim 3\%$ . Observations of the CO(1-0) (upper limit), CO(2-1), and CO(3-2) lines are represented by filled circles. *Right:* Same as *left* with a turbulent velocity  $v_{\text{turb}}$  of 30 km s $^{-1}$ . High-J CO transitions are suppressed.

To allow the gas to reach temperatures  $\leq 100$  K, there are two straightforward options that we explore. As a first step, we opt for a constant density instead of a constant pressure, in which case the pressure and the gas temperature decrease with  $A_V$ . Assuming a constant density is not realistic as the density is expected to increase deeper in the cloud, however, without tracers of denser phases, we have no information on the density profile to adopt. The second option is to include a microphysical turbulence in the model. It is expressed as a velocity term and its value is constrained by the line-width of the observed CO lines ( $\sim 50$  km s $^{-1}$ ), where  $v_{\text{obs}} = \sqrt{v_{\text{thermal}}^2 + v_{\text{turb}}^2}$ . Turbulence has an effect on the shielding and pumping of lines: it boosts the fluorescent excitation of lines by the continuum, but reduces the line opacity and shielding. It is included in the pressure balance, with  $P_{\text{turb}} \propto n_H u_{\text{turb}}^2$ , hence dissipating some energy away from the cloud.

The temperature profile in the cloud changes when adding turbulence. This is seen in Figure 5.10 (*left*), to be compared to Figure 4.4, without turbulence. The gas temperature decreases linearly with  $A_V$  in the molecular cloud, from 200 K down to 10 K, and stabilizes around 7 K in the CO-emitting region. This has a profound effect on the CO ladder, where high-J lines are emitted in a thinner region close to the cloud surface compared to low-J CO lines (Figure 5.9, *right*). The lowest transitions (lowest  $T_{\text{exc}}$ ) are enhanced and ratios of CO(3-2)/CO(2-1) hence decrease with increasing turbulent velocity. Figure 5.10 (*right*) shows the ratios of CO(3-2)/CO(2-1) predicted by CLOUDY as a function of turbulent velocity, in the two cases of constant density and constant pressure.

Note that if the gas temperature is now decreased in the molecular phase, it is no longer ‘transparent’ to the PDR emission of the [O I] lines (which have  $T_{\text{exc}} \geq 100$  K, Table 1.2). Hence the [O I] emission emerging from PDRs behind the molecular cloud would also be affected by geometry assumptions. We do not investigate further the effect of turbulence, or other parameter at play in the molecular phase, because there are too many free model parameters and too few observational constraints to disentangle between one model and another. Some limitations of this modeling work are discussed in Section 6.1.2.

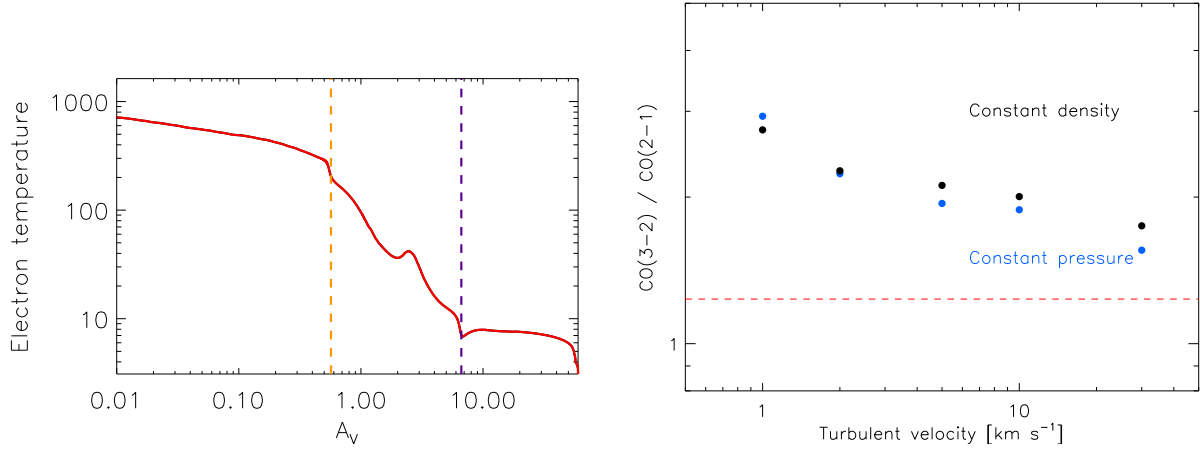


**Figure 5.10.** *Left:* Temperature profile in the cloud (PDR and molecular phase) when adding a turbulent velocity of  $30 \text{ km s}^{-1}$ . The legend is the same as in Figure 4.4. There is no H II region/PDR transition shown as the H II region is not recomputed here. *Right:* CLOUDY model predictions for the CO(3-2)/CO(2-1) ratio as a function of turbulent velocity. The two cases of constant density (in blue) and constant pressure (in dark) are considered. The horizontal dashed red line indicates the observed CO ratio. The models are stopped at  $A_V$  of 50 mag.

**Table 5.6.** Star formation rates (in  $M_{\odot} \text{ yr}^{-1}$ ).

Galaxy	$\text{SFR}_{\text{LIR}}^{(a)}$	$\text{SFR}_{24 \mu m + H\alpha}^{(b)}$	$\text{SFR}_{1.4 \text{ GHz}}^{(c)}$
Haro 11	32	19	33
Mrk 1089	6.4	4.7	15
Mrk 930	3.5	4.7	8.7
NGC 4861	0.059	0.0082	0.11
NGC 625	0.049	0.036	0.014
UM 311	0.93	0.098	1.4

Formulae (a): from Kennicutt (1998); (b) from Calzetti et al. (2007); (c) from Hopkins et al. (2002).

The *Spitzer*  $24 \mu\text{m}$  fluxes used are from Bendo et al. (2012).

References for the 1.4 GHz continuum: Condon et al. (1996) for NGC 625, Condon et al. (1998) for Haro 11 and Mrk 930, Thuan et al. (2004) for NGC 4861, and Hopkins et al. (2002) for Mrk 1089 and UM 311.

## 5.4 Star formation and total gas reservoir

### 5.4.1 Star formation tracers

Different methods to determine star formation rates (SFR) in galaxies are described in Section 1.3.2. With the lack of FUV data for all of the sources, we calculate SFRs for our 6 dwarf galaxies from  $L_{\text{TIR}}$ ,  $H\alpha + 24 \mu\text{m}$ , and 1.4 GHz in Table 5.6. The derived SFRs are comparable between the 3 methods. Only the  $H\alpha$ -derived SFRs in NGC 4861 and UM 311 are noticeably lower as their  $H\alpha$  emission is weak. We use the  $L_{\text{TIR}}$ -derived SFRs in the following analysis.

$[\text{C II}]/\text{CO}(1-0)$  can effectively be used as a star formation tracer in nearby normal galaxies (Stacey et al. 1991) and high-redshift galaxies ( $z \sim 1-2$ ; Stacey et al. 2010), with average values between 2000 and 4000 (for star-forming galaxies). The different cloud structure at low metallicity produces smaller CO cores and a larger PDR envelope which can in principle be traced by  $[\text{C II}]$ . This results in high  $[\text{C II}]/\text{CO}$  ratios as observed in low metallicity dwarf galaxies (Madden 2000). For our sample, we also find high ratios with  $[\text{C II}]/\text{CO}(1-0) \geq 10\,000$ . This is illustrated in Figure 5.11 (left) showing  $[\text{C II}]/\text{CO}(1-0)$  versus  $L_{\text{TIR}}$ . For Haro 11, if

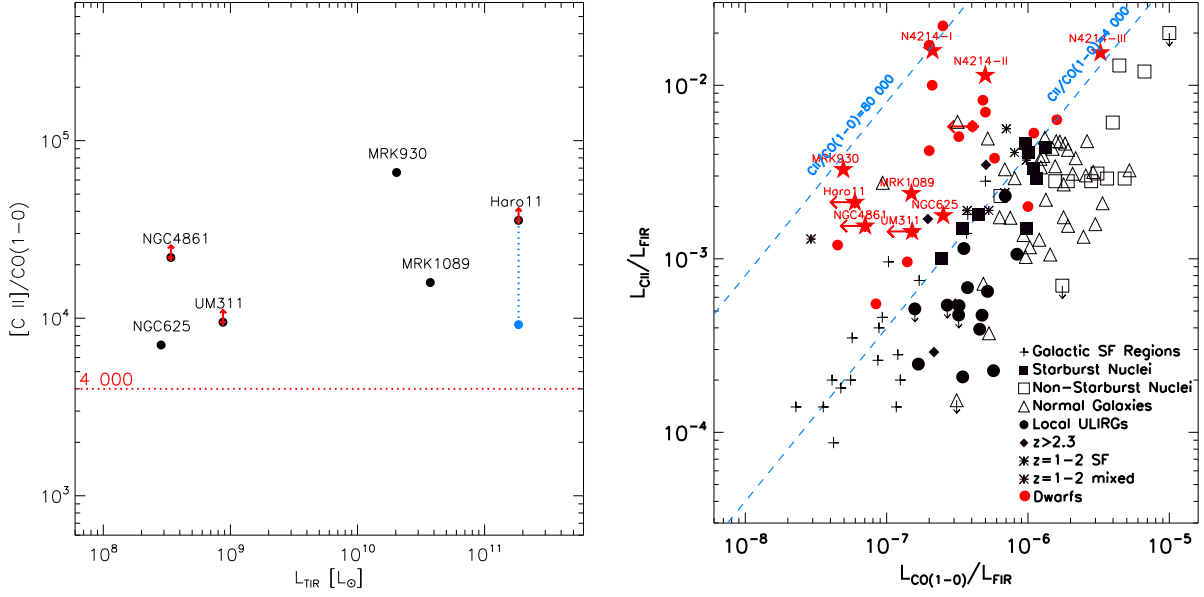


**Figure 5.11.** *Left:*  $[\text{C II}]/\text{CO}(1-0)$  versus  $L_{\text{TIR}}$ . The horizontal dotted line indicates the average ratio of 4000 observed in star-forming galaxies (Stacey et al. 1991). The blue circle corresponds to the model prediction for the  $[\text{C II}]/\text{CO}(1-0)$  predicted intensity and that  $\sim 10\%$  of the  $[\text{C II}]$  originates from the PDR (Cormier et al. 2012a). *Right:*  $[\text{C II}]/L_{\text{FIR}}$  vs.  $\text{CO}(1-0)/L_{\text{FIR}}$ . This is the same figure as 1.12 introduced in Chapter 1, where we add our data (star symbols).

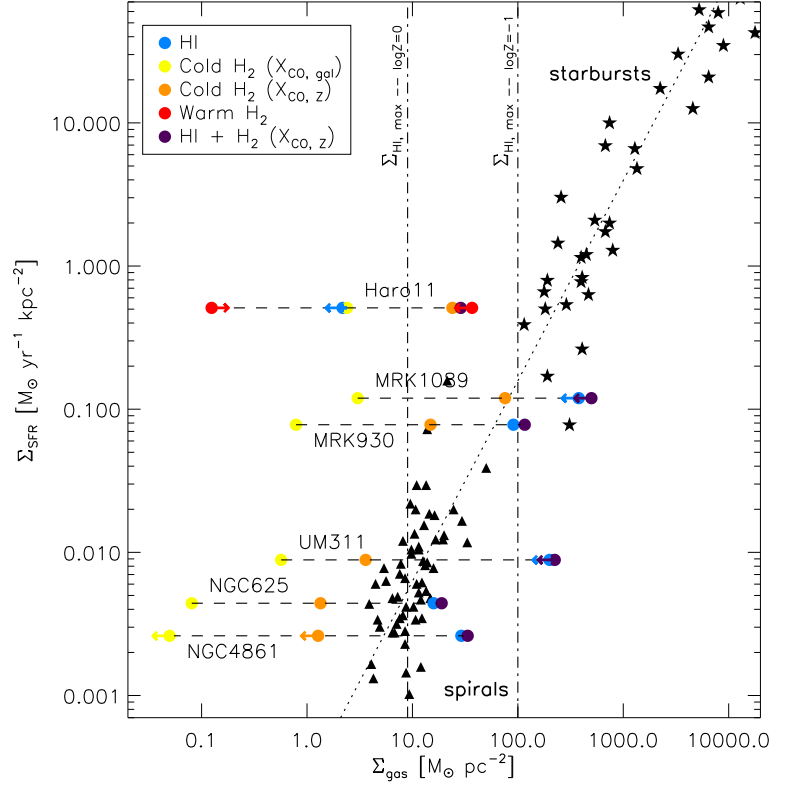
we consider the CO(1-0) predicted intensity, derived from modeling CO(2-1) and CO(3-2), and that at least  $\sim 10\%$  (up to 50%) of the  $[\text{C II}]$  emission originates from the PDR (Cormier et al. 2012a), the  $[\text{C II}]/\text{CO}(1-0)$  ratio decreases to  $\sim 10,000$ . Figure 5.11 (right) is an updated version of Fig. 1.12 from Chapter 1, with our new data (star symbols). The position of our galaxies is consistent with that of other low metallicity galaxies, displaying high  $[\text{C II}]/\text{CO}$  ratios.

#### 5.4.2 Which gas phase is fuelling the star formation?

Many active low metallicity dwarf galaxies are outliers in the Schmidt-Kennicutt law (e.g. Galametz et al. 2009), with high SFR and little observed gas, raising the possible presence of higher star formation efficiencies (SFE) or larger total gas reservoirs, mostly in the form of dark gas, on which it is difficult to get a good handle for now. From recent studies, underestimated gas masses are the most commonly accepted (Bigiel et al. 2008; Leroy et al. 2011; Schruba et al. 2012; Glover & Clark 2012).

Figure 5.12 shows the surface SFR ( $\Sigma_{\text{SFR}}$ ) versus surface gas mass  $\Sigma_{\text{gas}} = \Sigma_{\text{HI}+\text{H}_2}$  for our sample. We use the  $L_{\text{TIR}}$ -derived SFRs from Table 5.2 divided by the source size, which is taken as  $R_{25}$  for NGC 625 and NGC 4861 as it encompasses most of the TIR flux, and estimated to be  $\sim 20''$  for Haro 11 and Mrk 930, and  $\sim 30''$  for Mrk 1089, using the PACS  $160\mu\text{m}$  maps. For UM 311, we use the aperture of  $20''$ . For the gas mass, we consider the H I from the literature (Table 5.2) and the  $\text{H}_2$  derived from  $X_{\text{CO,gal}}$  and  $X_{\text{CO,Z}}$  scaled to the metallicity (Table 5.5). The H I mass quoted for Mrk 1089 and UM 311 refer to the full complexes, not the individual galaxies therefore we note them as upper limits on Figure 5.12. We see that all galaxies, except Haro 11, are dominated by their H I content and appear gas-rich, falling close to the Schmidt-Kennicutt relation. It is interesting to note that Bigiel et al. (2008) find a threshold in the H I surface density of  $\Sigma_{\text{HI,max}} \sim 9 \text{ M}_{\odot} \text{ pc}^{-2}$ . This threshold

**Figure 5.12.** Surface star formation rate ( $\Sigma_{\text{SFR}}$ ) versus surface gas mass ( $\Sigma_{\text{gas}}$ ). The galaxies presented here are in filled circles, and the colors show the contribution from the separate phases observed. The starbursts and spirals from Kennicutt (1998) are represented by stars and triangles respectively. The diagonal dark dotted line indicates fits to the Schmidt-Kennicutt law, with  $n \sim 1.4$  in Eq.1.1, to starbursts and spirals (Kennicutt 1998). The vertical lines indicate the threshold in H I column density ( $\Sigma_{\text{HI},\text{max}} = 9 - 100 \text{ M}_{\odot} \text{ pc}^{-2}$ ) observed by Bigiel et al. (2008) and modeled by Krumholz et al. (2009).



represents the density above which H I turns molecular, and is a function of metallicity. For the metallicities of our sample ( $Z \sim 1/2 - 1/5 Z_{\odot}$ ),  $\Sigma_{\text{HI},\text{max}} \simeq 10 - 100 \text{ M}_{\odot} \text{ pc}^{-2}$  (Krumholz et al. 2009, vertical dashed lines on Fig. 5.12). The H I contents of NGC 625, NGC 4861, and to a lesser extent Mrk 930, agree with that threshold, that of Haro 11 is below that threshold, while the H I contents of Mrk 1089 and UM 311 are higher than  $\Sigma_{\text{HI},\text{max}}$ , although these observations are upper limits (encompassing larger areas). The observed H I column densities of the dwarfs (at least for moderate metallicities) are compatible with the H I saturation predicted by Krumholz et al. (2009). All galaxies, except Haro 11, are located to the right of the Schmidt-Kennicutt correlation, even when taking only the H I into account. This may reflect again the clumpy nature of the molecular material in dwarf galaxies, which would lead to a situation where the ISM, within the beam, is never dominated by a fully molecular phase. The saturation of H I as an efficient star formation tracer is most likely due to a dominant molecular phase in the most active spiral galaxies. Haro 11 is the most extreme object (Fig. 5.12). Even with high  $X_{\text{CO}}$  values, it is difficult to reconcile with the Schmidt-Kennicutt law. Its molecular reservoir is greater than the H I upper limit.

For Haro 11, our detailed modeling also solves for the mass of each ISM component (see Figure 5.13), that we can compare with the observation-derived mass estimates. The mass budget of Haro 11 is dominated by the ionised and molecular gas phases. We notice that the PDR mass derived from CLOUDY is between the warm  $\text{H}_2$  mass estimates of Sect. 5.3.1 (red color). The cold  $\text{H}_2$  gas mass from the model is also between the two values derived from  $X_{\text{CO,gal}}$  and  $X_{\text{CO,Z}}$ . Although it does not have the same physical interpretation as the original definition of the  $X_{\text{CO}}$  factor, we can quote the value resulting from our modeling  $\alpha_{\text{CO,model}} \sim 40 \text{ M}_{\odot} (\text{K km s}^{-1} \text{ pc}^2)^{-1}$ , about 10 times  $\alpha_{\text{CO,gal}}$ , which relates the CO intensity to the total (warm+cold)  $\text{H}_2$  reservoir.



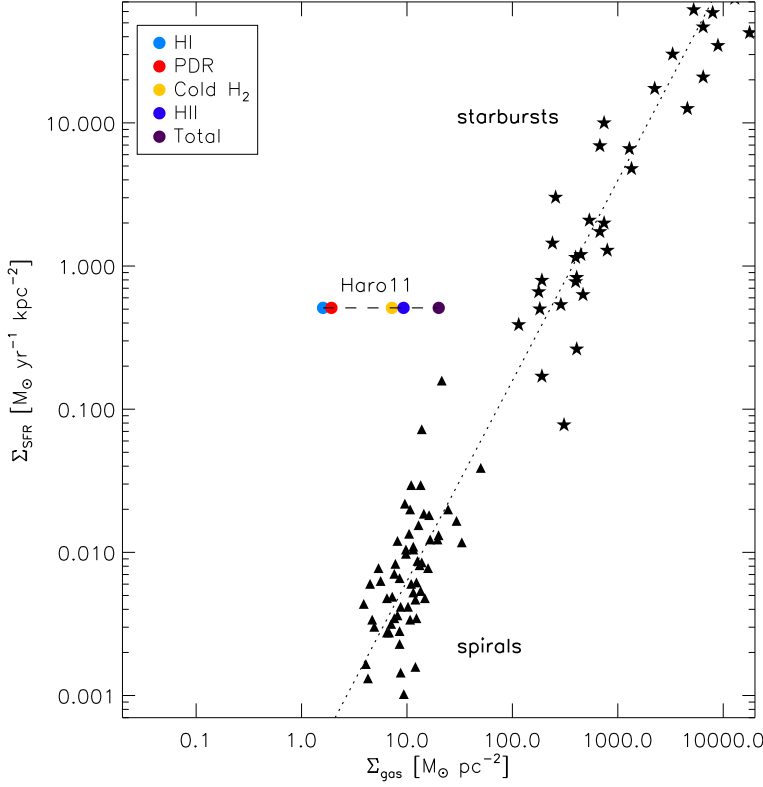


**Figure 5.13.** Same as Fig. 5.12 for Haro 11 from the CLOUDY model described in Sect. 5.3.2 and Cormier et al. (2012a).

### 5.4.3 Gas depletion times

The gas depletion time,  $\tau_{dep}$ , is the time needed for the present star formation rate to consume the existing gas reservoir, and is expressed as the inverse of the star formation efficiency:  $\tau_{dep} = \Sigma_{gas}/\Sigma_{SFR}$  [yr]. Taking the cold  $H_2$  ( $X_{CO,Z}$ ) mass values from Table 5.5, we get molecular depletion times of  $\sim 0.03$  Gyr (for Haro 11) up to 0.5 Gyr (for Mrk 1089). Sage et al. (1992) find similar values for their sample of dwarf galaxies, although they use relatively lower conversion factors, of 2-3 times  $X_{CO,gal}$ . Higher  $X_{CO}$  values could be used (here we already scaled to  $Z^{-2}$ ), but this is not supported by the modeling of Haro 11. The average molecular depletion time found by Bigiel et al. (2008) is 2 Gyr. The low  $\tau_{dep}$  values found here are typical of interacting systems.

The cold gas is thought to trigger the star formation and hence the gas phase that should regulate the activity. However the total gas ( $H\ I + H_2$ ) is found to correlated with SFR in galaxies (see Section 1.3.2). When adding the  $H\ I$ , the average total gas depletion time over the sample is  $\tau_{dep} \sim 3.5$  Gyr (with scatter 5 Gyr) for NGC 625, Mrk 1089, NGC 4861, and Mrk 930.

In principle, one can also consider the total gas reservoir ( $H\ II + H\ I + H_2$ ) if the phases are in global equilibrium, i.e. if the timescales to convert  $H^+$  to  $H\ I$  to  $H_2$  are small compared to the molecular gas depletion time (which may be the case if metallicities are not too low). Now taking the total gas reservoir of Haro 11 computed from the models (including the ionised gas),  $\tau_{dep} \sim 0.06$  Gyr. Is this low value a result of the extreme environment of Haro 11 or does it imply a higher efficiency? High SFE in dwarf galaxies could be understood in the picture of a dominant ionised gas phase in their ISM. Combining a porous ISM and hard ionising radiation field, hydrogen can be in the form of  $H^+$  rather than  $H\ I$  over large spatial scales. Hence the galaxy would not be  $H\ I$  dominated and would have high  $H_2/H\ I$  ratio, despite



photodissociation and low metallicity.

## 5.5 Conclusions on the molecular gas reservoir

The state of the molecular gas, observed through the molecule CO, is not well known in dwarf galaxies. To address this issue, we have obtained new CO observations of the J→1-0, J→2-1, and J→3-2 transitions in a subsample of 6 dwarf galaxies of the DGS. Out of the 6 targets, 5 are detected in, at least, one CO transitions, but NGC 4861 remains undetected in CO. Two of the targets, Haro 11 and UM 311, were never detected in CO before, and no CO data are reported in the literature for NGC 625. Yet, CO is found to be faint, especially relative to the [C II] 157  $\mu$ m line, as we derive [C II]/CO(1-0) ratios  $\geq 10\,000$ , which confirms results from previous studies (Madden 2000). In particular, this hints to low filling factor of the CO-emitting material, as has been suggested. It is as of yet unclear whether this clumpy nature of the cold ISM in the dwarf galaxies that we have studied is a result of their high level of star formation activity, i.e. efficient photodissociation, or points to a fundamentally different structure of the low metallicity ISM when compared to normal metallicity galaxies.

RADEX and CLOUDY PDR modeling seem to imply that this observed emission of the low-J CO lines originates from rather dense clouds ( $n_{\text{H}_2} > 10^3 \text{ cm}^{-3}$ ) of low temperature ( $T_{\text{kin}} < 50 \text{ K}$ ), where turbulence might play an important role in cooling the gas.

We have compared the star formation activity, as seen by  $L_{\text{TIR}}$ , to the gas reservoir through the Schmidt-Kennicutt law. All of our galaxies, except Haro 11, are, on global scales, H I dominated. Even when considering high  $X_{\text{CO}}$  conversion factors, the molecular content seems less important than the H I or ionised gas contents, highlighting again the clumpiness of the molecular material. What is the role of these ISM phases, and whether SFEs are truly higher in some dwarf galaxies, is still unclear. However, our interpretations are limited, due to the different antenna beam sizes, and the lack of information on the source size and distribution. These observations should be followed up by interferometry observations with *SMA* and *ALMA* (as well as *eVLA*).

# Chapter 6

## Discussion

### Contents

---

<b>6.1</b>	<b>Limitations of this work</b>	<b>146</b>
6.1.1	Observational limits	146
6.1.2	Modeling limits	147
<b>6.2</b>	<b>Perspectives</b>	<b>150</b>
6.2.1	<i>SOFIA</i>	150
6.2.2	<i>ALMA</i>	151
6.2.3	<i>CCAT</i>	154
6.2.4	Calibrating tracers of star formation	154
6.2.5	Multi-phase analysis	154

---

## 6.1 Limitations of this work

The different studies performed in the previous Chapters give insight into the role and utility of important emission lines in the MIR-submm range in diagnosing global ISM properties (conditions and structure) of dwarf galaxies. Conclusions are sometimes difficult to reach due to the lack of specific observables, spatial resolution to separate the ISM phases, constraints on physical processes, and due to the simplified geometry of PDR models.

### 6.1.1 Observational limits

Observational limits reside in two basic intrinsic properties of dwarf galaxies: the fact that they are small and faint objects. This implies that they often lie at the limit of the instrument sensitivity, even for powerful telescopes such as *Herschel*. Their ISM structure is most likely unresolved for targets beyond the Magellanic Clouds (60 kpc distance  $\leftrightarrow$  3 pc resolution for PACS). These limitations make the interpretation of the FIR emission with models difficult, leaving many degeneracies in the density – radiation field – filling fraction parameter space, and inviting assumptions on, e.g. unknown abundances or dust properties, which, in turn, affect greatly the model predictions and subsequent ISM structure.

Pushing sensitivities down to  $\sim 5 \times 10^{-19} \text{ W m}^{-2}$ , the DGS provides a unique dataset of FIR observations in low metallicity dwarf galaxies. Nevertheless, while [C II], [O III], [O I]63 are the easiest lines to access, the fainter and similarly useful lines of [O I]145 and [N II] remain scarcely observed. With a handful of observations, general conditions may be inferred, but some observables are necessary to be able to lift model degeneracies. Combining [O I]63 and [O I]145 brings information on the PDR temperature and may help evaluate optical depth effects. As for the [C II] origin, which has been discussed for many years (e.g. [Tielens & Hollenbach 1985](#); [Wolfire et al. 1995](#); [Stacey et al. 1991](#); [Madden et al. 1997](#)), observations of the [N II] 205 $\mu\text{m}$  turns out to be of primordial importance. Indeed, it is often pointed out that a fraction of [C II] may arise from the ionised gas. Since the ionisation potential of  $\text{C}^0$  is 11.26 eV, less than that of  $\text{H}^0$  (13.6 eV), in principle it can arise from the ionised gas phase, not only from the neutral regions. On the other hand, the ionisation of  $\text{N}^0$  requires 14.53 eV, hence  $\text{N}^+$  resides unambiguously in the ionised phase (Section 1.2.4). However, the estimation of the fraction of [C II] from the ionised gas depends on the dataset at hand. For instance, most of the *Spitzer* ionic lines are tracers of compact H II regions, where young star clusters reside. Depending on the density of the H II region, up to 20-30% of the [C II] emission can come from these regions, under low density conditions ( $n_{\text{H}^+} \sim 200 \text{ cm}^{-3}$ ; [Abel et al. 2005](#)), while the more compact H II regions should harbor little [C II]. But the ISM is multi-phase, and this does not mean that all the [C II] should then be attributed to PDRs. This is a particular precaution to take for dwarf galaxies, in view of their ISM structure which may be prominently filled by a diffuse ionised medium, as we found from bright [O III] emission and our CLOUDY modeling. To that respect, the [N II] 205 $\mu\text{m}$  line, with similar critical density and excitation potential as  $\text{C}^+$ , is an invaluable tool, but is lacking in our study. This, of course, applies to unresolved regions. Otherwise the [C II] distribution can be compared to that of [O I], PAHs, etc., for a coarse estimation of ionised gas associated with [C II] (i.e. [Lebouteiller et al. 2012](#)).

To investigate the  $\text{C}^+$  origin in dwarf galaxies, spectrally resolved observations of [C II] and [N II] 205 $\mu\text{m}$  can be accessed with the instrument GREAT onboard *SOFIA*, but with limited sensitivity. We discuss that further in Section 6.2.1.

Little investigated in this work, H I is of course a crucial tracer of the ISM morphology and structure. We left it aside in our CLOUDY modeling because it is not detected in Haro 11. The H I upper limit is however the main driver of our concluding picture of the ISM of Haro 11. With no detectable H I, there is no significant diffuse neutral component. The transition to the neutral phase must occur quickly at high densities, close to the cloud surface, and the diffuse gas must remain mostly ionised. In H I dominated galaxies, that picture may give way to a more standard description, with average density PDRs ( $\sim 10^3 \text{ cm}^{-3}$ ) and a large PDR contribution to the  $\text{C}^+$  emission. Perhaps the low metallicity star-forming galaxies residing in the early universe resemble more Haro 11 in terms of proportion of various galactic components.

Beyond the intrinsic low luminosity of dwarf galaxies, CO is also expected to be even fainter at low metallicity (Section 1.3.2), hampering its detection and thus rendering the properties of the molecular gas phase difficult to assess. The ISM picture that is laid out from Chapter 3 and Chapter 4, with the presence of dense PDR clumps of low filling factor, and extended ionised gas, reinforces our understanding of faint CO emission. Moreover, as opposed to ionic and PDR lines, CO emission arises from a lower volume emitting region, hence it is affected by beam dilution. Beams of the CO ( $\text{J} \rightarrow 1-0$ ) transition are  $30''$  at *Mopra* and  $22''$  at *IRAM*. For Haro 11, located at a distance of 92 Mpc, this corresponds to a scale of  $\sim 10$  kpc, which no longer resembles the size of Galactic GMCs. With  $1''$  resolution, *ALMA* observations of molecular clouds around 30-Doradus in the LMC reveal filaments of size only  $5-10''$  (1-2 pc, Indebetouw et al. 2012). Thus, even for Local Group galaxies at  $\geq 100$  kpc, we are probably still not resolving the molecular clouds with single beams.

We have attempted to observe CO in a sample of the most luminous dwarf galaxies from the DGS that had no (or incomplete) previous CO detections. In most cases, the CO ( $\text{J} \rightarrow 2-1$ ) and CO ( $\text{J} \rightarrow 3-2$ ) lines are detected while the CO ( $\text{J} \rightarrow 1-0$ ) is not, even after  $\sim 15$  h of integration time. We are clearly reaching sensitivity limits of current single dish telescopes and the necessity of CO interferometry observations for dwarf galaxies becomes more and more evident. This enables us to go to much smaller spatial scales hence reducing the effect of beam dilution and starting to localise the source of cold emission. We discuss what the interferometer *ALMA* can bring in the study of the cold ISM of dwarf galaxies in Section 6.2.2.

### 6.1.2 Modeling limits

#### Geometry assumptions

Probably the most important limitation that we have encountered for the modeling of Haro 11 is the simplified geometry of PDR models. This simplification will also affect modeling of other DGS galaxies, and has (at least) three aspects that we stress.

Ideally, if the FIR emission of the galaxy were spatially resolved, as it is most likely the case in the optical, one would construct an ensemble of regions, each with their own parameters that fit the data. The lack of information on the source distribution and the unresolved FIR emission prevent us to do that and force us to a simplified geometry, which consist of a single region made of a single central source surrounded by a single cloud. Geometrical parameters such as inner radius or shell thickness are then physically irrelevant, but tuned to match similar ionisation parameters,  $U$ , or gas mass. The parameters that are best constrained, irrespective of the geometry, are the electron density, temperature, and mass of the gas.

The second limitation, related to the first one, resides in the fact that, when considering several components to describe the multi-phase ISM, those components are computed separately as individual entities, but in reality the ISM is well mixed. If assuming that individual active regions can be modeled separately in, e.g., dusty starbursts, where the large columns of dust inhibit the UV transfer and isolate each region, this is certainly not valid for a porous ISM that describes dwarf galaxies. If the line predictions are less affected, the mixing and interplay between the regions has a strong influence on the effective dust column along the line of sight and extinction. Hence the difficulty to match the energy repartition between the UV-optical and FIR-submm wavelength ranges, and to model global dust SED.

The third aspect of the geometry limitation relates to the actual cloud geometry modeled. Ideally, one would represent the embedded dense clumps in a PDR envelope with an ensemble of spherical clumps of varying sizes and density profiles, and external directed illumination from an exciting star. Instead, PDR models use spherical or plane-parallel cloud geometries. In spherical cases, the illumination is isotropic, hence uniform at the cloud edges and simplified to a 1D problem, while a directed illumination is a 2D radiation problem, the radiation being different at the cloud edge relative to its distance to the star. The difference in geometry between spherical and plane-parallel clouds has been investigated by [Stoerzer et al. \(1996\)](#). This has several implications, on the radiative transfer and emission beam filling factors. They compare the cloud temperature profile and  $C^+/C/CO$  transition with external illumination in constant density and varying density cases. In uniform density models, the temperature profile is similar, with a shift of the transition deeper into the spherical cloud. With a density gradient prescribed through the cloud, important differences arise. CO always forms even in small clumps, where it is photodissociated in the constant density case. Differences are generally more pronounced in small size clumps.

### Tuning of the free parameters

With limited constraints on the input parameters of a PDR model, the uncertainty on the model output is large. And the constraints at hand are often too few to interpret model results and draw firm conclusions.

- *Elemental abundances*

For instance, knowing the individual elemental abundances is essential when looking at absolute line intensities or ratios of two different atoms. Ideally one would plug in abundances derived for each atom, but those are often unknown. Usually metallicities are given by the  $O$  abundance only, in which case abundances in the model can be scaled to the metallicity of the source. However, large uncertainties still reside in metallicity determinations (Section 1.1.3), and abundance variations can be important for specific species (e.g. nitrogen, Section 1.1.3). Thus uncertainties on the order of a factor of two in model predictions, from setting elemental abundances in PDR models, can be *systematic*, and, when applied to individual galaxies, it is necessary to adapt the model parameters to the modeled galaxy.

- *Energy sources*

What processes dominate the physics of the ISM of dwarf galaxies? Standard heating and cooling mechanisms are included by default in CLOUDY models (photoionisation, photoelectric effect, cosmic rays, etc.), but what is their relative importance? Should some processes be enhanced in specific cases? Which ones are left out? In Section 4.2.2, we find that the photoelectric effect completely dominates the heating in the surface layer of the PDR, at the

level of 85%, while collisions and cosmic rays take over at larger  $A_V$ . Cosmic rays are a major heating mechanism in diffuse neutral clouds and molecular clouds. As discussed previously, effects of magnetic fields and turbulence are also important in molecular clouds.

Meijerink et al. (2011) find that models exposed to significant UV radiation have moderate responses to high cosmic ray rates and mechanical feedback. If the PDR lines are controlled by the FUV field, the impact of additional heating on the molecular lines, shielded from irradiation, should be greater. Higher cosmic ray ionisation rates are evident in ULIRGs and regions of massive star formation. Enhanced rates could be traced by the [N II] lines, although  $N^+$  emission can also arise from H II regions. The [N II] lines are found to be relatively faint with PACS in the dwarfs of the DGS, thus cosmic rays may not play an obviously important role here.

Supernovae or stellar outflows may generate a turbulent dissipation in the cloud. Such mechanical heating modifies the temperature structure of the cloud, enhancing the warm molecular phase. Mechanical heating is not treated as a dynamical effect in PDR codes, but just as an additional source of heating. It is found to be necessary to account for molecular observations in luminous IR galaxies, changing the physical conditions of the molecular cloud with time (time required for massive stars to enter the SNe phase; Loenen et al. 2008). Kazandjian et al. (2012) discuss the role and relative importance of mechanical heating on the PDR/molecular cloud. They find that CO column densities may be underestimated at low metallicity when ignoring mechanical heating. If mechanical heating does not affect [C II] line excitation, for moderate heating rates and high densities, it affects the chemistry at higher  $A_V$ , shifting the  $C^0$ /CO transition towards the surface, which, in turn, result in higher total column densities of CO. Hence the possible role of mechanical heating in dwarf galaxies is not clear, and seems to depend on the shielding of CO in individual galaxies. If photodissociation of CO dominates on global scales, in regions where CO can form, it may form at lower  $A_V$ , with enhanced high-J transitions. High-J CO lines, probing warmer gas phases, are also observed with *Herschel*/SPIRE in low metallicity massive star-forming regions such as 30-Doradus, up to J→12-11 (Ronin Wu, private communication). The dwarf galaxies, in general, have low to moderate SFRs ( $0.005$  to  $50 \text{ M yr}^{-1}$ ), compared to more massive extreme star-forming galaxies, where SFRs can be  $\geq 100 \text{ M yr}^{-1}$ . Such SFRs in dwarfs would infer moderate (but non negligible) heating rates (on the order of  $\Gamma_{mech} \leq 10^{-18} \text{ erg cm}^{-3} \text{ s}^{-1}$ ; Kazandjian et al. 2012). Broad line profiles of [C II], [O I], and [O III] are observed with PACS in several dwarf galaxies, suggesting interesting kinematics and energetics. Line widths of [O I] and [O III] are around  $150\text{--}200 \text{ km s}^{-1}$  (unresolved [C II] with FWHM  $\sim 240 \text{ km s}^{-1}$ ) in Haro 2, Haro 3, He 2-10, NGC 4449, NGC 6822, LMC, and SMC. [C II], [O I], and [O III] are broadened up to  $300 \text{ km s}^{-1}$  in Haro 11, and  $350 \text{ km s}^{-1}$  in UM 448 (see Appendix B).

- *Molecular phase*

Modeling of the molecular phase is particularly challenging. Processes of star formation, even for well known Galactic regions, are poorly understood. Approaching the cores of star formation, pressure equilibrium is not valid, turbulent motions may dominate, density profiles are unknown, and we do not have the constraints to make unambiguous choices. While the physics of photoionisation and PDR gas has been extensively tested on various types of targets, the driving processes in the molecular gas are less understood. In the modeling of the molecular phase, we would like to caution that, at least for extragalactic sources, the derived parameters should not be over-interpreted. The danger is even more dramatic for dwarf galaxies where the low metallicity changes the cloud structure, chemistry, thermal structure, etc.



## 6.2 Perspectives

Some of the observational and model limitations, essentially related to the ISM structure, will be tackled with next generation instruments/telescopes. This Section briefly presents new telescopes beyond *Herschel* and projects/modeling aspects they open.

### 6.2.1 *SOFIA*

#### General description

The “*Stratospheric Observatory for Infrared Astronomy*” (*SOFIA*) is an airborne observatory resulting from a NASA / German Aerospace Center collaboration. The *SOFIA* science web page is hosted here: <http://www.sofia.usra.edu/Science/index.html>, and outlines the instrument performances. The telescope consist of a 2.7-m primary mirror mounted on a Boeing 747SP plane flying at an altitude of  $\sim 40\,000$  feet. The secondary mirror is attached to a chopping mechanism with the capability of  $5'$  throw. The telescope provides both imaging and spectroscopy capabilities, in the NIR to mm wavelength range ( $0.3$  to  $1600\,\mu\text{m}$ ). First early science flights were conducted in December 2010, and *SOFIA* will be in operation with an expected lifetime of 20 years.

Seven first generation instruments, either under development or already offered for the first science call for proposals, include 5 broadband instruments (FLITECAM, FORCAST, HAWC, and HIPO), and 3 spectrometers (EXES, FIFI-LS, and GREAT). Of particular interest compared to the *Herschel*/PACS spectrometer are the FIFI-LS and GREAT instruments which operate in the wavelength range  $\sim 40 - 240\,\mu\text{m}$ .

#### Possible science for dwarf galaxies

Technical aspects of FIFI-LS are very similar to those of PACS (effective performance will be established after the instrument launch), providing coverage from  $42$  to  $210\,\mu\text{m}$ . It is an integral field spectrometer ( $5\times 5$  pixels array) of field of view  $30\text{--}60''$ , with similar spectral resolutions, slightly higher beam sizes, and sensitivities roughly 10 times lower than PACS. Hence the same lines and science as presented in this work will be available, with the inclusion of the [O III]  $52\,\mu\text{m}$  line, provided the targets are bright. On top of that, FIFI-LS will extend the PACS observations of nearby dwarf galaxies with its improved mapping capabilities as it is a nimble instrument. PACS observations were limited in spatial coverage due to large overheads required to sample well the array and to map full galaxies.

The instrument GREAT on the other hand is more complementary to PACS. GREAT is a heterodyne spectrometer providing data in the  $60\text{--}240\,\mu\text{m}$  range. It has 4 bandpasses that will be able to observe the [O I]  $63\,\mu\text{m}$ , [N II]  $122\,\mu\text{m}$ , [C II]  $157\,\mu\text{m}$ , and [N II]  $205\,\mu\text{m}$  lines respectively. For the Cycle 1 (starting November 2012), [C II]  $157\,\mu\text{m}$  and [N II]  $205\,\mu\text{m}$  are available. High-J CO lines ( $J\geq 14\rightarrow 13$ ) from warm layers of PDRs are also accessible. It offers impressive spectral resolution ( $\leq 1\,\text{km s}^{-1}$ ), but its sensitivity is of course more limiting than PACS (roughly 10 times worse) and only the brightest/closest objects from the DGS can be targeted. The beams sizes (diffraction limited) are similar to those of PACS.

GREAT can help investigate the origin of the [C II] emission. As  $\text{C}^+$  is becoming one of the most popular tracer of the gas reservoir in high- $z$  galaxies with *ALMA*, calibrating [C II] capabilities and determining its limitations are essential. The full interpretation of [C II] is limited mainly by a lack of knowledge of the structure of the objects, and severe



mixing of different media in the observed beams. One way to bypass the lack of spatial resolution is to separate media along the line of sight via velocity resolution, which is possible with GREAT. The correlation of the  $C^+$  emission with either PDR or ionised gas can be studied with spectrally resolved observations of  $[C\ II]$ ,  $[O\ I]$ , and  $[N\ II]$ . We have successfully obtained *SOFIA* observing time in Cycle 1 to observe  $[C\ II]$  and  $[N\ II]$  with GREAT towards the massive star-forming region N11 in the LMC (P.I. V. Lebouteiller). These data will complement our *Herschel*/PACS observations in this region (Lebouteiller et al. 2012). If  $[N\ II]\ 205\mu m$  will be easily detected in nearby galaxies such as the LMC or other Local Group galaxies, the sensitivity of GREAT may still limit such spectral comparison in fainter galaxies. Nevertheless, even an integrated value (rebinned data) can be a helpful constraint on the density of the diffuse ionised gas (and contribution to the  $C^+$ ), thus facilitating the interpretation and calibration of this important gas coolant.

### Example of *SOFIA* and NGC 4214

NGC 4214 is a good example to promote the capabilities of GREAT. It is composed of 3 star-forming regions at different stages of their evolution, which are visible in the PACS  $[C\ II]$  map (see Section 3.3.5, and p. 171 in Appendix B). However the internal structure of each region is unknown as the emission is not resolved. Thus the only way to extract some structural information is to spectrally resolve the line. GREAT observations will elucidate the dynamical structure of the different components of the ISM, and most importantly the PDRs, in three star-forming regions that exhibit very different conditions.

With spectrally resolved data, the velocity information of the  $[C\ II]$  line will give access to the PDR structure. Of particular interest is the effect of the central super star cluster on the velocity structure of the different ISM phases. Comparing line widths between the diffuse and the dense phases allows us to study the turbulent character of the ISM. The winds in young stellar clusters, especially at low metallicity, should have a profound impact on the ISM structure and composition, while very little is known about their effects on the PDR component in low metallicity galaxies.

The star-formation activity toward these regions results in a complex velocity field, as seen in H I and CO high-resolution spectra (Walter et al. 2001). Comparing those to GREAT  $[C\ II]$  data will lift the ambiguity on the origin of the  $[C\ II]$ , determining the fraction of  $[C\ II]$  coming from the envelop of dense PDRs with associated CO, compared to more diffuse gas component, as traced by H I. Figure 6.1 shows a simulation of  $[C\ II]$  observations with GREAT in the 3 star-forming regions of NGC 4214. Associating the velocity-resolved  $[C\ II]$  features with CO and/or H I clouds may isolate a possible dark gas component, giving us a means to quantify the total  $H_2$ . This can also serve to test PDR models accounting for the  $[C\ II]$  emission due to ionised gas, questioning the accuracy of previous analyses of the PDR gas in galaxies, and give revised  $[C\ II]_{PDR}/CO$  ratios. These are the first steps in calibrating  $[C\ II]$  as a dark-gas tracer, and  $[C\ II]/CO$  as a star formation tracer.

### 6.2.2 ALMA

#### General description

The “Atacama Large Millimeter/submillimeter Array” (ALMA) is an interferometer located on the Chajnantor plateau in Chile, at the altitude of 5 000 m. The project is an international collaboration between Europe, North America, East Asia, and Chile. The European science portal is hosted here: <http://almascience.eso.org/>. The telescope provides both

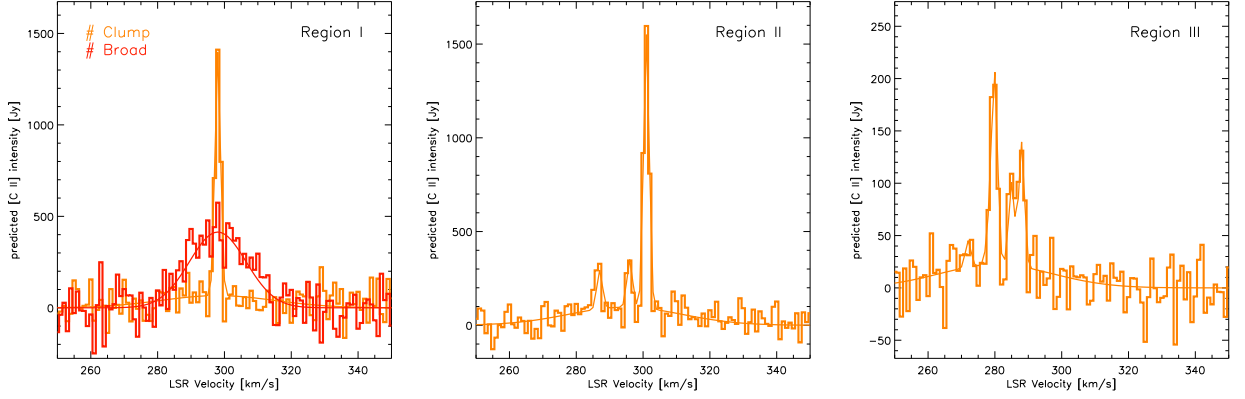


**Figure 6.1.** Simulation of the predicted [C II] 157  $\mu$ m GREAT spectra in the 3 star-forming regions of NGC 4214. The Gaussians represent the narrow (orange) and broad (red) components, including noise scaled for a S/N ratio  $\geq 5$  in the faintest detectable velocity components. This is based on the PACS (Cormier et al. 2010) and CO(1-0) observations (Walter et al. 2001).

imaging and spectroscopy capabilities, in the submm/mm wavelength range (10 mm down to 300  $\mu$ m separated in 8+2 bands). *ALMA* is a long term project. First tests were conducted early 2009, with an Early Science call for proposals in 2011.

*ALMA* consists of a giant array of 12-m antennas which can be moved into different configurations (different distributions of baseline lengths) to achieve desired spatial resolution. In full capacity (planned for 2013), *ALMA* will have 66 antennas, with baselines of up to 16 km. In addition, a compact array, consisting of twelve 12-m antennas and four 7-m antennas in fixed configuration, is available to recover extended emission.

### Possible science for dwarf galaxies

In full capacity, typical performance values at 115 GHz (CO J $\rightarrow$ 1-0 line) are: field-of-view of 50'', angular resolution from 0.04'' (most extended configuration) to 3.6'' (most compact configuration). The highest spectral resolution is 0.01 km s $^{-1}$ . Sensitivities are roughly two orders of magnitude better than *APEX* or *Mopra*.

Among other goals, *ALMA* is specifically designed for high quality imaging with high spectral and spatial resolutions, and in a reasonable amount of time, due to its impressive sensitivity and its ability to provide precise high dynamic range images at an angular resolution of 0.1''. *ALMA* is an invaluable observatory for many fields of astronomy, including the study of the cold ISM in dwarf galaxies, typified by faint emission from small clumps, and of the main ISM coolants for the high-redshift universe ( $z \geq 3 \leftrightarrow$  [C II] falls  $\leq 475$  GHz, where the atmospheric transmission, on average, gets better). More specifically, observations of low mass distant galaxies should reveal high [O III] 88  $\mu$ m emission relative to [C II], as we have find for dwarf galaxies (Chapter 3). First detections of the [O III] 88  $\mu$ m line at  $z \sim 3-4$  are reported by Ferkinhoff et al. (2010). Along with [C II], the [O III] line is a priority tracer for high-redshift studies. For nearby galaxies, the full CO ladder (up to J $\rightarrow$ 8-7), HCO $^+$  or HCN transitions, and [C I] 609 and 370  $\mu$ m lines are accessible. *ALMA* is an obvious tool to discover the cool and dense ISM of dwarf galaxies, which is not otherwise accessible from single-dish, lower sensitivity telescopes.

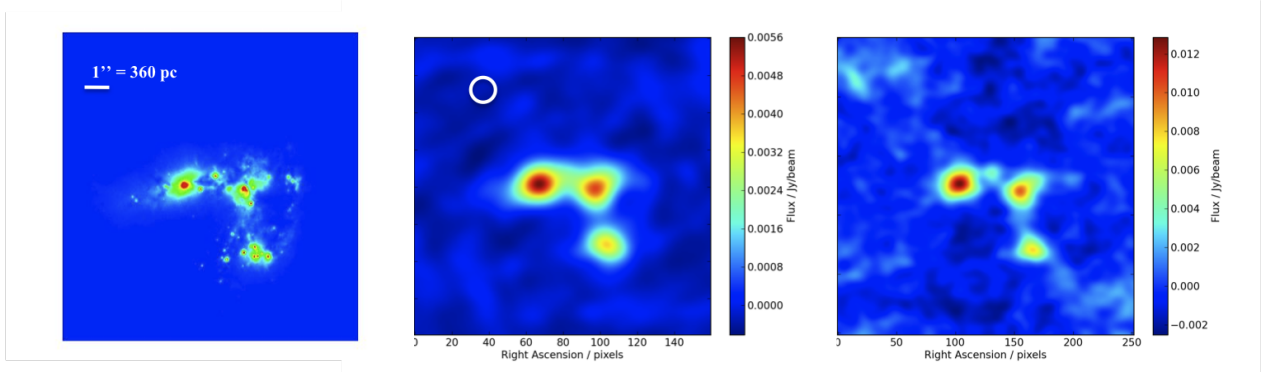


**Figure 6.2.** Simulation of what we would see in *ALMA* band 3 and 7 for Haro 11. The following is based on capabilities offered in the Cycle 1 call for proposals. *Left:* Input *HST* image of Haro 11 scaled to the expected CO intensity with increased contrast to simulate compact clumps as molecular cores. *Middle:* Output of the simulation in band 3 C32-4 configuration after 1.4h on-source; the 3 star-forming knots are well detected and clearly resolved. *Right:* Output of the simulation in band 7 C32-2 configuration after 0.2h on-source.

### Example of *ALMA* and Haro 11

The two main challenges in understanding star formation activity in dwarf starbursts are: (1) determining the origin of the observed submm excess emission (Galametz et al. 2009; Rémy et al. 2012; Madden et al. 2012a), and (2) measuring the mass of the molecular gas reservoir. We present an example of what *ALMA* can bring in understanding the cold ISM of Haro 11 to complement our view of the H II regions/PDRs laid out in Cormier et al. (2012a). One of the results from this study is that the PDR (hence molecular cores) have very low volume filling factor, implying that the neutral molecular gas must reside in small dense clumps. *ALMA* allows us to disentangle the ISM phases and to solve the paradox between the apparent lack of cold gas (molecular and even atomic in Haro 11) and the present, vigorous, star formation episodes.

A submm excess is evident in Haro 11 from *APEX*/LABOCA data, which, if interpreted as cold dust, would result in very low G/D mass ratio ( $\geq 0.01$ ), difficult to reconcile with chemical evolution limits (Galametz et al. 2009). To date, we do not know the origin, nor the location of this excess in galaxies. *ALMA* data at  $850\mu\text{m}$  (band 7) can help map the component which gives rise to the prominent submm excess in dwarf galaxies, eliminate scenarios on its origin, and determine firmer dust mass and D/G ratios.

While CO(1-0) is undetected at *Mopra* in Haro 11, CO(2-1) and CO(3-2) are detected with *APEX* (see Chapter 5; Cormier et al. 2012c), but their emission is not resolved as the expected source sizes are  $\leq 1''$ . This results in large uncertainties on physical conditions and in the determination of the mass of the CO-emitting cores with  $X_{\text{CO}}$  (as it is calibrated on CO(1-0)). Therefore, resolved CO(1-0) and CO(3-2) observations in bands 3 and 7 respectively are required to identify the sources of emission, quantify the cold molecular gas traced by CO(1-0), the total molecular gas reservoir adding [C II], and study the spatial variations of the CO excitation which may be wildly different from typical values in an extreme object such as Haro 11. This is essential to determine the structure and physical conditions of the cold ISM and particularly that of the PDR/molecular clouds. Figure 6.2 shows a simulation of what we would see in Haro 11 with *ALMA* band 3 and 7. The *ALMA* FOV covers the full galaxy, while the beam well isolates the three star-forming knots. This will lift some modeling degeneracies related to the source structure and geometry.

### 6.2.3 CCAT

*CCAT* is a submm telescope that will be located on Cerro Chajnantor in the Chilean Andes, at the altitude of 5600 m (above *ALMA*). It consists of a single-dish antenna of diameter 25-m. Performance goals are to cover the wavelength range from 200 to 2200  $\mu\text{m}$ , with FOV  $1^\circ$ , and resolution  $3.5''$ .

Similar science goals can be achieved with *CCAT* compared to *ALMA*, although the wide FOV of *CCAT* makes it especially essential for deep large surveys. While *ALMA* is more suited to compact objects, *CCAT* will provide direct imaging with an FOV much larger than that of *ALMA*, hence suited for large areas of extended emission. Such mapping capabilities are clearly needed to study the ISM of Local Group galaxies, particularly the Magellanic Clouds.

The *CCAT* consortium includes (for now) American, Canadian, and German universities (<http://www.ccatobservatory.org/index.cfm/>).

### 6.2.4 Calibrating tracers of star formation

The ratio of  $[\text{C II}]/\text{CO}(1-0)$  has been used in extragalactic studies as an estimator of the star formation activity (see Section 1.3.2).  $\text{CO}(1-0)$  has been difficult to observe in dwarf galaxies, while observations of the  $\text{CO}(2-1)$  and  $\text{CO}(3-2)$  transitions were more successful (Chapter 5). Access to those lines is becoming technically easier with *ALMA*.  $\text{CO}(3-2)$  probes warmer gas than  $\text{CO}(1-0)$  and may be enhanced relative to  $\text{CO}(1-0)$ , resulting in lower  $[\text{C II}]/\text{CO}(3-2)$  ratios in dwarf galaxies. Hence the  $[\text{C II}]/\text{CO}(3-2)$  is potentially a more accessible tracer of star formation than  $[\text{C II}]/\text{CO}(1-0)$ .

With either CO transition, studying the ratio of  $[\text{C II}]$ -to-CO as a function of metallicity and activity (star-forming vs. quiescent) is important to calibrate  $[\text{C II}]$  as a star formation tracer.  $[\text{C II}]$  and other FIR lines, such as  $[\text{O III}]$ , which is exceedingly bright, need to be calibrated as they are now accessible in high-redshift galaxies.

Higher-J CO transitions should also be investigated. There is recent evidence, from the limited *Herschel*/FTS observations existing for dwarf galaxies, that emission from the high-J CO lines is not negligible in low metallicity environments. Figure 6.3 shows the CO spectra and corresponding SLEDs, from  $J \rightarrow 4-3$  to  $J \rightarrow 12-11$ , in the star-forming region 30-Dor of the LMC. The SLED rises until CO  $J \rightarrow 9-8$ , and remains relatively flat for higher-J lines, while it usually peaks around CO  $J \rightarrow 4-3$  to 7-6 and then turns down in normal star-forming galaxies (e.g. M 83; Wu et al. 2012). CO lines up to  $J \rightarrow 8-7$  can be observed with *ALMA*.

### 6.2.5 Multi-phase analysis

A multi-phase approach is a logical step for an encompassing picture of the ISM of dwarf galaxies. It is important to understand the relative role and interplay between the different phases, dust and gas reservoirs, and their link to the evident star formation activity.

To connect the observed tracers with our physical picture of the multi-phase ISM requires an improvement in modeling, while the level of complexity of the existing models that can be constrained hinges on the existence of the appropriate data. As an example, the need for including clumpiness in the models is not well established but often suggested. The new data acquired for the dwarf galaxies with *Herschel*, in combination with future *SOFIA* and *ALMA* data in nearby star-forming regions will assess whether clumpiness is needed. Figure 6.4 is a schematic of such multi-phase modeling, as the next step beyond *Herschel*.

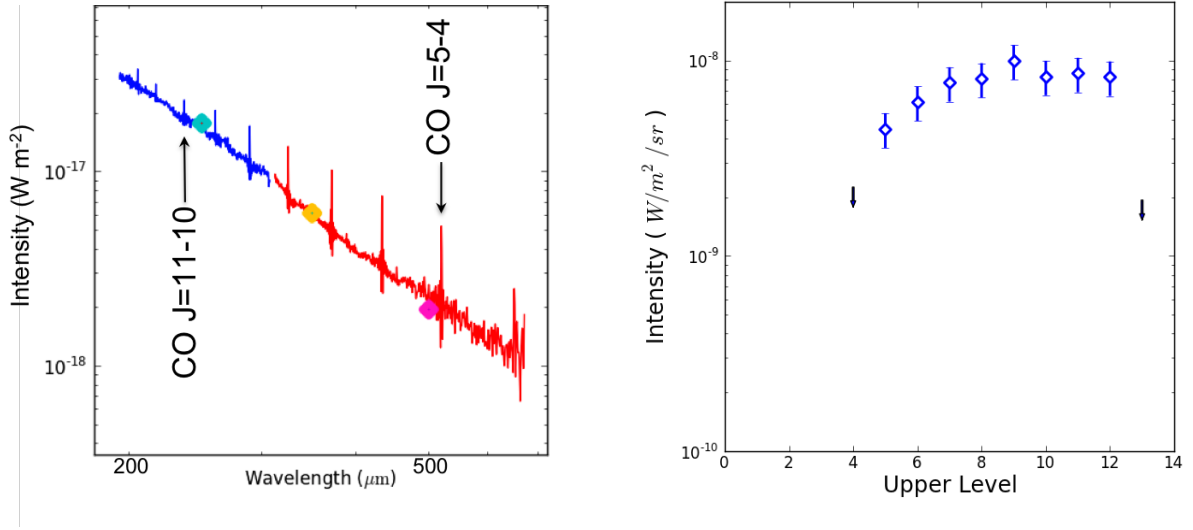


**Figure 6.3.** *Herschel*/FTS spectrum of the CO ladder (*left*) and corresponding SLED (*right*) towards 30-Doradus in the LMC (Ronin Wu, private communication).

Spatially resolved observations, in particular in the Magellanic clouds and other Local Group galaxies, can be used to benchmark the multi-phase models. By modeling well-resolved sources in their entirety, one can establish how the multi-phase models perform for unresolved sources, and whether there are any systematic biases to be addressed. Such detailed physical properties that can be studied in the wide range of nearby dwarf galaxies with improved multi-phase analyses, can then help interpret high-redshift galaxies, where such spatial resolution is not possible.

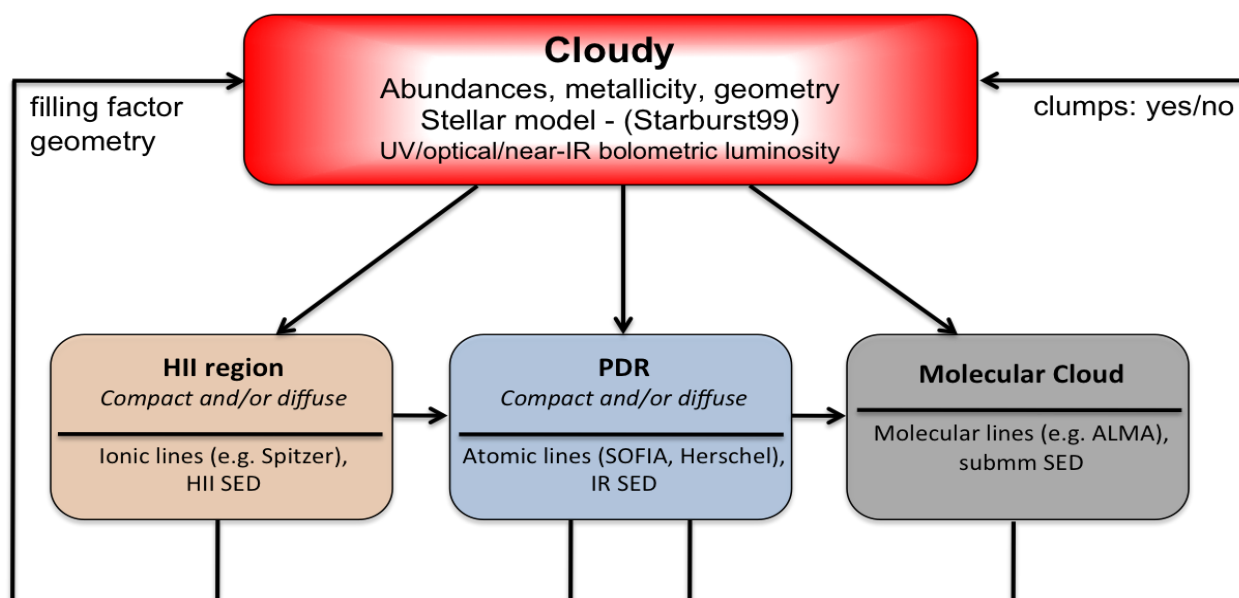


**Figure 6.4.** Strategy of the multi-phase modeling with CLOUDY. Observations help constrain the geometry and parameters of each phase, and establish the need for clumps in the models. With the models, we can derive the physical conditions in each ISM phase.

# Conclusions

The *Herschel* telescope has brought new insight on the low metallicity ISM with high-quality observations of FIR continuum and fine-structure cooling lines. In particular, the “Dwarf Galaxy Survey” has extended previous FIR studies of dwarf galaxies to lower metallicities and lower luminosities in a large sample of objects, hence providing statistical support. By acquiring additional molecular data from ground based telescopes, and making use of ancillary UV, optical, and MIR data, we are able to assess in a complete way the state of the dust and gas in the different ISM phases.

The analysis of spectral emission lines from the multi-phase ISM presented in this work has revealed (or confirmed) interesting global properties of the state of the gas in dwarf galaxies:

- The [O III]  $88\mu\text{m}$  line is in most cases the brightest cooling line, over the peak of star formation as well as on galaxy-wide scales. This supports the presence of a hard radiation field on galaxy-wide scales, previously inferred from high [Ne III]/[Ne II] and [S IV]/[S III] ratios. [O III] traces hard photons from the ionisation source, with larger mean free paths than in normal galaxies.
- The [C II]  $157\mu\text{m}$  line is the second brightest cooling line, followed by the [O I]  $63\mu\text{m}$  line. Along with the [O I]  $145\mu\text{m}$  line, they indicate the presence of dense PDRs with low volume filling factor. From our study of Haro 11, we have found that a large fraction of the [C II] emission may arise from diffuse neutral/ionised gas rather than the PDR. In the resolved sources of our sample, we notice that [C II] is the most spatially extended line. A large extended reservoir of diffuse gas is likely to fill most of the volume of the ISM of dwarf galaxies, in which bathe small dense PDRs.
- We have detected CO in a subset of dwarf galaxies and found its emission weak, with [C II]/CO(1-0) ratios  $\geq 10\,000$ . This confirms the difficulty in observing CO at low metallicity, and the presence of small CO cores associated to the PDRs, likely beam diluted in our observations. Although most of our galaxies are H I dominated, the possible existence of a large reservoir of unseen molecular gas (dark gas) is not excluded and seems evident from our modeling Haro 11. This should be accessed by calibrating [C II] or higher-J CO transitions.

The development of future more powerful telescopes is also promising for the study of the low metallicity ISM, especially for the issues surrounding the molecular gas. Establishing gas mass fractions in the different ISM phases and possibly linking them to the environment or morphological characteristics is important to understand what drives star formation in dwarf galaxies.



---

# Acknowledgements

Cette thèse a été effectuée au laboratoire AIM du CEA Saclay et financée par une CFR. Je tiens pour cela à remercier Pierre-Olivier Lagage, ainsi que tout le personnel du service, de m'avoir donné les moyens d'entreprendre ce projet. J'ai particulièrement apprécié sortir la tête du milieu interstellaire et des galaxies naines lors des séminaires et *Galaxy Lunch* organisés au laboratoire.

Je remercie évidemment Suzanne Madden de m'avoir accompagnée pendant cette thèse qui s'est avérée extrêmement intéressante et enrichissante. J'ai beaucoup apprécié son enthousiasme pour le domaine, la liberté laissée pour réaliser ce projet et définir ma propre ligne de travail, d'avoir néanmoins su parfois lire entre les lignes et m'orienter dans certains choix, et sa gestion unique de l'emploi du temps.

Ce travail n'aurait pas été possible sans l'équipe *nuages*, et je suis très reconnaissante envers Suzanne, Fred, Vianney, Sacha, Ronin, Aurélie, Maud, Willie, Marc, Pasquale, et Koryo, pour leur disponibilité, soutien, et complicité. J'ai eu beaucoup de plaisir, non seulement à collaborer dans une excellente ambiance, mais aussi à partager un grand nombre de moments chers avec eux. Je tiens particulièrement à remercier Fred et Sacha pour leur encadrement et conseils précieux, ainsi que mon co-bureau Vianney avec qui j'ai énormément apprécié travailler et discuter. Cela a été très important pour moi, à certains moments, de réellement progresser en équipe.

Ces trois années, riches en visites et voyages, n'auraient pas été aussi dynamiques sans Tara, Phil, Nick, Albrecht, Oskar, Ilse, Annie, Lynn, Dave, et Margaret. J'espère sincèrement pouvoir continuer à collaborer activement avec eux. Je suis aussi reconnaissante envers George, Lee, et Tamara de m'avoir donné l'envie de prendre ce chemin.

J'aimerais remercier tous les étudiants, postdocs, et amis d'avoir pimenté ces années CEA, avec petits-déjeuners, soirées, picnics, barbecues, et sorties voiles. Un grand merci à Sandrine, Doris, Vera, Henri, Marco, Katrien, Martin, Timea, Laurie, Fadia, Pedro, Roger, David, et ceux que j'oublie. Ainsi qu'à Sacha pour nous avoir divertis à tant d'occasions et pour tous les dîners organisés à Lozère.

Je remercie Suzanne et sa famille de m'avoir invitée chez eux, pour les délicieux repas, et après-midis dans le jardin.

Je tiens finalement à remercier ma famille pour son soutien, ainsi que les FAAATTs pour les distractions extra-scolaires et week-ends aventuriers.

Ces années sont passées trop vite, et je vous invite à visiter Heidelberg.

---

# Glossary

## Acronyms

ALMA	Atacama Large Millimeter Array
APEX	Atacama Pathfinder Experiment
BCD	Blue Compact Dwarf
dE	dwarf Elliptical
DGS	Dwarf Galaxy Survey
dIrr	dwarf Irregular
dS	dwarf Spiral
dSph	dwarf Spheroidal
(F)IR	(Far)-Infrared
FOV	Field-Of-View
(F)UV	(Far)-Ultraviolet
FWHM	Full Width Half Maximum
GMC	Giant Molecular Cloud
HIPE	Herschel Interactive Processing Environment
IDL	Interactive Data Language
IMF	Initial Mass Function
IRS	Infrared Spectrograph
ISM	Interstellar Medium
ISO	Infrared Space Observatory
LMC	Large Magellanic Cloud
MIR	Mid-Infrared
NED	NASA/IPAC Extragalactic Database
PACS	Photodetector Array Camera and Spectrometer
PAH	Polycyclic Aromatic Hydrocarbon
PDR	PhotoDissociation Region
RMS	Root Mean Square
SED	Spectral Energy Distribution
SFR	Star Formation Rate
SMC	Small Magellanic Cloud
SOFIA	Stratospheric Observatory For Infrared Astronomy
SSC	Super Star Cluster
submm	sub-millimeter
TIR	Total Infrared
(U)LIRG	(Ultra)-Luminous Infrared Galaxy
WR	Wolf-Rayet

## Notations

$A_V$	Visual Extinction
$D/G$	Dust-to-Gas mass ratio
EP	Excitation Potential
eV	electron-volt
IP	Ionisation Potential
$N$	Column density
$n_{crit}$	Critical density
pc	parsec
S/N	Signal-to-Noise
$U$	Ionisation Parameter
$X_{CO}$	CO-to-H <sub>2</sub> conversion factor
$Z$	Metallicity

---

# The Dwarf Galaxy Sample – Observing information

**Table A.1.** Technical details on the DGS observations.

Source Name	Coordinates <sup>(a)</sup> (J2000)		OBSID <sup>(b)</sup>	Mode <sup>(c)</sup>	Map size ( $''$ ) <sup>2</sup>	Line
Haro 11	0h36m52.50s	-33d33m19.0s	1342199236	CN	51x51	157, 145, 88
	0h36m52.50s	-33d33m19.0s	1342199237			63, 57, 122
	0h36m52.36s	-33d33m19.7s	1342234063		47x47	205
Haro 2	10h32m31.88s	+54d24m03.7s	1342221392	CN	47x47	63
			1342230081		71x71	157
			1342230082		47x47	88
Haro 3	10h45m22.41s	+55d57m37.4s	1342221890	CN	79x79	88
			1342221891		79x79	63
			1342221892		95x95	157
			1342221893		47x47	122
			1342221894		71x71	145
He 2-10	8h36m15.18s	-26d24m33.9s	1342221895	CN	63x63	57
			1342221971		47x47	57
			1342221972		47x47	145
			1342221973		53x53	88
			1342221974		53x53	63
HS 0017+1055	0h20m21.40s	+11d12m21.0s	1342221975	CN	51x51	157
			1342234065		47x47	157
			1342212588			88
HS 0052+2536	0h54m56.00s	+25d53m23.0s	1342213134	CN	47x47	157
			1342213135			63
			1342213136			88
HS 0822+3542	8h25m55.52s	+35d32m32.0s	1342220753	CN	47x47	157
HS 1222+3741	12h24m36.72s	+37d24m36.6s	1342232306	CN	47x47	157
			1342199399			88
HS 1236+3937	12h39m20.14s	+39d21m04.8s	1342199400	CN	47x47	157
HS 1304+3529	13h21m19.92s	+32d08m23.0s	1342199736	CN	47x47	157
	13h06m24.24s	+35d13m41.6s	1342232552			88
HS 1319+3224	13h21m19.71s	+32d08m25.2s	1342199227	CN	47x47	157
			1342232551			88
HS 1330+3651	13h33m08.28s	+36d36m33.1s	1342199734	CN	47x47	157
			1342199735			88
			1342232549			63
HS 1442+4250	14h44m12.81s	+42d37m44.0s	1342208927	CN	47x47	157
HS 2352+2733	23h54m56.70s	+27d49m59.0s	1342213133	CN	47x47	157
			1342234066			88
II Zw 40	5h55m43.10s	+3d23m20.0s	1342228249	CN	79x79	63
	5h55m43.10s	+3d23m20.0s	1342228250		71x71	88
	5h55m43.10s	+3d23m20.0s	1342228251		85x85	145
	5h55m43.00s	+3d23m31.4s	1342228252		47x47	122
	5h55m43.10s	+3d23m20.0s	1342228253		95x95	157
I Zw 18	9h34m01.44s	+55d14m34.8s	1342220973	CN	47x47	157
	9h34m02.03s	+55d14m28.1s	1342253757			63
	9h34m02.03s	+55d14m28.1s	1342253758			88
IC 10	0h20m26.10s	+59d17m17.6s	1342214364	UN	81x81	63
	0h20m52.12s	+59d17m42.4s	1342214365		47x47	122
	0h20m56.70s	+59d17m46.8s	1342214366		47x47	145

*Continued on next page*

**Table A.1.** Technical details on the DGS observations.

Source Name	Coordinates <sup>(a)</sup> (J2000)		OBSID <sup>(b)</sup>	Mode <sup>(c)</sup>	Map size ( $''$ ) <sup>2</sup>	Line
LMC-30Dor	0h20m26.10s	+59d17m17.6s	1342214367	UN	81x81	88
	0h20m48.32s	+59d18m09.0s	1342214368		115x183	157
	0h20m18.70s	+59d18m45.2s	1342214369		81x47	88
	0h20m14.00s	+59d19m53.0s	1342214370		149x81	157
	0h20m18.70s	+59d18m45.2s	1342214371		81x47	63
	0h20m13.30s	+59d19m57.5s	1342214372		115x47	63
	0h20m13.30s	+59d19m57.5s	1342214273		115x47	88
	0h20m18.00s	+59d18m44.0s	1342223371		47x47	122
	0h20m28.25s	+59d16m58.0s	1342223372		47x47	122
	0h20m28.25s	+59d16m58.0s	1342223373		47x47	145
	0h20m18.00s	+59d18m44.0s	1342223374		47x47	145
	5h38m35.00s	-69d05m39.0s	1342222085		143x47	88, 157
	5h38m48.00s	-69d06m37.0s	1342222086		71x47	63
	5h38m58.00s	-69d04m43.0s	1342222087		143x47	63
	5h38m58.00s	-69d04m43.0s	1342222088		143x47	88, 157
	5h38m48.00s	-69d06m37.0s	1342222089		71x47	88, 157
	5h38m56.66s	-69d04m56.9s	1342222090		47x47	145
	5h38m34.92s	-69d06m07.0s	1342222091		47x47	122
	5h38m45.00s	-69d05m23.0s	1342222092		191x47	63
	5h38m35.00s	-69d05m39.0s	1342222093		143x47	145
	5h38m45.00s	-69d05m23.0s	1342222094		191x47	88, 157
	5h38m46.10s	-69d04m58.8s	1342222095		47x47	122
	5h38m45.00s	-69d05m23.0s	1342222096		191x47	145
	5h38m35.00s	-69d05m39.0s	1342222097		143x47	63
	5h38m38.00s	-69d06m00.0s	1342231279		123x47	157
	5h38m30.00s	-69d06m07.0s	1342231280		123x47	88
	5h38m30.00s	-69d06m07.0s	1342231281		123x47	157
	5h38m55.00s	-69d03m49.0s	1342231282		85x47	63, 157
	5h38m30.00s	-69d06m07.0s	1342231283		123x47	63, 157
	5h38m56.00s	-69d04m50.0s	1342231284		85x47	122
	5h38m40.00s	-69d04m38.0s	1342231285		85x47	88
LMC-N11A	4h57m16.00s	-66d23m24.0s	1342214638	UN	47x47	157, 63
LMC-N11B	4h56m95.14s	-66d24m23.8s	1342188940	WS	127x127	88
LMC-N11C	4h56m95.14s	-66d24m23.8s	1342188941	UN	127x127	157, 63, 145, 122, 57, 205
	4h56m47.00s	-66d24m32.0s	1342219439		47x47	122
	4h56m57.20s	-66d25m13.0s	1342225175		47x47	122, 145
	4h57m48.00s	-66d28m30.0s	1342221976		47x47	88, 157
	4h57m48.00s	-66d28m30.0s	1342221977		47x47	63
	4h57m40.30s	-66d26m59.0s	1342221978		81x47	63
	4h57m50.59s	-66d29m49.7s	1342221979		81x81	157
	4h57m50.59s	-66d29m49.7s	1342221980		81x81	63
LMC-N11I	4h57m40.30s	-66d26m59.0s	1342221981	UN	81x47	88, 157
	4h55m44.00s	-66d34m24.0s	1342222769		115x47	63
LMC-N158	5h39m13.00s	-69d30m18.0s	1342222770	UN	115x47	88, 157
			1342214032		81x81	88, 157
LMC-N159	5h39m13.00s	-69d30m18.0s	1342214033	UN	81x81	63
			1342222075		47x47	145
			1342222076		47x47	145, 205
			1342222077		47x47	145
			1342222078		81x81	88, 157
			1342222079		115x47	63, 122
			1342222080		81x81	63
			1342222081		115x47	88, 157
			1342222082		81x81	63, 122
			1342222083		81x81	88, 157
			1342222084		81x81	145, 205
			1342222767		81x81	63
LMC-N159S	5h40m00.00s	-69d50m33.4s	1342222768	UN	81x81	157
			1342222768		81x81	157
LMC-N160	5h39m38.00s	-69d39m04.7s	1342222071	UN	47x47	145
			1342222072		75x103	63
			1342222073		47x47	145
Mrk 153	10h49m05.04s	+52d20m07.8s	1342222074	CN	76x105	88, 157
			1342209014		47x47	63
			1342209015			157
			1342232267	CN	47x47	88

Continued on next page



**Table A.1.** Technical details on the DGS observations.

Source Name	Coordinates <sup>(a)</sup> (J2000)		OBSID <sup>(b)</sup>	Mode <sup>(c)</sup>	Map size ( $''$ ) <sup>2</sup>	Line
Mrk 209	12h26m16.02s	+48d29m36.6s	1342199423	CN	47x47	88, 157
			1342199424			63
Mrk 930	23h31m58.29s	+28d56m49.9s	1342212518	CN	47x47	63
			1342212519		47x47	145
			1342212520		51x51	157
			1342212521		47x47	122
			1342212522		53x53	88
Mrk 1089	5h01m37.76s	-4d15m28.4s	1342217857	CN	47x47	88
			1342217858		47x47	145
			1342217859		51x51	157
			1342217860		51x51	122
			1342217861		53x53	63
Mrk 1450	11h38m35.62s	+57d52m27.2s	1342222067	CN	47x47	63
			1342222068		47x47	88
			1342222069		47x47	122
			1342222070		51x51	157
NGC 625	1h35m06.00s	-41d26m10.3s	1342222216	CN	63x63	88
			1342222217		47x47	63
			1342222218		85x85	157
NGC 1140	2h54m33.20s	-10d01m50.0s	1342214034	CN	95x95	157
	2h54m33.54s	-10d01m42.2s	1342214035		63x63	88
	2h54m33.54s	-10d01m42.2s	1342214036		47x47	63
	2h54m33.54s	-10d01m42.2s	1342225171		47x47	122
	2h54m33.54s	-10d01m42.2s	1342224588		47x47	145
NGC 1569	4h30m49.06s	+64d50m52.6s	1342225753	UN	95x143	157
			1342225754		95x79	63
			1342225755		119x71	88
NGC 1705	4h54m13.50s	-53d21m39.8s	1342222213	CN	63x63	88
			1342222214		47x47	63
			1342222215		71x71	157
NGC 2366	7h28m42.60s	+69d11m19.0s	1342220604		47x47	88
			1342220605		71x71	157
			1342220606		63x63	63
NGC 4214	12h15m39.17s	+36d19m36.8s	1342187843	CN	111x111	63
			1342187844			88
			1342187845		95x95	157
			1342188034			205
			1342188035			145
			1342188036			122
NGC 4449	12h28m11.90s	+44d05m39.6s	1342197813	UN	119x191	157
			1342197814			63
			1342197815	CN	47x47	157
			1342197816			63
			1342197817			157
			1342197818			63
			1342197819			157
			1342197820			63
	12h28m11.30s	44d05m30.6s	1342223138	UN	81x47	145
	12h28m11.30s	44d05m30.6s	1342223139	CN	81x81	88
	12h28m11.30s	44d05m30.6s	1342223140	UN	81x47	122
	12h28m15.40s	44d06m57.6s	1342223141		81x115	63
	12h28m15.40s	44d06m57.6s	1342223142		81x115	88
	12h28m15.40s	44d06m57.6s	1342223143		81x115	157
NGC 4861	12h59m02.34s	+34d51m34.0s	1342208901	CN	47x47	63, 145, 122, 205, 57
	12h59m02.34s	+34d51m34.0s	1342208902		85x215	157
	12h59m02.34s	+34d51m34.0s	1342208903		47x47	88
	12h59m00.30s	+34d50m43.6s	1342221887		47x47	63, 145
	12h59m00.30s	+34d50m43.6s	1342221888		47x47	88
NGC 5253	13h39m55.96s	-31d38m24.4s	1342202125	CN	78x78	63
			1342202126		94x141	157
			1342214026	CN	63x63	88
			1342214027		47x47	122
			1342214028		62x47	145
NGC 6822	19h45m05.00s	-14d43m22.1s	1342216633	UN	47x47	157
	19h44m50.00s	14d52m46.9s	1342216634		71x71	63

*Continued on next page*

**Table A.1.** Technical details on the DGS observations.

Source Name	Coordinates <sup>(a)</sup> (J2000)		OBSID <sup>(b)</sup>	Mode <sup>(c)</sup>	Map size ( $''$ ) <sup>2</sup>	Line
Pox 186	19h45m05.00s	-14d43m22.1s	1342216635	UN	47x47	88
	19h44m50.00s	14d52m46.9s	1342216636		77x47	157
	19h44m50.00s	14d52m46.9s	1342216637		77x47	88
	19h44m52.80s	-14d43m04.9s	1342216638		71x71	88, 157
	19h44m52.80s	-14d43m04.9s	1342216639		71x71	122
	19h44m52.80s	-14d43m04.9s	1342230147	CN	81x81	63
	19h44m52.80s	-14d43m04.9s	1342230148		47x47	145
	19h45m05.00s	-14d43m22.1s	1342230149		47x47	63
	13h25m48.66s	-11d36m37.8s	1342213284		47x47	88
			1342234995			157
SBS 0335-052	3h37m44.06s	-5d02m40.2s	1342214221	CN	47x47	157
			1342248295			88
			1342249197			63
SBS 1159+545	12h02m02.37s	+54d15m49.5s	1342199228	CN	47x47	157
			1342232309			88
			1342232310			63
SBS 1211+540	12h14m02.48s	+53d45m17.4s	1342199422	CN	47x47	157
SBS 1249+493	12h51m52.53s	+49d03m26.9s	1342232266	CN	47x47	157
SBS 1415+437	14h17m01.40s	+43d30m04.5s	1342199731	CN	47x47	63
			1342199732			88
			1342199733			157
SBS 1533+574	15h34m13.80s	+57d17m06.0s	1342199230	CN	47x47	157
			1342199231			88
			1342199232			63
			1342199399			88
SMC-N66	0h59m08.00s	-72d10m46.4s	1342214029	UN	149x47	88, 157
	0h59m08.00s	-72d10m46.4s	1342214030		149x47	63
	0h59m09.73s	-72d10m03.4s	1342214031		47x47	63, 157
Tol 1214-277	12h17m17.09s	-28d02m32.7s	1342199408	CN	47x47	157
			1342234059			88
			1342234060			63
UGC 4483	8h37m03.00s	+69d46m54.0s	1342203684	CN	47x47	157
	8h37m03.00s	+69d46m54.0s	1342203685			88
	8h37m03.00s	+69d46m31.0s	1342203686			157, 63
UM 133	1h44m41.28s	+4d53m25.9s	1342212533	CN	47x47	157
			1342235699			88
			1342235700			63
UM 311	1h15m32.00s	-0d51m38.0s	1342213288	CN	71x71	157
			1342213289		63x63	88
			1342213290		47x47	122
			1342213291		63x63	63
UM 448	11h42m12.40s	+0d20m02.7s	1342222199	CN	53x53	88
			1342222200		47x47	122
			1342222201		51x51	157
			1342222202		51x51	145
			1342222203		53x53	63
UM 461	11h51m33.35s	-2d22m21.9s	1342222204	CN	47x47	63
			1342222205		51x51	157
			1342222206		47x47	122
			1342222207		53x53	88
VII Zw 403	11h27m59.90s	+78d59m39.0s	1342199286	CN	47x47	122, 145
			1342199287		63x63	88
			1342199288		63x63	63
			1342199289		71x71	157

(a) Coordinates of the map center.

(b) Observation Identification number.

(c) Observing mode: UN=Unchopped, CN=Chopnod, WS=Wavelength Switching.

When left blank, the coordinates, observing mode, and map size are identical to the previous line.

## Appendix B

# The Dwarf Galaxy Sample – Spectral maps and line profiles

Appendix B contains all the PACS spectroscopic maps of the *Herschel* “Dwarf Galaxy Survey”. For each galaxy, we present the flux map of each observed line on the *left* hand side, and the rebinned spectrum of the brightest spatial pixel on the *right* hand side. The position of this spectrum is indicated by a dark cross on the map. Total fluxes are summarized in Table 3.1. For the extended sources, we also show the position of extra regions, for which we report surface brightness in Table 3.1, with orange crosses on the spectral maps. White circles represent the PACS beam sizes. Note that the maps have not been deconvolved for the PSF and therefore low level artifacts due to the shape of the beam may appear in the unresolved or barely resolved sources.

*Note: Only a selected subset of galaxy maps (Haro 11, NGC 4214, and LMC-30Dor) are displayed here. See the online version for the spectral maps and line profiles of the full sample.*

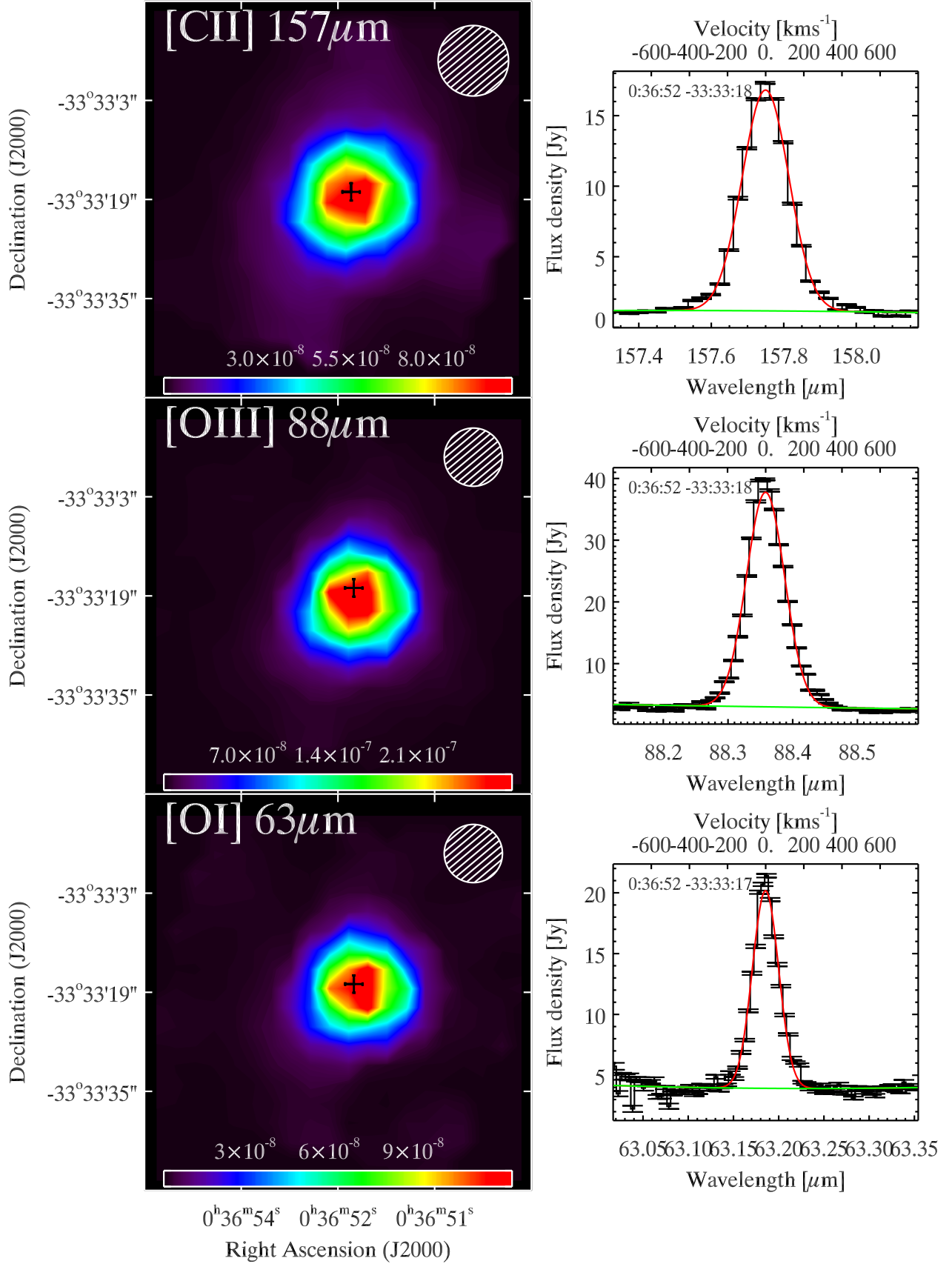
### List of sources

Haro 11 .....	p. 169
Haro 2	
Haro 3	
He 2-10	
HS 0017+1055	
HS 0052+2536	
HS 0822+3542	
HS 1222+3741	
HS 1236+3937	
HS 1304+3529	
HS 1319+3224	
HS 1330+3651	
HS 1442+4250	
HS 2352+2733	
II Zw 40	
I Zw 18	
Mrk 1089	

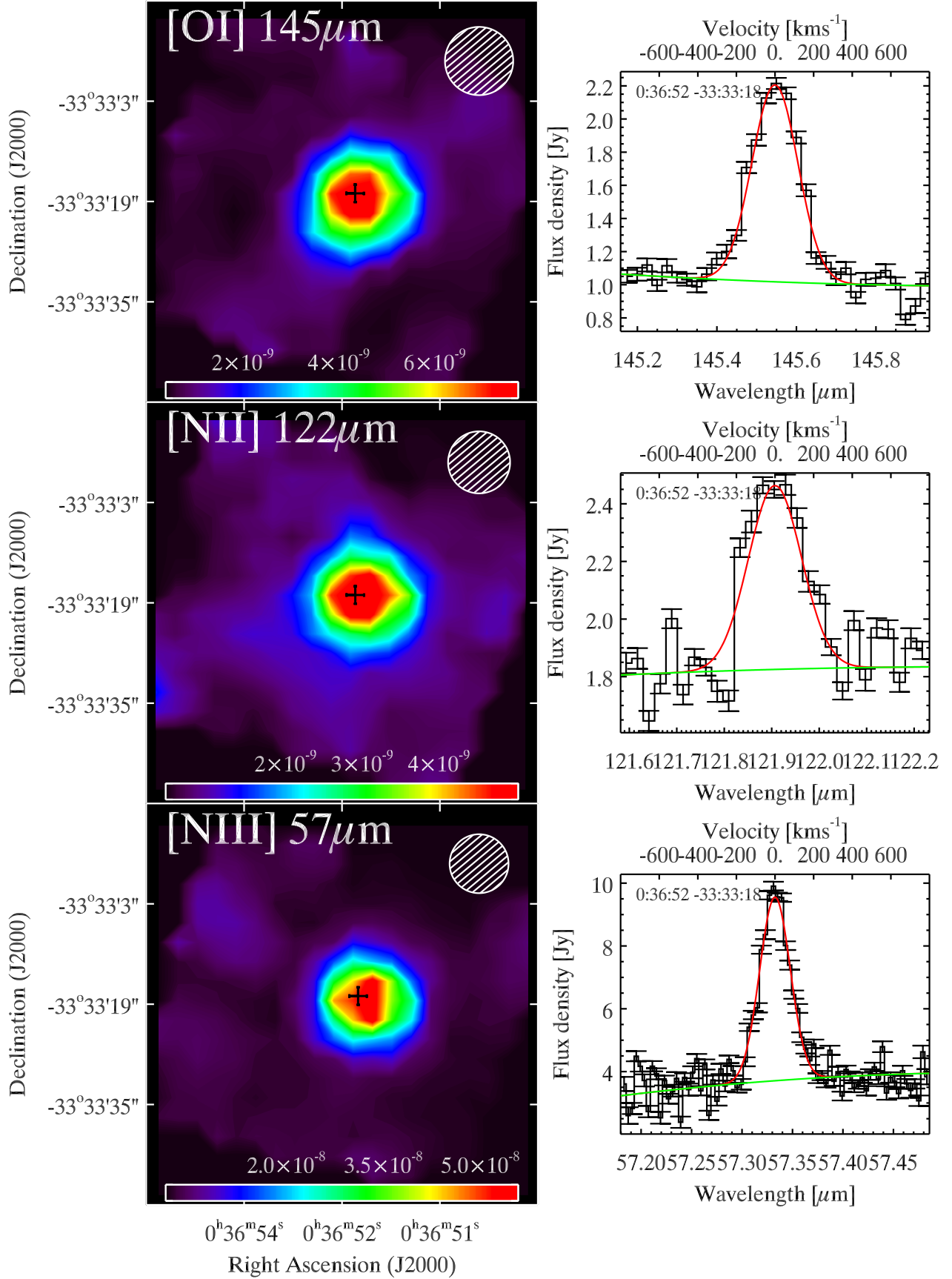
Mrk 1450	
Mrk 153	
Mrk 209	
Mrk 930	
NGC 1140	
NGC 1569	
NGC 1705	
NGC 2366	
NGC 4214 .....	p. 171
NGC 4861	
NGC 5253	
NGC 625	
Pox 186	
SBS 0335-052	
SBS 1159+545	
SBS 1211+540	
SBS 1249+493	
SBS 1415+437	
SBS 1533+574	
Tol 1214-277	
UGC 4483	
UM 133	
UM 311	
UM 448	
UM 461	
VII Zw 403	
IC 10	
LMC-30Dor .....	p. 173
LMC-N11A	
LMC-N11B	
LMC-N11C	
LMC-N11I	
LMC-N158	
LMC-N159	
LMC-N160	
SMC-N66	
NGC 4449	
NGC 6822	

## PACS spectral maps

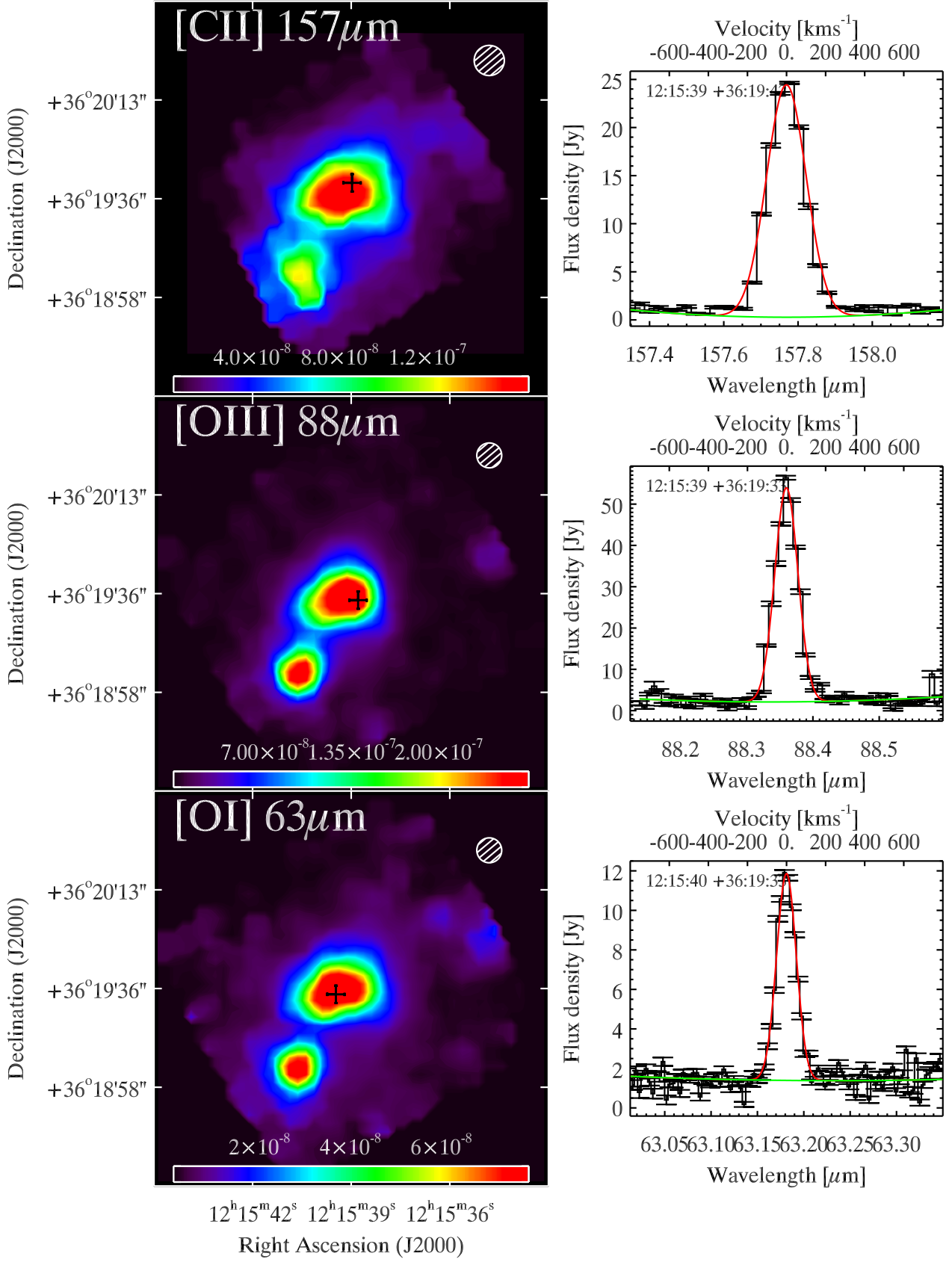
## Haro11



## Har011

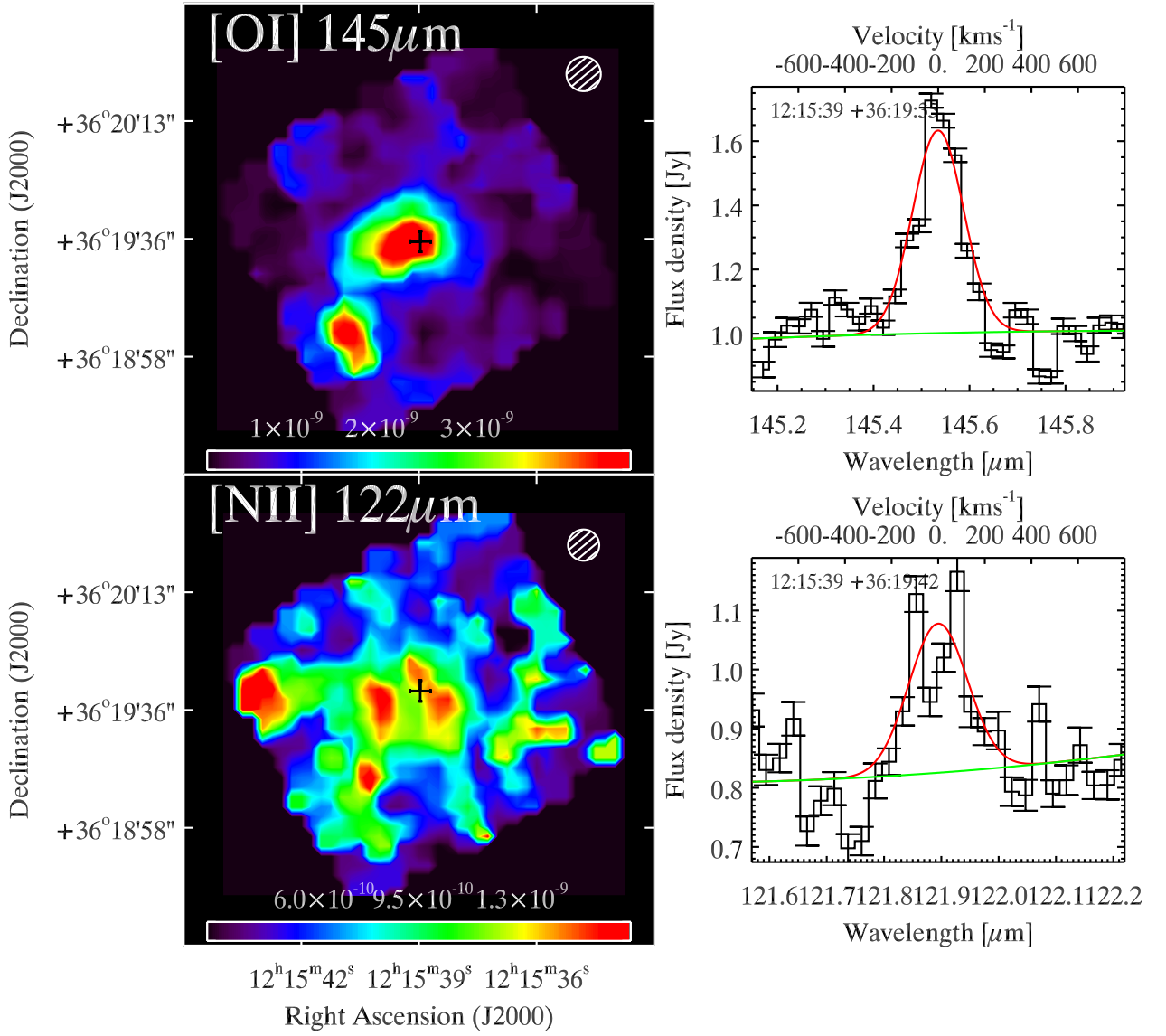


## NGC4214

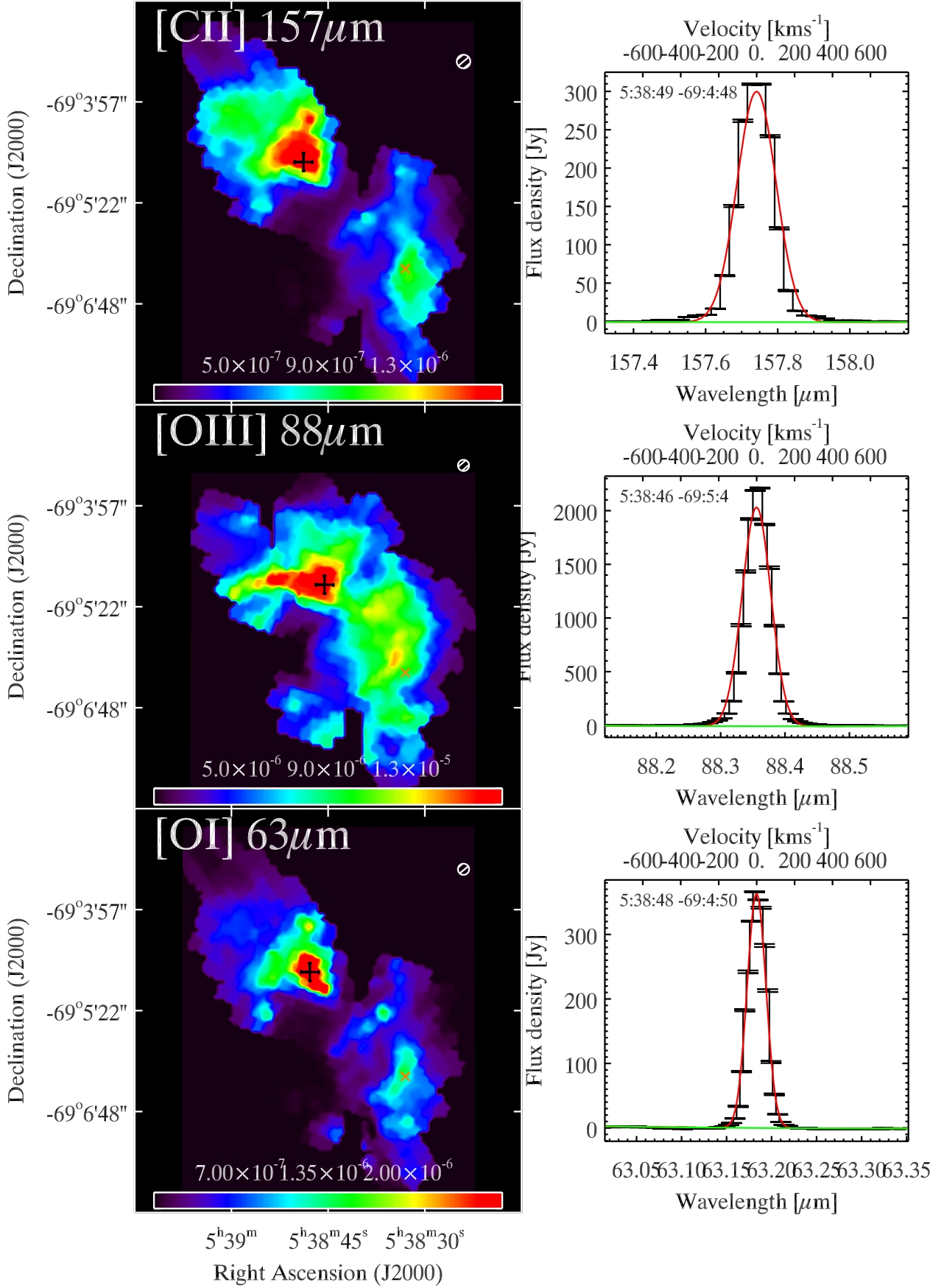




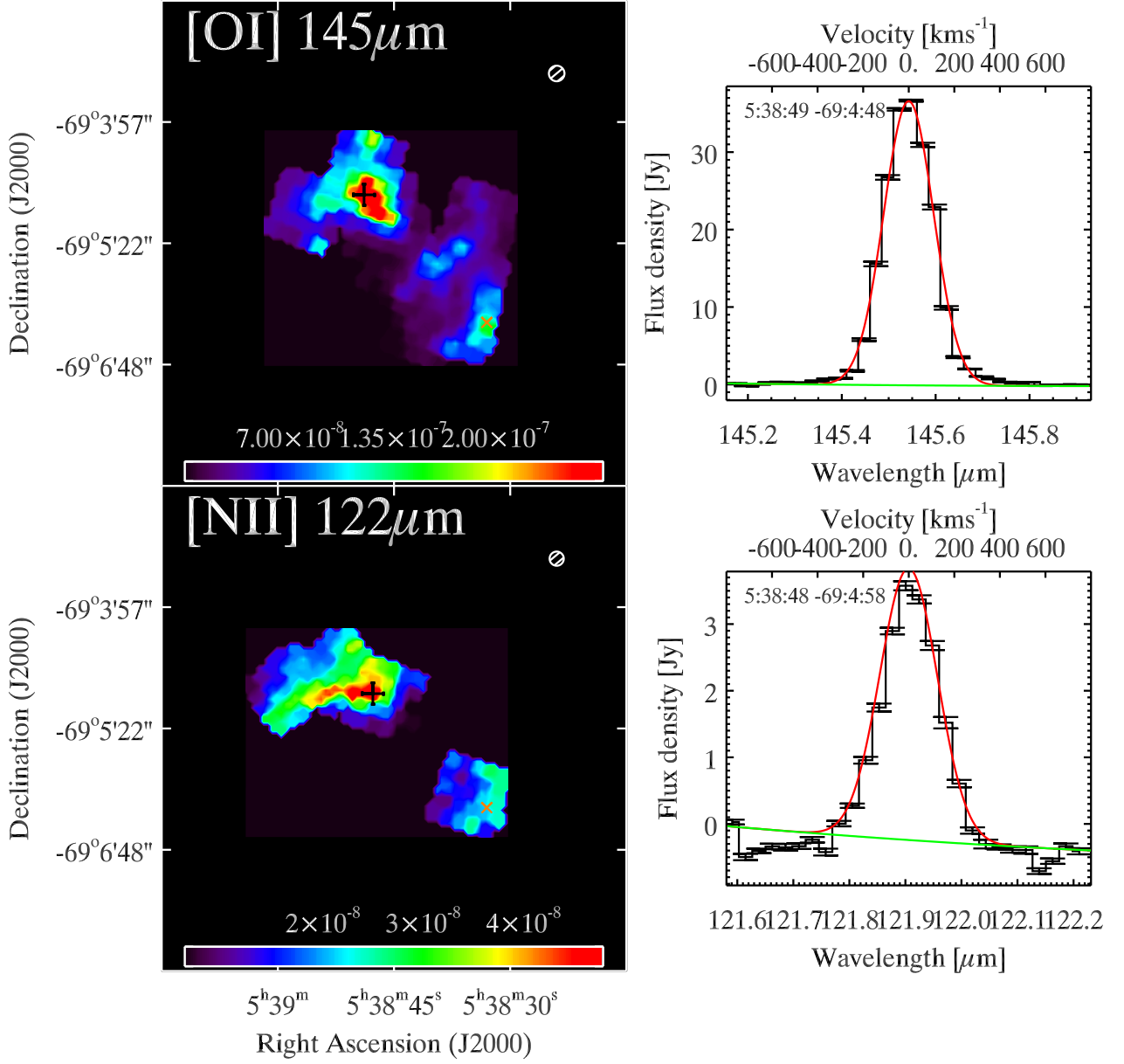
## NGC4214



## LMC-30Dor



## LMC-30Dor



# Bibliography

- Abel, N. P., Dudley, C., Fischer, J., Satyapal, S., & van Hoof, P. A. M. 2009, [ApJ](#), 701, 1147
- Abel, N. P., Ferland, G. J., Shaw, G., & van Hoof, P. A. M. 2005, [ApJS](#), 161, 65
- Abel, N. P., Sarma, A. P., Troland, T. H., & Ferland, G. J. 2007, [ApJ](#), 662, 1024
- Adamo, A., Östlin, G., Zackrisson, E., et al. 2010, [MNRAS](#), 407, 870
- Adamo, A., Östlin, G., Zackrisson, E., et al. 2011, [MNRAS](#), 415, 2388
- Allen, D. A., Wright, A. E., & Goss, W. M. 1976, [MNRAS](#), 177, 91
- Allen, M. G., Groves, B. A., Dopita, M. A., Sutherland, R. S., & Kewley, L. J. 2008, [ApJS](#), 178, 20
- Aniano, G., Draine, B. T., Calzetti, D., et al. 2012, [ArXiv e-prints](#)
- Arp, H. & Sandage, A. 1985, [AJ](#), 90, 1163
- Asplund, M., Grevesse, N., Sauval, A. J., & Scott, P. 2009, [ARA&A](#), 47, 481
- Bakes, E. L. O. & Tielens, A. G. G. M. 1994, [ApJ](#), 427, 822
- Bayet, E., Aladro, R., Martín, S., Viti, S., & Martín-Pintado, J. 2009a, [ApJ](#), 707, 126
- Bayet, E., Gerin, M., Phillips, T. G., & Contursi, A. 2004, [A&A](#), 427, 45
- Bayet, E., Gerin, M., Phillips, T. G., & Contursi, A. 2006, [A&A](#), 460, 467
- Bayet, E., Gerin, M., Phillips, T. G., & Contursi, A. 2009b, [MNRAS](#), 399, 264
- Bayet, E., Viti, S., Williams, D. A., Rawlings, J. M. C., & Bell, T. 2009c, [ApJ](#), 696, 1466
- Bendo, G. J., Galliano, F., & Madden, S. C. 2012, [ArXiv e-prints](#)
- Bennett, C. L., Fixsen, D. J., Hinshaw, G., et al. 1994, [ApJ](#), 434, 587
- Bergvall, N., Masegosa, J., Östlin, G., & Cernicharo, J. 2000, [A&A](#), 359, 41
- Bernard-Salas, J., Habart, E., Arab, H., et al. 2012, [A&A](#), 538, A37
- Bertelli, G., Bressan, A., Chiosi, C., Fagotto, F., & Nasi, E. 1994, [A&AS](#), 106, 275
- Besla, G., Kallivayalil, N., Hernquist, L., et al. 2012, [MNRAS](#), 421, 2109
- Bigiel, F., Leroy, A., Walter, F., et al. 2010, [AJ](#), 140, 1194
- Bigiel, F., Leroy, A., Walter, F., et al. 2008, [AJ](#), 136, 2846
- Bigiel, F., Leroy, A. K., Walter, F., et al. 2011, [ApJ](#), 730, L13
- Billett, O. H., Hunter, D. A., & Elmegreen, B. G. 2002, [AJ](#), 123, 1454
- Binggeli, B. 1994, in *Panchromatic View of Galaxies. Their Evolutionary Puzzle*, ed. G. Hensler, C. Theis, & J. S. Gallagher, 173
- Boissier, S., Prantzos, N., Boselli, A., & Gavazzi, G. 2003, [MNRAS](#), 346, 1215
- Bolatto, A. D., Jackson, J. M., Israel, F. P., Zhang, X., & Kim, S. 2000, [ApJ](#), 545, 234

- Bolatto, A. D., Leroy, A., Israel, F. P., & Jackson, J. M. 2003, [ApJ](#), 595, 167
- Bolatto, A. D., Leroy, A. K., Jameson, K., et al. 2011, [ApJ](#), 741, 12
- Bolatto, A. D., Leroy, A. K., Rosolowsky, E., Walter, F., & Blitz, L. 2008, [ApJ](#), 686, 948
- Boquien, M., Calzetti, D., Combes, F., et al. 2011, [AJ](#), 142, 111
- Boselli, A., Gavazzi, G., Lequeux, J., & Pierini, D. 2002a, [A&A](#), 385, 454
- Boselli, A., Lequeux, J., & Gavazzi, G. 2002b, [A&A](#), 384, 33
- Bot, C., Boulanger, F., Lagache, G., Cambr  sy, L., & Egret, D. 2004, [A&A](#), 423, 567
- Bot, C., Ysard, N., Paradis, D., et al. 2010, [A&A](#), 523, A20
- Bournaud, F. 2010, [Advances in Astronomy](#), 2010
- Bournaud, F., Elmegreen, B. G., Teyssier, R., Block, D. L., & Puerari, I. 2010, [MNRAS](#), 409, 1088
- Boyer, M. L., Sargent, B., van Loon, J. T., et al. 2010, [A&A](#), 518, L142
- Brauher, J. R., Dale, D. A., & Helou, G. 2008, [ApJS](#), 178, 280
- Brinchmann, J., Kunth, D., & Durret, F. 2008, [A&A](#), 485, 657
- Brinks, E. & Taylor, C. L. 1994, in European Southern Observatory Conference and Workshop Proceedings, Vol. 49, European Southern Observatory Conference and Workshop Proceedings, ed. G. Meylan & P. Prugniel, 263
- Cair  s, L. M., Caon, N., Zurita, C., et al. 2010, [A&A](#), 520, A90
- Calzetti, D., Kennicutt, R. C., Engelbracht, C. W., et al. 2007, [ApJ](#), 666, 870
- Calzetti, D., Kinney, A. L., & Storchi-Bergmann, T. 1994, [ApJ](#), 429, 582
- Campbell, A., Terlevich, R., & Melnick, J. 1986, [MNRAS](#), 223, 811
- Cannon, J. M., McClure-Griffiths, N. M., Skillman, E. D., & C  t  , S. 2004, [ApJ](#), 607, 274
- Cannon, J. M., Skillman, E. D., Sembach, K. R., & Bomans, D. J. 2005, [ApJ](#), 618, 247
- Cannon, J. M., Skillman, E. D., Sembach, K. R., & Bomans, D. J. 2006, in Astronomical Society of the Pacific Conference Series, Vol. 348, Astrophysics in the Far Ultraviolet: Five Years of Discovery with FUSE, ed. G. Sonneborn, H. W. Moos, & B.-G. Andersson, 489
- Carignan, C. & Beaulieu, S. 1989, [ApJ](#), 347, 760
- Castelli, F. & Kurucz, R. L. 2004, [ArXiv Astrophysics e-prints](#)
- Christensen, C., Quinn, T., Governato, F., et al. 2012, [ArXiv e-prints](#)
- Condon, J. J. 1992, [ARA&A](#), 30, 575
- Condon, J. J., Cotton, W. D., Greisen, E. W., et al. 1998, [AJ](#), 115, 1693
- Condon, J. J., Helou, G., Sanders, D. B., & Soifer, B. T. 1996, [ApJS](#), 103, 81
- Conti, P. S. 1991, [ApJ](#), 377, 115
- Contreras Ramos, R., Annibali, F., Fiorentino, G., et al. 2011, [ApJ](#), 739, 74
- Cormier, D., Lebouteiller, V., Madden, S. C., et al. 2012a, [ArXiv e-prints](#)
- Cormier, D., Madden, S. C., Hony, S., et al. 2010, [A&A](#), 518, L57
- Cormier, D. et al. 2012b, in preparation
- Cormier, D. et al. 2012c, in preparation
- Cowie, L. L., Songaila, A., Hu, E. M., & Cohen, J. G. 1996, [AJ](#), 112, 839

- Crawford, M. K., Genzel, R., Townes, C. H., & Watson, D. M. 1985, [ApJ](#), **291**, 755
- Croxall, K. V., Smith, J. D., Wolfire, M. G., et al. 2012, [ApJ](#), **747**, 81
- Da Costa, G. S., Hatzidimitriou, D., Irwin, M. J., & McMahon, R. G. 1991, [MNRAS](#), **249**, 473
- Daddi, E., Elbaz, D., Walter, F., et al. 2010, [ApJ](#), **714**, L118
- Dale, D. A. & Helou, G. 2002, [ApJ](#), **576**, 159
- Dame, T. M., Hartmann, D., & Thaddeus, P. 2001, [ApJ](#), **547**, 792
- De Breuck, C., Maiolino, R., Caselli, P., et al. 2011, [A&A](#), **530**, L8
- de Looze, I., Baes, M., Bendo, G. J., Cortese, L., & Fritz, J. 2011, [MNRAS](#), **416**, 2712
- De Looze, I., Baes, M., Parkin, T. J., et al. 2012, [MNRAS](#), **423**, 2359
- de Looze, I., Baes, M., Zibetti, S., et al. 2010, [A&A](#), **518**, L54
- Dekel, A. & Silk, J. 1986, [ApJ](#), **303**, 39
- Dolphin, A. E., Weisz, D. R., Skillman, E. D., & Holtzman, J. A. 2005, [ArXiv Astrophysics e-prints](#)
- Dopita, M. A. & Evans, I. N. 1986, [ApJ](#), **307**, 431
- Doublier, V., Kunth, D., Courbin, F., & Magain, P. 2000, [A&A](#), **353**, 887
- Draine, B. T., Dale, D. A., Bendo, G., et al. 2007, [ApJ](#), **663**, 866
- Draine, B. T. & Hensley, B. 2012, [ArXiv e-prints](#)
- Draine, B. T. & Lazarian, A. 1998, [ApJ](#), **494**, L19
- Draine, B. T. & Li, A. 2007, [ApJ](#), **657**, 810
- Duc, P.-A. & Mirabel, I. F. 1999, in *IAU Symposium, Vol. 186, Galaxy Interactions at Low and High Redshift*, ed. J. E. Barnes & D. B. Sanders, 61
- Dwek, E. 1998, [ApJ](#), **501**, 643
- Engelbracht, C. W., Gordon, K. D., Rieke, G. H., et al. 2005, [ApJ](#), **628**, L29
- Ferkinhoff, C., Hailey-Dunsheath, S., Nikola, T., et al. 2010, [ApJ](#), **714**, L147
- Ferland, G. J., Korista, K. T., Verner, D. A., et al. 1998, [PASP](#), **110**, 761
- Fischer, J., Sturm, E., González-Alfonso, E., et al. 2010, [A&A](#), **518**, L41
- Galametz, M., Madden, S., Galliano, F., et al. 2009, [A&A](#), **508**, 645
- Galametz, M., Madden, S. C., Galliano, F., et al. 2011, [A&A](#), **532**, A56
- Galametz, M., Madden, S. C., Galliano, F., et al. 2010, [A&A](#), **518**, L55
- Galametz, M. et al. 2012, in preparation
- Gallagher, J. S. 1996, in *Astronomical Society of the Pacific Conference Series, Vol. 98, From Stars to Galaxies: the Impact of Stellar Physics on Galaxy Evolution*, ed. C. Leitherer, U. Fritze-von-Alvensleben, & J. Huchra, 315
- Galliano, F., Hony, S., Bernard, J.-P., et al. 2011, [A&A](#), **536**, A88
- Galliano, F., Madden, S. C., Jones, A. P., Wilson, C. D., & Bernard, J.-P. 2005, [A&A](#), **434**, 867
- Galliano, F., Madden, S. C., Jones, A. P., et al. 2003, [A&A](#), **407**, 159
- Galliano, F., Madden, S. C., Tielens, A. G. G. M., Peeters, E., & Jones, A. P. 2008, [ApJ](#), **679**, 310
- Gao, Y. & Solomon, P. M. 2004, [ApJ](#), **606**, 271
- Garnett, D. R. 1990, [ApJ](#), **363**, 142

- Genzel, R. & Cesarsky, C. J. 2000, [ARA&A](#), **38**, 761
- Genzel, R., Tacconi, L. J., Combes, F., et al. 2012, [ApJ](#), **746**, 69
- Gerin, M. & Phillips, T. G. 2000, [ApJ](#), **537**, 644
- Gil de Paz, A., Boissier, S., Madore, B. F., et al. 2007, [ApJS](#), **173**, 185
- Gil de Paz, A., Zamorano, J., & Gallego, J. 2000, [A&A](#), **361**, 465
- Giveon, U., Sternberg, A., Lutz, D., Feuchtgruber, H., & Pauldrach, A. W. A. 2002, [ApJ](#), **566**, 880
- Glover, S. C. O. & Clark, P. C. 2012, [MNRAS](#), **421**, 9
- Glover, S. C. O., Federrath, C., Mac Low, M.-M., & Klessen, R. S. 2010, [MNRAS](#), **404**, 2
- Glover, S. C. O. & Mac Low, M.-M. 2011, [MNRAS](#), **412**, 337
- Goldreich, P. & Kwan, J. 1974, [ApJ](#), **189**, 441
- Gordon, K. D., Clayton, G. C., Misselt, K. A., Landolt, A. U., & Wolff, M. J. 2003, [ApJ](#), **594**, 279
- Gordon, K. D., Galliano, F., Hony, S., et al. 2010, [A&A](#), **518**, L89
- Graciá-Carpio, J., Sturm, E., Hailey-Dunsheath, S., et al. 2011a, [ApJ](#), **728**, L7
- Graciá-Carpio, J., Sturm, E., Hailey-Dunsheath, S., et al. 2011b, [ApJ](#), **728**, L7
- Grebel, E. K. 2001, in Dwarf galaxies and their environment, ed. K. S. de Boer, R.-J. Dettmar, & U. Klein, 45
- Grenier, I. A., Casandjian, J.-M., & Terrier, R. 2005, [Science](#), **307**, 1292
- Grimes, J. P., Heckman, T., Strickland, D., et al. 2007, [ApJ](#), **668**, 891
- Grossi, M., Hunt, L. K., Madden, S., et al. 2010, [A&A](#), **518**, L52
- Guseva, N. G., Izotov, Y. I., & Thuan, T. X. 1998, [Kinematics and Physics of Celestial Bodies](#), **14**, 41
- Habing, H. J. 1968, [Bull. Astron. Inst. Netherlands](#), **19**, 421
- Hailey-Dunsheath, S., Nikola, T., Stacey, G. J., et al. 2010, [ApJ](#), **714**, L162
- Haro, G. 1956, [Boletín de los Observatorios Tonantzintla y Tacubaya](#), **2**, 8
- Helou, G., Khan, I. R., Malek, L., & Boehmer, L. 1988, [ApJS](#), **68**, 151
- Henry, R. B. C. 1993, [MNRAS](#), **261**, 306
- Henry, R. B. C., Edmunds, M. G., & Köppen, J. 2000, [ApJ](#), **541**, 660
- Hickson, P. 1982, [ApJ](#), **255**, 382
- Higdon, S. J. U., Armus, L., Higdon, J. L., Soifer, B. T., & Spoon, H. W. W. 2006, [ApJ](#), **648**, 323
- Hodge, P., Lee, M. G., & Kennicutt, Jr., R. C. 1989, [PASP](#), **101**, 640
- Hodge, P., Smith, T., Eskridge, P., MacGillivray, H., & Beard, S. 1991, [ApJ](#), **379**, 621
- Hogerheijde, M. R. & van der Tak, F. F. S. 2000, [A&A](#), **362**, 697
- Hollenbach, D. & McKee, C. F. 1989, [ApJ](#), **342**, 306
- Hollenbach, D. J. & Tielens, A. G. G. M. 1999, [Reviews of Modern Physics](#), **71**, 173
- Hony, S., Galliano, F., Madden, S. C., et al. 2010, [A&A](#), **518**, L76
- Hopkins, A. M., Schulte-Ladbeck, R. E., & Drozdovsky, I. O. 2002, [AJ](#), **124**, 862
- Houck, J. R., Charmandaris, V., Brandl, B. R., et al. 2004, [ApJS](#), **154**, 211
- Houck, J. R., Shure, M. A., Gull, G. E., & Herter, T. 1984, [ApJ](#), **287**, L11



- Hunt, L. K., Thuan, T. X., Izotov, Y. I., & Sauvage, M. 2010, [ApJ](#), **712**, 164
- Hunt, L. K., Thuan, T. X., Sauvage, M., & Izotov, Y. I. 2006, [ApJ](#), **653**, 222
- Hunter, D. 1997, [PASP](#), **109**, 937
- Hunter, D. A. & Elmegreen, B. G. 2004, [AJ](#), **128**, 2170
- Hunter, D. A., Elmegreen, B. G., & Baker, A. L. 1998, [ApJ](#), **493**, 595
- Hunter, D. A., Ficut-Vicas, D., Ashley, T., et al. 2012, [ArXiv e-prints](#)
- Hunter, D. A., Hawley, W. N., & Gallagher, III, J. S. 1993, [AJ](#), **106**, 1797
- Hunter, D. A. & Kaufman, M. 2007, [AJ](#), **134**, 721
- Hunter, D. A., Kaufman, M., Hollenbach, D. J., et al. 2001, [ApJ](#), **553**, 121
- Hunter, D. A., O’Connell, R. W., & Gallagher, III, J. S. 1994, [AJ](#), **108**, 84
- Iglesias-Paramo, J. & Vilchez, J. M. 1997, [ApJ](#), **479**, 190
- Indebetouw, R. et al. 2012, in preparation
- Israel, F. P. 1997, [A&A](#), **328**, 471
- Israel, F. P., Maloney, P. R., Geis, N., et al. 1996, [ApJ](#), **465**, 738
- Israel, F. P., Tilanus, R. P. J., & Baas, F. 2006, [A&A](#), **445**, 907
- Izotov, Y. I., Chaffee, F. H., Foltz, C. B., et al. 1999, [ApJ](#), **527**, 757
- Izotov, Y. I., Guseva, N. G., Fricke, K. J., & Papaderos, P. 2009, [A&A](#), **503**, 61
- Izotov, Y. I., Papaderos, P., Guseva, N. G., Fricke, K. J., & Thuan, T. X. 2006a, [A&A](#), **454**, 137
- Izotov, Y. I., Stasińska, G., Meynet, G., Guseva, N. G., & Thuan, T. X. 2006b, [A&A](#), **448**, 955
- Izotov, Y. I. & Thuan, T. X. 1998, [ApJ](#), **500**, 188
- Izotov, Y. I. & Thuan, T. X. 1999, [ApJ](#), **511**, 639
- Izotov, Y. I. & Thuan, T. X. 2004, [ApJ](#), **616**, 768
- Izotov, Y. I. & Thuan, T. X. 2007, [ApJ](#), **665**, 1115
- Izotov, Y. I. & Thuan, T. X. 2010, [ApJ](#), **710**, L67
- Izotov, Y. I., Thuan, T. X., & Guseva, N. G. 2005, [ApJ](#), **632**, 210
- Izotov, Y. I., Thuan, T. X., & Guseva, N. G. 2012, [ArXiv e-prints](#)
- James, A., Dunne, L., Eales, S., & Edmunds, M. G. 2002, [MNRAS](#), **335**, 753
- James, B. L., Tsamis, Y. G., Barlow, M. J., et al. 2009, [MNRAS](#), **398**, 2
- James, P. 1991, [MNRAS](#), **250**, 544
- Jerjen, H., Binggeli, B., & Freeman, K. C. 2000, [AJ](#), **119**, 593
- Johnson, K. E., Leitherer, C., Vacca, W. D., & Conti, P. S. 2000, [AJ](#), **120**, 1273
- Kaufman, M. J., Wolfire, M. G., & Hollenbach, D. J. 2006, [ApJ](#), **644**, 283
- Kaufman, M. J., Wolfire, M. G., Hollenbach, D. J., & Luhman, M. L. 1999, [ApJ](#), **527**, 795
- Kazandjian, M. V., Meijerink, R., Pelupessy, I., Israel, F. P., & Spaans, M. 2012, [A&A](#), **542**, A65
- Kehrig, C., Vilchez, J. M., Sánchez, S. F., et al. 2008, [A&A](#), **477**, 813
- Kennicutt, R. C., Calzetti, D., Aniano, G., et al. 2011, [PASP](#), **123**, 1347

- Kennicutt, Jr., R. C. 1989, [ApJ](#), **344**, 685
- Kennicutt, Jr., R. C. 1998, [ApJ](#), **498**, 541
- Kennicutt, Jr., R. C., Armus, L., Bendo, G., et al. 2003, [PASP](#), **115**, 928
- Kennicutt, Jr., R. C., Calzetti, D., Walter, F., et al. 2007, [ApJ](#), **671**, 333
- Kennicutt, Jr., R. C., Lee, J. C., Funes, José G., S. J., Sakai, S., & Akiyama, S. 2008, [ApJS](#), **178**, 247
- Kester, D. J. M., Beintema, D. A., & Lutz, D. 2003, in ESA Special Publication, Vol. 481, The Calibration Legacy of the ISO Mission, ed. L. Metcalfe, A. Salama, S. B. Peschke, & M. F. Kessler, 375
- Kewley, L. J., Dopita, M. A., Sutherland, R. S., Heisler, C. A., & Trevena, J. 2001, [ApJ](#), **556**, 121
- Kewley, L. J. & Ellison, S. L. 2008, [ApJ](#), **681**, 1183
- Kim, S., Kwon, E., Madden, S. C., et al. 2010, [A&A](#), **518**, L75
- Kim, S., Staveley-Smith, L., Dopita, M. A., et al. 1998, [ApJ](#), **503**, 674
- Kobulnicky, H. A., Dickey, J. M., Sargent, A. I., Hogg, D. E., & Conti, P. S. 1995, [AJ](#), **110**, 116
- Kobulnicky, H. A. & Skillman, E. D. 1996, [ApJ](#), **471**, 211
- Kobulnicky, H. A., Skillman, E. D., Roy, J.-R., Walsh, J. R., & Rosa, M. R. 1997, [ApJ](#), **477**, 679
- Köppen, J. & Hensler, G. 2005, [A&A](#), **434**, 531
- Kramer, C., Mookerjea, B., Bayet, E., et al. 2005, [A&A](#), **441**, 961
- Krumholz, M. R. 2012, [ApJ](#), **759**, 9
- Krumholz, M. R., Leroy, A. K., & McKee, C. F. 2011, [ApJ](#), **731**, 25
- Krumholz, M. R., McKee, C. F., & Tumlinson, J. 2009, [ApJ](#), **693**, 216
- Krumholz, M. R. & Thompson, T. A. 2012, [ArXiv e-prints](#)
- Kunth, D., Leitherer, C., Mas-Hesse, J. M., Östlin, G., & Petrosian, A. 2003, [ApJ](#), **597**, 263
- Kunth, D., Lequeux, J., Sargent, W. L. W., & Viallefond, F. 1994, [A&A](#), **282**, 709
- Kunth, D., Matteucci, F., & Marconi, G. 1995, [A&A](#), **297**, 634
- Kunth, D. & Östlin, G. 2000, [A&A Rev.](#), **10**, 1
- Kunth, D. & Sargent, W. L. W. 1986, [ApJ](#), **300**, 496
- Lada, C. J. & Lada, E. A. 2003, [ARA&A](#), **41**, 57
- Lawton, B., Gordon, K. D., Babler, B., et al. 2010, [ApJ](#), **716**, 453
- Le Petit, F., Nehmé, C., Le Bourlot, J., & Roueff, E. 2006, [ApJS](#), **164**, 506
- Lebouteiller, V., Kunth, D., Lequeux, J., et al. 2006, [A&A](#), **459**, 161
- Lebouteiller, V., Kunth, D., Lequeux, J., et al. 2004, [A&A](#), **415**, 55
- Lebouteiller, V. et al. 2012, submitted to [A&A](#)
- Lee, J. C., Gil de Paz, A., Kennicutt, Jr., R. C., et al. 2011, [ApJS](#), **192**, 6
- Legrand, F., Kunth, D., Roy, J.-R., Mas-Hesse, J. M., & Walsh, J. R. 1997, [A&A](#), **326**, L17
- Leitherer, C., Ortiz Otálvaro, P. A., Bresolin, F., et al. 2010, [ApJS](#), **189**, 309
- Leon, S., Combes, F., & Menon, T. K. 1998, [A&A](#), **330**, 37
- Leroy, A., Bolatto, A., Stanimirovic, S., et al. 2007, [ApJ](#), **658**, 1027

- Leroy, A., Bolatto, A. D., Simon, J. D., & Blitz, L. 2005, [ApJ](#), 625, 763
- Leroy, A. K., Bolatto, A., Bot, C., et al. 2009a, [ApJ](#), 702, 352
- Leroy, A. K., Bolatto, A., Gordon, K., et al. 2011, [ApJ](#), 737, 12
- Leroy, A. K., Walter, F., Bigiel, F., et al. 2009b, [AJ](#), 137, 4670
- Leroy, A. K., Walter, F., Brinks, E., et al. 2008, [AJ](#), 136, 2782
- Levesque, E. M., Kewley, L. J., & Larson, K. L. 2010, [AJ](#), 139, 712
- Lisenfeld, U. & Ferrara, A. 1998, [ApJ](#), 496, 145
- Lisenfeld, U., Israel, F. P., Stil, J. M., & Sievers, A. 2002, [A&A](#), 382, 860
- Loenen, A. F., Spaans, M., Baan, W. A., & Meijerink, R. 2008, [A&A](#), 488, L5
- Luhman, M. L., Satyapal, S., Fischer, J., et al. 1998, [ApJ](#), 504, L11
- Luhman, M. L., Satyapal, S., Fischer, J., et al. 2003, [ApJ](#), 594, 758
- MacAlpine, G. M., Smith, S. B., & Lewis, D. W. 1977, [ApJS](#), 34, 95
- MacKenty, J. W., Maíz-Apellániz, J., Pickens, C. E., Norman, C. A., & Walborn, N. R. 2000, [AJ](#), 120, 3007
- Madau, P., Ferguson, H. C., Dickinson, M. E., et al. 1996, [MNRAS](#), 283, 1388
- Madden, S. C. 2000, [New Astronomy Review](#), 44, 249
- Madden, S. C., Galametz, M., Cormier, D., et al. 2011, in EAS Publications Series, Vol. 52, EAS Publications Series, ed. M. Röllig, R. Simon, V. Ossenkopf, & J. Stutzki, 95–101
- Madden, S. C., Galliano, F., Jones, A. P., & Sauvage, M. 2006, [A&A](#), 446, 877
- Madden, S. C., Poglitsch, A., Geis, N., Stacey, G. J., & Townes, C. H. 1997, [ApJ](#), 483, 200
- Madden, S. C., Remy, A., Galliano, F., et al. 2012a, [ArXiv e-prints](#)
- Madden, S. C. et al. 2012b, in preparation
- Maiolino, R., Caselli, P., Nagao, T., et al. 2009, [A&A](#), 500, L1
- Makarov, D. & Karachentsev, I. 2011, [MNRAS](#), 412, 2498
- Malhotra, S., Helou, G., Stacey, G., et al. 1997, [ApJ](#), 491, L27
- Malhotra, S., Kaufman, M. J., Hollenbach, D., et al. 2001, [ApJ](#), 561, 766
- Markarian, B. E. 1967, [Astrofizika](#), 3, 55
- Marlowe, A. T., Heckman, T. M., Wyse, R. F. G., & Schommer, R. 1995, [ApJ](#), 438, 563
- Martin, C. L. 1999, [ApJ](#), 513, 156
- Massey, P. & Johnson, O. 1998, [ApJ](#), 505, 793
- Mathis, J. S., Rumpl, W., & Nordsieck, K. H. 1977, [ApJ](#), 217, 425
- McConnachie, A. W. 2012, [AJ](#), 144, 4
- Meier, D. S., Turner, J. L., Crosthwaite, L. P., & Beck, S. C. 2001, [AJ](#), 121, 740
- Meijerink, R. & Spaans, M. 2005, [A&A](#), 436, 397
- Meijerink, R., Spaans, M., Loenen, A. F., & van der Werf, P. P. 2011, [A&A](#), 525, A119
- Meixner, M., Galliano, F., Hony, S., et al. 2010, [A&A](#), 518, L71
- Melisse, J. P. M. & Israel, F. P. 1994, [A&A](#), 285, 51
- Melnick, J., Moles, M., & Terlevich, R. 1985, [A&A](#), 149, L24

- Meny, C., Gromov, V., Boudet, N., et al. 2007, [A&A](#), 468, 171
- Moore, B., Ghigna, S., Governato, F., et al. 1999, [ApJ](#), 524, L19
- Nagamine, K. 2010, [Advances in Astronomy](#), 2010
- Narayanan, D., Krumholz, M. R., Ostriker, E. C., & Hernquist, L. 2012, [MNRAS](#), 421, 3127
- Neufeld, D. A., Nisini, B., Giannini, T., et al. 2009, [ApJ](#), 706, 170
- Oberst, T. E., Parshley, S. C., Stacey, G. J., et al. 2006, [ApJ](#), 652, L125
- O’Halloran, B., Galametz, M., Madden, S. C., et al. 2010, [A&A](#), 518, L58
- Ohta, K., Tomita, A., Saito, M., Sasaki, M., & Nakai, N. 1993, [PASJ](#), 45, L21
- Osterbrock, D. E. & Ferland, G. J. 2006, Astrophysics of gaseous nebulae and active galactic nuclei
- Östlin, G., Amram, P., Bergvall, N., et al. 2001, [A&A](#), 374, 800
- Östlin, G., Amram, P., Masegosa, J., Bergvall, N., & Boulesteix, J. 1999, [A&AS](#), 137, 419
- Otsuka, M., van Loon, J. T., Long, K. S., et al. 2010, [A&A](#), 518, L139
- Ott, S. 2010, in Astronomical Society of the Pacific Conference Series, Vol. 434, Astronomical Data Analysis Software and Systems XIX, ed. Y. Mizumoto, K.-I. Morita, & M. Ohishi, 139
- Pagel, B. E. J., Edmunds, M. G., Fosbury, R. A. E., & Webster, B. L. 1978, [MNRAS](#), 184, 569
- Pagel, B. E. J., Terlevich, R. J., & Melnick, J. 1986, [PASP](#), 98, 1005
- Papadopoulos, P. P., Isaak, K., & van der Werf, P. 2010, [ApJ](#), 711, 757
- Paradis, D., Reach, W. T., Bernard, J.-P., et al. 2011, [AJ](#), 141, 43
- Pérez-Montero, E., Vílchez, J. M., Cedrés, B., et al. 2011, [A&A](#), 532, A141
- Pierini, D., Leech, K. J., & Völk, H. J. 2003, [A&A](#), 397, 871
- Pilbratt, G. L., Riedinger, J. R., Passvogel, T., et al. 2010, [A&A](#), 518, L1+
- Pineda, J. L., Mizuno, N., Roellig, M., et al. 2012, [ArXiv e-prints](#)
- Pineda, J. L., Mizuno, N., Stutzki, J., et al. 2008, [A&A](#), 482, 197
- Planck Collaboration, Ade, P. A. R., Aghanim, N., et al. 2011, [A&A](#), 536, A19
- Poglitsch, A., Krabbe, A., Madden, S. C., et al. 1995, [ApJ](#), 454, 293
- Poglitsch, A., Waelkens, C., Geis, N., et al. 2010, [A&A](#), 518, L2+
- Portas, A., Scott, T. C., Brinks, E., et al. 2011, [ApJ](#), 739, L27
- Pustilnik, S., Kniazev, A., Pramskij, A., et al. 2004, [A&A](#), 419, 469
- Pustilnik, S. A., Kniazev, A. Y., Lipovetsky, V. A., & Ugryumov, A. V. 2001, [A&A](#), 373, 24
- Rangwala, N., Maloney, P. R., Glenn, J., et al. 2011, [ApJ](#), 743, 94
- Rémy, A. et al. 2012, in preparation
- Roberts, M. S. & Haynes, M. P. 1994, [ARA&A](#), 32, 115
- Röllig, M., Abel, N. P., Bell, T., et al. 2007, [A&A](#), 467, 187
- Röllig, M., Ossenkopf, V., Jeyakumar, S., Stutzki, J., & Sternberg, A. 2006a, [A&A](#), 451, 917
- Röllig, M., Ossenkopf, V., Jeyakumar, S., Stutzki, J., & Sternberg, A. 2006b, [A&A](#), 451, 917
- Roman-Duval, J., Israel, F. P., Bolatto, A., et al. 2010, [A&A](#), 518, L74

- Roussel, H., Helou, G., Hollenbach, D. J., et al. 2007, *ApJ*, 669, 959
- Roussel, H., Wilson, C. D., Vigroux, L., et al. 2010, *A&A*, 518, L66
- Roy, J.-R. & Kunth, D. 1995, *A&A*, 294, 432
- Rubin, D., Hony, S., Madden, S. C., et al. 2009, *A&A*, 494, 647
- Rubin, R. H., Simpson, J. P., Lord, S. D., et al. 1994, *ApJ*, 420, 772
- Sage, L. J., Salzer, J. J., Loose, H.-H., & Henkel, C. 1992, *A&A*, 265, 19
- Saintonge, A., Kauffmann, G., Wang, J., et al. 2011, *MNRAS*, 415, 61
- Sánchez-Janssen, R. & Sánchez-Janssen. 2011, in IAU Symposium, Vol. 277, IAU Symposium, ed. C. Carignan, F. Combes, & K. C. Freeman, 230–233
- Sanders, D. B. & Mirabel, I. F. 1996, *ARA&A*, 34, 749
- Sauvage, M., Vigroux, L., & Thuan, T. X. 1990, *A&A*, 237, 296
- Schaller, G., Schaerer, D., Meynet, G., & Maeder, A. 1992, *A&AS*, 96, 269
- Schiminovich, D., Catinella, B., Kauffmann, G., et al. 2010, *MNRAS*, 408, 919
- Schmidt, M. 1959, *ApJ*, 129, 243
- Schmitt, H. R., Calzetti, D., Armus, L., et al. 2006, *ApJS*, 164, 52
- Schruba, A., Leroy, A. K., Walter, F., et al. 2012, *ArXiv e-prints*
- Seale, J. P., Looney, L. W., Wong, T., et al. 2012, *ApJ*, 751, 42
- Searle, L. & Sargent, W. L. W. 1972, *ApJ*, 173, 25
- Sewilo, M., Indebetouw, R., Carlson, L. R., et al. 2010, *A&A*, 518, L73
- Shapley, A. E., Erb, D. K., Pettini, M., Steidel, C. C., & Adelberger, K. L. 2004, *ApJ*, 612, 108
- Sheffer, Y., Wolfire, M. G., Hollenbach, D. J., Kaufman, M. J., & Cordier, M. 2011, *ApJ*, 741, 45
- Shetty, R., Glover, S. C., Dullemond, C. P., & Klessen, R. S. 2011, *MNRAS*, 412, 1686
- Shields, J. C. & Kennicutt, Jr., R. C. 1995, *ApJ*, 454, 807
- Simon, J. D. & Geha, M. 2007, *ApJ*, 670, 313
- Simpson, C. E., Hunter, D. A., Nordgren, T. E., et al. 2011, *AJ*, 142, 82
- Skillman, E. D. 1998, in Stellar astrophysics for the local group: VIII Canary Islands Winter School of Astrophysics, ed. A. Aparicio, A. Herrero, & F. Sánchez, 457
- Skillman, E. D. & Bender, R. 1995, in Revista Mexicana de Astronomía y Astrofísica, vol. 27, Vol. 3, Revista Mexicana de Astronomía y Astrofísica Conference Series, ed. M. Pena & S. Kurtz, 25
- Skillman, E. D., Côté, S., & Miller, B. W. 2003, *AJ*, 125, 593
- Skillman, E. D., Kennicutt, R. C., & Hodge, P. W. 1989, *ApJ*, 347, 875
- Smoker, J. V., Davies, R. D., Axon, D. J., & Hummel, E. 2000, *A&A*, 361, 19
- Sobolev, V. V. & Gaposchkin, S. 1960, *JRASC*, 54, 254
- Solomon, P. M., Rivolo, A. R., Barrett, J., & Yahil, A. 1987, *ApJ*, 319, 730
- Stacey, G. J., Geis, N., Genzel, R., et al. 1991, *ApJ*, 373, 423
- Stacey, G. J., Hailey-Dunsheath, S., Ferkinhoff, C., et al. 2010, *ApJ*, 724, 957
- Stanimirović, S., Staveley-Smith, L., & Jones, P. A. 2004, *ApJ*, 604, 176
- Staveley-Smith, L., Davies, R. D., & Kinman, T. D. 1992, *MNRAS*, 258, 334

- Sternberg, A. & Dalgarno, A. 1995, [ApJS](#), **99**, 565
- Stoerzer, H., Stutzki, J., & Sternberg, A. 1996, [A&A](#), **310**, 592
- Strong, A. W., Bloemen, J. B. G. M., Dame, T. M., et al. 1988, [A&A](#), **207**, 1
- Taylor, C. L., Kobulnicky, H. A., & Skillman, E. D. 1998, [AJ](#), **116**, 2746
- Terlevich, R., Melnick, J., Masegosa, J., Moles, M., & Copetti, M. V. F. 1991, [A&AS](#), **91**, 285
- Thuan, T. X., Hibbard, J. E., & L  vrier, F. 2004, [AJ](#), **128**, 617
- Thuan, T. X., Hunt, L. K., & Izotov, Y. I. 2008, [ApJ](#), **689**, 897
- Thuan, T. X. & Izotov, Y. I. 2005, [ApJS](#), **161**, 240
- Thuan, T. X., Izotov, Y. I., & Lipovetsky, V. A. 1996, [ApJ](#), **463**, 120
- Thuan, T. X., Lecavelier des Etangs, A., & Izotov, Y. I. 2005, [ApJ](#), **621**, 269
- Thuan, T. X. & Martin, G. E. 1981, [ApJ](#), **247**, 823
- Tielens, A. G. G. M. 2005, The Physics and Chemistry of the Interstellar Medium
- Tielens, A. G. G. M. & Hollenbach, D. 1985, [ApJ](#), **291**, 722
- Tielens, A. G. G. M., Meixner, M. M., van der Werf, P. P., et al. 1993, [Science](#), **262**, 86
- Toomre, A. 1964, [ApJ](#), **139**, 1217
- Tosi, M., Aloisi, A., Mack, J., & Maio, M. 2007, in IAU Symposium, Vol. 235, IAU Symposium, ed. F. Combes & J. Palous, 65–66
- Tumlinson, J., Shull, J. M., Rachford, B. L., et al. 2002, [ApJ](#), **566**, 857
- Ugryumov, A. V., Engels, D., Pustilnik, S. A., et al. 2003, [A&A](#), **397**, 463
- Vader, J. P., Frogel, J. A., Terndrup, D. M., & Heisler, C. A. 1993, [AJ](#), **106**, 1743
- Valcke, S., de Rijcke, S., & Dejonghe, H. 2008, [MNRAS](#), **389**, 1111
- van den Bergh, S. 1959, [Publications of the David Dunlap Observatory](#), **2**, 147
- van der Tak, F. F. S., Black, J. H., Sch  ier, F. L., Jansen, D. J., & van Dishoeck, E. F. 2007a, [A&A](#), **468**, 627
- van der Tak, F. F. S., Black, J. H., Sch  ier, F. L., Jansen, D. J., & van Dishoeck, E. F. 2007b, [A&A](#), **468**, 627
- van Eymeren, J., Marcelin, M., Koribalski, B. S., et al. 2009, [A&A](#), **505**, 105
- van Zee, L., Salzer, J. J., & Skillman, E. D. 2001, [AJ](#), **122**, 121
- Vanzi, L., Combes, F., Rubio, M., & Kunth, D. 2009, [A&A](#), **496**, 677
- Vink, J. S. & de Koter, A. 2005, [A&A](#), **442**, 587
- Walsh, J. R., Dudziak, G., Minniti, D., & Zijlstra, A. A. 1997, [ApJ](#), **487**, 651
- Walter, F., Brinks, E., de Blok, W. J. G., et al. 2008, [AJ](#), **136**, 2563
- Walter, F., Cannon, J. M., Roussel, H., et al. 2007, [ApJ](#), **661**, 102
- Walter, F., Taylor, C. L., H  ttemeister, S., Scoville, N., & McIntyre, V. 2001, [AJ](#), **121**, 727
- Weingartner, J. C. & Draine, B. T. 2001, [ApJ](#), **548**, 296
- Weisz, D. R., Dalcanton, J. J., Williams, B. F., et al. 2011, [ApJ](#), **739**, 5
- Wilcots, E. M., Lehman, C., & Miller, B. 1996, [AJ](#), **111**, 1575
- Wilcots, E. M. & Miller, B. W. 1998, [AJ](#), **116**, 2363

## BIBLIOGRAPHY

---

- Williams, B. A., McMahon, P. M., & van Gorkom, J. H. 1991, [AJ](#), **101**, 1957
- Wilson, C. D. 1992, [ApJ](#), **391**, 144
- Wilson, C. D., Howe, J. E., & Balogh, M. L. 1999, [ApJ](#), **517**, 174
- Wilson, C. D. & Reid, I. N. 1991, [ApJ](#), **366**, L11
- Wilson, C. D., Warren, B. E., Israel, F. P., et al. 2009, [ApJ](#), **693**, 1736
- Wolfire, M. G., Hollenbach, D., & McKee, C. F. 2010, [ApJ](#), **716**, 1191
- Wolfire, M. G., Hollenbach, D., McKee, C. F., Tielens, A. G. G. M., & Bakes, E. L. O. 1995, [ApJ](#), **443**, 152
- Wolfire, M. G., Tielens, A. G. G. M., & Hollenbach, D. 1990, [ApJ](#), **358**, 116
- Wright, E. L., Mather, J. C., Bennett, C. L., et al. 1991, [ApJ](#), **381**, 200
- Wu, R. et al. 2012, in preparation
- Wu, Y., Charmandaris, V., Hao, L., et al. 2006, [ApJ](#), **639**, 157
- Wu, Y., Charmandaris, V., Houck, J. R., et al. 2008, [ApJ](#), **676**, 970
- York, D. G., Adelman, J., Anderson, Jr., J. E., et al. 2000, [AJ](#), **120**, 1579
- Young, L. M. & Lo, K. Y. 1996, [ApJ](#), **462**, 203
- Young, L. M. & Lo, K. Y. 1997, [ApJ](#), **490**, 710
- Ysard, N., Juvela, M., & Verstraete, L. 2011, [A&A](#), **535**, A89
- Zubko, V., Dwek, E., & Arendt, R. G. 2004, [ApJS](#), **152**, 211
- Zwicky, F. & Zwicky, M. A. 1971, Catalogue of selected compact galaxies and of post-eruptive galaxies